Wissenschaftliche Mitteilungen

aus dem
Institut für Meteorologie der Universität Leipzig

Meteorologische Arbeiten (XV) und Jahresbericht 2009 des Instituts für Meteorologie der Universität Leipzig

Hrsg.: Armin Raabe

Leipzig 2010   **Band 47**

Airborne remote sensing of Arctic boundary-layer mixed-phase clouds

André Ehrlich, Eike Bierwirth, Manfred Wendisch

Summary

This article gives an overview on the investigations on Artic boundary-layer mixed-phase clouds conducted within the Arctic Study of Tropospheric Aerosol, Clouds and Radiation (ASTAR) in spring 2007. In particular the horizontal and vertical disribution of ice crystals within the clouds was determined by three independent airborne instruments (lidar, in situ and solar radiation measurements).

Spectral measurements of cloud top reflectivity have been utilized to retrieve information on the ice phase by analyzing the spectral pattern of the cloud top reflectance in the wavelength range dominated by liquid water and ice absorption (1400-1700 nm). A new algorithm to derive an ice index which distinguishes pure ice, liquid water, and mixed-phase clouds was developed. The horizontal distribution of the ice index, observed during ASTAR 2007, agrees with airborne lidar and in situ measurements showing patches of glaciated clouds at an air mass transition zone within the investigated mixed-phase cloud fields.

Information on the vertical distribution of ice crystals in mixed-phase clouds was derived by comparing the measured cloud top reflectivity in the wavelength band 1400-1700 nm to radiative transfer simulations. To interpret the data, the vertical weighting of the measurements was calculated. In the investigated wavelength range the weightings differ according to the spectral absorption of ice and liquid water. From the observed spectral cloud reflectivity with low values in the ice absorption maximum (1400 nm) and higher values at the liquid water absorption maximum (1700 nm) it was concluded that ice crystals were present in the otherwise liquid dominated cloud top layer. Although in situ measurements (limited due to vertical resolution and detection limits) did confirm these findings only in certain limits, the retrieved vertical structure is in agreement with published ground based remote sensing measurements.

1   Arctic boundary-layer mixed-phase clouds

Mixed-phase clouds are common in the Arctic due to low temperatures. In particular, Arctic boundary-layer mixed-phase (ABM) clouds form above open sea in conjunction with cold air outbreaks. They consist of both, supercooled liquid water particles and solid ice crystals simultaneously, and were observed and investigated during numerous Arctic field experiments (e.g., Turner et al., 2003, Verlinde et al., 2007, Shupe et al., 2008).

The persistent coexistence of ice crystals (ice water content, IWC) and liquid water particles (liquid water content, LWC) in these clouds relies on the balance between the condensation rate of liquid water droplets (LWC rate), the ice crystal growth rate (IWC rate), and the removal of ice nuclei (IN) by precipitating ice crystals. Such a basic scheme was introduced by (Harrington et al., 1999) and is displayed in Figure 1.

The unstable temperature layering above the open sea induces convection by which liquid water nucleation occurs in the updrafts (increase of LWC). As the concentration of cloud condensation nuclei (CCN) is typically lower than the concentration of IN (*e.g.*, Fridlind et al., 2007, Morrison et al., 2008), the liquid water nucleation exceeds the ice crystal nucleation in this part
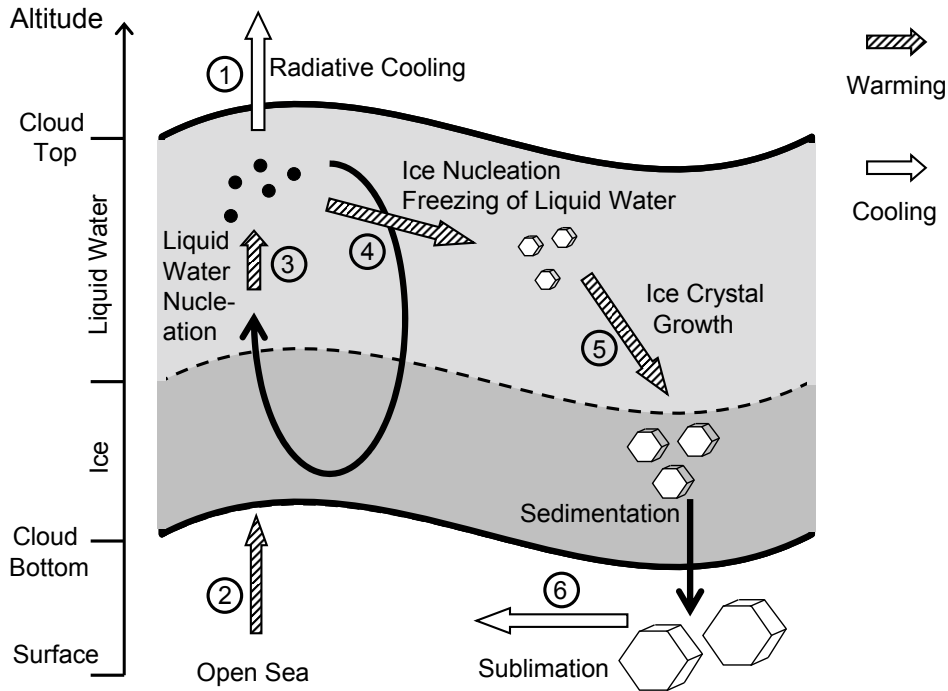
Figure 1: Illustration of the relevant processes present in ABM clouds. Processes that cause a cooling of the surrounding air are indicated by empty arrows; processes which lead to a warming are plotted with filled arrows.

of the cloud (LWC rate > IWC rate). However, once ice crystals have formed from IN or by freezing of liquid water droplets, they grow due to the Wegener-Bergeron-Findeisen mechanism at the expanse of the liquid water droplets. Finally, the ice crystals start to sediment which removes ice mass (decrease of IWC) and IN from the cloud system. The removal of IN due to the precipitating ice crystals reduces the ice crystal number concentration and prevents for total glaciation of the ABM clouds.

However, this equilibrium state is unstable. Slight changes might shift the fractional ice and liquid water component drastically (e.g. Morrison et al., 2008, Fan et al., 2008, Harrington et al., 1999). The radiative impact of such phase transitions in Arctic mixed-phase clouds was investigated by Ehrlich (2009) and Ehrlich et al. (2008b) using radiative transfer simulations. The local and temporary radiative forcing $\mathcal{F}_\Delta$ of an exemplary Arctic boundary-layer mixed-phase cloud was simulated in dependance of its ice volume fraction f_I which is defined by the ratio of IWC to total water content TWC,

$$f_I = \frac{IWC}{TWC}.$$ (1)

If a mixed-phase clouds glaciates into a pure ice cloud, which is consistent to an increase of f_I for constant TWC, the cloud optical thickness decreases due to the larger size of the ice crystals compared to the smaller liquid water droplets. The result is an decrease of the clouds radiative impact as shown in Figure 2. The simulations shown here are performed for a solar zenith angle of $\theta_0 = 71°$ and a typical ABM cloud with a total water path of $TWP = 100\,\mathrm{g\,m^{-2}}$, an ice crystal effective diameter of $D_{\mathrm{eff}}^I = 90\,\mu\mathrm{m}$ and water droplets with effective diameter of $D_{\mathrm{eff}}^W = 15\,\mu\mathrm{m}$. For both, surface and top of the atmosphere, $\mathcal{F}_\Delta$ increases significantly about $90\,\mathrm{W\,m^{-2}}$ with increasing f_I. This means that the cooling of the clouds is reduced when a
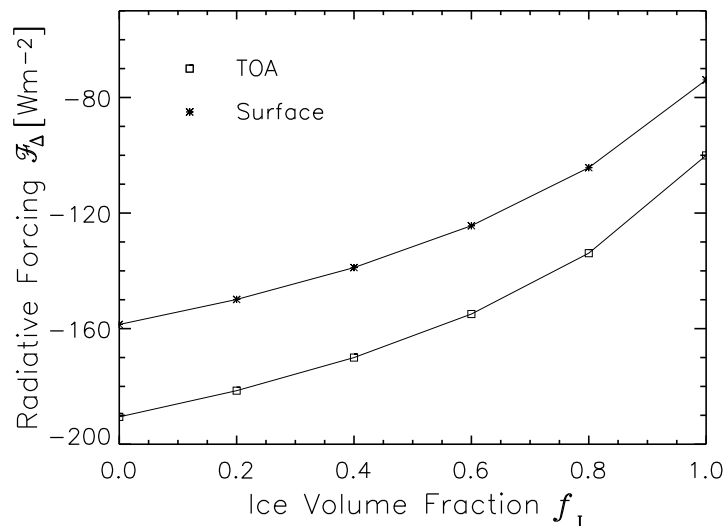
Figure 2: Radiative forcing $\mathcal{F}_\Delta$ of mixed-phase clouds calculated for the top of atmosphere (TOA) and the surface. The state of mixing was varied using f_I with $TWP = 100\,\mathrm{g\,m^{-2}}$, $D_\mathrm{eff}^\mathrm{I} = 90\,\mu\mathrm{m}$ and $D_\mathrm{eff}^\mathrm{W} = 15\,\mu\mathrm{m}$.

transition from liquid or mixed-phase to pure ice clouds occurs.

The investigations published by Ehrlich (2009) and Ehrlich et al. (2008b) have shown that knowledge on the thermodynamic state (liquid water, mixed-phase or ice) of clouds is essential to determine their radiative impact. On a global scale, satellite measurements are currently the only option to characterize clouds in this regard. Similar remote sensing techniques using airborne solar radiation measurements will be described in the following sections.

2 Airborne Measurements

Airborne measurements to characterize ABM clouds were obtained during the Arctic Study of Tropospheric Aerosol, Clouds and Radiation (ASTAR) 2007 campaign. The campaign took place in the vicinity of Svalbard ($78°$ N, $15°$ E) in March/April 2007 and focused on the sampling of ABM clouds.

During ASTAR 2007 the POLAR 2 aircraft, owned by the Alfred Wegener Institute for Polar and Marine Research (AWI), Bremerhaven, Germany, was equipped to probe clouds with airborne remote-sensing and in situ instruments. The Spectral Modular Airborne Radiation measurement sysTem (SMART) albedometer, the Airborne Mobile Aerosol Lidar (AMALi) and in situ instruments such as Polar Nephelometer, Cloud Particle Imager (CPI), and Particle Measuring System (PMS) Forward Scattering Spectrometer Probe (FSSP-100), operated on Polar 2, have been described in detail by Ehrlich (2009), Lampert et al. (2009a) and Gayet et al. (2009), respectively.

The SMART-Albedometer was used to perform remote sensing measurements using solar radiation (Wendisch et al., 2001, Bierwirth et al., 2009). The specific configuration of the SMART-Albedometer, operated during ASTAR 2007, has been introduced in detail by Ehrlich et al. (2008a). It provides measurements of downwelling and upwelling spectral irradiances ($F_\lambda^\downarrow$, $F_\lambda^\uparrow$) simultaneously with upwelling nadir spectral radiance ($I_\lambda^\uparrow$). These data were used to calculate spectral cloud-top reflectivities R in the wavelength range between $350\,\mathrm{nm}$ and $2150\,\mathrm{nm}$ by,

$$R(\lambda) = \frac{\pi\,\mathrm{sr}\cdot I_\lambda^\uparrow}{F_\lambda^\downarrow}. \tag{2}$$

In this definition $F_\lambda^\downarrow$ includes diffuse and direct solar radiation and is measured with respect to a horizontal plane $F_\lambda^\downarrow = F_\lambda^\downarrow(\cos\theta)$ with θ being the solar zenith angle. The spectral resolution of $R(\lambda)$ (full width at half maximum, FWHM) amounts to 2–3 nm in the wavelength range 350–950 nm and 9-16 nm for $\lambda = 950$–2150 nm wavelength.

AMALi is a two-wavelength (532 nm and 355 nm) backscatter lidar with depolarization measurements at 532 nm wavelength. For cloud observations, AMALi was installed in nadir-looking configuration. The vertical resolution was 7.5 m; the minimum horizontal resolution was about 900 m. The depolarization ratio derived from the 532 nm wavelength channel allows to distinguish lidar backscatter signals of ice crystals from those of liquid water droplets.

The in situ measurements of cloud microphysical properties include particle number size distribution in the size range of 3-27 μm for the FSSP and 23-2300 μm for the CPI, extinction coefficient, ice and liquid water content and effective diameter. The Polar Nephelometer provides the scattering phase function and the asymmetry parameter, a measure for the anisotropy of the scattering phase function.

The data of all three instruments have been used to derive information on the horizontal and vertical distribution of ice crystals in ABM clouds.

3   Horizontal distribution of ice

3.1   Methodology

The characteristics of the spectral reflectivity measurements of the SMART-albedometer were utilized in three different approaches to retrieve the cloud thermodynamic phase (pure liquid, mixed-phase and pure ice cloud). Two ice indices were calculated based on the differences in the spectral absorption of ice and liquid water. Therefore, a known two-wavelengths approach (spectral slope ice index) and a principle component analysis (PCA ice index) was applied. A third approach used the different scattering characteristics of ice crystals and liquid water droplets and combined albedo and reflectance measurements to obtain information on the cloud phase (anisotropy ice index). A detailed description of the methodology and a discussion on the applicability of these ice indices have been published in Ehrlich et al. (2008a).

The dimensionless spectral Slope Ice Index I_S was adapted from Acarreta et al. (2004) to the specifications of the SMART-albedometer using the wavelength range between $\lambda_a = 1550$ nm and $\lambda_b = 1700$ nm and is defined by,

$$I_S = 100 \cdot \frac{\lambda_b - \lambda_a}{R_{1640}} \cdot \left[\frac{dR}{d\lambda}\right]_{[\lambda_a, \lambda_b]} \tag{3}$$

Typical values for liquid water clouds range between $I_S = 5$ and $I_S = 15$. Ice clouds show a higher variability of I_S with values of up to 80.

The PCA ice index I_P utilizes the principle components of the reflectivity measurements which are related to ice PC_I and liquid water absorption PC_W. The dimensionless index is defined as,

$$I_P = \left(\frac{PC_I}{PC_W} - 0.94\right) \cdot 100. \tag{4}$$

The offset of 0.94 has been determined arbitrarily in order to obtain values close to zero for liquid water clouds ($I_P = 0$–1). For ice clouds, I_P ranges from values of 1 up to 8 clearly capable of being distinguished from liquid water clouds.

Sensitivity studies have shown that both indices, I_S and I_P, are most sensitive to the upper cloud layer. Further, their values depend strongly on the ice particle effective diameter and less on the cloud optical thickness for $\tau < 5$. Nevertheless, an ambiguity in the discrimination of

ice and liquid water phase occurs only between pure ice clouds with small ice crystals and low τ, and pure liquid water clouds of high τ. More crucial is the dependence on the ice particle effective diameter for the discrimination between mixed-phase and pure ice clouds. Here, *a priori* knowledge about the ice crystal dimensions is required.

Independently, the particle phase was determined from in situ data, based on the combination of asymmetry parameter and particle number concentration measurements (Gayet et al., 2009). As an approximation it was defined that the FSSP (size range 3–27 μm) measured liquid water droplets, whereas the CPI (23–2 300 μm) was used to determine the size distribution of large ice crystals. This assumption is based on the ice crystals sizes expected for mixed-phase conditions (*e.g.*, Korolev et al., 2003, Shupe et al., 2006). Due to the WBF process, the ice crystals rapidly grow to sizes larger than the range covered by the FSSP. This assumption was justified by simultaneous polar nephelometer measurements of the asymmetry parameter $\langle g \rangle$ (Ehrlich, 2009). The analysis of the data showed that the majority of the FSSP measurements coincide with $\langle g \rangle = 0.84$–0.86 indicating liquid water droplets. The CPI measured high particle number concentrations where the asymmetry parameter indicates nonspherical ice crystals ($\langle g \rangle = 0.78$–0.80).

The laser of the AMALi lidar did not completely penetrate the optically thick clouds. However, AMALi did identify a liquid water layer at cloud top by the depolarization signal (Lampert et al., 2009a). Although multiple scattering in the liquid water layer generated high depolarization values, comparable to the depolarization signal of ice crystals, the detailed analysis of the lidar profiles averaged over 15 seconds reveals differences in the vertical pattern of the depolarization. The depolarization related to multiple scattering of liquid water particles increases slowly with cloud depth whereas nonspherical ice crystals result in an instantaneous increase of the depolarization (Hu et al., 2007). From this analysis the precipitating ice below the clouds was identified in several cloud gaps.

3.2   Case Study on April 9, 2007

On April 9, 2007 concurrent radiation and microphysical measurements have been conducted along the path of the Cloud-Aerosol Lidar and Infrared Pathfinder Satellite (CALIPSO) over the Greenland Sea as marked in Figure 3. A stratus cloud field with cloud top up to 2000 m extended above the open ocean west to Svalbard. Due to the weakened advective supply of cold air from the northern sea ice, the cloud field was characterized by heterogenous structures which are related to an air mass intersection (Gayet et al., 2009, Lampert et al., 2009b).

The profile of the total attenuated backscatter signal measured by CALIPSO is shown in Figure 4a and displays distinct cloud patches with different cloud top altitudes and vertical thicknesses. The cloud top altitude tends to increase towards North what is confirmed by the AMALi measurements. Between $78.7°$ N and $78.9°$ N a larger cloud gap has been observed. The cloud top is indicated by slightly enhanced depolarization signal of AMALi. Multiple scattering by the liquid water droplets at the cloud top layer leads to depolarization of the polarized radiation emitted by the AMALi laser. This layer with slightly enhanced
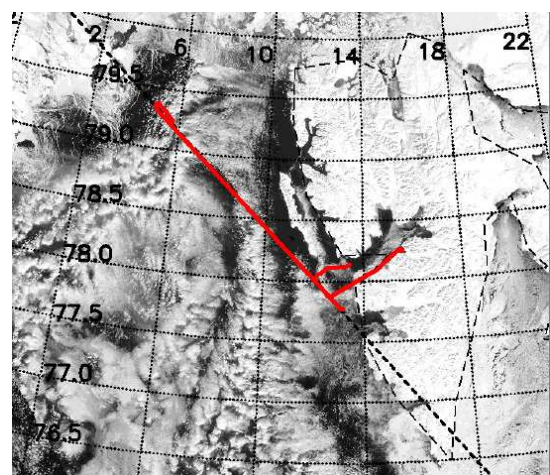
Figure 3: MODIS satellite image of April 9, 2007 overlaid with the flight track of POLAR 2 (red line) along the CALIPSO overpass (dashed black line). Numbers give the latitude and longitude respectively.

depolarization shows approximately the cloud top.

High depolarization ratios have been observed by AMALi between 78.5° N and 78.6° N and at about 79.0° N. The high depolarization indicates the presence of ice crystals. These areas coincide with high ice indices derived from the SMART-Albedometer measurements. Therefore, these cloud parts are identified as pure ice clouds. The in situ instruments did probe solely the ice cloud at 79.0° N. Here, ice crystal number concentrations up to $N_{\text{tot}} = 4\,\text{cm}^{-3}$ were measured. Although in situ measurements were taken at lower parts of this cloud, the remote sensing measurements reveal that the ice crystals were present up to the cloud top (Gayet et al., 2009).

The southern ice cloud was not completely sampled by the in situ measurements as the cloud top was significant lower at this location compared to the clouds observed in the surrounding area. The interruption of the cloud structure is visible at 78.5° N in the MODIS image taken at 10:00 UTC short before to the CALIPSO overpass (Figure 3). The lower cloud top and the ice crystals identified by the remote sensing instruments indicate that this part of the cloud mainly consists precipitating ice crystals which potentially have their origin in the surrounding clouds. South to 78.4° N the comparison of CALIPSO, in situ and remote sensing measurements fails due to the long time difference between the measurements. At the location between 78.2° N and 78.4° N a large cloud gap has been observed by CALIPSO and in situ instruments while the AMALi and SMART-Albedometer measurements indicate mixed-phase clouds with liquid cloud top layer.
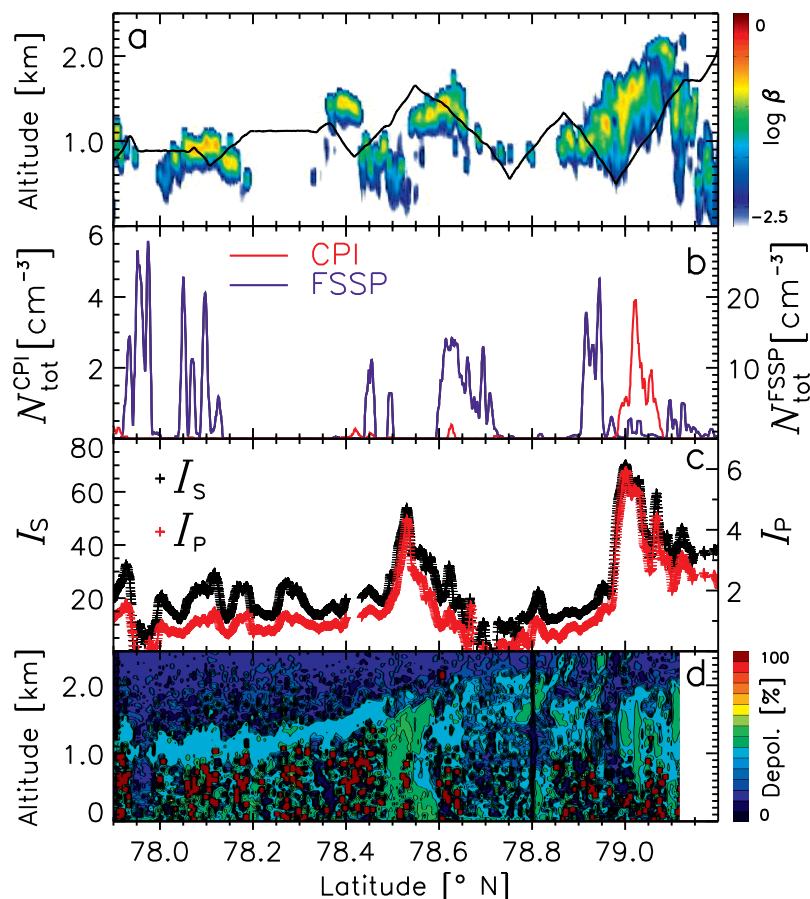
Figure 4: Profile of total attenuated backscatter coefficient β [sr^{-1} km^{-1}] measured by CALIPSO in the cloud observed on April 9th (a). The flight track of the in situ measurements is overlaid as a black line. Ice and liquid water particle number concentrations N_{tot} measured by CPI and FSSP along the flight track and the ice indices I_S and I_P for the same positions are given in panel b and c. The depolarization profile obtained from AMALi is given in panel d.

4 Vertical distribution of ice

All three types of measurement on board of Polar 2 (in situ, lidar and solar radiation) provide a view on the vertical distribution of ice crystals in ABM clouds. By ascents into the cloud layer vertical profiles of ice crystal and liquid water droplet concentration were obtained by the in situ instrumentation (Gayet et al., 2009).

A typical profile of measured particle number concentrations, asymmetry parameters, liquid LWC and ice water content IWC obtained on April, 7 2007 is given in Figure 5. The FSSP indicated particle concentrations and LWC up to $N_{\text{tot}}^{\text{FSSP}} = 50\,\text{cm}^{-3}$ and $LWC = 115\,\text{mg}\,\text{l}^{-l}$ between 1000–1700 m altitude. In the same layers the asymmetry parameter, measured by the Polar Nephelometer, was about 0.85 which is a typical value for spherical liquid water droplets (*e.g.*, Gerber et al., 2000, Garrett et al., 2001). A thin layer dominated by ice crystals was found between 800 m and 1100 m indicated by lower asymmetry parameters. In this layer the CPI measured particle number concentrations of up to $N_{\text{tot}}^{\text{CPI}} = 1.5\,\text{cm}^{-3}$ with maximum particle dimensions of up to 1000 μm. Although the ice crystal number concentration is about a magnitude lower than the liquid water droplet concentration the ice crystals dominate the total water content with $IWC = 70\,\text{mg}\,\text{l}^{-l}$. Below this layer, precipitating large ice particles have been observed down to 500 m by visual observation on board the aircraft and from in situ measurements (low ice water content and asymmetry parameter).
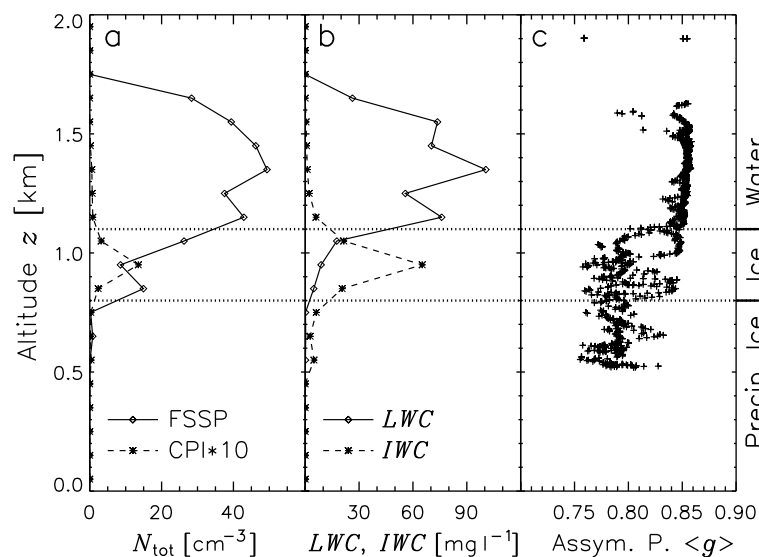
Figure 5: Profile of microphysical measurements obtained on April 7, 2007. Total particle number concentration N_{tot} measured by FSSP and CPI are given in panel a; LWC and IWC in panel b. The volumetric asymmetry parameter $\langle g \rangle$ obtained from the Polar Nephelometer is shown in panel c.

This vertical structure is typical for the Arctic stratus clouds, observed during ASTAR 2007, and was confirmed by detailed analysis of AMALi measurements (Lampert et al., 2009a). Although the lidar signal did penetrate the clouds layer only in cloud gaps with low optical thickness, a layer dominated by liquid water droplets was found at cloud top while precipitating ice crystals were observed in the cloud gap.

4.1 Vertical weighting functions

Independently, the vertical distribution of the ice crystals was estimated from the SMART-Albedometer measurements by comparison with radiative transfer simulations (Ehrlich et al., 2009). Therefore, the vertical weighting functions $W(z)$ of the reflectivity measurements in the
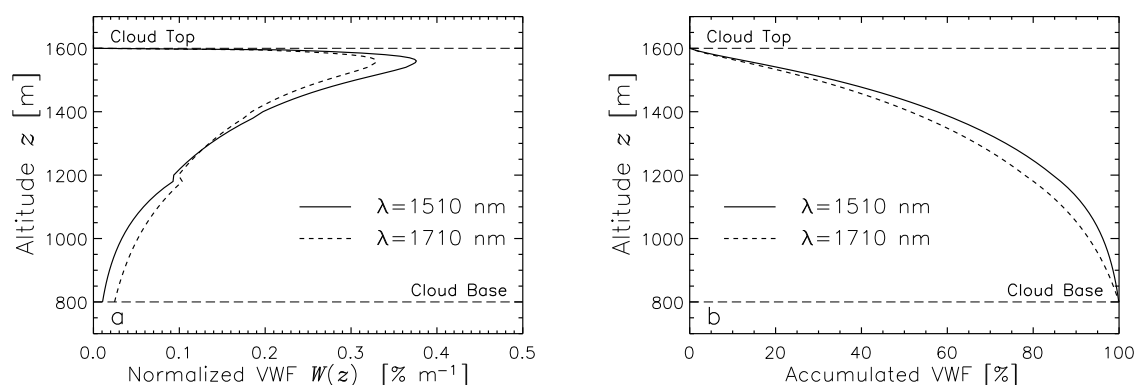
Figure 6: Vertical weighting function $W(z)$ for the radiance measurements of the SMART-Albedometer with respect to absorption by cloud particles (panel a). The accumulated weighting is given in panel b.

wavelength range dominated by ice and liquid water absorption (1300–1800 nm) were calculated by methods described by Platnick (2000).

The calculated $W(z)$ in units of [% m^{-1}] referring to the geometrical thickness of the cloud are given in Figure 6a for two wavelengths exemplary for strong ice (1510 nm) and liquid absorption (1710 nm). In Figure 6b $W(z)$ is accumulated over altitude starting with 0 % at cloud top. For both wavelengths, the weighting shows the highest contribution for cloud layers close to cloud top at 1550 m altitude. The maximum values of $W(z)$ are found to be higher for $\lambda = 1510$ nm than for $\lambda = 1710$ nm. With the higher values of $W(z)$ the cloud-top reflectivity at $\lambda = 1510$ nm is more dominated by absorption by particles at cloud top than R at $\lambda = 1710$ nm. Therefore, R at $\lambda = 1510$ nm is more suitable to retrieve the particle size at cloud top.

These spectral differences in $W(z)$ provide a tool to retrieve information on the vertical distribution of the cloud particle effective diameter, as described by Chen et al. (2007). Wavelengths where liquid water and ice absorption are strong can be used to derive particle properties at cloud top, whereas wavelengths with weaker absorption give information on particles located at lower cloud layers. Utilizing the spectral differences between the maxima of ice and liquid water absorption, separate vertical profiles for ice crystals and liquid water droplets can be derived.

4.2 Radiative transfer simulations

In this regard, radiative transfer simulations of cloud reflectivities have been performed for different vertical cloud geometries and compared to the measurements. Here the three most suitable cases out of those presented by Ehrlich et al. (2009) are shown. A cloud adapted to the vertical structure observed by the in situ instruments was simulated in Case A with an ice crystal layer topped by a liquid water layer (ice crystals in the upper cloud layer are neglected). In Case E a thin ice layer is situated adjacent to cloud top within the original cloud (mixed-phase cloud top); for Case F a thin ice layer is added above cloud top.

The spectral cloud-top reflectivity R simulated for the cases A, E, and F is shown in Figure 7. The measurements of R show that for wavelengths below $\lambda = 1700$ nm stronger absorption is measured than shown by the simulation of Case A. The maximum differences overlap with the ice absorption maximum ($\lambda = 1490$ nm). At wavelengths between 1700–1800 nm weaker absorption is observed.

Following the findings discussed above, the strong absorption at $\lambda = 1490$ nm implies that ice crystals of large effective diameter are present in the upper cloud layers. On the other hand,

8
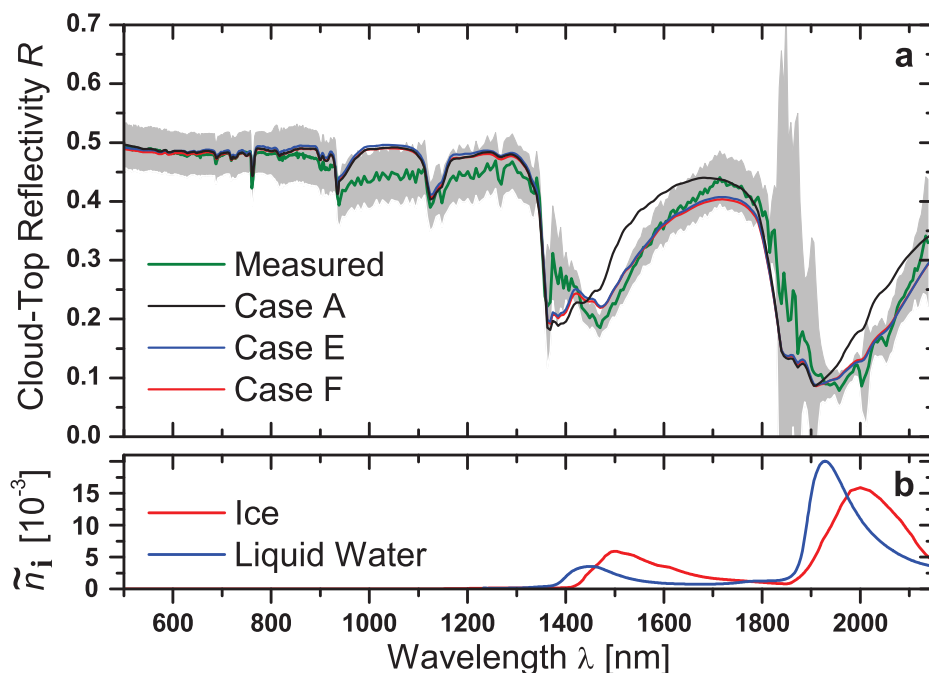
Figure 7: Measured and simulated spectral cloud-top reflectivity R for cases A, E and F (panel a). The measurement uncertainty is illustrated by the gray area. In Panel b shows the refractive index $\tilde{n}_i$ of liquid water (Wieliczka et al., 1989) and ice (Warren and Brandt, 2008).

the high values of R between 1700–1800 nm wavelength indicate cloud particles with smaller effective diameter at cloud top and at lower cloud layers. For cases E and F which have almost identical results these simulations fit into the uncertainty range of the observed R at all wavelengths. Especially the spectral pattern in the wavelength range dominated by ice and liquid water absorption is closer to the measurements than simulations without additional ice layer. This reveals that ice crystals situated at cloud top are necessary to explain the observed absorption features with strong absorption at 1490 nm and weak absorption at wavelengths about 1750 nm. It has to be stated that this holds only for ice crystals of large effective diameter which, if added, describe the observed ice absorption in the measurements. Ice crystals of small effective diameter in low concentration which do not contribute as strongly to the ice absorption might be located throughout the cloud.

Further simulations analyzed the observation of backscatter glories during ASTAR 2007 which generally indicates the presence of liquid water droplets at cloud top. Implementing ice crystals directly within the uppermost cloud layer (Case E) reproduced a weak but visible backscatter glory and explains the observations. Situating the thin ice layer above the original cloud (Case F) eliminated the backscatter glory. From this analysis it is concluded that Case E rather than Case F does suit the remote-sensing observation above ABM clouds obtained during ASTAR 2007.

5   Conclusion and outlook

Airborne measurements with three different core instruments including solar radiation, in situ and lidar measurements were conducted during the ASTAR 2007 campaign to investigate Arctic boundary-layer mixed-phase clouds. Each instrument provided independent information on the horizontal and vertical distribution of ice crystals and liquid water droplets in these clouds.

For the remote sensing measurements of solar radiation new methods have been developed to determine the cloud phase and the vertical distribution of ice crystals. The spectral measurements in the wavelength range 1500–1700 nm where absorption of radiation by ice and liquid water is evident was found to be suitable to retrieve these information.

Case studies of ASTAR 2007 have shown that the horizontal distribution of cloud phase can be highly inhomogeneous especially if the extended cloud fields are disturbed by changing meteorological conditions. This might have a non-negligible impact on the 3-dimensional radiative transfer within this clouds.

Further, the vertical structure of the ABM clouds was identified by all three instruments. Basically the data showed a cloud top layer dominated by liquid water and a lower cloud layer dominated by ice crystals. In more detail the solar radiation measurements indicated that ice crystals were also present in the upper layers of the observed clouds. Analysis of the in situ and lidar measurements could neither confirm nor reject these results. The absence of ice crystals in the in situ measurements at cloud top is probably due to the flight strategy (vertical profiling) providing only short passages of this cloud layer and the horizontal variability of ABM clouds as shown by Gayet et al. (2009). The lidar measurements are highly affected by multiple scattering processes and are not suitable to detect few ice crystals within numerous liquid water droplets. However, similar clouds have been investigated by McFarquhar et al. (2007), Shupe et al. (2006, 2008) who confirmed the presence of ice crystals throughout the entire clouds by in situ and ground-based measurements.

Based on the proof of concept studies shown here, further investigations on the horizontal distribution of ice and liquid water in mixed-phase clouds are planned. Therefore, airborne measurements will be conducted within the study on Solar Radiation and Phase Discrimination of Arctic Clouds (SORPIC) in April/May 2010. The core instruments operated on the Polar 2 aircraft during ASTAR 2007 will be installed on the new Polar 5 aircraft of AWI. Additionally, a sun photometer, polarized solar radiance measurements, and the hyperspectral camera system AISA Eagle will be integrated on Polar 5 during SORPIC.

The in situ and remote sensing measurements aim to derive detailed horizontal maps of the distribution of ice and liquid water in mixed-phase clouds. This information will be used by 3d radiative transfer simulations to estimate the impact of these cloud phase inhomogeneities on the radiative forcing and remote sensing of these clouds. Additionally, it is assumed to obtain new insight into the dynamics of ABM clouds by the combination of data from the independent measurements methods on board of Polar 5.

References

Acarreta, J. R., Stammes, P., and Knap, W. H., 2004: First retrieval of cloud phase from SCIA-MACHY spectra around $1.6\,\mu$m, Atmos. Res., 72, 89–105.

Bierwirth, E., Wendisch, M., Ehrlich, A., Heese, B., Tesche, M., Althausen, D., Schladitz, A., Müller, D., Otto, S., Trautmann, T., Dinter, T., von Hoyningen-Huene, W., and Kahn, R., 2009: Spectral surface albedo over Morocco and its impact on the radiative forcing of Saharan dust, Tellus, 61B, 252–269.

Chen, R. Y., Chang, F. L., Li, Z. Q., Ferraro, R., and Weng, F. Z., 2007: Impact of the vertical variation of cloud droplet size on the estimation of cloud liquid water path and rain detection, J. Atmos. Sci., 64, 3843–3853.

Ehrlich, A., 2009: The impact of ice crystals on radiative forcing and remote sensing of arctic boundary-layer mixed-phase clouds, Ph.D. thesis, Johannes Gutenberg University Mainz, Germany.

Ehrlich, A., Bierwirth, E., Wendisch, M., Gayet, J.-F., Mioche, G., Lampert, A., and Heintzenberg, J., 2008a: Cloud phase identification of Arctic boundary-layer clouds from airborne spectral reflection measurements: Test of three approaches, Atmos. Chem. Phys., 8, 7493–7505.

Ehrlich, A., Wendisch, M., Bierwirth, E., Herber, A., and Schwarzenböck, A., 2008b: Ice crystal shape effects on solar radiative properties of Arctic mixed-phase clouds - Dependence on microphysical properties, Atmos. Res., 88, 266–276.

Ehrlich, A., Wendisch, M., Bierwirth, E., Gayet, J.-F., Mioche, G., Lampert, A., and Mayer, B., 2009: Evidence of ice crystals at cloud top of Arctic boundary-layer mixed-phase clouds derived from airborne remote sensing, Atmos. Chem. Phys., 9, 9401–9416.

Fan, J., Ovtchinnikov, M., Comstock, J., McFarlane, S., and Khain, A., 2008: Modeling Arctic mixed-phase clouds and associated ice formation, in Proceedings of the ICCP Conference, Cancun, Mexico, July 7-11.

Fridlind, A. M., Ackerman, A. S., McFarquhar, G., Zhang, G., Poellot, M. R., DeMott, P. J., Prenni, A. J., and Heymsfield, A. J., 2007: Ice properties of single-layer stratocumulus during the Mixed-Phase Arctic Cloud Experiment: 2. Model results, J. Geophys. Res., 112, D24 202.

Garrett, T. J., Hobbs, P. V., and Gerber, H., 2001: Shortwave, single-scattering properties of arctic ice clouds, J. Geophys. Res., 106, 15.155–15.172.

Gayet, J. F., Mioche, G., Dornbrack, A., Ehrlich, A., Lampert, A., and Wendisch, M., 2009: Microphysical and optical properties of Arctic mixed-phase clouds. The 9 April 2007 case study., Atmos. Chem. Phys., 9, 6581–6595.

Gerber, H., Takano, Y., Garrett, T. J., and Hobbs, P. V., 2000: Nephelometer measurements of the asymmetry parameter, volume extinction coefficient, and backscatter ratio in Arctic clouds, J. Atmos. Sci., 57, 3.021–3.034.

Harrington, J. Y., Reisin, T., Cotton, W. R., and Kreidenweis, S. M., 1999: Cloud resolving simulations of Arctic stratus - Part II: Transition-season clouds, Atmos. Res., 51, 45–75.

Hu, Y., Vaughan, M., Liu, Z., Lin, B., Yang, P., Flittner, D., Hunt, B., Kuehn, R., Huang, J., Wu, D., Rodier, S., Powell, K., Trepte, C., and Winker, D., 2007: The depolarization attenuated backscatter relation: CALIPSO lidar measurements vs. theory, Optics Express, 15, 5327–5332.

Korolev, A. V., Isaac, G. A., Cober, S. G., Strapp, J. W., and Hallett, J., 2003: Microphysical characterization of mixed-phase clouds, Quart. J. Roy. Meteor. Soc., 129, 39–65.

Lampert, A., Ehrlich, A., Drnbrack, A., Jourdan, O., Gayet, J.-F., Mioche, G., Shcherbakov, V., Ritter, C., and Wendisch, M., 2009a: Microphysical and radiative characterization of a subvisible midlevel Arctic ice cloud by airborne observations a case study, Atmos. Chem. Phys., 9, 2647–2661.

Lampert, A., Ritter, C., Hoffmann, A., Gayet, J.-F., Mioche, G., Ehrlich, A., Drnbrack, A., Wendisch, M., and Shiobara, M., 2009b: Observations of boundary layer, mixed-phase and multi-layer Arctic clouds with different lidar systems during ASTAR 2007, Atmos. Chem. Phys. Diss., 9, 15 125–15 179.

McFarquhar, G. M., Zhang, G., Poellot, M. R., Kok, G. L., Mccoy, R., Tooman, T., Fridlind, A., and Heymsfield, A. J., 2007: Ice properties of single-layer stratocumulus during the Mixed-Phase Arctic Cloud Experiment: 1. Observations, J. Geophys. Res., 112, D24 201.

Morrison, H., Pinto, J. O., Curry, J. A., and McFarquhar, G. M., 2008: Sensitivity of modeled Arctic mixed-phase stratocumulus to cloud condensation and ice nuclei over regionally varying surface conditions, J. Geophys. Res., 113, D05 203.

Platnick, S., 2000: Vertical photon transport in cloud remote sensing problems, J. Geophys. Res., 105, 22 919–22 935.

Shupe, M. D., Matrosov, S. Y., and Uttal, T., 2006: Arctic mixed-phase cloud properties derived from surface-based sensors at SHEBA, J. Atmos. Sci., 63, 697–711.

Shupe, M. D., Daniel, J. S., de Boer, G., Eloranta, E. W., Kollias, P., Long, C. N., Luke, E. P., Turner, D. D., and Verlinde, J., 2008: A focus on mixed-phase clouds: The status of ground-based observational methods, Bull. Amer. Meteor. Soc., 89, 1549–1562.

Turner, D. D., Ackerman, S. A., Baum, B. A., Revercomb, H. E., and Yang, P., 2003: Cloud phase determination using ground-based AERI observations at SHEBA, J. Appl. Meteor., 42, 701–715.

Verlinde, J., Harrington, J. Y., McFarquhar, G. M., Yannuzzi, V. T., Avramov, A., Greenberg, S., Johnson, N., Zhang, G., Poellot, M. R., Mather, J. H., Turner, D. D., Eloranta, E. W., Zak, B. D., Prenni, A. J., Daniel, J. S., Kok, G. L., Tobin, D. C., Holz, R., Sassen, K., Spangenberg, D., Minnis, P., Tooman, T. P., Ivey, M. D., Richardson, S. J., Bahrmann, C. P., Shupe, M., DeMott, P. J., Heymsfield, A. J., and Schofield, R., 2007: The mixed-phase Arctic cloud experiment, Bull. Amer. Meteor. Soc., 88, 205.

Warren, S. G. and Brandt, R. E., 2008: Optical constants of ice from the ultraviolet to the microwave: A revised compilation, J. Geophys. Res., 113, Art. No. D14 220.

Wendisch, M., Müller, D., Schell, D., and Heintzenberg, J., 2001: An airborne spectral albedometer with active horizontal stabilization, J. Atmos. Oceanic Technol., 18, 1856–1866.

Wieliczka, D. M., Weng, S. S., and Querry, M. R., 1989: Wedge Shaped Cell For Highly Absorbent Liquids - Infrared Optical-Constants Of Water, Appl. Opt., 28, 1714–1719.

Impact of aerosol particles on measured and simulated polarized solar radiation

Author: Clemens Fricke, André Ehrlich

Abstract

Solar radiation scattered within the atmosphere by atmospheric particles and aerosol particles has been investigated with regard to their state of polarization. Therefore measurements are performed with the COmpact RAdiation measurement System CORAS to analyze the individual components of the Stokes vector describing the measured radiation. For this purpose new optical inlets including a polarization filter have been developed. In parallel, radiative transfer simulations are conducted to interpret the measurements. For this purpose, two different radiative transfer solvers (SCIATRAN and polRadtran) were used. The simulations have been compared with the measurements to characterize the aerosol optical thickness and the predominant aerosol type.

Introduction

The electromagnetic radiation emitted by the Sun (solar radiation) is unpolarized. That means the oscillation of the electromagnetic waves has no preferred orientation. In the atmosphere scattering of solar radiation by air molecules and atmospheric particles (aerosol and/or clouds) may change the state of polarization. The intensity of the polarized radiation depends on several parameters like scattering angle, wavelength of radiation, particle size and shape. Thus, measurements of the polarization state of the scattered solar radiation enable a variety of analysis to retrieve detailed information on the scattering particles. (Emde et al, 2009)

Aerosol particles are one key element in the current debate on the Earth's climate change. The effect of aerosols on the radiation budget and cloud formation is still not sufficient understood (IPCC, 2007). Therefore, new measurement methods to characterize aerosol by polarized radiation have been developed. While active methods obtain information on the polarization state already exist (i.e. using lidar for

example, (Weitkamp, 2005)), there is also an interest to apply passive techniques utilizing solar radiation as it is more applicable to retrieve information without the need of a simulated input. In this work ground-based radiance measurements were performed to characterize the state of polarization of sky light for clear sky conditions.

The state of polarization of an electromagnetic wave is described by the Stokes-vector which is defined by

$$\vec{S} = \begin{pmatrix} I \\ Q \\ U \\ V \end{pmatrix}$$

The components *I, Q, U* and *V* of the Stokes vector are defined as time averages of linear combinations of the electromagnetic field vector,

$$I = \langle E_l E_l^* + E_r E_r^* \rangle \tag{1}$$

$$Q = \langle E_l E_l^* - E_r E_r^* \rangle \tag{2}$$

$$U = \langle E_l E_r^* + E_r E_l^* \rangle \tag{3}$$

$$V = \langle E_l E_r^* - E_r E_l^* \rangle \tag{4}$$

where E_l and E_r and the corresponding complex conjugated values (*) are the components of the electromagnetic field vector $\vec{E}$. E_l describes the fraction parallel to the reference plane, and E_r the fraction perpendicular to the reference plane. There are three different kinds of polarization, all described by the direction and the value of the field vector in fixed coordinates. The linear, circular and elliptic polarization.

Due to the use of linear polarization filters only the measurements did not cover circular and elliptic polarization (Stokes parameter V). Therefore investigations on circular and elliptic polarization are excluded in this work.

With knowledge of the Stokes parameters the degree of linear polarization is given by:

$$P_I = \frac{\sqrt{Q^2 + U^2}}{I} \tag{5}$$

A value of $P_I=0$ corresponds to unpolarized radiation; $P_I=1$ indicates total linear polarized radiation. Here, P describes the polarized part measured within the total radiance.

Polarization measurement and simulations

The measurements were done with the Compact Radiation measurement System (CORAS).

CORAS was configured to measure spectral radiances in the wavelengths range between 300nm and 700nm, where aerosol affects are expected to be high. To retrieve the influence of aerosols only, "clear-sky" measurements were made. In this way the influence of water-droplets and/or ice-crystals could be excluded.

It receives radiances using a multi channel spectrometer (grating spectrometer, manufactured by Zeiss) with spectral resolution (full mean of half width) between 2-3nm wavelength. The optical inlet includes a polarization filter with an effective spectral range of 400-700nm. Radiances are measured in zenith direction.

To measure the full Stokes vector radiances have to been measured using a polarization filter. Four different orientations of a polarization filter ($I_{0°}$, $I_{45°}$, $I_{90°}$, $I_{135°}$) have to be realized during one measurement as illustrated in *Fig. 1*. The parameters *I, Q, U* and (and *V*) are then calculated by:

$$I = I_{0°} + I_{90°} \tag{6}$$

$$Q = I_{0°} - I_{90°} \tag{7}$$

$$U = I_{45°} - I_{135°} \tag{8}$$

$$(V = I_{RZ°} - I_{LZ°}) \tag{9}$$
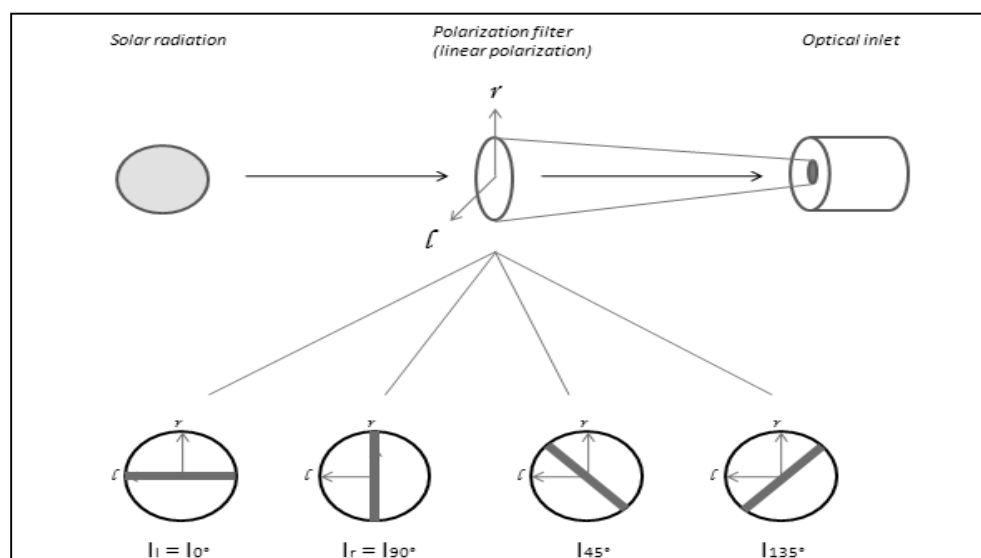
Fig. 1: Principle of measurement: The axis of the polarization filter is illustrated by a thick gray line. The parameters I0°, I90°, I45° and I135° are obtained by turning the polarization filter in intervals of 45°.

To analyze the ground-based measurements it is necessary to compare the measured data with radiances simulated by radiative transfer models (in the following RTM). To simulate polarized radiation the applied RTMs have consider all components of the Stokes vector. As a basic element, the RTMs include the interaction of the solar radiation with atmospheric molecules (Rayleigh scattering). Aerosol is implemented using the scattering properties of aerosol particles calculated from Mie-Theory. For investigations presented here two different RTM were applied; the polradtran solver (Evans et al. 1991,1995) as part of the „library for radiative transfer calculations" (libRadtran, Mayer 2005)) and a new vector radiative transfer model included in the SCIATRAN 3.0 package (Rozanov et al. 2006). The aerosol optical properties accord to the standard WMO-model (Kokhanovsky, 1986) for SCIATRAN and to the OPAC database (Hess et al., 1998) for the polRadtran solver. In line with the presented radiation measurements, validation and tests of SCIATRAN will be discussed.

Results

Polarization measurements have been obtained with CORAS on August, 7th and August, 20th 2009 during clear sky conditions. The total radiances for the two measurements in zenith direction are displayed in *Fig. 2a*.

At first, the radiances of two measurements are displayed on the left, done on August, 7th and August, 20th 2009 *(Fig.2)*. The corresponding degrees of linear polarization (P_I) are shown in *Fig.2b*
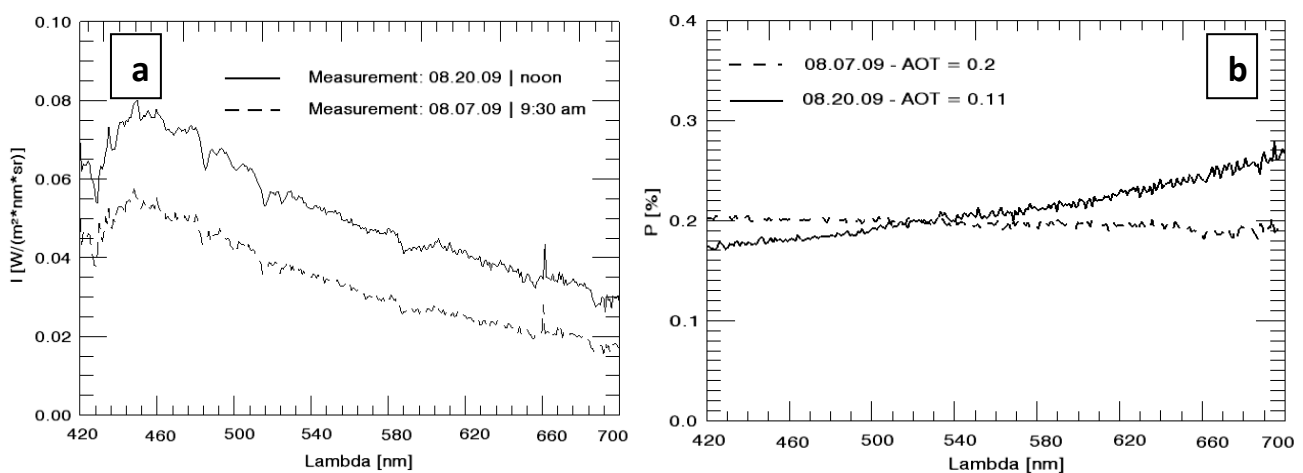
Fig.2: Measured radiances obtainedon August, 20th (solid line, θ = 41,68°) and August, 7th (dashed line θ = 56,75°) are shown in panel a. The corresponding degree of polarization is displayed in panel b.

The direct comparison of both cases shows that the radiance was higher for August, 20th than for August, 7th. The difference results mainly from the different solar zenith angle θ (42° for August, 20th and. 57° for August 7th), which alters the available amount of solar radiation. Potential effects caused by different aerosol optical thicknesses (AOT) are weaker than changes of θ and thus not observable in the radiances shown here. Nevertheless, the differing aerosol optical thickness has beside of the solar zenith angle a significant impact on the degree of the linear polarization. As shown in *Fig.2b*, for lower case of low AOT (0.2) measured on August, 20th, P_I increases with increasing wavelengths. The change of the spectral characterization of the polarization goes with the different AOT of both measurements. Regarding to theory, the lower SZA on August, 20th compared to August, 7th supports the increase of P with wavelength (Coulson, 1960: Tables related to radiation emerging from a planetary atmosphere with Rayleigh scattering)

To analyze and evaluate the impact of each factor simulations of spectral radiance and degree of polarization by RTMs are employed. Next to the point, that as cause of restrictions of the polarization filter, data acquisition is limited to the visible spectral range between 350nm-700nm the RTM's force this spectral window as well. They only calculate the aerosol optical properties within these wavelengths.
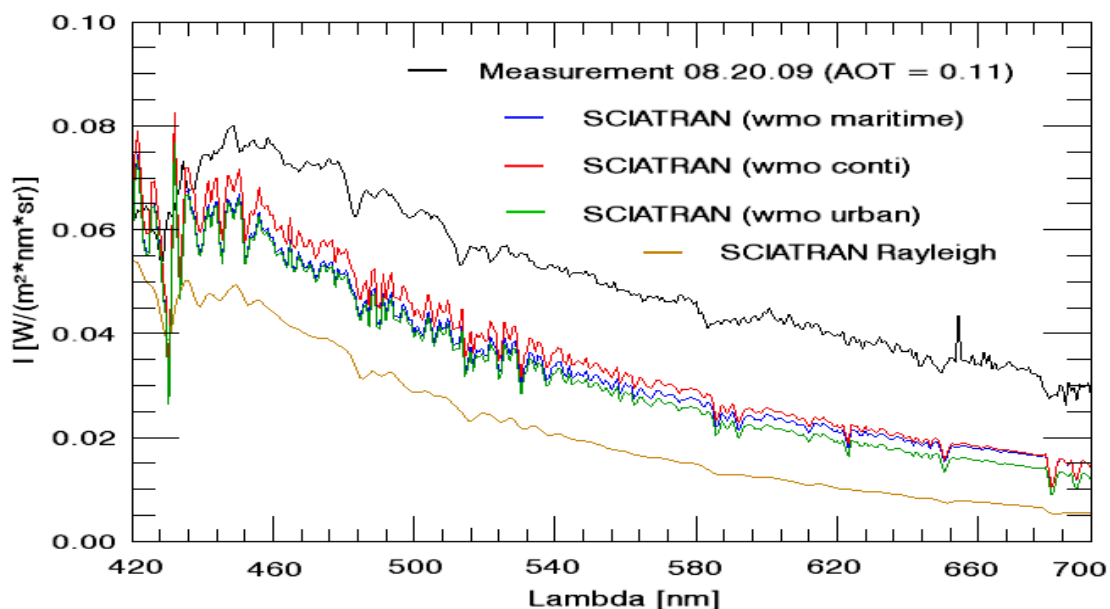
Fig. 3: SCIATRAN simulations for Rayleigh atmosphere and different aerosol situations.
For all simulations with aerosol AOT was set to 0.2. The Rayleigh case is convoluted.
As comparison, the measured radiance from August, 20th (Fig. 2) is added.

Fig.3 displays a comparison of simulated and measured radiances for August, 20th . Four calculated radiances simulated for different aerosol properties are shown. The ocher-colored line refers to the radiance simulated for a pure Rayleigh-atmosphere (AOT=0). With no aerosol particles included this is the reference case. The three colored lines show radiances simulated with aerosol particles included. The data bases use pre-defined mixtures of different aerosol types. For the simulations an urban (green line in Figure 4), continental (red line) and maritime aerosol composite (blue line) was used. The continental and maritime aerosol type contains 90% water-soluble aerosol, while the maritime one adds sea salt-accumulated aerosol. The urban composite contains 50% soot. While the simulations for the Rayleigh atmosphere have been convoluted with the according spectral resolution of the measurements, the simulations including aerosol are displayed in full spectral resolution of one nm.

In comparison to the measurements of August, 20th the modeled radiances show similar results. However, higher AOT's are necessary to obtain equal results. The simulations were performed with an AOT of 0.2 while AOT measurements from August, 20th showed an average of AOT=0.11 which was given by the AErosol RObotic NETwork (AERONET) station of the Institute for Tropospheric Research (IfT), Leipzig.

One possible reason for this difference may result from the data-averaging due to AERONET. An uncertainty resulting from the RTM is the impact of the surface albedo, which was set to 0.15 for the simulations. A higher albedo may result in increasing upwelling and consequently downwelling radiances and reduce the degree of linear polarization. Further simulations are scheduled to analyze the explicit impact and weight of the albedo.

A further aspect that is present in *Fig. 3* is the difference between the three simulated aerosol calculations. Using urban aerosol the radiance has lower values than for the other composites. This is caused by the soot particles included in the urban composite. The soot absorbs radiation, which results in a greater attenuation of the incoming radiation and in lower sky radiances.

Furthermore, a difference between the spectral characteristic of the radiances for the different aerosol cases can be observed. Simulations with maritime aerosol-case show a weaker decrease of the radiance with wavelength compared to the other compositions. This is caused by spectral differences of the according scattering phase function of sea salt in the marine composition. However, these differences are small and difficult to observe in measurements. To derive more assured information on the aerosol properties, the degrees of linear polarization was calculated from the results of the simulations.
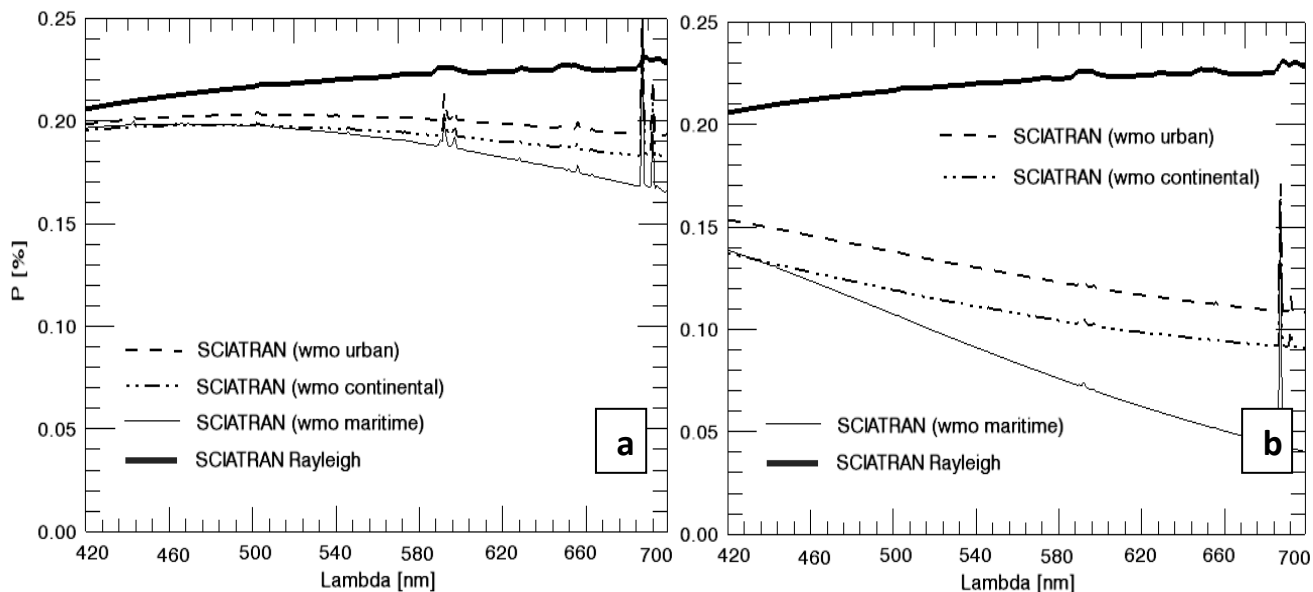
Fig.4: Degree of polarization for an AOT of 0.02 simulated with SCIATRAN based on the measurement from August, 20th is presented in panel a, while the degree of polarization for panel b was calculated for an AOT of 0.2

Fig.4 display simulations of SCIATRAN using the different aerosol composites and the Rayleigh-case as introduced above. The simulations shown in *Fig.4a* are performed with an AOT of 0.02 while the results displayed in *Fig.4b* are obtained for an AOT of 0.2. In general, the degree of linear polarization decreases with increasing AOT, while the maximum values are given by the Rayleigh case. Without aerosol P_I increases slightly with the wavelength. In comparison, the spectral pattern of P_I obtained for AOT=0.02 shows a slight increase of P_I up to 500 nm. For wavelengths above there is a decrease. For AOT=0.2 P_I decreases over the entire wavelength range. In comparison to the measurement from August, 20th the spectral pattern of the measured P_I is not fully reproduced yet. Further investigations to determine the reasons are scheduled.

The comparison of these simulations has shown that P_I is highly sensitive to even smallest aerosol optical thicknesses. For AOT=0.02 P_I deviates from the Rayleigh-case up to 25% at a wavelength of 700 nm. Contrarily, the simulated radiances for AOT=0.02 (not shown here) differ only up to 3%. Thus the measurements of P_I are more suited to detect low aerosol concentration below AOT<0.05 than measurements of spectral radiances.

However, P_I is also strongly affected by the relative position of optical inlet and the Sun. To analyze the effect of the changing solar zenith angle in comparison to AOT changes simulations with different θ are shown in *Fig.6*.
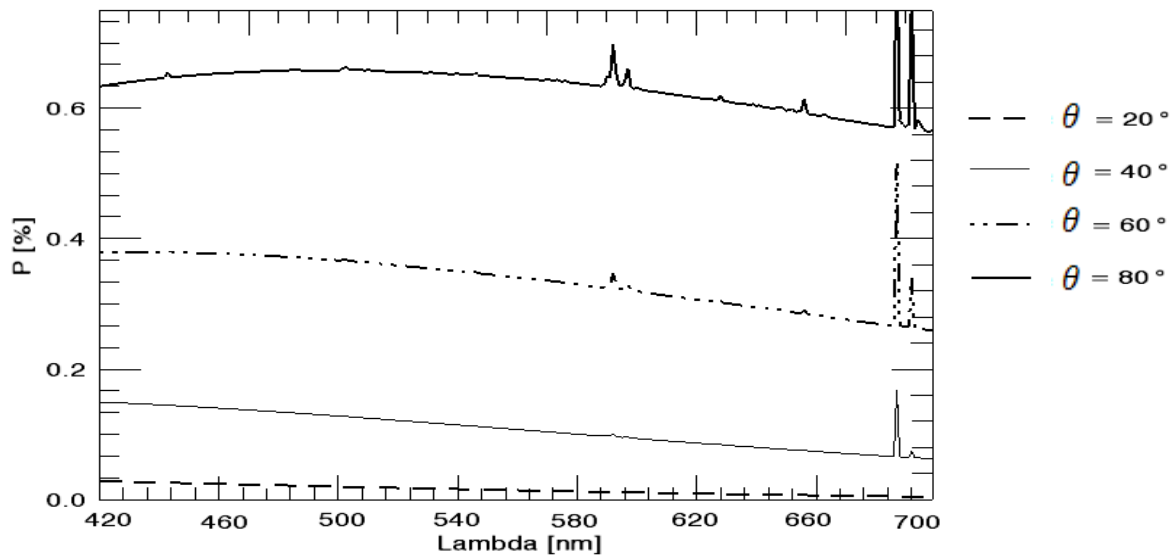
Fig.5: Impact of θ on linear polarization simulated with SCIATRAN. A maritime aerosol setting is used (AOT=0.1). The viewing direction is zenithal.

Presented are simulations for a continental aerosol setting with AOT=0.1. In general, for the chosen zenithal viewing direction the simulations reveal that an increase of θ increases the degree of polarization. While for small scattering angles ($\theta = 20°$) P_I almost diminishes, simulation with $\theta = 80°$ result in the highest P_I of up to 70%. This is due to the fact that the Rayleigh-scattered radiation has a maximum of polarization for 90° scattering angle. Compared to the simulation using a fixed θ but different AOT shown in *Fig. 5* the impact of θ exceeds the impact of aerosol. Thus the geometrical configuration of the measurement setup (inlet viewing angle and θ) have to be considered correctly to retrieve precise information on aerosol properties. In relation to the measurements shown in *Fig.2b* where both AOT and θ have changed, these simulations have shown that both attributes explain the different spectral characteristic of P_I obtained for August, 20 and August, 7.

Conclusions

The influence of aerosol on the linear polarized radiation has been analyzed by radiation measurements and simulation by the RTM SCIATRAN. The measurements and the simulated radiances were obtained for different θ and AOT. The impact of both parameters on the spectral radiance and P_I was analyzed. It has been shown that both measured quantities I and P_I are influenced by changing AOT and θ. However, P_I was found to be affected much stronger than the radiance.

Furthermore, differences in the impact of AOT and θ on the measured and simulated radiation were analyzed. While the absolute effects are higher for a changing θ, AOT was found to have a higher impact on the spectral characteristics of P_I. In contrary the spectral characteristic of the radiance is only slightly affected by different θ and AOT. This reveals that P_I is suited better then measurements of the radiance to retrieve information about aerosol properties from solar sky radiation measurements. The higher absolute and spectral sensitivity of P_I with respect to changes in the aerosol properties enables to identify even small amount of aerosol AOT<0.01 which are not detectable by measurements of the radiance. Additionally, P_I is a relative measure and therefore independent on the accuracy of the radiometric calibration of the instrument.

References:

Emde, C., Buras, R., Mayer, B., Blumthaler, M., 2010: The impact of aerosols on polarized sky radiance: model, development, validation, and applications. Atmos. Chem. Phys., 10, S. 384-393

Oikarinen, L., 2001: Polarization of light in UV-visible limb radiance, Journal of geophysical research. Journal of geophysical research, Vol. 106, No. D2, S. 1533-1544

Boesche, E., Stammes, P., Ruhtz, T., Preusker, R., Fischer, J., 2006: Effect of aerosol microphysical properties on polarization of skylight: sensitivity study and measurements. Applied Optics, Vol. 45, Issue 34, S. 1-53

Zaitseva, V. A, Kravchenko, A. E., Plyuta, V. E., Spitsyn, I. G., Yanovskaya, E. A., Yanovskii, A. F., 1985: Study of the spectral-polarization characteristics of surfaces in the environment from different altitudes. Zhurnal Prikladnoi Spektroskopii, Vol. 42, No. 2, S. 239-244

Solomon, S., D. Qin, M. Manning, Chen, Z., Marquis, M., Averyt, K.B., Tignor, M., Miller, H.L. (eds), 2007: IPCC: Summary for Policymakers. In: Climate Change 2007: The Physical Science Basis. Contribution of Working Group I to the Fourth Assessment Report of the Intergovernmental Panel on Climate Change, Cambridge University Press, Cambridge, United Kingdom and New York, NY, USA, S. 1-18

Evans, K.F., Stephens, L., 1991: A New Polarized Atmospheric Radiative Transfer Model, *J.* Quant. Spectrosc. Radiat. Transfer Vol. 46, No. 5, pp. 413--423, 1991

Rozanov, A., Rozanov, V., Buchwitz, M., Kokhanovsky, A., Burrows, J. P. 2004/2005: SCIATRAN 2.0 - A new radiative transfer model for geophysical applications in the 175-2400 nm spectral region, in: Atmospheric remote sensing:

Earth's surface, troposphere, stratosphere and mesosphere - I, edited by Burrows, JP and Eichmann, KU, vol. 36 of Adv. Space Res., pp. 1015–1019

Hess, M., Koepke, P., Schult, I., 1998: Optical Properties of Aerosols and clouds: The software package OPAC, Bull. Am. Met. Soc. 79, S.831-844.

World Meteorological Organisation, 1986: WMO International Association for Meteorology and Atmospheric Physics Radiation Commission: A preliminary cloudless standard atmosphere for radiation computation, World Climate Program, WCP-112, WMO TD-24

Coulson, K.L., 1960: Tables related to radiation emerging from a planetary atmosphere with Rayleigh scattering, Planetary and Space Science, Volume 1, Issue 4, September 1959, Pages 265-276

Weitkamp, C., 2005: Lidar: range-resovlved optical remote sensing of the atmosphere

Connection of Planetary Waves in the Stratosphere and Ionosphere by the Modulation of Gravity Waves

P. Hoffmann, Ch. Jacobi

Abstract

A possible connection of planetary waves (PW) and ionospheric planetary wave type oscillations (PWTO) at midlatitudes is studied by analyzing MetOffice stratospheric reanalysis data and maps of the Total Electron Content. Although the seasonal variability looks similar, the vertical coupling between stratosphere and ionosphere is known to only happen indirectly through processes such as the modulation of gravity waves (GW) by PW. To investigate possible coupling processes, information about GW are retrieved from SABER temperature profiles (30-130 km) by calculating the potential energy (E_p) and generating daily maps of E_p. For the period of time from 2003-07-19 to 2005-07-20 proxies of stationary and travelling PW were calculated to obtain a general picture of PW activity, modulation of GW by PW and activity of PWTO in the ionosphere. The results reveals that mostly PW itself cannot reach lower thermospheric heights, but their signatures propagate upward up to 120 km and above, where they can trigger PWTO.

Zusammenfassung

Ein möglicher Zusammenhang zwischen dem Auftreten planetarer Wellen (PW) und typischer Oszillationen planetarer Wellen (PWTO) der Ionosphäre in mittleren Breiten wird auf der Basis von Analysen stratosphärischer Reanalysen und Karten des Gesamtelektronengehalts untersucht. Obwohl das saisonale Verhalten ähnlich erscheint, kann die Kopplung nur auf indirektem Wege erfolgen, wie z.B. durch die Modulation von Schwerewellen (GW) durch PW. Die für die Analysen notwendigen Informationen über GW können aus Temperaturprofilen (30-130 km), abgeleitet von Satellitenbeobachtungen (z.B. SABER), durch die Bestimmung der potentiellen Energie von GW, gewonnen werden. Zusammengefasst in täglichen Daten (2003-07-19 to 2005-07-20) stellen Proxies stationärer und wandernder PW ein vereinfachtes Bild des Prozesses der Modulation durch PW dar. Die Ergebnisse zeigen, dass sich PW selbst nicht bis in die unteren Thermosphäre ausbreiten können. Jedoch die Signatur, getragen durch GW, könnte auf diesem Wege als PWTO abgebildet werden.

1. Introduction

The variability of the ionosphere is mainly driven by regular and irregular variations of the extreme ultra-violet solar radiation (EUV) and the Earths magnetic field. However, planetary wave type oscillation (PWTO) having periods of several days have also been observed in ionospheric parameters (e.g. Total Electron Content and f_oF2), and show a similar seasonal behavior in comparison to stratospheric planetary waves (PW) at midlatitudes (Borries et al., 2007) and to the meridional neutral winds in the mesosphere/lower thermosphere (MLT) region (Altadill et al., 2003). Until now no clear evidence exist that such oscillations are forced by waves coming from the lower atmosphere. From theory and model experiments (e.g. Pogoreltsev et al., 2007) is known that stationary and long-period PW cannot propagate vertically into the lower thermosphere due to the critical layer filtering near the mesopause region and other processes such as diffusion. However, indirect coupling processes could exist, such as the modulation of GW by PW (e.g. Laštovička, 2006), which may transport signatures of PW from the stratosphere/mesosphere to the thermosphere.

Since 2002 a space-based temperature data set from the SABER instrument onboard the TIMED satellite is available, which covers the lower and midlatitudes (52°N to 52°S) from the stratosphere up to the lower thermosphere (130 km) without gaps. To extract information about GW from globally distributed temperature profiles one may calculate the potential energy (E_p) from these. Climatologies of GW E_p taken from satellite-borne temperatures are presented in e.g., Tsuda et al. (2000), Preusse et al. (2002), Preusse et al. (2006) and Fröhlich et al. (2007).

By calculating the potential energy of GW one may study the modulation by global scale waves such as PW in comparison to stratospheric PW and ionospheric PWTO. A detailed description of this method is given in section 2. The analysis of PW and the modulation of GW by PW is performed calculating proxies of PW in the space-time domain. Without any spectral decomposition we obtain a general picture of stationary and travelling components and their effects on GW amplitudes. The principle is given in section 3. However, in order to demonstrate a possible transmission path of vertical coupling through the modulation of GW, information about small scale Travelling Ionospheric Disturbances (TID) are essential. Their signatures over Europe can be retrieved from GPS signals as presented in Borries at al. (2009) and the data are used here to find the connection between TID and PWTO in comparison to stratospheric GW and PW.

Before studying the mechanism of coupling processes (in sections 5 and 6), a comparison of PW results obtained by MetOffice and SABER is presented in section 4, similar to Pancheva et al. (2009a), but using PW-proxies, to confirm the reliable picture of PW activity.

2. SABER data analysis

The TIMED satellite was launched on 7th of December 2001 into a 625 km orbit of 74.1° inclination to investigate the dynamics of the mesosphere, thermosphere and ionosphere. The SABER instrument on board of the spacecraft began making observations in late January 2002. By step-scanning the atmospheric limb SABER measures height profiles
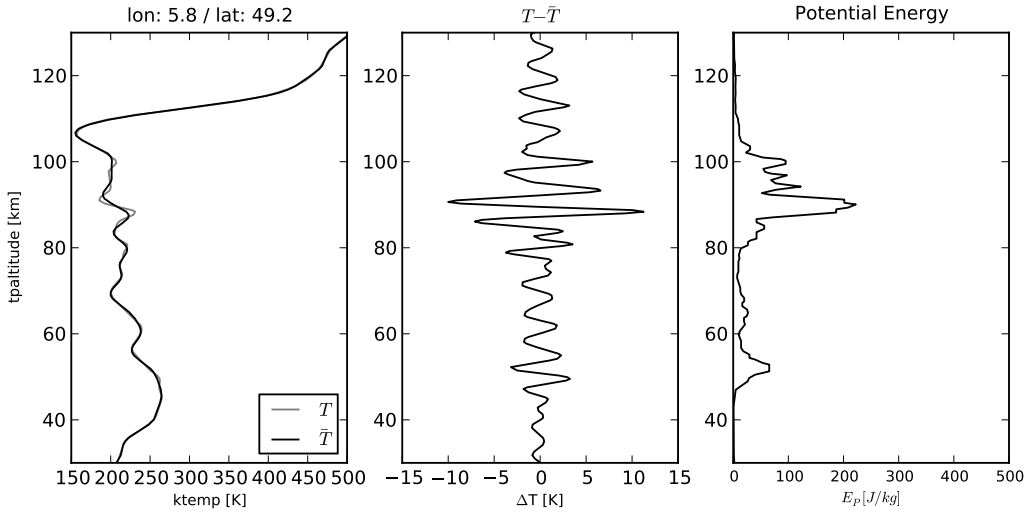
Figure 1: *Example of potential energy calculation (2003-12-12, 49.2°N, 5.8°E). Left panel: SABER temperature profile (T, grey line) and lowpass ($\lambda_z > 6\,km$) filtered profile ($\bar{T}$, black line). Middle panel: Residuals T'. Lower panel: potential energy E_p after Eq.1.*

of temperatures and selected chemical species from 10-180 km altitude with a horizontal resolution along track of about 400 km. The multispectral radiometer operates in the near to mid-infrared over the range 1.27 µm to 17 µm (7865 cm^{-1} to 650 cm^{-1}). It measures CO_2 infrared limb radiance from approximately 20-120 km altitude and the kinetic temperature profiles are retrieved over this heights using a full non-LTE inversion (Mertens et al., 2004). The used SABER L2A data (version 1.07) were downloaded from the web site: *http://saber.gats-inc.com.*

The SABER latitude coverage extends from about 52° of one hemisphere to 83° of the other. This latitude range is reversed by a yaw manoeuvre every 60-days. Due to the sun-synchronous orbital geometry the spacecraft passes the equator always at the same local time (12LT) on the dayside. Before collecting the observations of one day and adapting the orbital data to a regular 3D-grid, all geolocation information, temperature profiles (T) and the geometric height were extracted from the L2A product files and separated into ascending (T_{asc}) and descending (T_{dsc}) overflights (Oberheide et al., 2003). Thereby, the disturbing impact of the diurnal migrating tide can be reduced. Each single profile (Fig.1, left panel) having a vertical resolution of $\Delta z = 0.5\,km$ between 30-130 km is decomposed into harmonics (sine and cosine functions with $\lambda_z < 6\,km$) using the least-squares fit and reconstructed combining all harmonics having a vertical wavelength ($\lambda_z > 6\,km$) to obtain a filtered temperature profile $\bar{T}(z)$. As shown on Figure 1 (middle panel), the residual profile $T'(z)$ between the original $T(z)$ and the filtered profile $\bar{T}(z)$ reveals the vertical structure of GW amplitudes and their specific potential energy (right panel):

$$E_p = \frac{1}{2}\left(\frac{g}{N}\right)^2 \left(\frac{T'}{\bar{T}}\right)^2 ; \tag{1}$$

whereas g and N represents the acceleration due to gravity and the Brunt-Vaisala frequency. This method is also used in e.g. Fröhlich et al. (2007) to extract GW energy

in the lower stratosphere from GPS radio occultation measurements. The spatial and temporal variations of the total energy integrated over a sliding vertical column (10 km) is used to study the modulation of GW. Note that the limb-scanning of the atmosphere by instruments satellites (e.g. SABER on TIMED) only certain parts of the GW spectrum is visible due to the integration along the line of sight (Preusse et al., 2006). Information about the horizontal wavelength vector, in particular perpendicular to the spacecraft orbit, are difficult to detect and only part of the GW energy is visible depending on horizontal resolution and viewing geometry with respect to the wavenumber vector.

A daily regular gridded picture for several parameters (T_{asc}, T_{dsc}, E_p) is obtained by median averaging all observations lying within a 3D-grid ($\Delta\lambda = 10°$, $\Delta\varphi = 5°$, $\Delta z = 2\,km$) covering the region from 45°S to 45°N between 30-130 km. Possible outliers getting less weight which reduces the day to day variation of the retrieved values and the data quality of the GW potential energy. A more technical description of this regularization using the programming language Python is given in Hoffmann et al. (2009). Due to the orbital geometry alising effects occur especially for analysing tidal waves in the mesosphere/lower thermosphere (MLT) region, and short-period PW.

The daily products of this procedure are depicted on Figure 2 for 45°N from the 2003-07-19 to 2005-07-20. The upper panel shows the daily zonal standard deviations

$$\sigma_x\left\{T_{dsc}\right\} = \sqrt{\frac{1}{nx}\sum_\lambda (T_{dsc} - \bar{T}_{dsc})^2} \tag{2}$$

as an approximation of PW activity, with nx being the number of data points in the zonal direction and λ is longitude. Below 80 km, the picture indicates the well known seasonal cycle of PW activity, with a maximum during winter. Above 80 km, the structures are somewhat questionable due to alising effects caused by tidal waves, which are subharmonics of the solar day composed into migrating and non-migrating components. Those amplitudes increase with altitude. The zonal mean $m_x\left\{T_{dsc}\right\} = \frac{1}{nx}\sum_\lambda T_{dsc}$ given in Figure 2 (middle panel) illustrates the background thermal structure of the middle atmosphere and its seasonal behavior. The lower panel in Figure 2 shows the daily zonal standard deviation of the GW potential energy $\sigma_x\left\{E_p\right\}$ (similar to Eq.2) as an approximation of modulation effects. The daily values predominately maximize, according to the increase of potential energy with altitude, in the mesopause region near 90 km, where GW become unstable, break and deposit momentum to the background flow leading to the background wind reversal. For the vertical propagation of PW this region acts like a barrier, only fast PW some GW are able to penetrate the lower thermosphere. Below 80 km a seasonal cycle similar to those of PW appears. Thus, information about the indirectly vertical propagating of PW can be retrieved by analyzing the modulation of GW. The signals of GW separated from PW and tides, which having typically greater vertical wavelength, are minor influenced by alising effects and can deliver a clearer picture of the vertical coupling process.
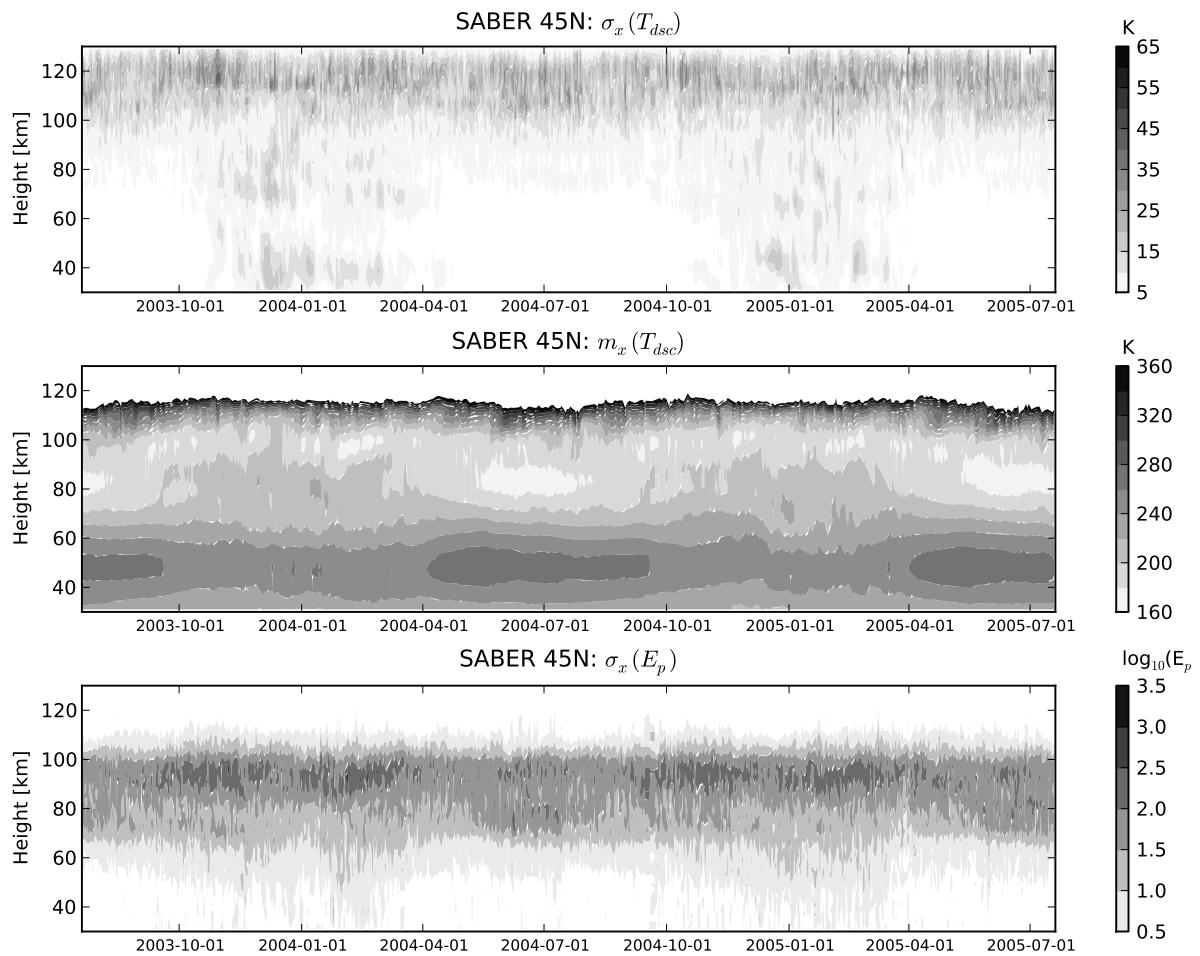
Figure 2: *Height-time cross-sections of SABER data at 45°N. Shown are daily zonal standard deviations ($\sigma_x\{T_{dsc}\}$, upper panel), daily zonal means ($m_x\{T_{dsc}\}$, middle panel) and daily zonal standard deviations of the potential energy ($\sigma_x\{E_p\}$, lower panle).*

3. Proxies of Planetary Waves

The space-time spectral analysis of PW first presented in Hayashi (1971) or PWTO at one latitude circle delivers a large number of wave components which are difficult to interpret. Thus, proxies of PW are introduced combining mean (m) and standard deviation (σ) in the longitude- (x) time (t) domain to study the problem of vertical coupling by the modulation of GW to obtain a general picture of such mechanism. Thereby, we simply differ between a proxy for stationary waves

$$\sigma_x(m_t\{A\}) = \sqrt{\frac{1}{nx-1}\sum_\lambda \left(\left\{\frac{1}{nt}\sum_t A(t,x)\right\} - \overline{\left\{\frac{1}{nt}\sum_t A(t,x)\right\}}\right)^2}, \quad (3)$$

with A as the parameter under investigation, such as (T_{1hPa}, T_{dsc}, E_p), and a proxy for travelling waves defined as the difference between a proxy including all propagating components

$$m_x(\sigma_t\{A\}) = \frac{1}{nx}\sum_\lambda \left\{\sqrt{\frac{1}{nt-1}\sum_t \left(A(t,\lambda) - \bar{A}(t,\lambda)\right)^2}\right\}, \quad (4)$$

and the variation of the zonal mean

$$\sigma_t(m_x\{A\}) = \sqrt{\frac{1}{nt-1}\sum_t \left(\left\{\frac{1}{nx}\sum_\lambda A(t,\lambda)\right\} - \overline{\left\{\frac{1}{nx}\sum_\lambda A(t,\lambda)\right\}}\right)^2}. \quad (5)$$

Both proxies, characterized here, are the most prominent features of the middle atmosphere dynamics. To obtain a temporally resolved behavior of wave signals, the proxies are applied for a 48-days running window shifted by one day for each height. The integer $(nx, nt = 48\,d)$ denotes the length of the sample in longitude and time, respectively.

Concerning the PW-proxy amplitudes derived from SABER data we use only nocturnal values (T_{dsc}) and normalize these by the long-term total standard deviation

$$\sigma_{tot} = \sqrt{\frac{1}{nt\cdot nx - 1}\sum_t \sum_\lambda (A - \bar{A})^2} \quad (6)$$

for each latitude and height, separately. The length of the time interval used here has the value $nt = 730$. For the analysis of PW, possible tidal effects are clearly reduced above 80 km and the increasing amplitudes of GW amplitudes with altitude are weighted by σ_{tot} to obtain a stronger picture of modulation effects by PW from the stratosphere to the lower thermosphere.

4. Validation of Planetary Wave Results

The temperature data from the MetOffice reanalysis product (0-60 km) overlap with those retrieved from SABER (30-130 km). Thus, in this section we compare PW results obtained from these two different data sets.

Figure 3 presents a height-latitude cross-section of stationary (left panel) and travelling (right panel) PW-proxies derived from MetOffice (contours) and SABER (greyscaling)
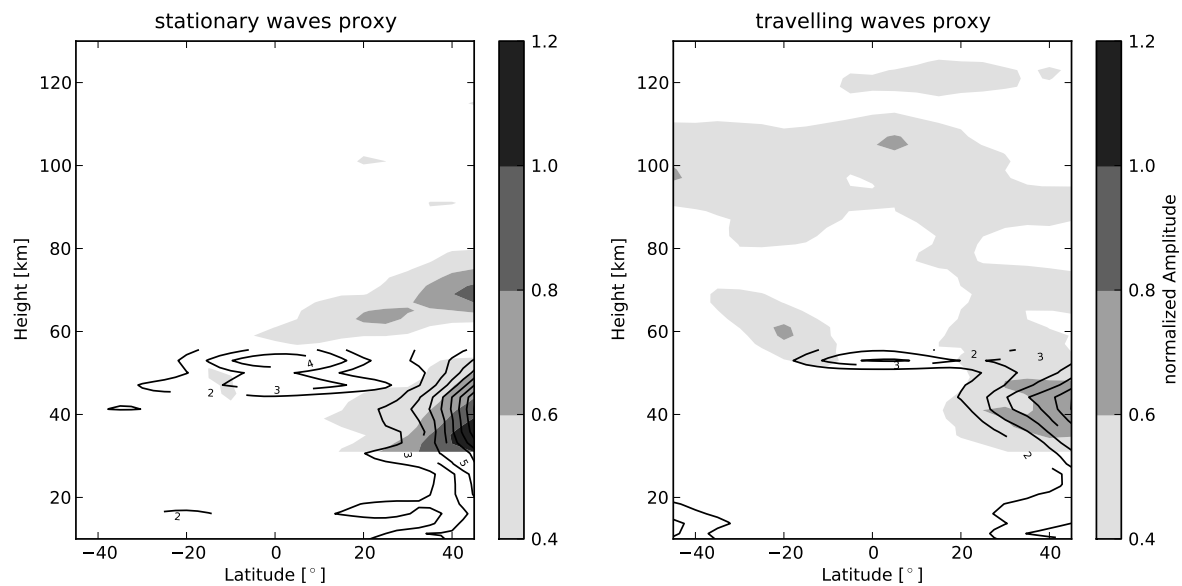
Figure 3: *Height-latitude cross-section of stationary (left panel) and travelling (right panel) wave activity applying PW-proxies to MetOffice (contours) and SABER (greyscaling) temperature data. The picture represents the averaged situation for the winter 2003/04*

temperature data. The distribution of PW activity was averaged for the winter (Dec-Jan) situation (2003/04). The PW amplitudes obtained from SABER are normalized by the total standard deviation (as described in section 3). The picture on the winter hemisphere (+45°N) is determined by stationary- and travelling PW. Using such a proxy of travelling PW both westward propagating Rossby waves and eastward wave components are collected. Between 30-60 km both data sets show a generally good agreement, however, around the equator differences occur near 50 km. We discuss this problem in the next paragraph.

The time-latitude picture at 50 km ($\sim$1 hPa) shown in Figure 4 reveals that the signatures of the stationary component (upper panel) in MetOffice data (contours) around the equator have a semi-annual period with an amplitude of 3-4 K. This phenomenon is not visible in the SABER data (greyscaling). In Pancheva et al. (2009a) a northern hemisphere time-latitude plane of the stationary PW (SPW1, SPW2, SPW3) is presented near 40 km. Differences around the equator exist but they are smaller than 1 K. One may speculate that the reanalyses at lowlatitudes above 40 km could be questionable. Due to the decreased number of observation with height, and the forcing mechanism of the equatorial semi-annual oscillation due to equatorial waves, the reliability in the troposphere/lower stratosphere is much higher. Notwithstanding possible problems with PW analyses at equatorial regions, the PW at midlatitudes retrieved from both data sets indicate a good agreement. Due to the averaging process by fitting the satellite measurements to the 3D-grid, the SABER wave amplitudes are a little smaller ($<$1 K) in comparison to MetOffice.

The height-time cross-sections of PW-proxies at 45°N are presented in Figure 5. While MetOffice data are regularly produced up to 0.1 hPa ($\sim$60 km), space based temperature
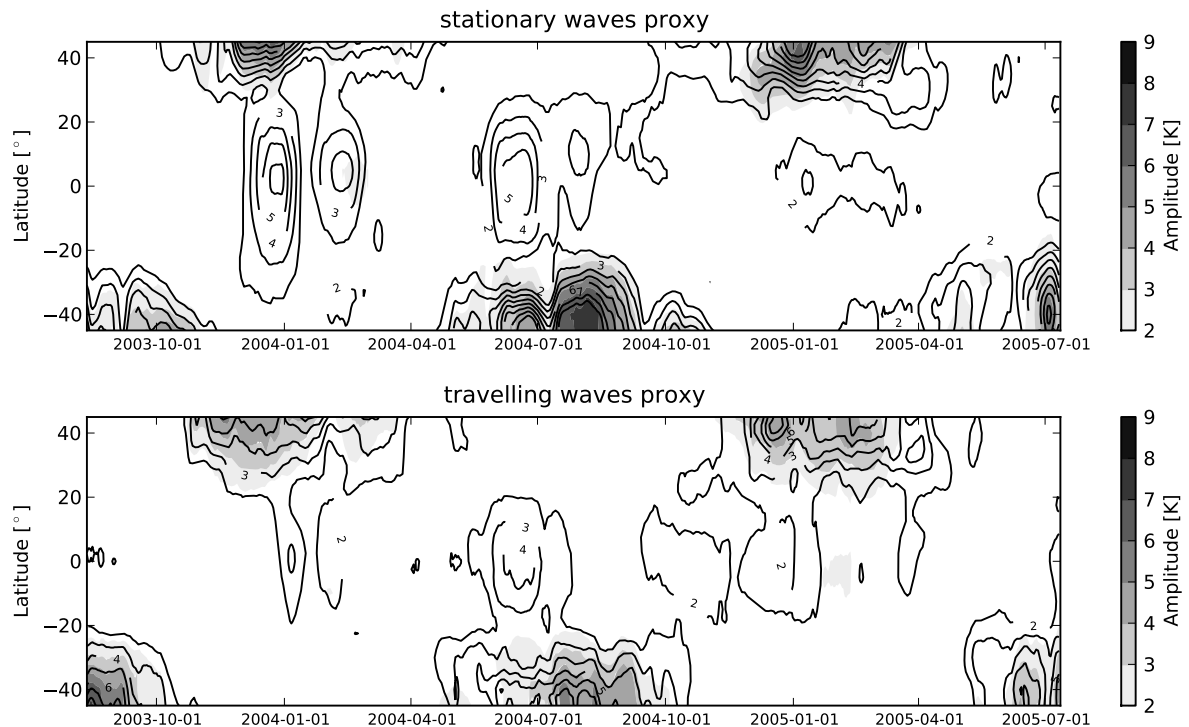
Figure 4: *Time-latitude plane at about 50km of the stationary PW-proxy (upper panel) and travelling PW-proxy (lower) derived from SABER (greyscaling) and MetOffice (contours).*

measurements including the mesosphere and lower thermosphere up to 130 km. Note, that the data above 80 km are aliased due the tidal wave amplitudes increasing with altitude. To reduce this effect the amplitudes of proxies are normalized by σ_{tot} (see section 3). The temporal and spatial structure of the stationary (upper panel) and travelling (lower panel) PW-proxy at 45°N seems consistent with the amplitude of SPW1 and long-period PW (winter 2003/04) presented in Pancheva et al. (2009a). Two maxima of the stationary wave occur around 40 km and 70 km in both cases as well as the break in January 2004 caused by major sudden stratospheric warming (SSW). Finally, from Figure 5 one can see that PW are not able to propagate directly into the lower thermosphere.

5. Modulation of GW by PW

GW, which cover a broad range of horizontal and vertical wavelengths shorter than those of PW as well as frequencies between buoyancy and inertial frequency, are considered to be able to transfer signals of stratospheric PW into the upper neutral atmosphere. Their amplitudes cause fluctuations in the thermosphere density and composition modulated by PW from below. Due to the connection of the thermosphere and ionosphere, signatures of PW then should be also visible in the ionised component.

Analogue to the previous section, PW-proxies are determined to obtain a general picture
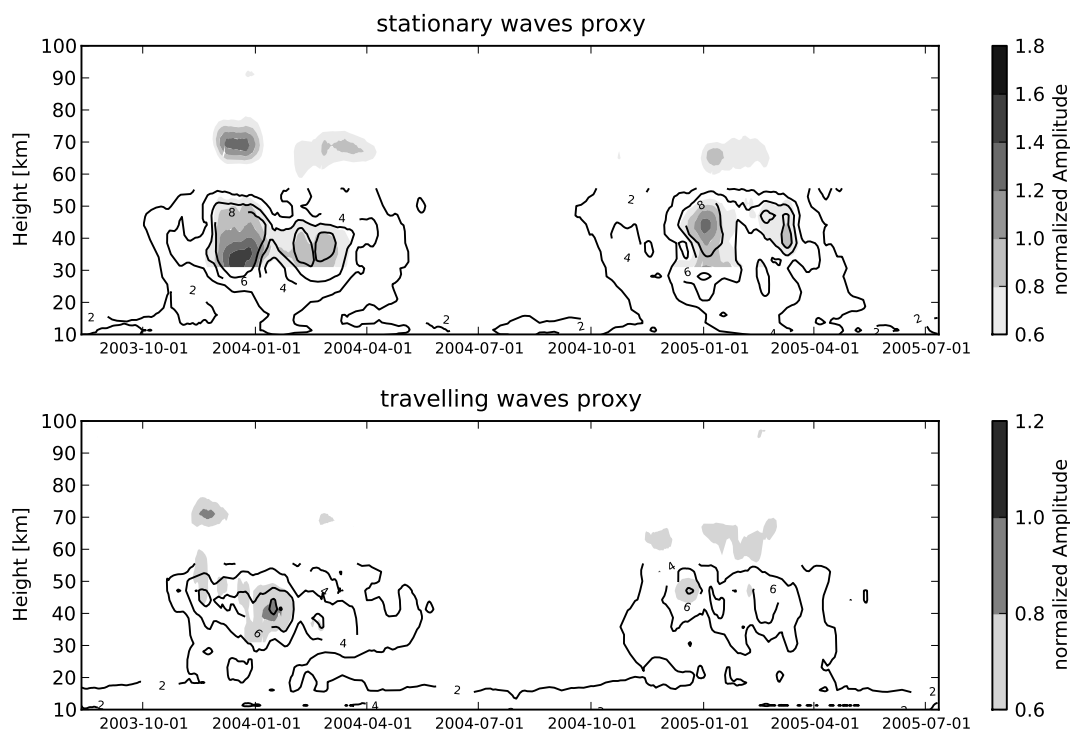
Figure 5: *Time-altitude cross-section at 45°N of the stationary PW-proxy (upper panel) and travelling PW-proxy (lower panel) derived from SABER (greyscaling) and MetOffice (contours). The PW-proxies in SABER are normalized by the total standard deviation in the time-longitude domain at each height.*

of modulation effects of GW by global scale waves such as PW. The latitude-height cross-section presented in Figure 6 shows the GW modulation by stationary (left) and travelling (right) PW for winter 2003/04 (Dec-Jan). The latitudinal distribution reveals signatures of stratospheric PW in the GW potential energy at mid-latitudes (greyscaling). At lower latitudes and in the southern hemisphere no signals of PW exist. In the mesosphere/lower thermosphere (80-130 km) a similar latitudinal structure of GW modulation by PW can be observed only for the travelling component. However, a maximum of this proxy near the summer mesopause (80 km) at 45°S is found. Figure 7 depicts the modulated GW potential energy (greyscaling) by stationary (upper panel) and travelling (lower panel) components. The magnitudes are again normalized by σ_{tot} for each altitude. The contour lines show the associated PW activity derived from MetOffice for the stationary- and travelling proxies, respectively.

In section 4 we have already shown that PW cannot propagate directly into the thermosphere, but we suppose that signatures of PW are able to be transfered from the stratosphere to the lower thermosphere indirectly by the modulation of GW. These have smaller horizontal and vertical scales than PW, which enables them to overcome the mesopause and penetrate the lower thermosphere. From Figure 7 we can conclude that especially travelling PW modulate GW at stratospheric heights and these signatures are detected,
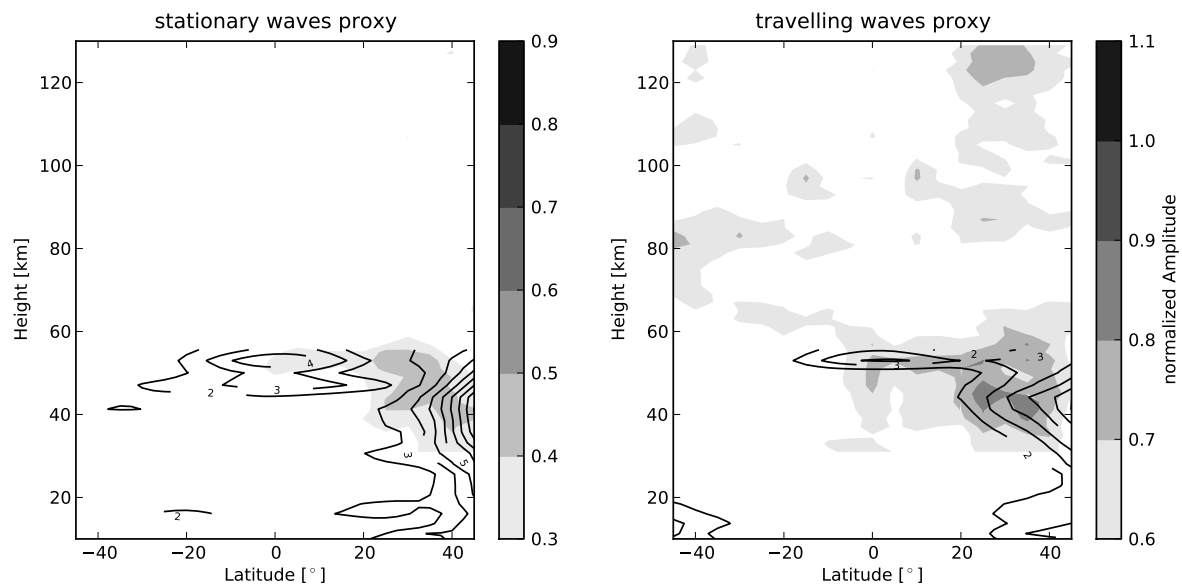
Figure 6: *Similar to Figure 3, but the normalized potential energy of GW derived from SABER (greyscaling) is shown.*

although slightly modified at 120 km similar to PW activity. In mid-winter 2003/04, we observe two maxima of travelling proxy amplitudes in GW potential energy signals during early and late winter. This behaviour is connected to SSW showing a break in the stationary proxy and the modulation of GW by travelling PW. The same structure can be observed between 90-120 km. In winter 2004/05 (without SSW), the modulation of GW is not disturbed, but the signals of GW above 90 km appear different to the stratosphere.

A special phenomenon is observed around the summer mesopause which shows a maximum of GW modulation, probably caused by in situ processes. A connection to the quasi-2-day wave (QTDW) is assumed, which maximises in summer at midlatitudes (Jacobi et al., 1997). In this connection, the low values of the normalized proxies that occur in the winter mesopause are caused by the large summer amplitudes such that the winter PW are underestimated. Thus, the signature of PW should be continuously visible by the modulation of GW.

6. Coupling between atmosphere/ionosphere

As already demonstrated in the previous section, PW may modulate GW and their signatures can propagate into the lower thermosphere almost continuously. In this section we present evidence of the indirect coupling mechanism between stratosphere travelling PW and ionospheric PWTO by an example of the modulation of GW at 45°N.

Figure 8 shows the time series of travelling PW-proxy applied to data at different heights from the stratosphere (40 km) up to the ionosphere (∼300 km). Their amplitudes are normalized and scaled in according to the corresponding height. The stratospheric PW from MetOffice data at about 40 km (thick dark line) represents the actual wave activity of the travelling components. In addition, the modulation of GW by travelling PW
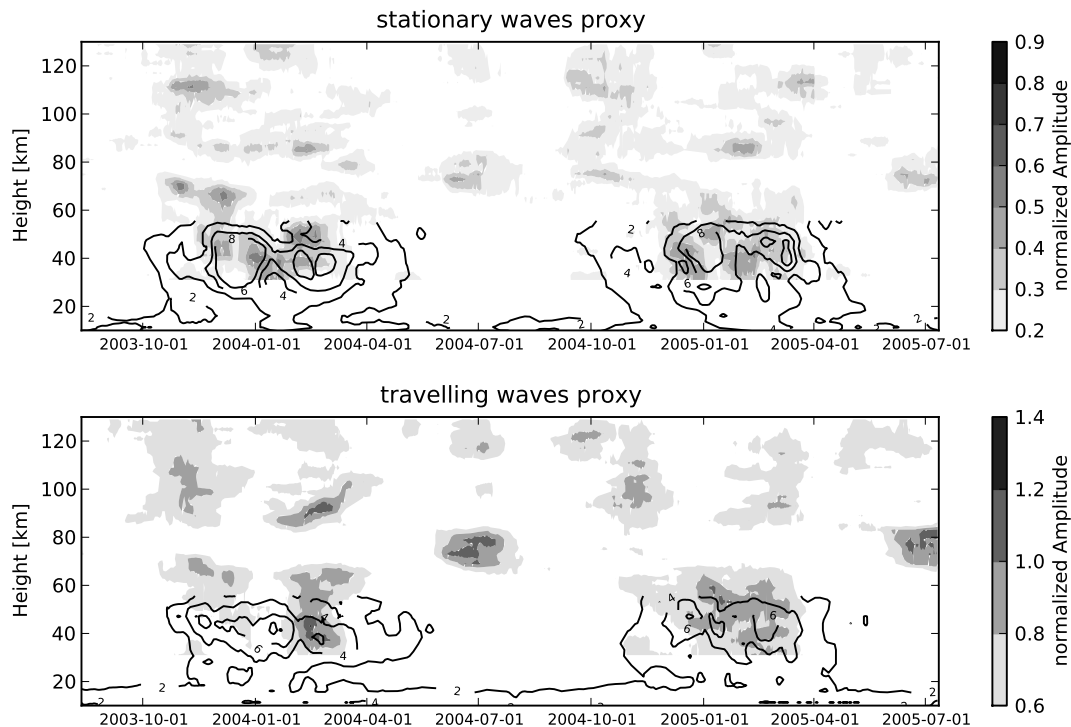
Figure 7: *Time-altitude cross-section at 45°N of GW modulation by stationary (upper panel) and travelling (lower panel) PW. The PW-proxies of GW (greyscaling) derived from SABER are normalized by the total standard deviation in comparison to PW-proxies obtained from MetOffice (contours).*

derived from SABER at 8 different heights (thin grey lines) averaged over 10 km are added from the stratosphere (30 km) to the lower thermosphere (120 km). The time series of the modulated signal reproduces the one of the PW activity especially in early and late winter 2003/04 (grey shaded). One observes a signal of PW in the stratosphere and a modulation of GW up to 120 km. At the same time signatures of PW in the ionosphere by modulation of TID (thick dotted line) and PWTO (thick dashed line) derived from TEC can be detected. We may consider this result as a supporting evidence for an indirect vertical coupling between the stratosphere and ionosphere. The situation in winter 2004/05 differs from the previous one. There is no SSW and the modulation of GW by PW follows the course of the PW activity up to 90 km relatively well. Above, the character occur slightly changed, however, a possible correspondence can be found with respect to proxies derived from ionospheric data. However, there is no clear similarity in the behaviour of the different parameters, especially in December 2004. At 120 km the GW potential energy shows a minimum while TID signatures indicate a maximum. In contrast to that, the proxy of PWTO reveals no important change. We may conclude that there is a possible coupling between PW, GW modulation, TID and PWTO, however, this coupling is intermittent and does not occur necessarily in every winter.

The summer maximum around 80 km seems to be caused by in situ processes in connection

with the QTDW. Neither stratospheric PW nor signatures of PW in the ionosphere are visible in the TID and TEC data.
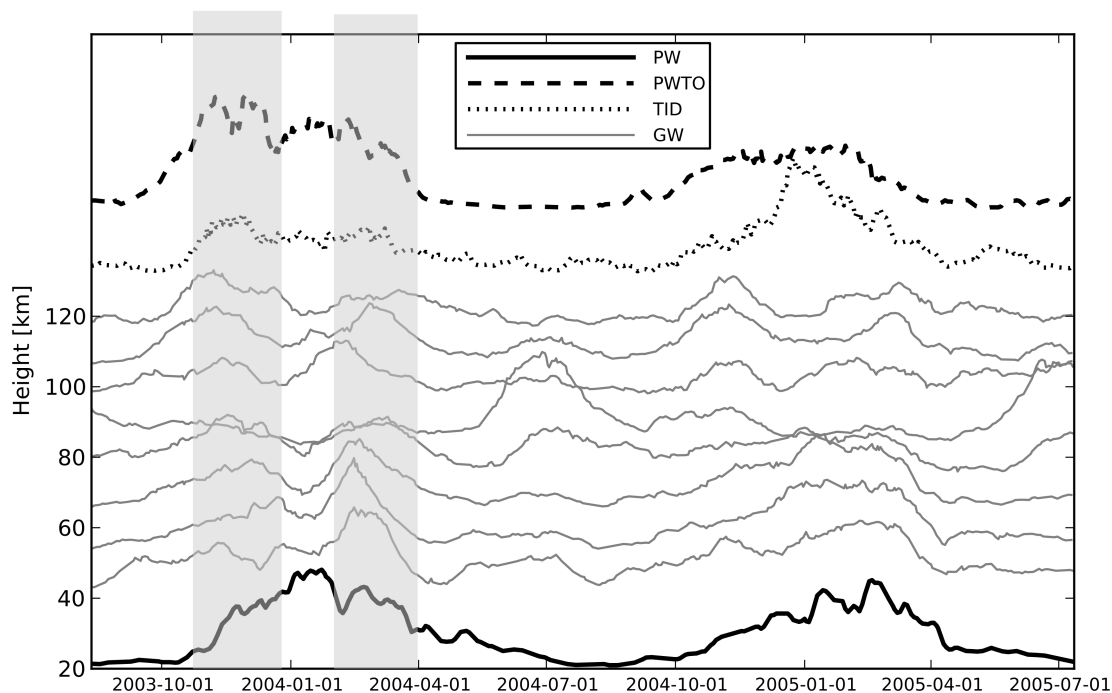
Figure 8: *Time series of travelling PW-proxies for different parameters at several heights. Starting from below: PW (thick dark line), GW (thin grey lines), TID (dotted line) and PWTO (dashed line). All amplitudes (A) are normalized by the long-term mean ($\bar{A}$) and scaled according to the corresponding height:*
$A_{PW} = 20 + 10 \cdot (A/\bar{A})$, $A_{GW} = h_z + 30 \cdot (A/\bar{A})$, $A_{TID} = 130 + 10 \cdot (A/\bar{A})$, $150 + A_{PWTO} = 10 \cdot (A/\bar{A})$

7. Conclusions

A possible connection between stratospheric PW and ionospheric PWTO by the modulation of GW potential energy derived from SABER (space-based) temperature profiles is presented in this paper using proxies of PW activity. To this end, we have used SABER temperatures and MetOffice reanalyses. At first, we have shown that PW proxies (stationary and travelling) derived from both data sets are conform at midlatitudes. Up to about 70 km the SABER data deliver reliable results of PW without aliasing effects that are, near the mesopause, caused by the sun-synchronous observation and the increasing tidal amplitudes in the upper mesosphere. However, using the normalization by σ_{tot} this influence can be reduced. The results of our analysis confirm literature results that stationary waves cannot propagate higher than about 80 km.

Furthermore, the mechanism of vertical coupling between the stratosphere and ionosphere through the modulation of GW by PW has been analysed. It could be demonstrated that during some winters GW amplitudes are modulated by PW and propagate directly upward

up to the lower thermosphere where they may cause fluctuations in density and composition. Due to the interaction between the neutral and ionised component of the upper atmosphere possible modulation effects could trigger TID and finally PWTO, which had been demonstrated by the corresponding time serie of these parameters during one winter. The mechanism of vertical coupling, which is proved for the winter seasons 2003/04 indicates promising results that stratospheric PW activity modulates GW (PW→GW) well seen in Nov. 2003, Feb. 2004 and Feb. 2005. During these periods of time GW obviously propagate directly upward into the lower thermosphere (120 km). Due to the fact that ionospheric plasma acts to a certain degree as a tracer in the neutral atmosphere, the temporally behavior between the PW-proxy derived from GW potential energy and TID signatures appears comparable (GW→TID), except for Dec. 2004.

Although, the applied method using proxies of PW delivers only a general view of such coupling mechanism, but the results manifestate the likely relation between PW and PWTO by the transmission path PW→GW→TID→PWTO.

Acknowledgments

References

Altadill, D., Apostolov, E. M., Jacobi, C., Mitchell, N. J., 2003: Six-day westward propagating wave in the maximum electron density of the ionosphere. Ann. Geophys., 21, 1577-1588.

Borries, C., Jakowski, N., Jacobi, Ch., Hoffmann, P., Pogoreltsev, A., 2007: Spectral analysis of planetary waves seen in the ionospheric total electron content (TEC): First results using GPS differential TEC and stratospheric reanalyses. J. Atmos. Solar.-Terr. Phys., Vol. 69, 2442-2451, doi:10.1016/j.jastp.2007.02.004.

Borries, C., Jakowski, N. and Wilken, V., 2009: Storm induced large scale TIDs observed in GPS derived TEC. Ann. Geophys., 27, 1605-1612.

Fröhlich, K., Schmidt, T., Ern, E., Preusse, P., de la Torre, A., Wickert, W., Jacobi, Ch., 2007: The global distribution of gravity wave energy in the lower stratosphere derived from GPS data and gravity wave modelling: Attempt and challenges. J. Atmos. Solar.-Terr. Phys., 69, 2238–2248.

Hayashi, Y., 1971: A General Method of Resolving Disturbances into Progressive and Retrogressive Waves by Space Fourier and Time Cross-Spectral Analyses. J. Meteor. Soc. Japan, 49, 125-128.

Hoffmann, P., Ch. Jacobi, and S. Gimeno-Garcia, 2009: Using Python language for analysing measurements from SABER instrument on TIMED satellite. Rep. Inst. Meteorol. Univ. Leipzig 45, 139-151.

Jacobi, Ch., R. Schminder and D. Kürschner, 1997: The quasi two-day wave as seen from D1 LF wind measurements over Central Europe (52°N, 15°E) at Collm, J. Atmos. Solar-Terr. Phys., 59, 1277-1286.

Laštovička, J., 2006: Forcing of the ionosphere by waves from below. J. Atmos. Solar-Terr. Phys., 68, 479-497.

Oberheide, J., Hagan, M. E., Roble, R. G., 2003: Tidal signatures and aliasing in temperature data from slowly precessing satellites. J. Geophys. Res., Vol. 108(A2), doi:10.1029/2002JA009585.

Mertens, C. J., et al., 2004: SABER observations of mesospheric temperatures and comparisons with falling sphere measurements taken during the 2002 summer MaCWAVE campaign. Geophys. Res. Lett., 31, L03105, doi:10.1029/2003GL018605 .

Pancheva, D., Mukhtarov, P., Andonov, B., Mitchell, N. J., Forbes, J. M., 2009a: Planetary waves observed by TIMED/SABER in coupling the stratosphere–mesosphere–lower thermosphere during the winter of 2003/2004: Part 1 - Comparison with the UKMO temperature. J. Atmos. Solar.-Terr. Phys., Vol. 71, 61-74,doi:10.1016/j.jastp.2008.09.016.

Pancheva, D., Mukhtarov, P., Andonov, B., Mitchell, N. J., Forbes, J. M., 2009b: Planetary waves observed by TIMED/SABER in coupling the stratosphere–mesosphere–lower thermosphere during the winter of 2003/2004: Part 2 - Altitude and latitude planetary wave structure. J. Atmos. Solar.-Terr. Phys., Vol. 71, 75-87,doi:10.1016/j.jastp.2008.09.027.

Pogoreltsev, A. I., A. A. Vlasov. K. Fröhlich, and Ch. Jacobi, 2007: Planetary waves in coupling the lower and upper atmosphere. J. Atmos. Solar-Terr. Phys. 69, 2083-2101.

Preusse, P., Dornbrack, A., Eckermann, S.D., Riese, M., Schaeler, B., Bacmeister, J.T., Broutman, D., Grossmann, K.U, 2002: Space based measurements of stratospheric mountain waves by CRISTA, 1. Sensitivity, analysis method and a case study. J. Geophys. Res., 107, 8178.

Preusse, P., Ern, M., Eckermann, S.D., Warner, C.D., Picard, R.H., Knieling, P., Krebsbach, M., Russell, J.M., Mlynczak, M.G., Mertens, C.J., Riese, M., 2006: Tropopause to mesopause gravity waves in August: measurement and modelling. J. Atmos. Solar.-Terr. Phys., 68, 1730–1751.

Tsuda, T., Nishida, M., Rocken, C., Ware, R. H, 2000: A global morphology of gravity wave activity in the stratosphere revealed by the GPS occultation data (GPS/MET). J. Geophys. Res., 105, 7257-7273.

Addresses of the Authors:

Peter Hoffmann (phoffmann@uni-leipzig.de)
Christoph Jacobi (jacobi@uni-leipzig.de)

Institute for Meteorology
University of Leipzig
Stephanstr. 3
04103 LEIPZIG

Piecewise linear trend detection in mesosphere/lower thermosphere wind time series

R. Q. Liu and Ch. Jacobi

Summary

A piecewise linear model is developed to detect climatic trends and possible structural changes in time series with a priori unknown number and positions of breakpoints. The initial noise is allowed to be interpreted by the first- and second-order autoregressive models. The goodness of fit of candidate models, if the residuals are accepted as normally distributed white noise, is evaluated using the Schwarz Bayesian Information Criterion. The uncertainties of all modeled trend parameters are estimated using the Monte-Carlo method. The model is applied to the mesosphere/lower thermosphere winds obtained at Collm (52°N, 15°E) during 1960-2007. A persistent increase after ~1980 is observed in the annual mean zonal wind based on the primary model while only a weak positive trend arises in the meridional component. Major trend breakpoints are identified around 1968-71 and 1976-79 in both the zonal and meridional winds.

1. Introduction

As with global change near the Earth's surface, there is also of interest to detect long-term trends in the upper atmosphere and attribute them to their primary causes. Recently, a relatively consistent pattern of middle and upper atmosphere temperature trends has been presented, showing cooling in the stratosphere/mesosphere, weak trend around the mesopause, and cooling in the thermosphere (Laštovička et al., 2008). However, when dynamical parameters in the middle and upper atmosphere are considered, a much less clear picture is found. Now available mesosphere/lower thermosphere (MLT) wind time series of more than three decades indicate that wind trends may be interrupted, or change direction (Portnyagin et al., 2006; Jacobi et al., 2009; Merzlyakov et al., 2009).

These changes in trends may be analysed using statistical models. Unlike in some pioneer structural change trend analyses, e.g. on the turnaround and recovery of the total ozone column (Reinsel et al., 2002) or changes of the global surface temperature anomaly (Seidel and Lanzante, 2004), where the possible change dates are specified in advance, the number and times of possible trend breaks in MLT winds are a priori unknown (Tome and Miranda, 2004), i.e., they can only be determined according to some basic mathematical principles that underpin the proposed model. This also increases the complexity and skill needed from a practical algorithm. In addition, an integral trend model should be able to not only detect possible trend breakpoints (BPs) and measure the associated partial trends but also as fully as possible account for the variability of an original time series. So an implicit fundamental assumption for a statistical model is that the ultimate modeled errors need (or can) not be explained any more, e.g., the residuals can be regarded as independent and identically distributed (i.i.d.) random variables with zero mean and common variance (Reinsel et al., 2002; Seidel and Lanzante, 2004).

A statistical model for structural change trend assessment, incorporating the methods proposed by Tome and Miranda (2004) and Seidel and Lanzante (2004), has been developed. It will be applied to analyze the climatic trends and their structural changes in the mid-latitude MLT wind series obtained at Collm (52°N, 15°E) during 1960-2007.

2. A piecewise linear trend model

As a natural extension of the linear regression model, let us consider the following structural change linear regression model with m BPs T_1, T_2, … T_m (and thus $m+1$ regimes or segments) applied to a time series of the length T:

$$Y_t = \sum_{i=1}^{m+1} I_{\{T_{i-1}+1 \leq t \leq T_i\}}(a_i + b_i t) + N_t, \quad (t = 1, \ 2, \ ..., \ T), \tag{1}$$

where $T_0 = 0$, $T_{m+1} = T$. I_A denotes an indicator variable equal to one if the event A is true (e.g. when $t \in [T_{i-1}+1, \ T_i]$) and zero otherwise (e.g. when $t \notin [T_{i-1}+1, \ T_i]$). A continuity condition at each turning point is imposed as

$$a_i + b_i T_i = a_{i+1} + b_{i+1} T_i, \quad (i = 1, \ 2, \ ..., \ m). \tag{2}$$

In Eq. (1), Y_t is the observed dependent variable at time t, a_i and b_i ($i = 1, \ 2, \ ..., \ m+1$) are the corresponding trend regression coefficients (i.e. intercept and slope) for each segment, and N_t is the unexplained noise term often assumed to be autoregressive with time lag of 1 or 2 (AR(1) or AR(2), e.g. Reinsel et al., 2002; Seidel and Lanzante, 2004). That is, $\{N_t\}$ satisfies $N_t = \varphi N_{t-1} + \varepsilon_t$ or $N_t = \varphi_1 N_{t-1} + \varphi_2 N_{t-2} + \varepsilon'_t$, where the errors ε_t (ε'_t) are independent random variables with mean 0 and common variance σ_ε^2 ($\sigma_{\varepsilon'}^2$) and

$$\varphi = \rho_1, \quad \varphi_1 = \rho_1(1-\rho_2)/(1-\rho_1^2), \quad \varphi_2 = (\rho_2 - \rho_1^2)/(1-\rho_1^2) \ ,$$

when assuming $\{N_t\}$ is a stationary random process with standard lag-one and -two autocorrelations ρ_1 and ρ_2.

Note that this is a partial structural change model in the sense that the autoregressive parameters are assumed to be constant across regimes. The BPs T_1, T_2, … T_m are explicitly treated as unknown. Our procedure is first to estimate the unknown piecewise linear trend coefficients together with the times of BPs when T observations on Y_t are available. Then the produced noise term will be tentatively interpreted, respectively, by the first- and second-order autoregressive models as well as that one without autoregression (AR(0)) when the N_t themselves can be regarded as independent random errors with zero mean and common variance σ_N^2. Finally, the uncertainties of all modeled trend parameters (including the positions of BPs) are estimated using the Monte-Carlo method.

In general, the number of structural breaks m is also unknown. However, at the beginning, we treat it as known (i.e. apply the procedure with different m) and its determination will be treated later as a problem of model selection. The method of estimation considered is that based on the least-squares principle (Bai and Perron,

1998). For each m-partition $(T_1,\ T_2,\ ...,\ T_m)$, the associated least-squares estimates of trend coefficients are obtained by minimizing the "sum of squared residuals (SSR)" (as in Tome and Miranda (2004), we treat slopes of line segments and intercept of the first segment as the independent regression coefficients and so employ an efficient algorithm proposed therein to create the design matrix):

$$S_T = \sum_{t=1}^{T}\left[Y_t - \sum_{i=1}^{m+1} I_{\{T_{i-1}+1 \le t \le T_i\}}(a_i + b_i t)\right]^2, \tag{3}$$

and the estimated BPs $\hat{T}_1,\ \hat{T}_2,\ ...,\ \hat{T}_m$ are such that

$$(\hat{T}_1,\ \hat{T}_2,\ ...,\ \hat{T}_m) = \arg\min_{T_1,\ ...,\ T_m} S_T(T_1,\ T_2,\ ...,\ T_m), \tag{4}$$

where the minimization is taken over all partitions $(T_1,\ T_2,\ ...,\ T_m)$ subject to a set of appropriate constraints on the minimum distance between two consecutive BPs, the minimum length for the first and last segments and the minimum amount of trend change at BPs (Tome and Miranda, 2004; 2005).

In practice, one can start with the case of zero BP (i.e. the simple linear case when Eqs (1) and (3) are still valid but (2) and (4) disappear naturally), up to a maximum of $m\ (\ge 1)$ BPs. For each of the $m+1$ cases the following step is to augment the corresponding regression trend with the first- and second-order autoregressive components. As did in Seidel and Lanzante (2004), we assess the goodness of fit of the residuals (hereafter i.e. the modeled errors) to a one-dimensional (1-D) Gaussian distribution, both with removal of the AR(1) or AR(2) behavior in the noise and directly with the model AR(0), by using the Anderson-Darling (AD, e.g. Romeu, 2003) statistic to test the null hypothesis of normally distributed residuals. We eliminate from further consideration any model for which the null hypothesis is rejected at the 5% significance level (see Table 1A in Stephens, 1974). On the other hand, the mean and the standard lag-one and -two autocorrelations of each accepted normally distributed residual series are calculated to check whether it can be regarded as a realization of a white noise process. Only after this we, in principle, employ the standard form of the Schwarz Bayesian Information Criterion (BIC, Ng and Perron, 2005; Portnyagin et al., 2006):

$$S(q) = T\ln\left[\frac{1}{T}\sum_{t=1}^{T}\left(Y_t - \hat{Y}_t\right)^2\right] + q\ln T, \tag{5}$$

where $\hat{Y}_t$ denotes the modeled value (vs. the residual) of the dependent variable at time t and $q = 2m+2$ for AR(0), $q = 2m+3$ for AR(1) and $q = 2m+4$ for AR(2) (Seidel and Lanzante, 2004), to select the primary/best and secondary models as those with the lowest and second-lowest values of BIC, provided that the residuals are accepted as 1-D normally distributed white noises.

Finally, an important and unavoidable issue is the statistical significance of the estimated BPs and partial trends whereas it is still an open discussion (Tome and Miranda, 2005). For each accepted residual series (hereafter, as a 1-D normally distributed white noise), however, it is reasonable to assume that the residuals are i.i.d. and follow a common distribution $N(0,\sigma_N^2)$ for AR(0), $N(0,\sigma_\varepsilon^2)$ for AR(1) or $N(0,\sigma_{\varepsilon'}^2)$ for AR(2). Thus it is convenient, using the Monte-Carlo simulation approach, to estimate

the standard deviations of all modeled trend parameters (one can repeatedly generate the corresponding pseudorandom normally distributed residual series (Press et al., 1992), add it to the modeled sequence of the dependent variable and run the first step of the foregoing procedure, and at last compute the sample mean and variance of all the fitted trend parameters).

3. Application to Collm wind data

The model is applied to Collm MLT zonal and meridional prevailing winds during 1960-2007. The data evaluation and first trend analysis results have already been presented in Jacobi et al. (1997) and Jacobi and Kürschner (2006). There have been several changes in measuring strategy, which can potentially lead to inhomogeneity in the time series and thus to possible artifacts in trend analysis. During the first decade of the measurements, data analysis has been performed manually, with smaller measuring density in the early years. In particular, before 1968 data have been only taken during the evening hours, so that these years cannot be regarded as reliable in a trend analysis. The switch from manual to automatic data analysis in 1972 has been accompanied by a very long (several years) parallel analysis, so that artifacts due to this change are improbable. The change from the analysis of single time series to an average over three measuring paths is connected with a smoothing of the time series. Therefore, year-to-year variability before and after 1979 may show an apparent change, which is not of meteorological origin. However, the analysis of long-term trends should not be seriously affected.

Because we are mainly concerned about the climatic trends and their structural changes in the MLT winds and to avoid so-called end effects (Tome and Miranda, 2005), the minimum distance between adjacent BPs and the minimum length for the first and last segments are both set to 5 years in this study. The allowed minimum amount of trend change at BPs is 0.01 ms^{-1}/year. These constraints are optimized for our problem and changing them moderately would not have a significant effect on the modeled results. To accurately estimate the standard deviations of all fitted trend parameters when using the Monte-Carlo method, we always generate 10000 pseudorandom series (actually only ~8300 series are used because ~17% of them are rejected at a 15% significance level through the AD test) to simulate the corresponding normally distributed i.i.d. residuals. Some model parameters and input/output data files are listed in Appendix A.

The model is applied to annual mean winds, which are expected to disclose stable trend results, although one has to keep in mind that annual mean winds in the MLT have limited physical meaning.

Fig. 1 shows annual mean zonal winds with corresponding trends added, based on different pure trend models with 0 BP up to 5 BPs (from bottom to top) but without autoregression. At first, the AD tests (hereafter at the 5% significance level) and related statistic calculations (see Table 1) reveal that only the models with 2 up to 5 BPs can produce acceptable residuals. In other words, both the simple linear assumption and the 1-BP pure trend model (showing results similar to those obtained in Portnyagin et al. (2006) but with a larger variance of the break point time) have to be eliminated from further consideration owing to the non-Gaussian distribution of their residual series and the large lag-one autocorrelations as well. Then from Table 2 we find that the best choice

according to BIC is the 2-BP pure trend model (i.e., without autoregressive component). It exhibits 2 major turning points, respectively, in 1971 and 1979, and after that a persistently positive trend (0.22 ms^{-1}/year) arises. Nevertheless, the large wind variability before the late 1970s has not yet been completely removed by annually averaging (refer to Fig. 3 below). This strong variability probably includes some artifacts, and in turn, it will "mislead" the BIC (see the right hand side of Eq. (5)) to select a simpler model having BPs only before ~1980. In this case, as the number of fitting parameters q increases, the second term $q\ln T$ will increase rapidly whereas the first term (proportional to the SSR) decrease slowly (refer to Fig. 3 below), together leading to an increase of the value of BIC. This suggests that in reality the 3- and 4-BP pure trend models should also be considered as acceptable choices (we reject the 5-BP fit, which shows the same times of the last 4 BPs as in the 4-BP model, because of its high value of BIC). This provides 2 additional possible trend breaks, i.e. those in 1991 and 1998/99. These BPs are almost independent/quasi-stable solutions because their respective uncertainty intervals have no evident overlaps with those of other BPs. Or, more properly, they can be regarded as "minor shifts" which are superposed on a persistently increasing background wind after 1979.
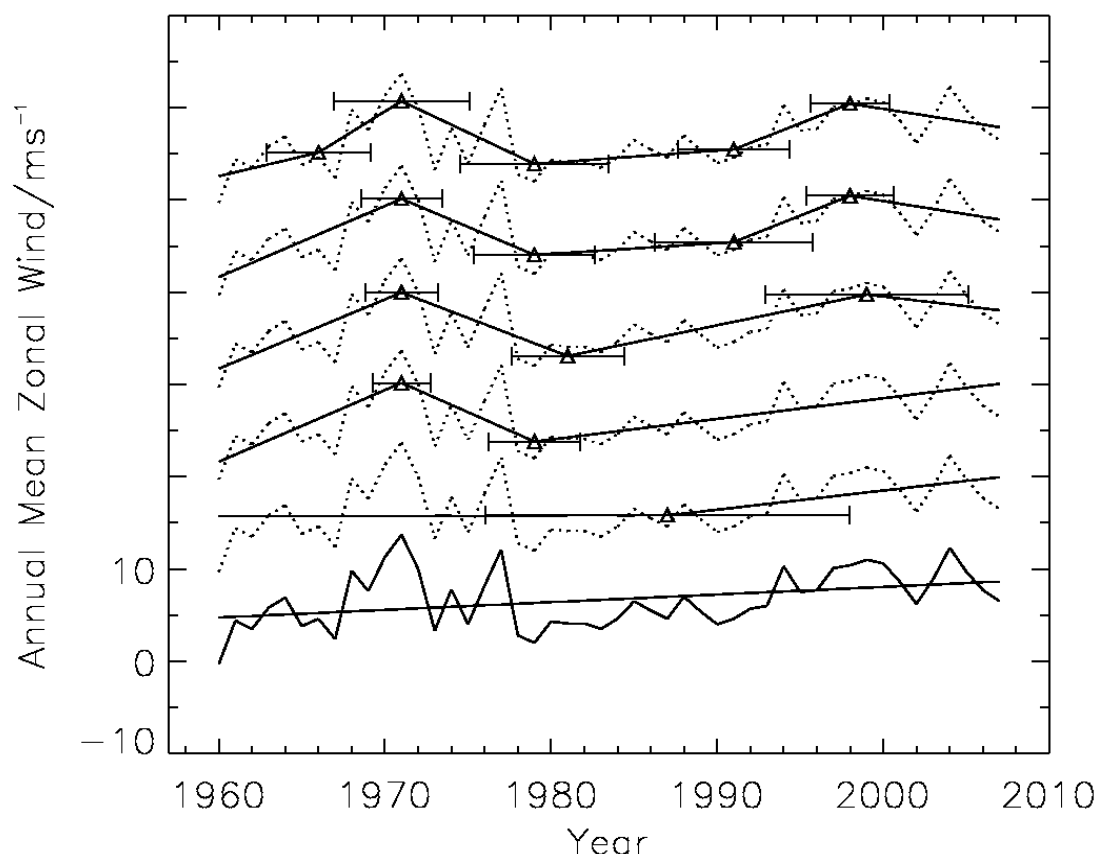
Fig. 1. *Time series of the annual mean zonal wind with corresponding trends added in turn, from bottom to top, based on different pure trend models (with 0 BP up to 5 BPs but without autoregression).*

All the trend break years detected above have, within the limits of their uncertainty, been identified in the winter prevailing zonal wind observed over Obninsk (55°N, 37°E) as well using a sophisticated WZ-method (Merzlyakov et al., 2009). Furthermore, the turnaround at ~1990 has been given particular attention recently in the combined Collm and Obninsk winds, because it may indicate a structural change in trends in dynamics of the whole northern mid-latitude middle atmosphere up to the lower thermosphere (Portnyagin et al., 2006; Jacobi et al., 2009).

Table 1: *Mean (μ), standard lag-one (ρ_1) and -two (ρ_2) autocorrelations, AD-statistic (A^{2*}) and associated significance level (α) of normal distribution testing of each residual series based on different pure trend models (i.e., with m -BP trend but without autoregressive component) applied to the time series of annual mean zonal wind. The number symbols (#) indicate unacceptable residuals at the 5% significance level, but the corresponding statistic values are still listed for comparison.*

m AR(0)	0	1	2	3	4	5
μ (ms-1)	.00	.00	.00	.00	.00	.00
ρ_1	.42	.35	.12	.06	.02	-.01
ρ_2	.18	.09	-.19	-.26	-.28	-.28
A^{2*}	.90	.83	.38	.28	.50	.61
α	# <.05	# <.05	>.15	>.15	>.15	>.10

Table 2: *Values of BIC based on different pure trend or combination models (i.e., with m -BP trend plus r -order autoregressive component) applied to the time series of annual mean zonal wind. The best model is identified with an asterisk (*). The number symbols indicate cases of unacceptable residuals, but the corresponding BIC values are still listed for comparison.*

m r	0	1	2	3	4	5
0	# 108.52	# 113.39	* 100.44	104.12	108.90	115.41
1	102.88	110.26	103.56	107.80	112.75	119.28
2	106.35	114.16	105.17	108.02	112.66	# 119.40

As in the analysis for the zonal wind, the annual mean meridional wind and its candidate trends, based on different pure trend models, are presented in Fig. 2. From Tables 3 and 4 we find that only the models with 2 up to 4 BPs produce acceptable residuals and again the best fit, according to BIC, is provided by the 2-BP pure trend model. It exhibits 2 major turning points, respectively, in 1968 and 1975. After that only a weak positive trend (0.06 ms^{-1}/year) arises in the annual mean meridional wind, which is due to the different trends in different seasons (Jacobi and Kürschner, 2006). As is the case with the zonal wind, we suggest that in reality the 3- and 4-BP pure trend models should be considered as reasonable alternatives. This discloses 2 expanded trend breaks, i.e. those in 1981 and 2001 (while adjusts the second major BP from 1975 to 1976), though the first one indicates a large uncertainty interval overlapping with the small one of the major BP in 1976.
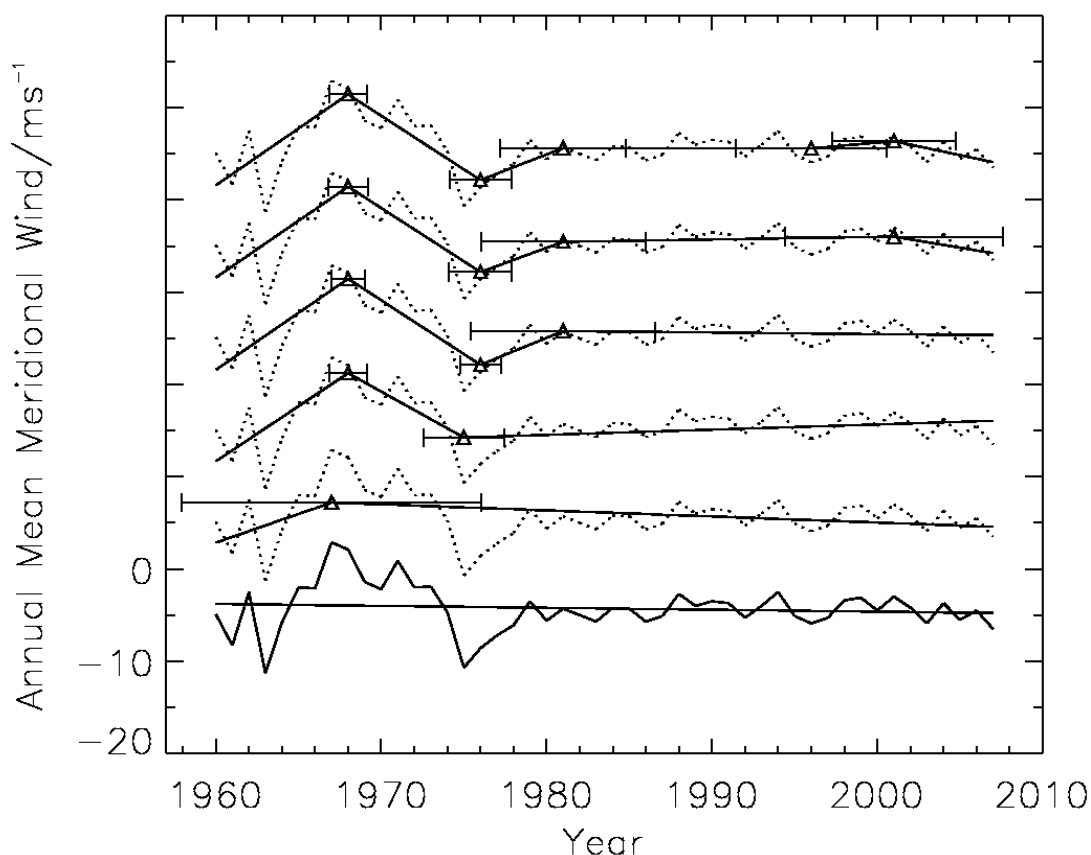
Fig. 2. *Same as Fig. 1 except for the annual mean meridional wind.*

Table 3: *Same as Table 1 except for the annual mean meridional wind.*

m AR(0)	0	1	2	3	4	5
μ (ms^{-1})	.00	.00	.00	.00	.00	.00
ρ_1	.48	.41	.05	-.07	-.09	-.09
ρ_2	.34	.32	.03	-.04	-.06	-.06
A^{2*}	1.11	.84	.55	.61	.76	.79
α	# <.01	# <.05	>.15	>.10	>.05	# <.05

Table 4: *Same as Table 2 except for the annual mean meridional wind.*

m \ r	0	1	2	3	4	5
0	# 99.51	# 100.98	* 85.74	87.56	93.93	# 101.44
1	# 91.31	# 96.05	89.47	91.17	97.41	104.90
2	# 94.19	# 97.59	93.18	95.08	101.23	108.74

Fig. 3 demonstrates the variations of the estimated SSR (sum of squared residuals) and BIC with different pure trend models applied to the annual mean zonal and meridional winds, respectively. One can see that, compared with the simple linear assumption and the 1-BP case, the 2-BP pure trend model leads to a drastic decrease of the SSR and thus to a sharp drop of the BIC. However, once the BPs assumed in the winds exceed 2, the SSR only decreases slowly so that the BIC turns to increase almost linearly with the increasing number of BPs. Therefore the 2-BP pure trend models obtain the minimum BIC. Nevertheless, as mentioned above, because the large wind variability before the late 1970s probably includes some artifacts and, in turn, contributes to the drastic decrease of the SSR, the 3- and 4-BP pure trend models, which prove to produce acceptable residuals, should in principle be considered as alternative choices.
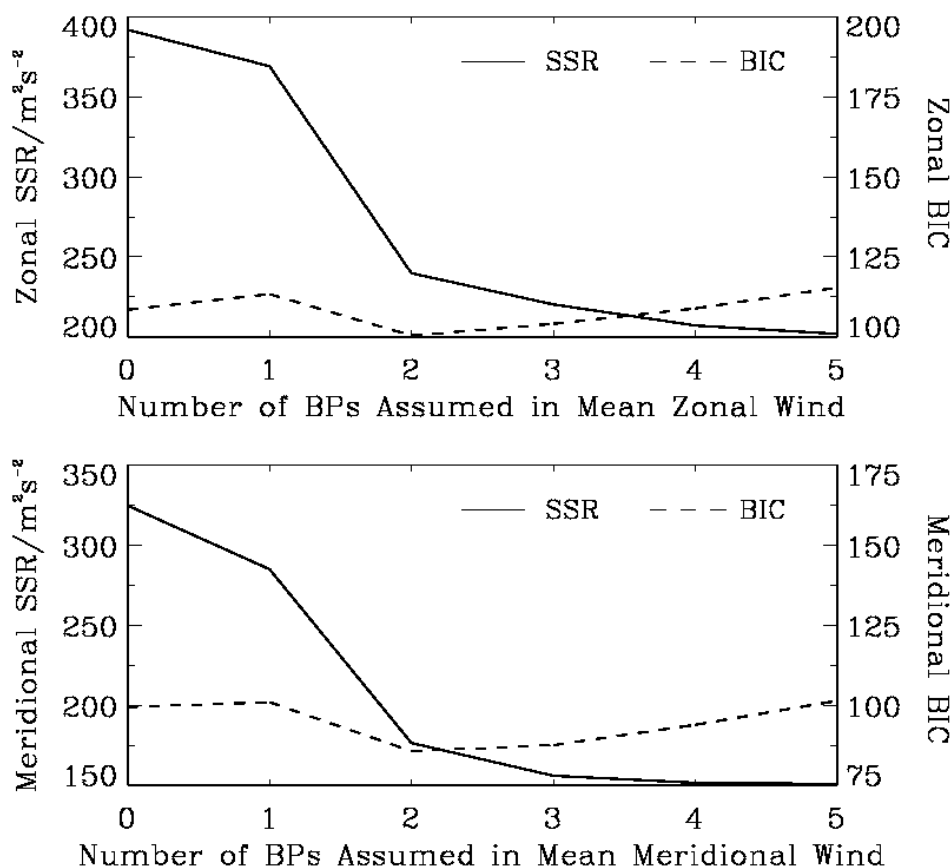
Fig. 3. *Variations of the estimated SSR (solid lines) and BIC (dashed lines) with different pure trend models (with 0 BP up to 5 BPs but without autoregression) applied, respectively, to the annual mean zonal (upper panel) and meridional (lower panel) winds.*

The complete modeling results (modeled series plus residuals) of the annual mean zonal and meridional winds based on the primary and secondary models selected according to BIC (see Tables 2 and 4) are displayed in Fig. 4. One can find that the two fits for the zonal wind are from different (pure trend and combination) structural models since the secondary model has incorporated a first-order autoregressive component, while for the meridional component the two fits are from the same (pure trend) structural models. However, for the zonal wind the reference meaning of the secondary fit is weak because the pure linear trend assumption has proved to be unacceptable (Table 1) and the secondary model has a value of BIC (102.88) much closer to those (103.56 and 104.12) of the third and fourth models than to the BIC (100.44) of the primary model (Table 2). For the meridional component the reference meaning of the secondary fit is strong since the 3-BP pure trend model proves to produce acceptable residuals (Table 3) and the first four models have almost equally spaced BIC values (85.74, 87.56, 89.47 and 91.17, see Table 4).
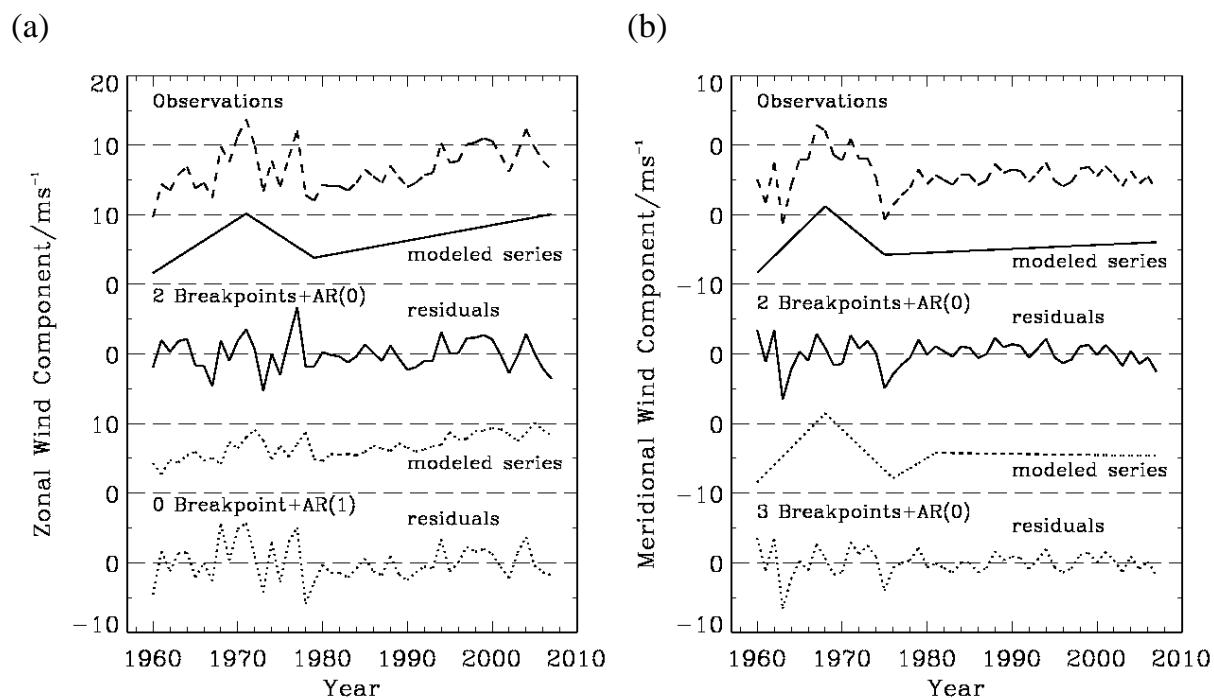
Fig. 4. *Time series of the annual mean (a) zonal and (b) meridional winds (dashed line) and their complete modeling results based on the primary (2 BPs plus AR(0) in both cases: solid lines for the modeled series and the residuals) and secondary (linear plus AR(1) for (a) and 3 BPs plus AR(0) for (b): dotted lines for the modeled series and the residuals) models selected according to BIC.*

4. Discussion

In some cases (e.g. in the seasonal mean winds, not shown here) the initial noises must be further interpreted by an AR(1) or AR(2) even if based on the primary models, suggesting that other unidentified factors or processes may also play a role in determining the evolution of the mesospheric winds. So a multivariate linear regression model (Reinsel et al., 2005) would be a subsequent extension of the basic model in (1) to estimate the effects of other natural factors, possibly including the equatorial Quasi-biennial Oscillation and/or the Southern Oscillation, on the behavior of the MLT winds.

Although attempting to perform the trend analyses as objectively as possible, some subjective decisions unavoidably remain. In particular, when incorporating an AR component in the piecewise linear trend model one always assumes that the initial noise term is a stationary random process. In addition, although the results obtained according to BIC may be statistically robust, there is no unique criterion to select models (Seidel and Lanzante, 2004).

In the case of data showing large local variability in time, it is desirable to consider a heteroskedastic autoregressive component in our model. However, it seems difficult to obtain exact-meaning solutions for all unknown parameters when the form of heteroskedasticity of errors is also unknown, though some statistical-meaning solutions can be modeled, based on the maximum likelihood principle and the use of Gibbs sampler, assuming a WZ-model in which the level, trend and error variance are subject

to synchronous structural changes (Wang and Zivot, 2000; Merzlyakov et al., 2009).

We have also only used the annual mean data starting from 1968, i.e. those during 1968-2007 to do the corresponding analyses, and found that the most reasonable fits are from the 1-, 2- and 3-BP pure trend models that produce piecewise linear trends resembling those shown in Figs 1 and 2 based on the 2-, 3- and 4-BP pure trend models but removing the first segments. So there are only 3 trend BPs identified in the zonal and meridional winds with almost same times as those last three shown in Figs 1 and 2, while the first two BPs in 1976 and 1981 in the meridional wind (during 1968-2007) can even be distinguished with independent uncertainty intervals. However, considering that longer data with more samples will generally produce more reliable modeling we only show the results using the data during 1960-2007.

5.   Conclusions

A piecewise linear regression model is developed to detect climatic trends and possible structural changes in the time series with a priori unknown number and positions of breakpoints based on the least-squares principle. The initial noise term is allowed to be interpreted by the first- and second-order autoregressive models. In principle, the goodness of fit of candidate models, provided that the modeled residuals are accepted as 1-D normally distributed white noises, is evaluated using the Schwarz Bayesian Information Criterion. The standard deviations of all modeled trend parameters are estimated using the Monte-Carlo method. As an example, this piecewise linear model is applied to the mesosphere/lower thermosphere winds obtained at Collm (52°N, 15°E) during 1960-2007. The main results are as follows:

After ~1980 a persistent increase is observed in the annual mean zonal wind based on the primary model selected according to BIC. During nearly the same period of time, however, only a weak positive trend arises in the annual mean meridional wind due to different trends in different seasons.

Major trend BPs are identified in 1968/71 (maybe physically meaningless because of the possible data artifacts before 1968) and ~1976/79 in the annual mean meridional and zonal winds according to BIC. However, in view of the large wind variability before the late 1970s, the 3- and 4-BP pure trend models, which prove to produce acceptable residuals, should in principle be considered as alternative choices. This provides 4 additional possible minor breaks, i.e. those in 1981, 2001 and in 1991, 1998/99, respectively, in the meridional and zonal winds. In fact, the last three of them are almost independent/quasi-stable solutions, and the first one is even selected by BIC itself as a secondary solution although it indicates a large uncertainty interval overlapping with that small of the major BP in 1976.

Acknowledgments

References

Bai, J., Perron, P., 1998: Estimating and Testing Linear Models with Multiple Structural changes. *Econometrica*, *66*, 47–78.

Jacobi, Ch., R. Schminder, D. Kürschner, J. Bremer, K. M. Greisiger, P. Hoffmann, and W. Singer, 1997: Long-term trends in the mesopause wind field obtained from D1 LF wind measurements at Collm, Germany, *Adv. Space Res.*, *20*, 2085–2088.

Jacobi, Ch., Kürschner, D., 2006: Long-term trends of MLT region winds over Central Europe. *Phys. Chem. Earth*, *31*, 16–21.

Jacobi, Ch., Hoffmann, P., Liu, R. Q., Križan, P., Laštovička, J., Merzlyakov, E. G., Solovjova, T. V., Portnyagin, Yu. I., 2009:, Midlatitude mesopause region winds and waves and comparison with stratospheric variability. *J. Atmos. Sol.-Terr. Phys.*, *71*, 1540–1546.

Laštovička, J., Akmaev, R. A., Beig, G., Bremer, J., Emmert, J. T., Jacobi, C., Jarvis, G. Nedoluha, M. J., Portnyagin, Yu. I., Ulich, T., 2008 : Emerging pattern of global change in the upper atmosphere and ionosphere. *Ann. Geophys.*, *26*, 1255–1268.

Merzlyakov, E. G., Jacobi, Ch., Portnyagin, Yu. I., Solovjova, T. V., 2009: Structural changes in trend parameters of the MLT winds based on wind measurements at Obninsk (55°N, 37°E) and Collm (52°N, 15°E). *J. Atmos. Sol.-Terr. Phys.*, *71*, 1547–1557.

Ng, S., Perron, P., 2005: Practitioners' corner: a note on the selection of time series models. *Oxford Bulletin of Economics and Statistics*, *67*, 115–134.

Portnyagin, Yu. I., Merzlyakov, E. G., Solovjova, T. V., Jacobi, Ch., Kürschner, D., Manson, A., Meek, C., 2006: Long-term trends and year-to-year variability of mid-latitude mesosphere/lower thermosphere winds. *J. Atmos. Sol.-Terr. Phys.*, *68*, 1890–1901.

Press, W. H., Teukolsky, S. A., Vetterling, W. T., Flannery, B. P., 1992: Transformation method: exponential and normal deviates. Numerical recipes in Fortran 77, 2nd ed., Cambridge University Press, Cambridge, pp. 277–280.

Reinsel, G. C., Weatherhead, E. C., Tiao, G. C., Miller, A. J., Nagatani, R. M., Wuebbles, D. J., Flynn, L. E., 2002: On detection of turnaround and recovery in trend for ozone. J. Geophys. Res., 107(D10), 4078, doi:10.1029/2001JD000500.

Reinsel, G. C., Miller, A. J., Weatherhead, E. C., Flynn, L. E., Nagatani, R. M., Tiao, G. C., Wuebbles, D. J., 2005: Trend analysis of total ozone data for turnaround and dynamical contributions, J. Geophys. Res., 110, D16306, doi:10.1029/2004JD004662.

Romeu, J. L., 2003: Anderson-Darling: a goodness of fit test for small samples assumptions. *Reliability Analysis Center*, Selected Topics in Assurance Related Technologies, *10*, 1–6.

Seidel, D. J., Lanzante, J. R., 2004: An assessment of three alternatives to linear trends for characterizing global atmospheric temperature changes. *J. Geophys. Res.*, *109*, D14108, doi:10.1029/2003JD004414.

Stephens, M. A., 1974: EDF Statistics for goodness of fit and some comparisons. *J. Am. Stat. Assoc.*, *69*, 730–737.

Tomé, A. R., Miranda, P. M. A., 2004: Piecewise linear fitting and trend changing points of climate parameters. *Geophys. Res. Lett.*, *31*, L02207, doi:10.1029/2003GL019100.

Tomé, A. R., Miranda, P. M. A., 2005: Continuous partial trends and low-frequency oscillations of time series. *Nonlinear Processes in Geophysics*, *12*, 451–460.

Wang, J., Zivot, E., 2000: A Bayesian Time Series Model of Multiple Structural Changes in Level, Trend and Variance. *Journal of Business and Economic Statistics*, *18*, 374–386.

Appendix A: Model parameters and input/output data files

The model is written in FORTRAN source code. Input and output files and parameters are described in the following.

A1: Input parameters. Only these 8 parameters need to be set appropriately before running the model. Currently this has to be done in the source code. All other parameters have fixed values.

Parameter[*]	*Notation*
ITM	Number of data points of the original time series.
NTS	Actual number of data points extracted from the original time series for the piecewise linear trend analysis.
NEND	Minimum length for the first and last segments set to avoid end effects.
NSPACE	Minimum distance between adjacent BPs.
CSLOPE	Minimum amount of trend change at BPs.
MINCYCLE	Minimum number of Monte Carlo loops set to estimate the standard deviations of all modeled trend parameters.
MULTIPLE	A multiplication factor set to skip Monte Carlo loop numbers between the MINCYCLE and MAXCYCLE.
MAXCYCLE	Maximum number of Monte Carlo loops set to estimate the standard deviations of all modeled trend parameters.

[*] Names of variables in the source code.

A2: Input. There is only one input file. The file contains the data in one column.

Input Data File[*]	*Notation*
AVWINDE.DAT	Original time series.

[*]Currently to be set in the source code (status='old').

A3: Output files.

Output Data File[*]	Notation
MBPYEAR.DAT	A 5*6 matrix where the non-zero elements in each column denote the times of BPs.
MSR.DAT	A 3*6 matrix where each column elements denote the minimum SSR obtained when assuming the order of autoregression is equal to the row index.
MQR.DAT	A 3*6 matrix where each column elements denote the minimum BIC obtained when assuming the order of autoregression is equal to the row index.
MCOEFF.DAT	A 7*6 matrix where the non-zero elements of each column denote the (m+2)-element fit vector $\{b_1, b_2, ..., b_{m+1}, a_1\}$, i.e. the slopes of (m+1) segments and the intercept of the first segment.
MEYTS.DAT	A NTS*6 matrix where each column denotes the piecewise linear fit of the original time series without autoregression.
MRYTS.DAT	A NTS*6 matrix where each column denotes the initial noise series obtained without autoregression.
MSTATISTICS.DAT	An 11*6 matrix where each column denotes the statistics of the initial noise series, i.e. sample mean, standard deviation, lag-zero/one/two autocorrelations, standard lag-one (or coefficient for AR(1)) and -two autocorrelations, lag-one and -two coefficients for AR(2), and the AD-statistic and associated significance level at which the null hypothesis of normally distributed residuals is not rejected.
MARMBP.DAT	The best and secondary choices of AR and BPs according to BIC.
MUBPYEAR.DAT	Mean times of BPs obtained via different numbers of loops (MCYCLE) of Monte-Carlo simulations for AR(0) residuals.
STDBPYEAR.DAT	Standard deviations of BPs obtained via different numbers of loops (MCYCLE) of Monte-Carlo simulations for AR(0) residuals.
MUCOEFF.DAT	Means of fit vector $\{b_1, b_2, ..., b_{m+1}, a_1\}$ obtained via Monte-Carlo simulations for AR(0) residuals.
STDCOEFF.DAT	Standard deviations of fit vector $\{b_1, b_2, ..., b_{m+1}, a_1\}$ obtained via Monte-Carlo simulations for AR(0) residuals.
MACSTDBPYEAR.DAT	Similar to STDBPYEAR.DAT but obtained via MAX-CYCLE loops of Monte-Carlo simulations.
MACSTDCOEFF.DAT	Similar to STDCOEFF.DAT but obtained via MAX-CYCLE loops of Monte-Carlo simulations.

[*]A data matrix of 6 columns in an output file (status='new') assumes the corresponding number of BPs is equal to the column index minus one. Data files including "1" or "2" in the filenames are corresponding to the file without number, but are valid for a combination of the model with an AR(1) or AR(2) component (e.g., MEYTS.DAT, ME1YTS.DAT, ME2YTS.DAT).

EUV-TEC - an index to describe ionospheric variability using satellite-borne solar EUV measurements: first results

C. Unglaub[1], Ch. Jacobi[1], G. Schmidtke[2], B. Nikutowski[1,2], R. Brunner[2]

[1]Institut für Meteorologie, Universität Leipzig, Stephanstr. 3, 04104 Leipzig
[2]Fraunhofer-Institut für Physikalische Messtechnik (IPM), Heidenhofstraße 8, 79110 Freiburg

Summary

Primary ionisation of major ionospheric constituents is calculated from satellite-borne solar EUV measurements. Number densities of the background atmosphere are taken from the NRLMSISE-00 climatology. From the calculated ionisation rates, an index termed EUV-TEC, which is based on the global total ionisation is calculated, and describes the ionospheric response to solar EUV and its variability. The index is compared against global mean ionospheric total electron content (TEC) derived from GPS data. Results show that the EUV-TEC index provides a better overall representation of global TEC than conventional solar indices like F10.7 do. The EUV-TEC index may be used for scientific research, and to describe the ionospheric effects on radio communication and navigation systems.

1. Introduction

ISO 21348 (ISO, 2007) defines the wavelength range of the EUV radiation between 10 and 121 nm; adjacent wavelength ranges are soft X-rays for shorter and FUV (Far Ultraviolet Radiation) for longer wavelengths. The total amount of EUV energy flux is by about five orders of magnitude smaller than the total solar irradiance integrated over all wavelengths. EUV radiation is completely absorbed at altitudes above 50 km, so that it does not reach neither the troposphere nor the Earth's surface. This absorption occurs mainly in the upper atmosphere (thermosphere) so that EUV radiation is a very important parameter at these heights. The EUV radiation interacts with the atoms and molecules of the upper atmosphere mainly through ionisation, the latter at wavelengths up to 102 nm. Thus, the planetary ionosphere essentially develops through this photoionisation. However, notwithstanding the nature of the primary absorption process (i.e. ionisation, photodissociation), finally the EUV radiation energy is transformed into heat. Thus, EUV radiation is also decisive for the heating of the upper atmosphere.

The EUV radiation is not emitted by the sun at constant rates, but varies on different time scales. An overview of recent measurements and modelling of solar EUV has been provided by Woods (2008). The primary long-term irradiance variability is related to the 11-year Schwabe sunspot cycle. The primary short-term variability is caused by the solar rotation with an average period of 27 days (Carrington rotation period). If there are active regions of the sun, they will also follow this rotation and so they will not always emit their radiation towards the Earth. Solar flare events, associ-

ated with particle eruption events and appearing more frequently during solar maximum than during solar minimum, can affect solar irradiance over a broad wavelength range up to 180 nm. They are short-lived with time scales from minutes to hours. Nevertheless, they cause abrupt changes in density, temperature, and composition of the upper atmosphere.

The solar cycles, and other variability at shorter time scales, affect the absorption and ionisation. Both depend on the incident radiation and the composition of the atmosphere, which is also influenced by the variability of the EUV radiation. Thus, ionospheric changes are strongly related to the variations in the EUV spectral region. Solar, and subsequently upper atmosphere variations can affect the orbits of satellites and spaceships through changes in the drag due to thermospheric density changes. Furthermore, ionospheric fluctuations may cause disturbances of communication and navigation systems (e.g., Pap and Fox 2004).

Solar indices may be used to describe the solar activity. The most frequently used indices are the sunspot number and the solar radio flux F10.7, which is defined as the radio emission from the sun at a wavelength of 10.7 centimetres. However, different indices may be useful to either describe the solar spectrum or the effect of solar EUV on the atmosphere and ionosphere. In this work we present first results to calculate an EUV index for the ionosphere derived from solar EUV radiation measurements, which is intended to describe the ionospheric variability (Schmidtke et al., 2006). This index will be compared with the F10.7 solar radio flux.

2. EUV data

Solar spectra in the wavelength range from 0.1 nm to 200 nm are available from the Solar EUV Experiment (SEE) on board the TIMED satellite. The TIMED mission started in January 2002 with the goal, to observe the Earth's upper atmosphere and the sun simultaneously. TIMED is orbiting the Earth at an altitude of 625 km. Four instruments measure, among others, atmospheric densities, temperatures, winds, ultraviolet emission and solar ultraviolet radiation. SEE is one of these four instruments observing the solar irradiance in the wavelength range from 1 nm to 195 nm using a grating spectrograph and a set of silicon photodiodes (Woods et al., 2000; Woods et al., 2005).

As an example, two spectra from TIMED SEE are shown in Fig. 1. The black line is a spectrum measured near the end of the last solar maximum and the red line represents a spectrum from the last solar minimum, which was very extended. The irradiance variations from solar minimum to solar maximum in the EUV range reach up to 200%. For longer wavelengths this variability decreases rapidly. But in the radio wavelength range at 10.7 cm wavelength as generated in the transition region of the solar atmosphere the solar variability is similar to the variability in the EUV wavelength range, so that the F10.7 radio flux is frequently used as a proxy for solar UV/EUV variability. The total variation of the solar spectrum is only 0.1 to 0.2 % (e.g., Lean et al., 2005).
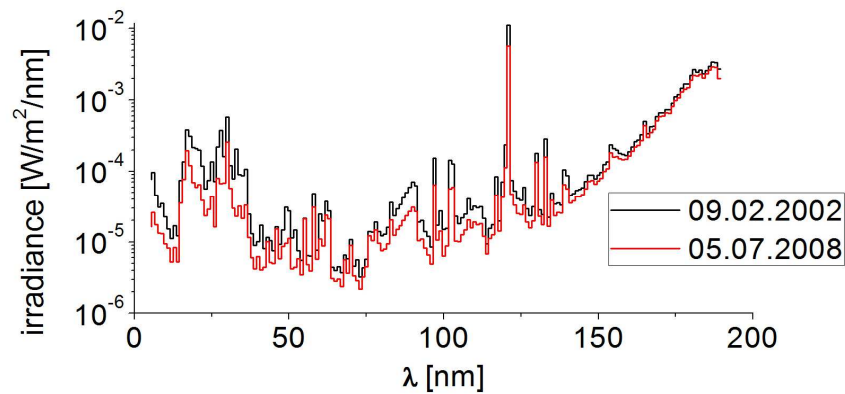
Fig.1: Two examples of EUV spectra as measured by TIMED SEE for solar maximum (black) and minimum (red) conditions.

3. Ionospheric primary ionisation

If EUV radiation meets the upper atmosphere, it interacts with the atmospheric gas. Thus, EUV radiation will be attenuated due to absorption, which in turn is mainly owing to ionisation. The decrease of the radiation can be described by the Lambert-Beer law:

$$dI_E(\lambda) = I_E(\lambda) \cdot \sigma(\lambda) \cdot n \cdot dz \,, \tag{1}$$

where σ is the absorption cross-section and I_E is the spectral incoming radiation, both dependent on wavelength λ, n is the number density of the absorbing gas, and z is the way through the atmosphere. Note that z does not need to point vertically.

In Fig. 2 the absorption and ionisation cross-sections of four upper atmosphere major constituents, namely atomic oxygen, atomic nitrogen, molecular oxygen and molecular nitrogen, are shown. These cross-sections have been taken from Fennelly and Torr (1992) and Metzger and Cook (1964). The photoionisation cross-sections include multiple ionisation, i.e. possible detachment of more than one electron. Ionisation only occurs at wavelengths up to 102 nm. In the adjacent wavelength range up to 135 nm only the absorption cross-sections for molecular oxygen are shown, because the atomic constituents do not absorb in this region. Huffman (1969) indicates the maximal absorption cross-sections of molecular nitrogen in this region as less than 10^{-25} m^2, so that they can be neglected. Naturally, both the absorption and ionisation cross-sections of the molecular components are greater than the cross-sections of the atomic components. Furthermore, the absorption cross-sections of the atomic constituents are equal to their ionisation cross-sections, because the atoms can only absorb through ionisation.

The number densities, which are necessary to calculate absorption after Eq. (1), are calculated using the NRLMSISE-00 model (Picone et al., 2002). Fig. 3 (left panel) shows the diurnal averages of the densities for the four important components of the upper atmosphere for different values of solar radio flux, but on the same location

(0°N, 0°E), as predicted by NRLMSISE-00. The day 09.02.2002 represents a day with high solar activity and the 05.07.2008 represents a day with very low solar activity. The influence of the solar activity on the composition of the atmosphere is clearly visible in the model.
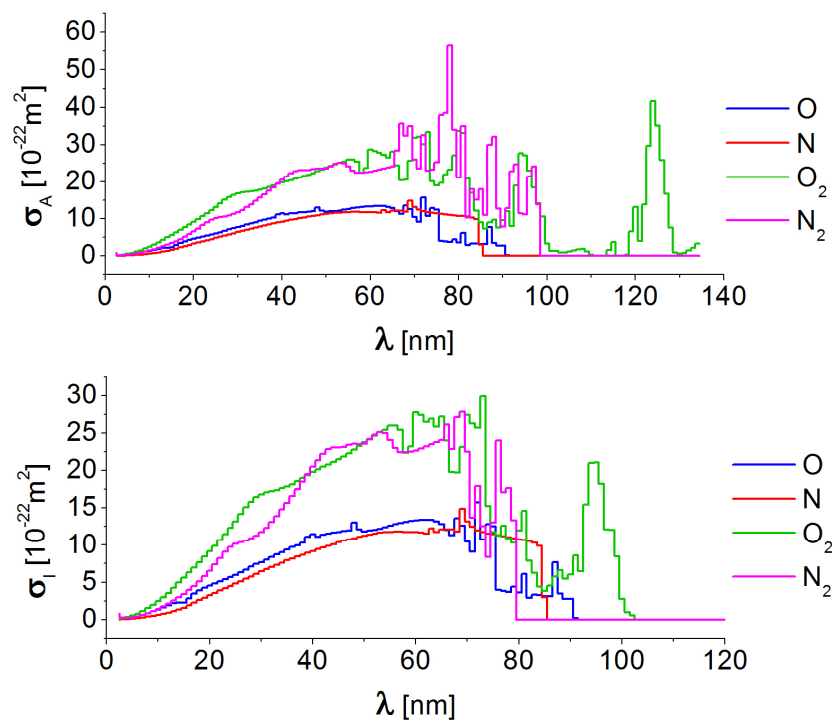
Fig. 2: *Absorptions cross-sections (upper panel) and photoionisation cross-sections (lower panel) for four major constituents of the atmosphere. Data taken from Fennelly and Torr (1992) and Metzger and Cook (1964).*
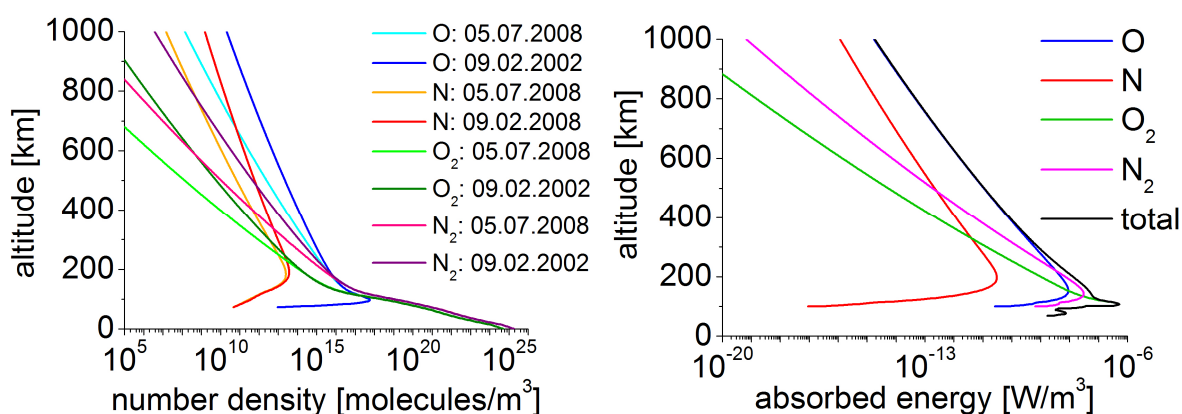
Fig. 3: *Left panel: Daily mean NRLMSISE-00 number densities at 0°E, 0°N of four atmospheric gases for different solar activities. Right panel: Absorption profiles on 15.04.2005 for four atmospheric gases calculated for zero zenith angle.*

To calculate the absorption and ionisation a model atmosphere is assumed. This atmosphere consists only of the four constituents shown in Fig. 3, and has an altitude of 1000 km. To calculate the absorption, energy deposition and ionisation, essentially Eq. (1) is numerically solved along radiation paths through the atmosphere with a vertical resolution of 1 km. Vertical ionisation profiles are calculated for each latitude and longitude.

The calculation is based on spherical approximations outlined in Fig.4, thereby assuming a spherical atmosphere and a spherical Earth. For each layer, the decrease of the radiation along the radiation path for each single ray must be calculated. To this aim, an angle of entry will be defined, under which the radiation enters the model atmosphere at its upper edge. With this angle the path dS_1 (see Fig. 4) through the uppermost atmospheric layer, and subsequently the absorption and ionisation along this way are calculated. Then the procedure is repeated for the next layer, and then continued until the actual angle corresponds to the zenith angle χ under consideration, providing the spectral radiation energy flux as well as energy deposition at a specific height at a given longitude and latitude. This analysis is then repeated for rays reaching other heights over the grid point under consideration. In this way the absorption and the ionisation are determined for each altitude, and absorption and ionisation profiles will be obtained for a specific zenith angle χ, or a given latitude-longitude grid point at a specific time, respectively.
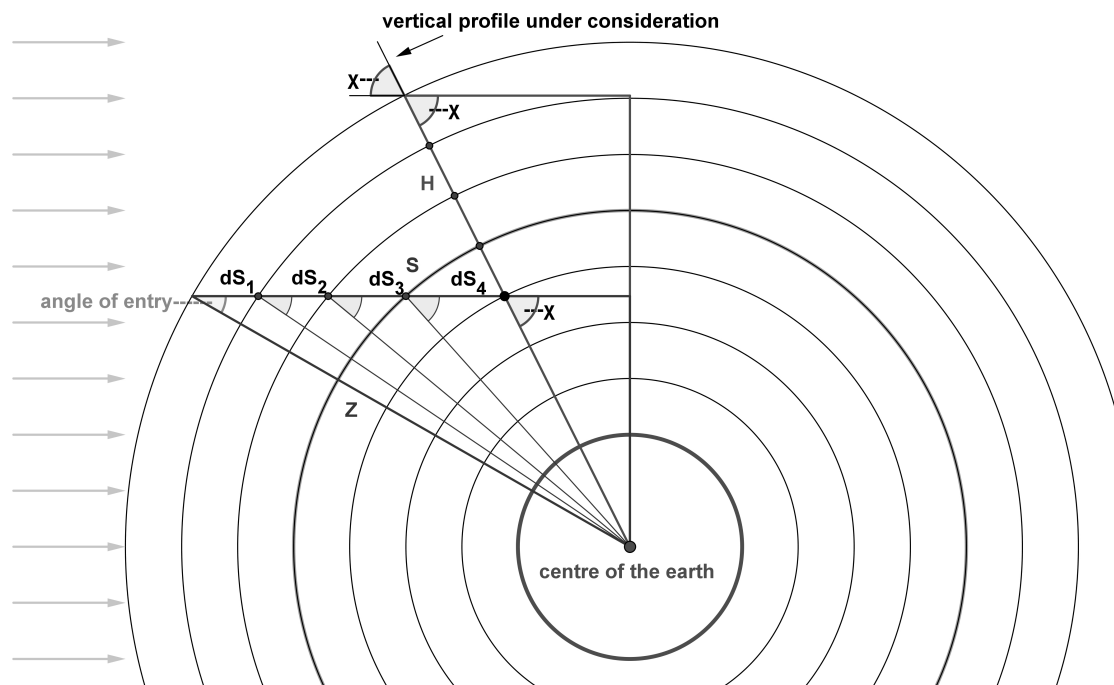
Fig. 4: Sketch of absorption/ionisation calculation for a specific point with given zenith angle.

In Fig. 3 (right panel) the absorption profiles for moderate solar activity for a zero zenith distance on 0°N and 0°E are shown. For altitudes above 300 km absorption through atomic components, especially through atomic oxygen, dominates. The absorption through molecular components prevails at altitudes below 300 km. This is simply owing to the fact that the heavier molecular components dominate at lower altitudes and the lighter atomic components dominate in higher altitudes (see Fig. 3, left panel).

The spectral photon flux density I_{Ph} is calculated from the spectral energy flux density I_E divided by the energy of the photons at the respective wavelength:

$$I_{Ph}(\lambda) = I_E(\lambda) \bigg/ \frac{h \cdot c}{\lambda}, \tag{2}$$

in order to determine the primary ionisation. The assumption is made that only photons contribute to the ionisation. Secondary ionisation processes like photoelectron impact ionisation are neglected. As an example, in Fig. 5 the primary ionisation profiles for moderate solar activity for two different zenith distances on 0°N and 0°E are shown. For $\chi=0°$ the profiles look similar to the absorptions profiles in Fig. 3. For $\chi=100°$ ionisation takes place at much greater altitudes. Because of the preponderance of the atomic constituents at higher altitudes the ionisation for large zenith distances will be dominated by these atomic components.

In the left panel of Fig. 6 the total primary ionisation profiles for four different zenith distances are shown. With increasing χ the altitude of maximum ionisation shifts to greater altitudes and the maximum ion production rate will be smaller. Furthermore, the influence of the ionisation by atomic/molecular constituents increases/decreases. The smaller ion production rates at extremely large zenith angles can be explained by the fact that on the one hand part of the radiation passes the atmosphere without being absorbed. On the other hand, at large χ much absorption already appears before the zenith distance under consideration is reached.
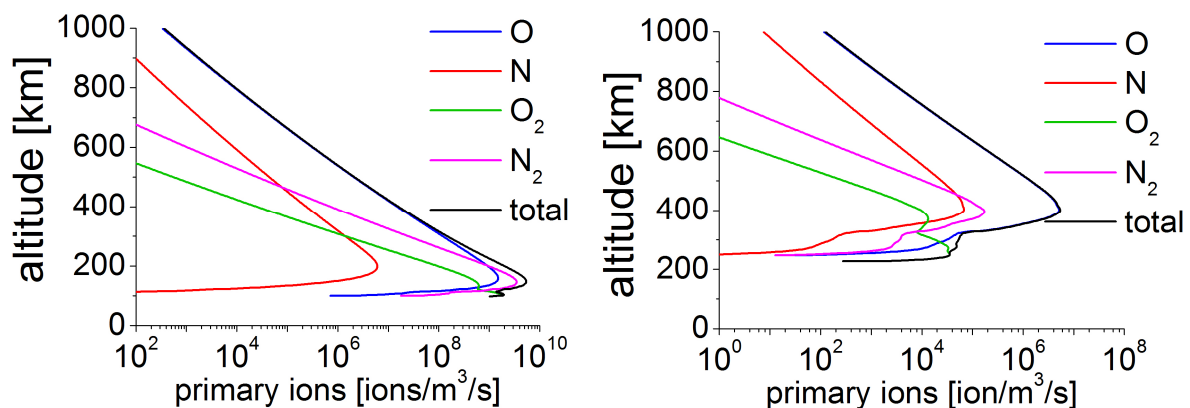
Fig. 5: Primary photoionisation profiles on 15.04.2005 for four atmospheric gases calculated for zero zenith distance $\chi=0°$ (left panel) and $\chi=100°$ (right panel).
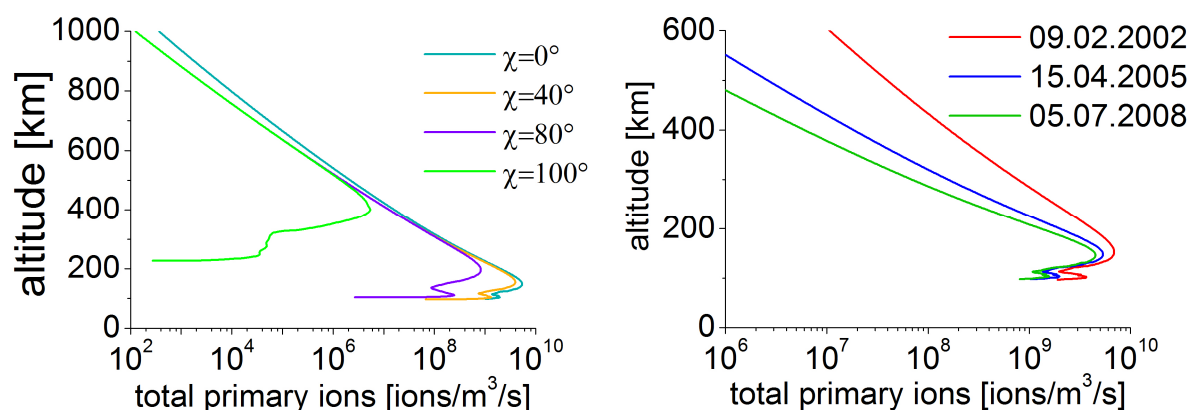
Fig. 6: Primary photoionisation profiles on 15.04.2005 for different zenith distances χ (left panel) and for different solar activities at $\chi=0°$ (right panel).

On the right panel of Fig. 6 the total primary ionisation for zero zenith distance, but for different solar activities are shown. The day 09.02.2002 represents a day of high solar activity, 15.04.2005 represents a day of moderate solar activity and 05.07.2008 is a day of low solar activity. Clearly, the primary ionisation depends on the solar activity. Above 300 km the variability of the ion production rates between solar maximum and solar minimum conditions amounts to one order of magnitude or more. However, the altitude of maximum ionisation shifts only marginally.

4. Results: EUV-TEC index

From the calculated ionisation rates a global ionisation rate is determined through averaging ionisation rates that are calculated for each longitude and latitude on a given day. The single ionisation rate profiles included in this averaging were calculated using global average number densities as input. From these ionisation rates at every grid point a mean global ionisation rate is calculated, and termed EUV-TEC index.

Obviously, ionisation rates may, locally, not be an appropriate measure to describe electron densities, essentially because of the influence of dynamics. However, on a global scale a relatively strong correlation is expected. Thus, in the following the EUV-TEC index will be compared against a global mean Total Electron Content (TEC). To check whether the index is able to describe a considerable part of global ionospheric variability better than existing indices do, global TEC is also compared with the solar radio index F10.7, which is frequently used to describe solar variability.

For the calculation of global TEC, local vertical TEC was used, which is based on a routine evaluation of GPS dual-frequency tracking data (Hernández-Pajares et al. 2009). These data are recorded with the IGS tracking network. The datasets are available every 2 hours for different longitudes and latitudes. To compare the new EUV-

TEC index with global TEC, the local TEC data were weighted with their geographical latitude and then a global diurnal mean was be calculated.

In Fig. 7 the time series of EUV-TEC and F10.7, both together with global mean TEC, are shown from 1-JAN-2002 to 31-DEC-2009. A good correlation between EUV-TEC and F10.7 exists during high solar activity. This behaviour is due to the respective origin of the solar EUV flux and the 10.7 cm radio emission. The F10.7 index is originated primarily in the high temperature transition region of the solar atmosphere whereas the solar EUV flux is primarily originated in the chromosphere and to less extend in the transition region and corona. The 10.7 cm radio flux undergoes stronger changes at higher solar activity. During these periods the EUV emissions from higher excited atoms in the solar atmosphere are showing a good correlation with F10.7. As a rule of thumb, the lower the wavelengths of the solar EUV emissions, the higher is their variability with solar activity. In detail, the highly variable FeIX-FeXII lines between 16 nm to about 30 nm are also primarily originated in the solar transition region explaining the stronger correlation at enhanced solar activity.

However, at lower solar activity the EUV emissions from the transition region to a lesser extent contribute to the total EUV activity, hence F10.7 is correlating less strongly with the total EUV radiation during these periods. Consequently, during solar minimum the correlation in Fig. 7 is weaker. Comparing the time series of the EUV-TEC index and global TEC index, however, the seasonal pattern at low solar activity is well visible in both time series. One may conclude that F10.7 does not represent ionospheric variability that well as the EUV-TEC index does, in particular during times of low solar activity.
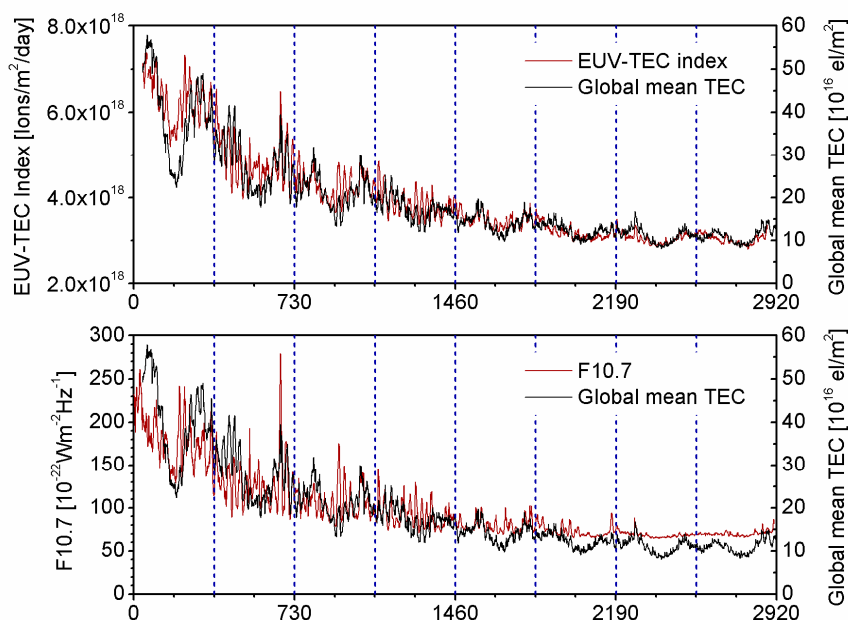
Fig. 7: Time series of daily EUV-TEC indices and global mean TEC (upper panel) and time series for global mean TEC index and F10.7 solar radio flux (lower panel) during 2002 to 2009.
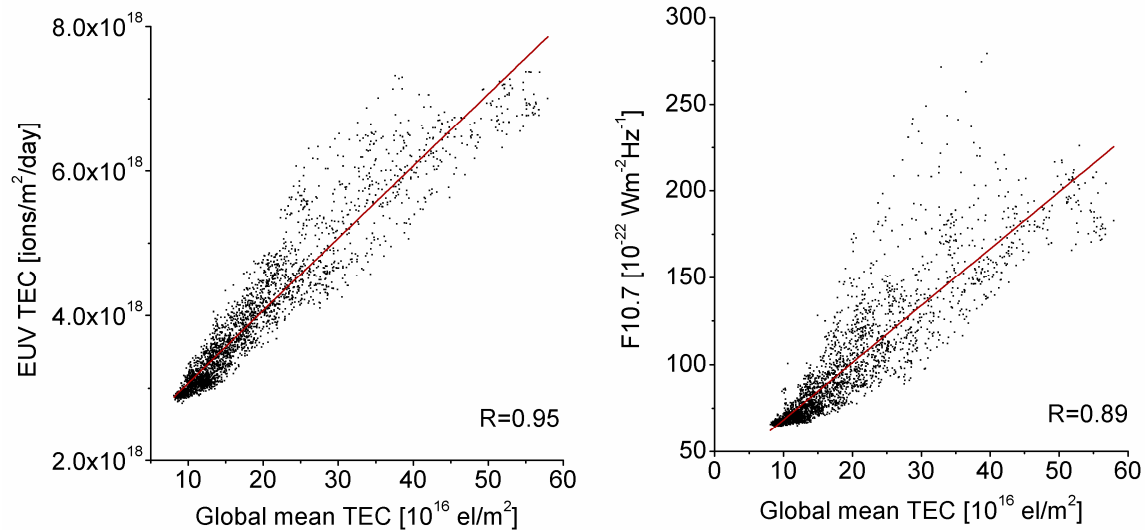
Fig: 8: EUV-TEC index (left panel) and F10.7 (right panel) vs. global mean TEC during 2002 to 2009.

On the left panel of Fig. 8 the EUV-TEC index is compared with the global TEC index from 1.1.2002 to 31.12.2009. There is a strong correlation between these indices with a correlation coefficient of 0.95. In comparison, on the right panel of Fig. 8 the solar radio flux F10.7 is shown vs. the global TEC index. A weaker correlation, with a correlation coefficient of 0.89 only, is obtained. Note that in Figs. 7 and 8 all indices based on the time interval 2002-2009 are compared. Thus, the majority of data points refer to solar minimum conditions rather than during solar maximum conditions, essentially because the last solar minimum was very extended from 2007 to 2009.

5. Conclusions

From solar EUV spectra, global mean primary ionisation rates have been calculated on a daily basis. This provides an index - EUV-TEC -, which to a certain degree describes the influence of solar variability on the ionosphere. Comparison of the index variability with that of global mean TEC provided by GPS measurements show that the index is strongly correlated with TEC. In particular, the index is able to represent the seasonal global TEC cycle during solar minimum, which is not present in other indices used for solar variability description. In particular, for representing ionospheric variability, the new index performs better than the frequently used F10.7 radio flux.

Acknowledgements

References

Fennelly, J. A., and Torr, D. G., 1992: Photoionization and photoabsorptions cross sections of O, N2, O2 and N for aeronomic calculations, Atomic Data and Nuclear Data Tables, 51, 321-363.

Hernández-Pajares, M., Juan, J. M., Sanz, J., Orus, R., Garcia-Rigo, A., Feltens, J., Komjathy, A., Schaer, S. C., and Krankowski, A., 2009: The IGS VTEC maps: a reliable source of ionospheric information since 1998, J. Geod., 83, 263–275.

Huffman, R. E., 1969: Absorption cross-sections of atmospheric gases for use in aeronomy, Canadian Journal of Chemistry, 47, 1823-1834.

ISO, 2007: ISO 21348:2007(E). Space environment (natural and artificial) — Process for determining solar irradiances, ISO, 12 p.

Lean, J., Rottmann, G., Harder, J., and Kopp, G., 2005: Source contributions to new understanding of global change and solar variability, Solar Physics, 230, 27-53.

Metzger, P. H. and Cook, G. R., 1964: A reinvastigation of the absorption cross-sections of molecular oxygen in the 1050-1800 A region, J. Quant. Spectrosc. Radiat. Transfer., 4, 107-116.

Pap, J. M., and Fox, P., 2004: Solar Variability and Its Effects on Climate, American Geophysical Union, 1. Ed., 366 p.

Picone, J. M., Hedin, A. E., and Drob, D. P., 2002: NRLMSISE-00 empirical model of the atmosphere: Statistical comparisons and scientific issues, J. Geophys. Res., 107, 1468, doi:10.1029/2002JA009430.

Schmidtke, G., Eparvier, F. G., Solomon, S. C., Tobiska, W. K., and Woods, T. N., 2006: The TIGER (thermospheric-ionospheric geospheric research) program: Introduction, Adv. Space Res., 37, 194-198.

Woods, T. N., Bailey, S., Eparvier, F., Lwarence, G., Lean, J., McClintock, B., Robie, R., Rottmann, G. J., Solomon, S. C., Tobiska, W. K., and White, O. R., 2000: TIMED Solar EUV Experiment, Phys. Chem. Earth (C), 25, 393-396.

Woods, T. N., Francis, G. E., Bailey S. M., Chamberlin, P. C., Lean, J., Rottmann, G. J., Solomon, S. C., Tobiska, W. K., and Woodraska, D. L., 2005: Solar EUV Experiment (SEE): Mission overview and first results, J. Geophys. Res., 110, A01312, doi: 10.1029/2004JA010765.

Woods, T. N., 2008: Recent advances in observations and modeling of the solar ultraviolet and X-ray spectral irradiance, Adv. Space Res., 42, 895-902.

Hydrocarbons in indoor air and their health-effects

Carolin Rösch, Astrid Ziemann[1], Uwe Schlink[2]

[1] Leizpig Institute of Meteorology
[2] Helmholtz Centre for Environmental Research Leipzig

Summary

Concentrations of harmful airborne substances are much higher in indoor air than outdoors. Furniture, cleansing agents, paints, solvents, carpets and floors release numerous **v**olatile **o**rganic **c**ompounds (VOCs), which can only be reduced through adequate ventilation.

The present investigation considered data of 463 participants in the fourth year of age within a project of the Helmholtz Centre for Environmental Research. 39 of them developed wheezing symptoms, 148 bronchitis and 397 infections.

A novel model, based on logistic regression, was used to find associations between certain VOC concentrations and the outcome of airway diseases. The analysis involved gender, contact with cats, environmental tobacco smoke (ETS), and the prevalence of atopy in both parents. The aim was to find threshold concentrations of VOCs and to give recommendations for the abatement of environmentally caused diseases.

The present research proved findings of other studies, for instance, that "wheezing ever" appeared when high concentrations of hexane, benzene, ethylbenzene, and chlorbenzene were reported. Such relationships were observed for "wheezing ever" in the past year. The number of wheezing participants was low (39) and, therefore, also some other airway diseases (infection, bronchitis and asthma) were tested for their relationship to VOC concentrations.

1   Introduction

VOCs play a huge role for both human health and atmospheric processes. They comprise a large group of carbon-based chemicals whose vapour pressure at 20°C is greater than 1.3 hPa and less than 1013 hPa (Hester et al., 1995).

The VOC concentration in the urban atmosphere depends on human behaviour, geographic location, meteorological parameters and the time-dependent contributions of different sources. In cities, a diurnal cycle of VOCs is observable especially for those, which are produced by vehicle exhausts. In the early morning, the VOC concentration is at lowest because of a nocturnal dilution of the emissions from the previous day. The commuter traffic in cities leads to an increase in VOC concentration twice a day.

Adults spend a lot of their time in offices, housings and workplaces. For this reason, special attention has to be put on indoor air pollutants that are emitted by furnishings and can impair human health. The exposure to certain VOC is extremely variable. Nevertheless, many studies suggest, that long-term exposure to low levels as well as short-term exposure to high levels have severe health effects, like eye and nose irritation, headaches, dizziness, worsening of asthma symptoms (short-term exposure) and cancer, liver, and kidney damages and also damages on central nervous system (long-term exposure) (www.health.state.mn.us). To prevent such harmful impact, threshold concentrations were specified for adults. (Umweltbundesamt 2007, Öppel et al., 2000, Sagunski, 1996, Sagunski et al., 2004, Seifert, 1999).

Children, in comparison to adults, are most affected. They rest the majority of their time in rooms because of less mobility. Therefore, the concentration of indoor VOCs and outdoor air pollutants, which infiltrate through windows and porous walls, is essential for health effects (Koenig et al., 2005). Additionally, the formation of particles from VOCs is important, and to assign them to their sources.

In previous studies, however, threshold concentrations for children were not specified. For that reason, a purpose of the present study is to find threshold values for certain VOCs for the protection of children's health. In addition, it is an aim to investigate whether there is any difference in the harmfulness of different VOCs on wheezing or on other airway complaints, and how it depends on the VOC concentration. A population study of the Helmholtz Centre for Environmental Research UFZ Leipzig was used to find answers for these questions.

Adgate et al. (2004) showed that households with attached garages possess elevated concentrations of benzene, styrene and chloroform and that non-urban concentrations are significantly lower than urban concentrations. Based on the fact that tobacco smoke in pregnancy and early childhood causes prenatal damage, poor growth indicators, respiratory illness like cough and wheezing and asthma (Hawamdeh et al., 2003, Cook et al., 1997), health studies have to adjust for this so-called confounder. Wheezing is a precursor for asthma in the development of children (Lemanske, 2002).

Indoors, VOCs are emitted by a variety of home or personal care products and from vehicle exhausts of attached garages (Sexton et al., 2004). Building materials and indoor activities determine the indoor concentration, see table 1 (Morales et al., 2009, Belanger et al., 2006, Diez et al., 2002, Sexton et al., 2004, Sagunski, 1996, Umweltbundesamt, 2007).

Table 1: VOC sources and items, which release such pollutants.

Sources	Items
Outdoor	Traffic, industry, forests, vegetation
Building material	Insulation, paint, plywood, adhesives
Furnishing materials	Furniture, floor/wall covings
Garage and combustion appliances	Vehicle emission, tobacco smoke, candles
Consumer products	Cleaning, personal care products
Equipment	Laser printers, photocopiers, PC
Indoor activities	Cooking, tobaccos smoke, use of solvents
Ventilation system	Filters of heating ventilation, air conditioning
Biological	Humans, moulds, bacteria, plants, fruits

2   Data and Methods

2.1 Datasets

In epidemiologic data, questionnaire data are often used for different purpose. Firstly, they can give a short survey over a long period to research the everyday life. Secondly, they can be used to detect changes, for instance in the effect of medicine, for short-term analysis.

The used questionnaire for the presented study gathered information as to the parents' atopies, allergies, school education as well as smoking in presence of the expectant mother. Nutrition during pregnancy, nutrition allergies, infections and associated medication were asked as well. This basic information shall be used to research an

association between atopic disease and factors from the indoor and outdoor environment in the future. All in all, 80 questions plus sub questions were asked.

The study-population of Leipzig contained 579 participants in the third year and 670 in the fourth year of life. However, 39 participants suffered from "wheezing symptoms ever between their third and fourth birthday".

This investigation is focused on associations between the VOC concentration and the occurrence of wheezing and searches for concentration thresholds for children that help to protect against respiratory symptoms. For the occurrence of a disease, not only VOC concentrations and environmental factors are determining. Personal susceptibility and genetic factors are crucial for the manifestation of asthma, allergies and respiratory diseases (Schwartz, 2009). For that reason, the answer to the questionnaire item of parental atopy was included as a confounder in the data analysis.

2.2 VOC measurements

The concentration of VOCs was measured at the end of the third year of life using a 3M organic vapour monitor 3500 (http://www.shop3m.com). These samplers were fixed at the ceiling in the middle of a room, where the child spent most of its time, at a height of 1.5 - 2 m with a minimum distance of 50 cm to the next furniture. At best, the measurements lasted for one month. In this period, the behaviour of the dwellers should not have been differed from other parts of the year. Furthermore, any activity that could have led to an increase in VOC concentrations had to be documented. Many factors were considered: position of the sampler, smoking in the sampling room (benzene), usage of purifier, solvents and pesticides (cyclic hydrocarbons) as well as newspaper in the proximity of the sampler (toluene). For avoiding any misinterpretation of high concentrations, questions about burning candles, dust development outside and adjustment and air tightness of the windows were asked. All in all the measurements give an overview about the VOC concentration in the whole year. A sampling interval of 4 weeks was selected, which can be assumed to describe the personal exposure much better (and integrative) than a short-term measurement.

A series of organic compounds can be collected with these samplers using the principle of diffusion. At the end of the sampling period, each monitor was tightly closed by a cap belonging to it, and stored at room temperature until analysis.

The VOC analysis was performed on the Perkin Elmer GC-MS system Turbomass equipped with an RTX-1 column (60 m x 0.32 mm I.D., 1.0 µm film thickness; Restek). A sample volume of 1 µl was split-less injected. Integrated areas of selected fragment ions from each of the 28 studied VOCs were obtained with the software Turbomass, Version 4.4 (Perkin Elmer).

The detection limits for the components were estimated as the three-fold standard deviation of 5 replicate measurements of monitor blanks. For components with blank values too low to be registered, it is usual practice to use the three-fold standard deviation of replicate measurements of a low-level standard solution. The detection limits of the GC/FID/ECD system were observed to be between 0.01 µg/m³ and 1.0 µg/m³ regarding a sampling interval of 4 weeks. For the GCMS system detection limits from 0.01 µg/m³ to 0.05 µg/m³ were found, converted to a sampling interval of four weeks.

The storage stability of 5 passive samplers was tested in a period of 5 months at room temperature and no significant loss was observable. The precision was evaluated as the

percent relative standard deviation (% RSD). The % RSD was typically below 10% (Rehwagen et al., 2003).

Calculation of concentration

For the statistical analysis, time weighted average concentration of the contaminant in mg/m³ or µg/m³ were used. This can be calculated as follows:

$$c(\mu g/m^3) = mt^{-1}r^{-1}A$$

Here, m is the absolute weight of an adsorbed contaminant on the monitor in µg, A is a calculation constant, r represents the recovery coefficient by incomplete desorption from the sampler and t is the sampling interval in minutes. The coefficient A is influenced by temperature and pressure. The correcting factor is 1.0 (reference) for 25°C and 1013 hPa. All measurements refer to normal conditions. For an increase of 10 K above or below the reference value, one percent correction is required for temperature. For differences in pressure no correction is needed. The additional error attributable to different (unknown) environmental conditions can be assumed to be below 13% (Rehwagen et al., 2003). The recovery coefficients were determined by direct injection of a known amount of the standard into a 3M sampler and subsequent extraction with carbon disulfide containing 1% methanol. The recovery was between 98% and 102%.

Table 2: Measured VOCs and their half detection limit in combination with the number of taken replacements.

VOC	half detection limit [µg/m³]	replacements with detection limit
Hexane	0.206	64 (14.71%)
Heptane	0.053	4 (0.92%)
Octane	0.003	0
Nonane	0.012	1 (0.23%)
Decane	0.073	7 (1.61%)
Undecane	0.132	4 (0.92%)
Dodecane	0.065	3 (0.69%)
Tridecane	0.048	7 (1.61%)
Methylcyclopentene	0.04	22 (5.06%)
Cyclohexane	0.054	6 (1.38%)
Methylcycloheptan	0.019	0
Benzene	0.091	3 (0.69%)
Toluene	0.0248	0
Ethylbenzene	0.003	0
m-p-Xylene	0.179	3 (0.69%)
Styrene	0.139	62 (14.25%)
o-Xylene	0.019	1 (0.23%)
4-Ethyltoluene	0.007	1 (0.23%)
3-Ethyltoluene	0.007	1 (0.23%)
2-Ethyltoluene	0.013	24 (5.52%)
Methylbezoat	0.001	4 (0.92%)
Chlorbenzene	0.234	365 (83.91%)
Trichlorethylene	0.002	11 (2.53%)
Tetrachlorethylene	0.0005	0
α-Pinene	0.015	0
β-Pinene	0.001	1 (0.23%))
Δ-3 Carene	0.0005	0
Limonene	0.0029	0

Data processing

VOCs were measured for only 95% of the participants completing the questionnaire (555 VOC measurements out of 579 possible apartments). Measured concentrations below the detection limit were replaced with the half detection limit (table 2, column 2). To judge them in the right way, the percentage as to the entirety is given in brackets. The third column of table 2 contains the number of replacements for each VOC.

Because of their strong seasonal variation, the VOC concentration values were adjusted by the season when they have been collected. The factor, which is higher in summer than in winter, is between one and four in this study and differs between different cities and VOC groups (Schlink et al., 2004).

2.3   Statistical modelling

In the analysis of epidemiological data, regression is used to describe the association between exposure variables and a disease or illness outcome. Linear and logistic regression with their parameters and **o**dds **r**atios (OR), **c**onfidence **i**ntervals (CI) and R^2 are used to solve multivariable problems. Thereby, it should be kept in mind that experiments were made to research the influence of environmental factors on the health of children. "Sick" or "healthy" were the two possibilities of the dichotomous data. They were coded for the statistical modelling as follows: sick into "1" and healthy into "0".

This dichotomy of the data must be reflected by the statistical model. Therefore, the regression analysis is a generalized statistical method with the ambition to describe the values of the dependent variable D for independent variables X_1, X_2, ... , X_n (Harrell Jr., 2001). The character and the amount of a generalised linear association between the dependent and the independent variable are modelled.

From the regression results *dose-response* relationships can be derived easily. The response changes because of a change in the dependent variable. The questionnaire data, quoted before, and the aim of our investigation (environmental impact on health) show that control variables like gender, age, existence of a cat and smoking must be included for adjustment, even when they are not of direct interest. They define the dependent variable (sick/healthy) and represent the multivariable problem leading to a multiple regression.

Logistic regression model

To cover nonlinear relationships between outcome and predictors, the normal model must be extended. In classical linear models the outcomes are independent and normally distributed with equal variance. These conditions do not apply here.

In dichotomous data, like with (1) or without (0) outcome of a disease, either 1 or 0 appears. For such data, a binomial distribution with D~Bin(n = 1, p) and 0 < p < 1, is suitable. Because of the binomially character of the data set, the logit-link has to be used in the logistic regression, which is a special form of the generalized linear regression.

The probability p($\mathbf{x}$) is an indicator for the risk of an individual to become sick. An s-shaped link-function is used in the analysis and shows that the individual risk is low till a special "level" is reached. It was the aim of this investigation that, for different VOCs, these "levels" are calculated for children, depending on age, gender, and the other adjustments mentioned before. Thus, the logistic model is defined by

$$P\{D = 1 | X_1, X_2, X_3, \ldots, X_n\} = \frac{1}{1 + e^{-(\alpha + \sum_{k=1}^{n} \beta_k X_k)}} = p(\mathbf{x})$$

while P{D=1} is the probability to become sick with individual variables. α and β are constant terms representing unknown parameters for the strength of the control variables X. α is the intercept and accounts for the effect of all time-independent factors on the average symptom level of an individual.

In the following table 3 the variables of the data set and the logistic model are presented:

Table 3: Abbreviations for the used logistic regression model of dependent (d), control (c), and independent (i) variables.

variable	Variable and adjustments (abbreviations)	Classification (d, c, i)
D	Asthma, wheezing, infection, bronchitis (D_1)	d
X_1	Gender (S_2)	c
X_2	Cats as domestic animal (Cda_3)	c
X_3	Cats in surroundings (Cs_4)	c
X_4	Passive smoking indoors (Psi_5)	c
X_5	Passive smoking elsewhere (Pse_6)	c
X_6	Education index of parents (Edu_7)	c
X_7	Twice positive atopy in family (Tpa_8)	c
X_8	VOC concentration (VOC_9)	i

From this follows:

$$p(\mathbf{x}) = \frac{1}{1 + e^{-(\alpha + \beta_1 S + \beta_2 Cda + \beta_3 Cs + \beta_4 Psi + \beta_5 Pse + \beta_6 Edu + \beta_7 Tpa + \beta_8 VOC)}}$$

explaining the association between the linear combination of influencing factors and logit p(**x**):

$$logit\ p(\mathbf{x})\ = \log \frac{p(\mathbf{x})}{1 - p(\mathbf{x})} = \alpha + \sum_{k=1}^{n} \beta_k X_k$$

Maximum-Likelihood method

Logistic regression is commonly used for ease of interpretation and computation. Using the maximum-likelihood method, the unknown parameters α, β_1, … , β_8 can be estimated. Likelihood-based inference affords point estimators with good properties and affords the ability to assess the variability of estimators. The likelihood is a measure of how reasonable is each candidate value of the unknown parameter as a model for the data (Pawitan, 2001). After the estimation step, the parameter values are used to calculate p(**x**), which gives the individual predicted risk to become sick under special circumstances (control variables).

Odds Ratio

The estimation of the effect of VOCs on children's health results in odds ratios. They give the personal risk to become sick under special circumstances, here: VOC concentration. The odds ratio is a quotient of Disease & Exposure Yes/No and Disease Yes & Exposure No (and vice versa).

See table 4 for illustration; E is for **e**xposure, D for **d**isease, 1 for yes, and 0 for no. The population is split into groups of exposed and of not-exposed persons. The group of E=1 (exposed) contains **a** persons suffering from the disease and **c** healthy persons; analogously, in the not exposed group (E=0) **b** individuals are sick and **d** healthy. For the odds ratio, the odds of both groups, exposed and not exposed, have to be calculated. The ORs are defined as:

Table 4: Contingency table used in calculating the odds ratio, E=1 is the exposed group and E=0 is the not-exposed group.

$$odds\ ratio = \frac{P(a)P(d)}{P(b)P(c)}$$

	E=1	E=0
D=1	a	b
D=0	c	d

Therefore, odds ratio is a ratio of the event of interest occurring and not occurring in two groups. While P(a)/P(c) represents the odds of the exposed group, P(b)/P(d) represents the odds of the not-exposed group. In the odds, the numerator is always the sick group and the denominator is the healthy one.

From the odds ratio, the chance of becoming sick can be estimated. If the odds ratio is equal to 1, then there is no difference in the pathogenic outcome of the variables of sick and healthy persons. If the odds ratio is smaller than 1, special circumstances lead to a protective effect and the odds of the healthy persons is higher than the odds of the sick ones. In the reverse case, when the amount of the sick persons is higher than the healthy persons the odds ratio is above 1 and the chance of becoming sick is exceeded (Kleinbaum et al., 2002).

Table 5: The meaning of the OR-values.

Odds Ratio	meaning
=1	no effect on healthiness
>1	higher chance to become sick
<1	protective effect

Confidence Interval

By estimating the values of model parameters it is much better to acknowledge the uncertainty in the estimate by providing a range of plausible values for the parameter than top state single numbers. This range is called confidence interval. It is a random interval that differs with variable data. The confidence statement says that, in 95% of hypothetical replications of the current situation, the confidence intervals obtained would include the true value.

The CI has an upper (UCI) and a lower (LCI) limit. The CIs are directly connected with the number of ill children: The CI becomes larger if the number of children, who show symptoms, decrease. That means the less children are affected, the more uncertain is the estimate of the effect of the VOC concentration on this individual.

R² - coefficient of determination

R^2 is the coefficient of determination and gives information about the connection of dependent and independent variable.

The value is a percentage which explains how much is described by the used model. It is a weighting of the model and specifies report of the reality. R^2 is between 0

(worst case) and 1 (best case) whereas a model with $R^2 = 1$ describes the variable completely and includes that all observation points are on the regression line.

2.4 Developed model

Using the logistic regression model with adjustments and VOCs as covariates, the coefficients, R^2 and the p-values were calculated. The R 2.5.1 software (© 2007 The R Foundation for Statistical Computing) generated function "glm" was used, with binomial distribution function and logit link-function.

All coefficients were estimated and the validity of the statistical model was proved by comparing the R^2s. The estimated coefficients were used to calculate the ORs, UCIs and LCIs of the VOCs. The distinction between VOCs, which influence and which do not influence the health of children, was based on these parameters. For visualization and a visual detection of differences for several VOCs, the OR with UCI and LCI were drawn. Significant VOCs are plotted with CI in figure 1, while non-significant VOCs are just marked by a small circle. The significant VOCs
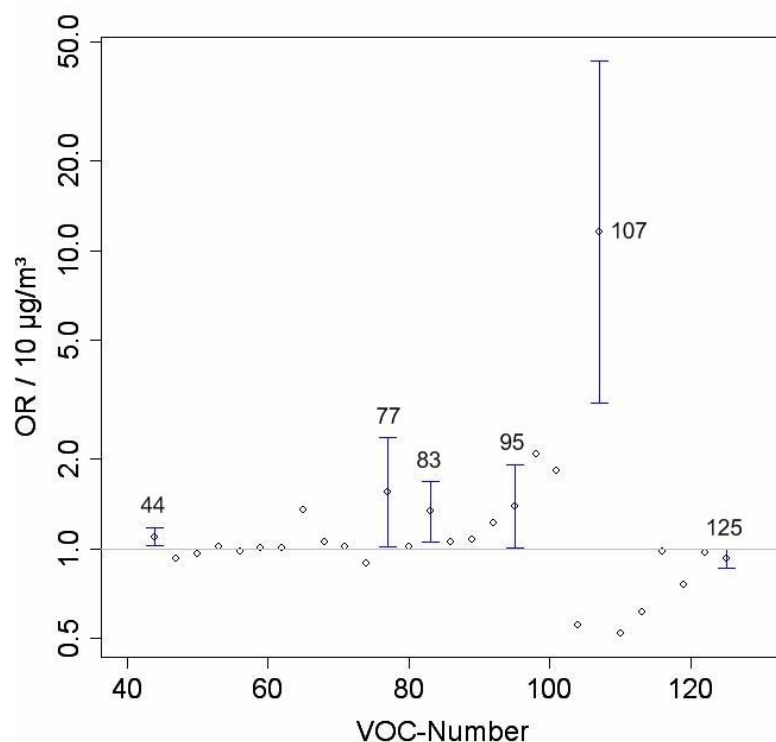
Figure 1: Six VOCs were observed to be in relation to wheezing ever in children age four. The numbers declare the VOC (44 – hexane, 77 – benzene, 83 – ethylbenzene, 95 – 4-ethyltoluene, 107 – chlorbenzene, 125 – limonene).

were used for a subsequent threshold calculation. The VOCs were considered according to their appearance in the chart, hexane at first, consequently. This paper describes the threshold calculation for hexane in relation to "wheezing ever" in children age four. Further results will be presented in a following paper.

Threshold calculation

The threshold calculations were done for these six significant VOCs only. All others have not been considered.

At first, every VOC concentration was classified into 10 categories. Then we decided to use a minimum criterion: The first category started at the lowest threshold (minimum) and included all values greater than or equal to the half detection limit. The 10th threshold (maximum) sequence was set to be equal to or higher as the highest measured value. This sequence included no values and was ignored.

The threshold codomain of the dataset was estimated in the model by an "if-then" command: "If the values of row 1, column 1:500, are greater than or equal to the prior calculated threshold, then take these values. Otherwise set them to zero".

Considering this, the first threshold concentration category contains all values. The second threshold codomain contains all values except those, which are smaller than the second threshold concentration category and so on. The last section includes only a few children, those who had concentrations between the calculated threshold concentration for the ninth class and above, consequently.

For all categories, the ORs, UCIs and LCIs were calculated and printed (figure 2). In an ideal case, the LCIs and UCIs should be very small and the ORs should be constant till a special concentration value is reached. Then, a strong increase in OR should appear. For the specification of a threshold, the OR should be about one, when the outcomes of diseases are not mainly influenced by certain VOCs and should significantly differ from one, when the VOC concentration influences the outcome of a disease.

3 Results

Table 6: Survey of VOC concentrations measured during one year.

VOC	Minimum	Maximum	Mean	25-perc	50-perc	75-perc	95-perc
Hexane	0.206	238.37	10.614	1.604	4.161	11.319	31.512
Heptane	0.053	396.082	22.013	2.838	6.522	18.837	103.7
Octane	0.00749	90.035	3.836	0.977	1.728	3.582	15.166
Nonane	0.0132	279.224	6.022	1.273	2.504	5.538	16.177
Decane	0.080	327.503	8.507	1.677	3.856	8.625	23.988
Undecane	0.145	218.531	9.479	2.372	4.071	8.603	33.685
Dodecane	0.072	135.574	5.022	1.496	2.467	4.301	18.275
Tridecane	0.048	47.656	3.237	1.248	1.999	3.292	9.411
Methylcyclopentene	0.044	135.139	6.291	0.998	2.234	6.571	24.522
Cyclohexane	0.054	405.476	14.805	2.268	4.592	12.068	64.573
Methylcycloheptane	0.072	637.36	14.061	1.198	4.125	11.338	63.154
Benzene	0.091	42.338	4.736	2.593	3.909	5.543	10.709
Toluene	0.947	568.74	43.907	18.777	29.533	51.116	120.181
Ethylbenzene	0.009	79.04	5.283	2.098	3.355	5.480	13.998
M-p-Xylene	0.008	273.267	11.787	4.122	3.114	10.792	30.455
Styrene	0.139	212.618	3.901	0.845	1.704	3.489	11.823
O-Xylene	0.021	74.08	3.608	1.316	2.176	3.581	9.002
4-Ethyltoluene	0.008	65.22	2.936	0.9995	1.628	2.906	8.999
3-Ethyltoluene	0.008	25.632	1.383	0.478	0.775	1.473	3.993
2-Ethyltoluene	0.013	33.394	1.316	0.393	0.733	1.299	3.878
Methylbezoat	0.001	14.146	1.122	0.035	0.073	0.462	6.050
Chlorbenzene	0.234	9.216	0.868	0.328	0.655	0.866	2.878
Trichlorethylene	0.002	34.646	0.849	0.188	0.318	0.596	2.232
Tetrachlorethylene	0.001	133.414	2.196	0.134	0.309	0.742	9.022
α-Pinene	0.157	965.493	75.460	17.177	37.669	95.377	273.1
β- Pinene	0.001	190.868	9.363	2.670	5.255	10.483	31.06
Δ- 3 Carene	0.036	335.504	24.633	3.852	10.57	28.867	99.7
Limonene	0.084	771.971	41.161	13.503	28.636	52.532	109.9

Descriptive statistics of VOCs
555 samples were taken during the study period. The concentration range (see table 6) is from 0.001 (tetrachlorethylene, β-pinene) up to 965.493 µg/m³ (α-pinene).
The VOC concentrations were checked for normal distribution with Shapiro-Wilks-test with SoftStat Statistica 8. The test turned out to be negative. Hence, the null hypothesis had to be rejected and all concentrations are not normally or log-normally distributed.

Risk assessment
The ORs and p-values were calculated for the model with gender, cat indoor/outdoor, smoking indoor/outdoor, education index and twice positive atopy in family as core model, symptom as dependent variable and VOC concentration as independent variable. The model estimated the associations between several VOCs and respiratory symptoms. The present paper contains the result for hexane and wheezing in children age four. Hexane is used as diluent for adhesives and varnish and also in fuels. Strong sources of hexane are renovation of the flats and outside chemical industry.

Figure 2 refers to an increase in hexane of 10 µg/m³, because the concentration range is from 0.206 to 238.37 µg/m³. A threshold can be identified when the CIs of the different ORs are so small that one does not cover the range of another one. This does not apply to the case of hexane (Figure 2). The CIs are too large and nearly totally overlap the other CIs so that no threshold can be specified, although there might be an indication of a threshold between 50 and 100 µg/m³. Further information for other VOCs and diseases can be found in Rösch (2010).
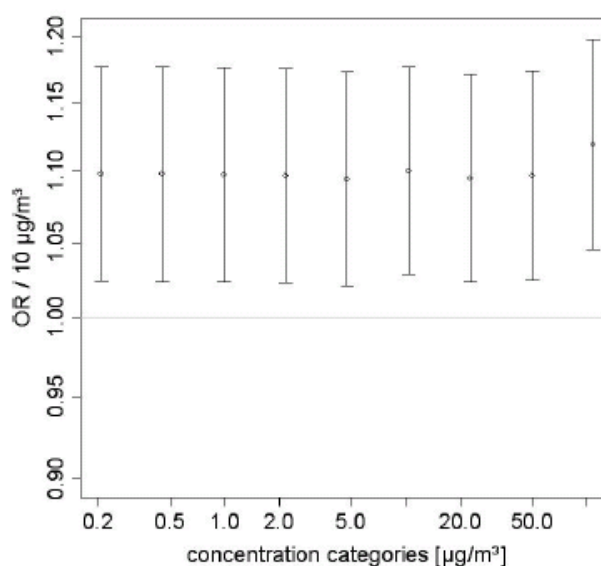
Figure 2: Calculation of concentration categories for hexane causing wheezing. The ORs are given for an increase of 10 µg/m³.

A slight increase in OR, which can be taken as an increase in the chance to become sick, is located between 50 µg/m³ and 100 µg/m³. This, however, can not be interpreted as a statistically significant threshold because of the too small increase in OR compared to the large CIs. The CIs are so large, because only a small subgroup is diseased. All CIs cover a very wide range so that no threshold can be identified clearly. The category of highest concentrations, referring to the percentage of children with symptoms, includes the smallest group of diseased participants. The large CIs are caused by the small number of participants in the ninth concentration category compared to the base group.
The hexane concentration of a previous study in Leipzig between November 1994 and October 2001 (Schlink et al. (2004)) for 50th percentile was 3.1 µg/m³ and for

95th percentile 23.1 µg/m³. The 50th percentile of hexane measured in this study is 4.3 µg/m³, which is a little bit higher than the previous value of Schlink et al., 2004. Also the 95th percentile of this research with a concentration of 32.197 µg/m³ is higher than the 95th percentile (23.1 µg/m³) of Schlink et al. (2004). That leads to the suggestion, that more hexane is emitted by certain sources. Highest hexane concentrations were measured in rooms that were renovated in the former year.

4   Discussion

579 persons were inquired with regard to their behaviour, habits in their housing and the physical health of their children. The questionnaire arrived at the parents within four weeks of the child's birthday. It contained almost equal number of males and females (49.7% (230) males and 50.3% (233) females). 39 participants of the cohort complained about "wheezing ever".

10 (25.6%) children of the wheezing sub-cohort were directly exposed to tobacco smoke indoors and 28 (71.8%) suggested being exposed in the daily environment. However, it is not known whether the parents or other persons are the smoke emitting sources in the outdoor air.

Domestic animals play an important role for allergy, asthma and wheezing. Cats were found to be the most influential factor. The used adjustment included that; even though only 54 families housed cats (wheezer: 3) and 142 noticed contact to a cat outside (wheezer: 13).

VOC corrections

In the test phase, much more models with different combinations of adjustments were tested. VOCs were involved with and without correction of seasonality. In result, uncorrected VOCs had a lot more protecting effects than VOCs corrected for season and detection limit (table 2). These protecting effects are not plausible and not supported by any literature. In contrast, the effects found from corrected VOCs were invigorated by certain references.

Developed model

The assessment of the influence of VOCs on children's health was the aim of this investigation. For this purpose, 28 common VOCs were collected in the living area but only hexane and some other VOCs had a significant influence on wheezing in children age four. In summation the seven adjustments have been gender, exposure to smoke indoor/outdoor, cats indoor/outdoor, educational index and twice positive atopy in family. The R^2 were highest in the model described above. They correspond to other epidemiological studies (lowest: 0.035 for hexane and wheezing ever in children age four). Models without atopy in family or only one atopic family member showed worse coefficients of determination (0.025 for hexane and wheezing ever in children age four). Because R^2 is a measure for the quality of the model, the one with the highest R² should be used.

The model was stable when children with high concentration values have been eliminated for test purposes. This verifies that the used model was a good choice for detecting the influence of VOC concentrations on the health of children. The study demonstrates that children, exposed to high concentrations, normally suffer from airway diseases.

Results

In particular, we studied the effect of hexane on airway diseases like wheezing.

The measured VOCs in houses have a wide spectrum of sources and combinations, and this complicates the classification. The mixture of too many unknown sources and sinks allows only a suggestion of the effect on human health. The concentration of the VOCs gives no evidence for the amount of ventilation or usage of cleaners, solvents or factors of furnishings. Through the comparison with other literature some reasons could be found, but further research has to be done. Expected threshold concentrations, below which there is no adverse health effect, have not been observed.

5   Conclusion

The used statistical model was developed for calculating the OR for concentration categories of various VOCs. The background was to estimate thresholds of the observed concentration range and to find out how many diseased children are located in the specific section. For several VOCs, which can cause airway diseases like wheezing, we did not find threshold concentrations below which there is no adverse effect.

Retrospectively, that might be caused by the characteristic and design of the study. It is constructed for the influence of environmental and genetic effects on the health of children and gathered the concentration of different VOCs as a plus to determine which are correlated with personal indoor (cooking, smoking, cleaning) and outdoor air (traffic, industry). The connection between outdoor air pollutants and reactions of the respiratory tract were found in recent studies (Koenig et al., 2005, Adgate et al., 2004, Carslaw et al., 2009, Wichmann et al., 2009). The result that no threshold could have been found is also a notice that wheezing appears already at concentrations below the detection limit.

This investigation showed that wheezing at age four was associated with high concentrations of hexane. This finding corresponds to studies of Arif et al. (2007), Trevillian et al. (2005), Rumchev et al. (2004), Venn et al. (2003), and Cook et al. (1997). Hence, hexane is important in relation to the development of wheezing in children and mroe attention has to be put in minimizing hexane sources. The dissappointment of the determination of a threshold for hexane might be strengthened by concentrations below the detection limit in combination with wheezing.

The kind and released concentration of VOCs which are emitted by combinations of indoor activities, furniture and outdoor sources is not well understood until yet. Concluding this report with the result that no threshold for any VOC was found but an association between certain VOCs (and concentrations) and health problems could be corroborated. For further information and results see Rösch (2010).

References

http://www.health.state.mn.us/divs/eh/air, 29.09.2009. VOCs in your home

Adgate, J., Eberly, L., Stroebel, C., Pellizzari, E., Sexton, K.,2004: Personal, indoor, and outdoor VOC exposures in a probability sample of children. Journal of Exposure and Environmental epidemiology 14, S4 – S13

Arif, A., Shah, S., 2007: Association between personal exposure to VOCs and asthma among US adult population. Int Arch Occup Environ Health 80, 711 – 719

Ayoko, GA., 2004: Volatile Organic Compounds in Indoor Environments. The Handbook of Environmental Chemistry 4, Part F, 1 – 35

Belanger, K., Gent, J., Triche, E., Bracken, M., Leaderer, B., 2006: Association of indoor nitrogen dioxide exposure with respiratory symptoms in children with asthma. American Journal of Respiratory and Critical Care Medicine 173, 297 – 303

Borbon, A., Coddeville, P., Locoge, N., Galloo, JC., 2004: Characterising sources and sinks of rural VOC in eastern France. Chemosphere 57, 931 – 942

Carslaw, N., Langer, S., Wolkoff, P., 2009: New Directions: Where is the link between reactive indoor air chemistry and health effects? Atmospheric Environment 43, 3808 – 3809

Charles, S.M., Jai, C., Bettermann, S.A., Godwin, C.: VOC and particulate emissions from commercial cigarettes: Analysis of 2.5-DMF as an ETS tracer. Environmental Science and technology 42, 1324 – 1331

Cook, D.G., Strachan, D.P., 1997: Parental smoking and prevalence of respiratory symptoms and asthma in school age children. Thorax 52, 1081 – 1094

Diez, U., Borte, M., Herbarth, O.,2002: Risikofaktoren aus der Umwelt für die Entstehung von Atemwegserkrankungen bei Säuglingen. Umwelt-Medizin-Gesellschaft 3, S. 211 – 216

Fromme, H., Lahrz, T., Piloty, M., Oddoy, A., 2005: Polyzyklische aromatische Kohlenwasserstoffe in der Innenraumluft von Wohnungen, Kindergärten und Schulen. Umweltmedizin in Forschung und Praxis 10, 35 – 41

Harrell Jr., F.E., 2001: Regression modeling strategies. Springer, 568 S.

Hawamdeh, A., Kasasbeh, F.A., Ahmad, M.A., 2003: Effects of passive smoking on children's health: a review. Eastern Mediterranean Health Journal 9, 441 – 447

Hester, R.E., Harrison, R.M., 1995: Volatile Organic Compounds in the Atmosphere, Issues in Environmental Science and Technology. The Royal Society of Chemistry, 132 S.

Karl, T., Crutzen, P.J., Mandl, M., Staudinger, M., Guenther, A., Jordan, A., Fall,R., Lindinger, W., 2001: Variability-lifetime relationship of VOCs observed at the Sonnblick Observatory 1999-estimation of OH-densities. Atmospheric Environment 35, 5287 – 5300

Kleinbaum, D.G., Klein, M., 2002: Logistic Regression: A Self learning Text. Springer Verlag New York, Berlin, Heidelberg, 513 S.

Koenig, J., Mar, T., Alle, R., Jansen, K., Lumley, T., Sullivan, J., Trenga, C., Larson, T., Liu, L., 2005: Pulmonary effects of indoor- and outdoor-generated particles in children with asthma. Environmental Health Perspectives 113, 499 – 503

Lemanske, J.R.R.F., 2002: Inflammation in childhood asthma and other wheezing disorders. Pediatrics 109, 368 – 372

Liu, Y., Shao, M., Lu, S., Chang, C.C., Wang, J.L., Chen, G, 2008: Volatile Organic Compound (VOC) measurements in the Pearl River Delta (PRD) region, China. Atmospheric Chemistry and Physics 8, 1531 – 1545

Morales, E., Julvez, J., Torrent, M., de Cid, R., Guxens, M., Bustamante, M., Künzli, N., Sunyer, J., 2009: Association of early-life exposure to household gas appliances and indoor nitrogen dioxide with cognition and attention behavior in preschoolers. American Journal of Epidemiology 169, 1327 – 1336

Öppel, R., Höder, B., Lange, A., 2000: Innenraumluft und TVOC: Messung, Refernz- und Zielwerte, Bewertung. Bundesgesundheitsblatt-Gesundheitsforschung-Gesundheitsschutz 43, 13 – 518

Pawitan, Y., 2001: In all Likelihood: Statistical modelling and inference using likelihood. Clarendon Press, Oxford, 528 S.

Phoa, L.L., Toelle, B.G., Ng, K., Marks, GB., 2004: Effects of gas and other fume emitting heaters on the development of asthma during childhood. Thorax 59, 741 – 745

Rehwagen, M., Schlink, U., Herbarth, O., 2003: Seasonal cycle of VOCs in apartments. Indoor Air 13, 283–291

Rösch, C., 2010: Indoor air and health effects, 77 S.

Rumchev, K., Spickett, J., Bulsara, M., Phillips, M., Stick, S., 2004: Association of domestic exposure to VOCs with asthma in young children. Thorax 59, 746 – 751

Sagunski, H., 1996: Richtwerte für die Innenraumluft: Toluol. Bundesgesundheitsblatt 416 – 421

Sagunski, H., Heger, W., 2004: Richtwerte für die Innenraumluft: Naphthalin.
Bundesgesundheitsblatt-Gesundheitsforschung-Gesundheitsschutz 47, 705 – 712

Schlink, U., Rehwagen, M., Damm, M., Richter, M., Borte, M., Herbarth, O., 2004: Seasonal cycle of indoor-VOCs: comparison of apartments and cities. Atmospheric Environment 38, 1181 – 1190

Schwartz, D., 2009: Gene-Environment interactions and airway disease in children. Pediatrics 123, 151 – 160

Seifert, B., 1999: Richtwerte für die Innenraumluft. Bundesgesundheitsblatt-Gesundheitsforschung-Gesundheitsschutz 42, 270 – 278

Sexton, K., Adgate, J., Church, T., Ashley, D., Needham, L., Ramachandran, G., Fredrickson, A., Ryan, A., 2004: Children's exposure to volatile organic compounds as determined by longitudinal measurements in blood. Environmental Health Perspectives 113, 342 – 349

Trevillian, L., Ponsonby, A., Dwyer, T., Kemp, A., Cochrane, J., Lim, L., Carmichael, A., 1005: Infant sleeping environment and asthma at 7 years: A prospective cohort study. American Journal of Public Health 95, 2238 – 2245

Umweltbundesamt, 2007: Naphthalin/Naphthanole und Human-Biomonitoring.
Bundesgesundheitsblatt-Gesundheitsforschung-Gesundheitsschutz 50, 1357 – 1364

Venn, A., Cooper, M., Antoniak, M., Laughin, C., Britton, J., Lewis, A., 2003: Effects of VOC, damp, and other environmental exposures in the home on wheezing illness in children. Thorax 58, 955 – 960

Wichmann, F.A., Müller A., Busi, L.E., Cianni, N., Massolo, L., Schlink, U., Porta, A., Sly, P.D., 2009: Increased asthma and respiratory symptoms in children exposed to petrochemical pollution. Journal of Allergy and Clinical Immunology 123, 3808 – 3809

Measurement and modelling of the cumulated thermal stress in Leipzig

Friedrich, A., Ziemann, A., Schlink U.

Abstract

This paper shows first results of mobile measurements, which carried out in summer 2009 to evaluate the thermal comfort for a 'standardized' pedestrian in several urban areas of Leipzig. The analysis of the obtained data was conducted by calculating the mean radiant temperature as well as the Predicted Mean Vote (PMV). The results were compared to simulations applying the RayMan-program. Additionally to these findings to short-term stress, a study to the cumulated thermal stress was implemented into the analysis for the first time. Thereby, the thermal stress was considered which is perceived by a healthy 'standardized' person during a one hour walk. As a first step a time rate of change of the PMV was defined for a measurement period. Using the example of the 20th August, 2009 in Leipzig, urban district Lößnig, a cumulated PMV-aggregation of 0.7 was calculated and hence, a total (cumulated) PMV of 3.4 results in comparison to an arithmetically averaged PMV of only 2.7 for all measurement points along the route that were taken that day. Thus, a person perceives a severe thermal stress when walking the typical pedestrian route in Leipzig-Lößnig in one hour.

Introduction

Urban areas represent only 0.2 percent of the earth´s surface [Fezer, 1995], but nevertheless over 70 percent of the world population are living in cities [Hupfer und Kuttler, 2006].

The growing population density in urban areas and hence the enhanced urbanization influence and modify the climate of a city. Thereby, the co-action of natural (e.g.: relief or altitude) and anthropogenic (e.g.: the form and density of the buildings, heat storage capacity of the building materials or degree of surface sealing) features affect the particular urban climate.

In the past, studies on urban climate in Leipzig have been carried out e.g. by Müller (1997), who made extensive measurements by car and generated urban climate maps (especially temperature maps) for Leipzig. Schwab and Heinz (1997) worked out special maps to evaluate the urban climate and air quality. Also the office of environmental protection of Leipzig carried out urban climate studies. On the 12th and 13th August, 1997 thermal scanner photographs and mobile measurements of the air temperature, humidity and wind velocity were accomplished during calm and almost cloudless weather conditions. The results show for most urban areas in Leipzig a thermal stress situation because of higher temperature values in comparison to surrounding areas [Amt für Umweltschutz, 2007].

The here presented study is also dealing with the thermal factors of the urban climate in Leipzig outgoing from recently measured data. Changed meteorological conditions due to climate changes may have especially an effect on the habitants of a city, because an enhanced thermal stress is expected. This possible impact of the global changes to the local urban climate is interesting for the personal well-being and health status of the people in a city.

The research was focussed on the thermal stress related to a 'standardized' person, who represents the thermal sensibility of the majority of the population. Hence, the focus lied on the methods and results to evaluate the thermal comfort. Furthermore, the following questions should be answered by the study:

1. Which urban area generates stress?
2. What's the amount of the thermal stress?
3. How improvements could be achieved and what significant points should be considered in future landscape design processes?

Characteristics of the urban climate

The climate of a city is characterized by the modification of the meteorological parameters. Well verifiable is the heat island effect, which is characterized by higher air and surface temperatures compared to rural areas [Oke, 1987]. Most of the heating occurs in the urban areas, which are sealed and covered with buildings very densely. These are typically the downtown areas. The intensity of the urban heat island averages 1 to 3 K, especially at night it can reach up to 10 K.

The general temperature anomalies of urban areas in comparison to the rural environment are caused by an interaction of several effects, which are due to the urban structure:

- The reduction of the horizon (sky view factor), reduces the diffuse radiation [Häckel, 2005]. This has an impact on the radiation balance.
- The effect of 'solar trapping', i.e. multiple reflections of the radiation, leads to an additional heating of the air.
- The increased heat conductance of the materials typically used in cities (asphalt, concrete, etc.) influences also the temperature regime. Because these surfaces are quite dark, they absorb most of the visible sun light which is followed by a heating.
- The built surfaces in cities lead to a reduced evaporation and therewith changed energy balance components (enhanced sensible heat fluxes).
- Also the anthropogenically generated heat due to traffic, industry and household results in a warming of the urban air.

Thermal assessment methods

The human organism has the ability to be responsive to atmospheric variations. Changes of meteorological parameters such as air temperature, humidity and wind velocity as well as short-wave and long-wave radiation have an impact on the well-being of the people. To evaluate the thermal impulse on a person, the different fluxes involved in heat exchange have to be regarded. This was realized in several heat balance models [Hupfer and Kuttler, 2006]. The basis for these investigations is the heat balance equation for a human body.

In the VDI-Guideline 3787 Part 2 (1998) the comfort equation according to Fanger (1972) is recommended for standard applications. The result of this equation is the thermal index PMV. This scale of values provides information on the average degree of the thermal stress perceived by a large collection of individuals [VDI, 1998]. The

PMV equation was originally developed for indoor conditions and is a basis to quantify the thermal sensibility based on a psycho-physical scale. Coupling the comfort equation according to Fanger with the short-wave and long-wave radiation fluxes has become widespread as a planning instrument under the name "Klima-Michel-Model" [e.g. Jendritzky et al., 1990; Grätz et al., 1994].

Using the procedure of the above mentioned VDI-Guideline a mean radiation temperature t_{mrt} is calculated from the short-wave and long-wave radiation fluxes. [VDI 3787 Part 2, 1998]. In addition to the meteorological parameters with physiological relevance such as air temperature, water vapour pressure and wind velocity, the PMV also depends on the individual input variables clothing (controls the heat transition resistance of the clothing) and activity (controls the metabolic rate and the energy transformation as a result of the mechanical efficiency).

At PMV = 0, no one should feel uncomfortable. In fact, according to Fanger (1972), even then about 5% of individuals are expected to feel discomfort. Table 1 shows the PMV-values and their thermal perception as well as the corresponding stages of stress.

Table 1: *Predicted Mean Vote PMV, thermal perception and stages of stress [VDI 3787, 1998].*

PMV	Thermal perception	Stages of stress	
> 3.5	very hot	extreme stress	
> 2.5…3.5	hot	great stress	heat
> 1.5…2.5	warm	moderate stress	stress
> 0.5…1.5	slightly warm	slight stress	
-0.5…0.5	comfortable	no stress	
> -0.5…-1.5	slightly cool	slight stress	
> -1.5…-2.5	cool	moderate stress	cold
> -2.5…-3.5	cold	great stress	stress
> -3.5	very cold	extreme stress	

Measurement and analysis methods

The data collection was carried out by mobile measurements. Especially for this study a transport trolley equipped with several devices was developed and used (figure 1). The advantage of this measurement setup was that the instruments were transportable to every measuring point without a car. It was the first time that urban climate studies in Leipzig were made with such a measurement setup.

The values of the air temperature and the humidity as well as the horizontal wind velocity and the short wave radiation fluxes were determined by appropriate instruments on a tripod. Additionally an infrared thermometer was used to measure the surface temperature and to estimate long-wave radiation fluxes. These measurement instruments were connected with a data logger, which recorded and saved the measuring data. To get representative values for the prevailing areas a measuring time of 10 minutes was chosen at one place.

Figure 1: *Measurement setup, positioned at a measuring point in Leipzig-Paunsdorf.*

The interesting areas for the investigations were, beside the downtown area, also the urban areas with many inhabitants, which are at the periphery of the city. It was decided to investigate a developing area in the east of Leipzig (Paunsdorf). Furthermore, the urban area Lößnig and the park area Lößnig-Dölitz were chosen to examine measurement points with natural surfaces as well. The measurements were primarily carried out at sites near public institutions or at places where many citizens often come together. In the 3 studied districts of Leipzig a measurement route was chosen, which contained 6 measuring points characteristically for the district. The total lengths of the measurement routes were about 4 km's. This is a distance which a pedestrian may cover in 1 hour. The measurements were done at various times of the day and were also repeated for different weather conditions to get a general statement about the thermal stress during summer 2009 in Leipzig. Each route contained at least one measuring day at which the solar radiation was maximal due to cloudless conditions. Furthermore, at each route it was tried to get a comparison of the thermal stress of sunny places with shadowed places. Additionally, at several measuring points measurements were taken in the evening to detect cooling rates depending on the kind of surface (densely built or green areas).

To analyze the obtained data several programs were used. To determine the mean radiation temperature a Fortran-program at the basis of VDI 3789 (1994) was developed (see Friedrich, 2010). The incoming long-wave radiation was calculated due to the cloud coverage at different heights. Furthermore, the measured air and surface temperature were used and therewith the outgoing long-wave radiation fluxes were calculated. The measured short-wave radiation fluxes were also used to compute, together with the calculated long-wave radiation fluxes, the mean radiation temperature. Then, the mean radiation temperature is used in a program for determining the thermal stress, i.e. the PMV [VDI 3787 Part 2, 1998]. To compare the measured and calculated data the RayMan-model was used, which is a program for

modelling the radiation fluxes and the thermal stress in urban structures [Matzarakis, 2001]. RayMan simulates the short- and long-wave radiation fluxes at a certain time and place using the real urban structures. As one result of the simulations the PMV-value can be calculated.

Results

The results of the thermal comfort analysis show, that already at temperatures of 20°C a slight thermal stress (PMV-values greater than 0.5) exists. At temperatures of about 25°C there result partly PMV-values higher than 2.5. Therefore, a moderate thermal stress occurs most likely, although thermal comfort in the shadowed zones is also possible. On hot summer days (air temperature higher than 30°C) the healthy "standard" person (without additional regulation) feels even in shadowed zones no thermal comfort with its environment. On such days a great, partly extreme thermal stress with PMV-values of about 4.0 can be expected.

To study the influence of shadowed areas on the thermal stress the measured 10-minute averages of the data from all measuring days from Leipzig-Lößnig and the city centre were considered and compared. In both urban districts there were shadowed measuring places during the whole day due to buildings or trees. Independent from the special weather conditions it was discovered, that the PMV-values in shadowed areas were reduced by about 30% in comparison with places, where the sun was shining directly. At PMV-values of 2.0 and greater (in the sun) this reduction of the thermal stress of30 % makes out one entire stage of stress (according to Fanger). It has to be mentioned that the thermal stress can be reduced even by staying for a short period of time in shadowed places.

In the following, additional results of the study are summarized (see also Friedrich, 2010).

Intensity of the Heat Island Effect

The urban heat island is a well-known phenomenon in the urban climate and is formed by the temperature difference between the city centre and the surrounding areas. The intensity depends on the weather conditions and reaches its maximum at calm nights. The intensity of the heat island in Leipzig was verified by comparing the measured air temperatures at the LIM (Leipzig Institute for Meteorology) and at the park in Lößnig for the 20th August, 2009. The observed measuring points are both on a grassland site. The park in Lößnig represents the less sealed areas at the periphery of the city, which cool rapidly down after sunset in comparison to the city centre. The measuring point at the LIM represents the air masses of the centre, which are additionally heated by the released heat of the surrounding buildings.

During the day with the high solar radiation and the cloudless sky the temperature difference between the city centre and the Lößnig park site was 1.1 K. In the evening the temperature difference was even 2 K. This result verifies the findings of other studies that the heat island effect is especially distinctive at night [Häckel, 2005].

Intensity of the nocturnal cooling

On the 20th August, 2009, which was the hottest day in this summer, additional measurements were taken in the evening hours in Lößnig. The aim was to show that the cooling over unsealed surfaces, such as the grassland in the park, is enhanced. The measured air and surface temperatures are plotted in figure 2. During the measurements a difference between the measuring points in the park and those within the blocks of houses became apparent. The air temperature still increases in the evening hours once there was a change in the location away from the grassland to a closed location of buildings. This behavior is caused by the fact that the air masses are heated due to the release of the stored heat of the buildings. This effect is verified by the measured surface temperatures. Specially the sealed surfaces are storing more heat because of their material composition and deliver this heat after sunset to the overlying volume of air. Also, the influence of the 'solar trapping' between the buildings plays a role. Thus the air between the blocks of houses is heated additionally. Whereas natural ground surfaces have a less storage capacity and therefore their cooling is more rapidly.
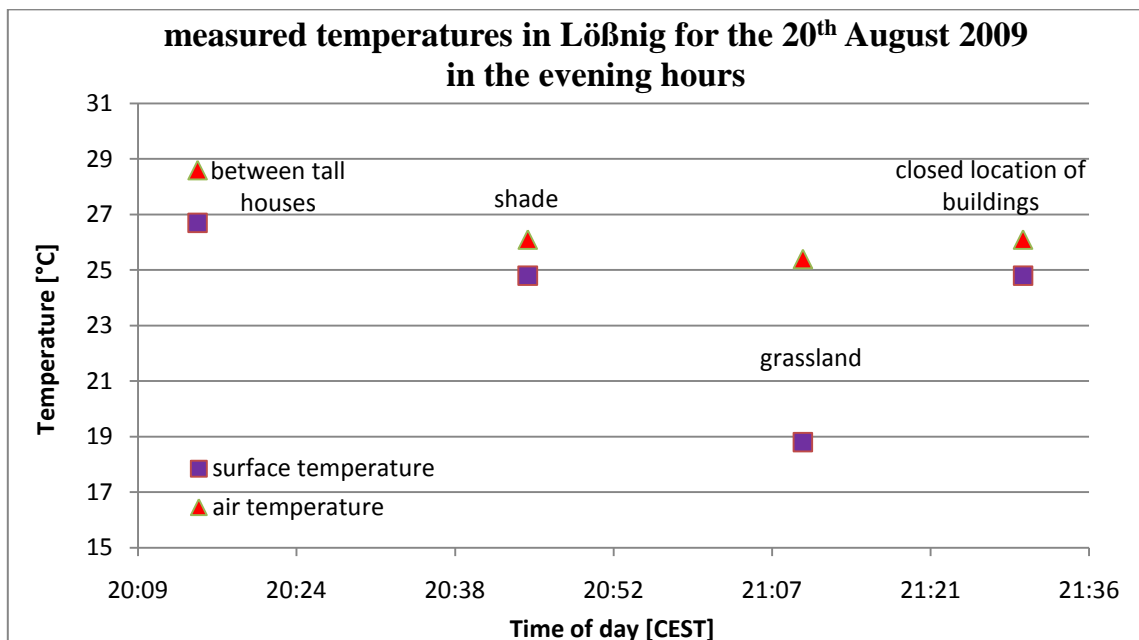
Figure 2: *10-minutes-average of the measured air and surface temperature on the 20th August, 2009 in Lößnig in the evening hours.*

The different cooling effect of different surfaces is also reflected by the values of the PMV (figure 3). Generally, there is a less thermal stress expected in the evening hours, while in contrast the abidance on grassland is already perceived as slightly cool (negative PMV). According to the simulation with the RayMan-program a person standing on the grassland in the park at the measurement time still feels comfortable.
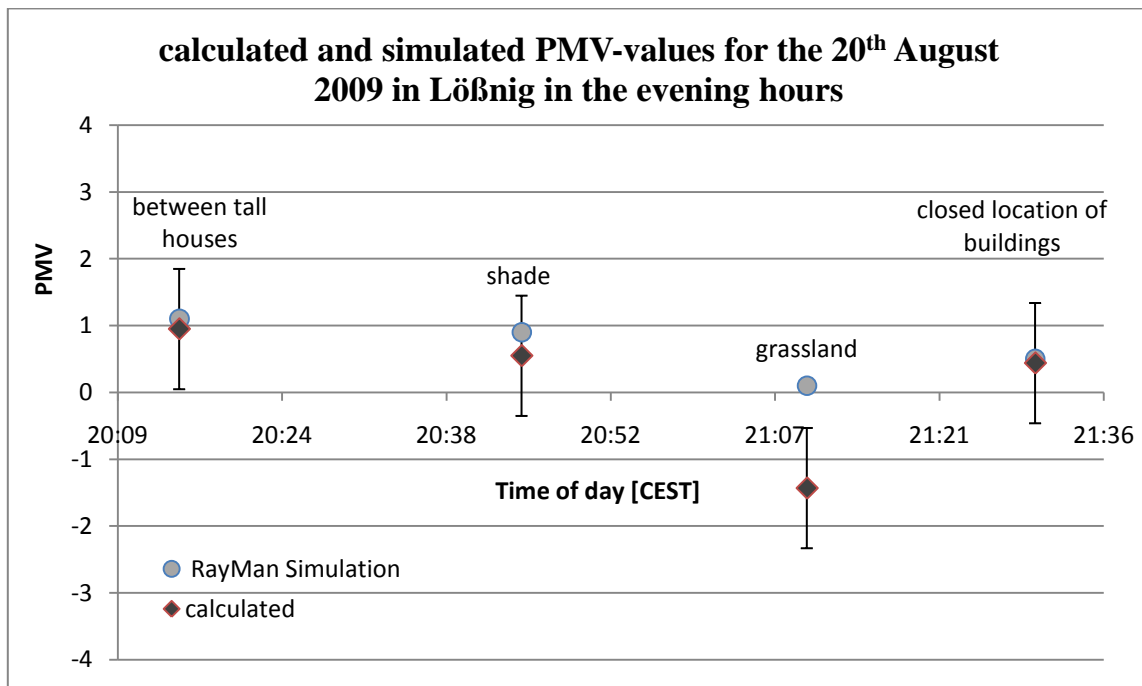
Figure 3: *Calculated/measured (10-minutes-average) and simulated (RayMan) PMV-values on the 20th August, 2009 in Lößnig in the evening hours.*

An error of ± 0.9 for the PMV was calculated with the Gaussian propagation of uncertainty method (see fig. 3, error bars). For the measurement point in the park (grassland) the result of the simulated PMV-value by RayMan shows a difference to the calculated result outside the error bar for the measurement, which cannot be explained up to now. It is possible that any prefactor is the reason for the deviation between the simulated and the calculated values of the PMV.

All in all, the example shows that the differing thermal behavior of natural and sealed surfaces is well demonstrated. The unsealed surfaces cool off more rapidly by comparison. This effect is caused, e.g., by the less reduction of the horizon and the additionally released heat of the buildings and the sealed surface.

Cumulated thermal comfort

A person perceives a particular thermal stress when remaining at one place just for a short time. Whereas by walking a certain route over a long time, the person is effected not only by the thermal stress dependent on a position but additionally by the change of the thermal stress dependent on the time of day. What thermal stress perceives a 'standard' person by walking a certain distance in one hour?

The study of Fanenbruck (2001) shows approaches of such a cumulated point of view. He not only involved the 'standard' person in his calculation, but also concentrated on several groups with different age and their variable adaptability. In the calculation algorithm Fanenbruck (2001) uses the thermo-physiological stress [unit °C]. Furthermore, the cumulated thermal stress is the integrated thermo-physiological stress by the time. Hence a time-integrated total exposure can be given. The approaches made by Fanenbruck (2001) could not be assigned for this study because the PMV equation contains a lot of time-dependent parameters, and hence an integration difficulties not operationally applicable.

A likewise method could be to calculate a mean average and afterwards add a defined cumulated aggregation, which is determined by the chronologically change of the PMV-value from one measuring point to the next one. Because the time difference between each measurement of every measuring point is irregular, a change of the PMV per minute was determined. Afterwards this change per minute is generated over the total measurement period. The result is an average of the change of the PMV per minute over a certain measurement time. To derive a statement for the cumulated thermal stress for a certain time range within the measurement time (e.g. one hour), the change of the PMV per minute can be multiplied with the required number of minutes (see also Friedrich, 2010). This calculation formalism shall be shown using the example of the 20th August, 2009, measurements in Lößnig. Therefore, the results of the calculated PMV-values at each measurement point in Lößnig for the current time of the day are presented in figure 4.
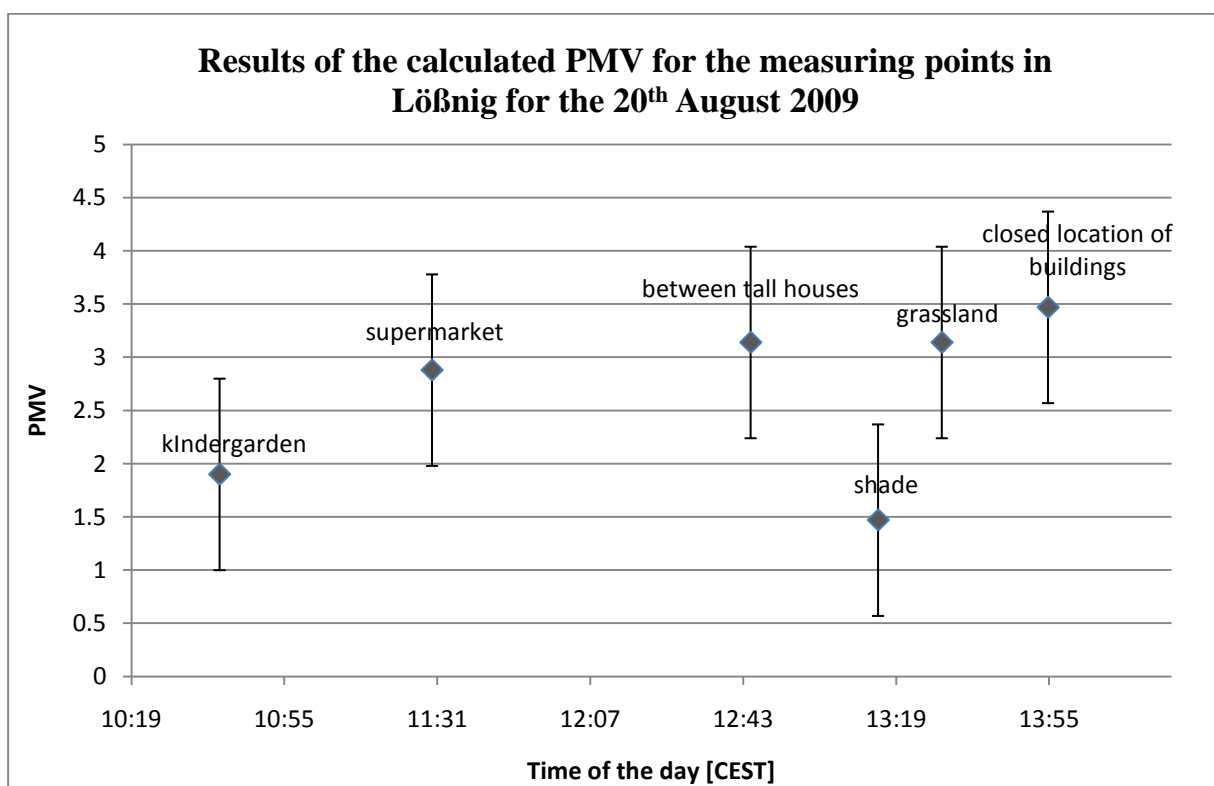
Figure 4: *Calculated/measured (10-minutes-average) PMV-values for the measurement points in Lößnig on the 20th August 2009 in the daytime hours.*

The calculated PMV-values result in an arithmetically averaged value of about 2.7. Table 2 shows the results of the further evaluation. For every time range from one measuring point to another the change of the PMV was determined (column 3, table 2) and divided by the corresponding minutes (column 4, table 2). The resulted changes of the PMV per minute for each measuring point were then averaged. Thereby a negative change of the PMV (decline of the PMV in shady places) was considered. Further, the average change of the total measurement period (3 ½ hours) is multiplied by 60 minutes and hence a cumulated change of the PMV per hour of 0.7 was calculated using the example of the 20th August 2009 in Lößnig. This is the appointed cumulated aggregation, which is added to the calculated average of 2.7. A total mean PMV of 3.4

results, which means, that a person walking along the measuring route in Lößnig in one hour perceives a great thermal stress (see table 1).

Table 2: *Calculated/measured PMV and the results of the change of the PMV-values for every measurement point in Lößnig on the 20th August 2009 in the daytime hours.*

measurement point	calculated PMV	change of the PMV within the time from one measurement point to the next one	change of the PMV per minute
kindergarden	1.90		
supermarket	2.88	+ 0.98 in 45 min	+ 0.0217
between tall houses	3.14	+ 0.26 in 60 min	+ 0.0043
shade	1.47	- 1.67 in 15 min	- 0.111
grassland	3.14	+ 1.67 in 6 min	+ 0.278
closed location of buildings	3.47	+ 0.33 in 15 min	+ 0.022
		average change of the PMV	+ 0.043

The consideration of a time-dependent cumulated change of the PMV is necessary, because the PMV itself can change due to varying environmental as well as meteorological conditions. If a person already feels uncomfortable, a natural increase for example in the air temperature or solar radiation can indicate a higher sensed PMV as currently calculated at one place and moment. An individual perceives an additional thermal stress, although he/she already feels too hot. This was respected with the above chosen approach for the evaluation of the cumulated thermal comfort. The given method for the calculation of an hourly cumulated change of the PMV has to be applied for each measurement period to incorporate possibly changing environmental conditions.

For future studies it should be tried to generalize the method to evaluate the cumulated thermal comfort.

Conclusions and Outlook

The formation of the urban climate is, mostly, due to the high percentage of sealed areas in a city.

In general a thermal stress occurs at air temperatures of 20°C. Only parks and shades provide an adjustment to high thermal impact, which has been proved by means of various sealed areas in Lößnig. During the cooler evening hours, there is still a low thermal stress or thermal comfort between the blocks of houses (PMV-values range from 0.4 to 1.0) whereas in parks and on grassland a PMV of -1.4 was calculated, which is already chilly. According to the statement of Becker (Deutscher Wetterdienst-DWD, 2008) the air temperature rises from 0.3 to 0.4°C with every 10 percent additional degree of surface sealing. Because the climatic radius of operation of planted areas is limited, it is important that rebound (little parks and green spots) is created close to places of residence. Under trees and in shades the thermal stress can decrease by about 30%. The aim of landscape design processes should be to reduce new sealed areas and to utilize grassland or porous pavement more intensive.

To propose the conclusion how high the thermal stress is, a "standard" human perceives during a one hour walk, the PMV-values were being cumulated. Therefore, a cumulated thermal loading was defined, which results in the time rate of change of the meteorological parameters. Using the example of the 20th of August 2009 in Lößnig, a cumulated loading of the PMV of 0.7 was calculated and added to the average of the PMV during the measuring period (2.7). Hence, a total PMV of 3.4 results, which means that a person, who walks the route in Lößnig in one hour senses a great thermal stress.

Finding an adequate calculation formalism for the cumulated thermal stress is very hard in respect of using the Predicted Mean Vote as an index of thermal stress. In following studies the presented approaches should be improved. Also, other indexes such as the Perceived Temperature could be used to define a cumulated thermal stress with the unit of degree Celsius.

In conclusion, the obtained results are still insuffient to make a general statement, which urban area in Leipzig is mostly thermal loaded. For that reason, following studies must be carried out to enhance the data set. Additional and isochronic measurements are necessary to confirm the shown results and to gain an overview of the thermal stress of all areas in Leipzig. Therefore, more urban areas should be embraced. Furthermore measurements at "Neuseenland", south of Leipzig, are recommendable to pinpoint the contrast between the city centre and the nearby rural areas. Also, for a qualitative analysis of the heat island effect, there should be measurements at night. With more available date there can be made generalized statement of the thermal stress all over the town of Leipzig.

Adresses of the authors:

Anett Friedrich and Astrid Ziemann: Institute for Meteorology, University of Leipzig, Stephanstraße 3, 04103 Leipzig, A. Ziemann at present at the Leibniz Institute for Tropospheric Research Leipzig

Uwe Schlink: Helmholtz Centre for Environmental Research – UFZ, Permoserstraße 15, 04318 Leipzig

References

Amt für Umweltschutz: Umweltbericht 2007, Stadt Leipzig, Dezember 2007

Becker Dr. P, 2008: Stadtplanung im Zeichen des Klimawandels, Deutscher Wetterdienst, Kongress Energie.Stadt.Geld Frankfurt

Fanenbruck O., 2001: Ein thermophysiologisches Bewertungsmodell mit Anwendung auf das Leipziger Stadtgebiet, Wiss. Mitteilung aus dem Institut für Meteorologie der Universität Leipzig, Bd. 24, Dissertation, 151 Pages.

Fezer F., 1995: Das Klima der Städte, 1. Auflage, Justus Perthes Verlag Gotha, 199 Pages

Friedrich A., 2010: Messung und Modellierung der kumulierten thermischen Belastung in Leipzig, diploma thesis, 106 Pages

Häckel H., 2005: Meteorologie, 5. Auflage, Verlag Eugen Ulmer Stuttgart. 447 Pages

Helbig A., Baumüller J., Kerscher M. J., 1999: Stadtklima und Luftreinhaltung, 2. Auflage, Springer-Verlag Berlin, 467 Pages

Hupfer P., Kuttler W., 2006: Witterung und Klima: Eine Einführung in die Meteorologie und Klimatologie , 12. Auflage, B. G. Teubner Verlag, 553 Pages

Kratzer P. A., 1956: Das Stadtklima, 2. Auflage Friedr. Vieweg & Sohn Braunschweig, 184 Pages

Matzarakis A., 2001: Die thermische Komponente des Stadtklimas, Ber. Meteor. Inst. Univ. Freiburg Nr. 6, 286 Pages

Müller U., 1997: Stadtklima Leipzig – Ergebnisse experimenteller Untersuchungen, Wiss. Mitteilung aus dem Institut für Meteorologie der Universität Leipzig, Pages 120-125

Müller U., Tetzlaff G., 1999: Zur thermischen Belastung in Innenräumen, Wiss. Mitteilung aus dem Institut für Meteorologie der Universität Leipzig, Pages 142-148

Oke T. R., 1987: Boundary layer climates, 2. Auflage, Routledge Verlag, 435 Pages

Schwab U., STEINICKE & STREIFENDER Freiburg und Heinz P., Amt für Umweltschutz der Stadt Leipzig 1997: Stadtklimauntersuchung Leipzig 1997, Eine klima- und immissionsökologische Bewertung, Wiss. Mitteilung aus dem Institut für Meteorologie der Universität Leipzig, Pages 116-119

Seifert P., 2004: Seminarvortrag Stadtklima, 21 Pages

VDI 3789 Blatt 2, 1994: Umweltmeteorologie - Wechselwirkungen zwischen Atmosphäre und Oberflächen - Berechnung der kurzwelligen und der langwelligen Strahlung, VDI-Richtlinien, 52 Pages

VDI 3787 Blatt 2, 1998: Umweltmeteorologie – Methoden zur human-biometeorologischen Bewertung von Klima und Lufthygiene für die Stadt- und Regionalplanung Teil 1: Klima, VDI-Richtlinien, 29 Pages

Verein Deutscher Ingenieure, 1988: Stadtklima und Luftreinhaltung, Herausgegeben von der VDI-Kommission Reinhaltung der Luft, Springer-Verlag Berlin, 426 Pages

Studies about the influence of turbulence on the sound propagation in the atmosphere and its simulation

Florian Rost, Astrid Ziemann and Armin Raabe

Summary

Noise is still an unsolved problem of our time and influences the public health and well-being. So sound-exposure gains more and more in importance. This study examines the influence of turbulent vertical profiles of wind and temperature on the sound propagation, using the model SMART (**s**ound propagation **m**odel of the **a**tmosphere using **r**ay-**t**racing). For several states of atmospheric stability, ten-minute-time series of vertical wind and temperature profiles were constructed and used as input data for the model. Simulations of the sound attenuation showed that turbulence affects the sound propagation in the atmosphere. This influence is reflected in a reduction of the sound attenuation level in the downwind area, whereas the sound shadow remains almost unaffected. The influence increases with the distance to the source and depends on the atmospheric stability.

Beside the average influence due to turbulence, a "worst-case" scenario with the highest noise immission during the simulated time range was analyzed.

Based on the results of this study, a new SMART-module, taking turbulence into account by parameterizations, was developed. The developed turbulence module is an upgrade of the sound model SMART and helps to improve the sound immission forecasts, including meteorological effects.

1 Introduction

In Germany, more than 15 million people feel disturbed by noise [1]. Noise is not only unpleasant. It can cause people falling ill. For noise levels greater than 60 dB, the myocardial infarction risk increases continuously. Pear year, approx. 4000 myocardial infarction cases are attributed to the road traffic noise [2]. A very meaningful tool in environmental protection is the forecast of sound immission. At the *Leipziger Institut für Meteorologie* a sound propagation model, SMART (**s**ound propagation **m**odel of the **a**tmosphere using **r**ay-**t**racing), was developed [3]. In contrast to the idea that sound propagates in form of waves, this model deals with the estimation of sound energy propagation by sound rays. This is the basic principle of the geometrical acoustics [4], which is the foundation of SMART. This model computes the sound attenuation level, taking into account meteorological influences on the sound propagation by vertical profiles of wind velocity, wind direction and temperature.

In previous simulations only stationary profiles were considered. In the lowest 1 to 2 km of the atmosphere (the atmospheric boundary layer) wind shear and solar heating of the ground produce turbulent fluctuations of the vertical profiles. These fluctuations lead to sound scattering that influences the sound attenuation level [4], [5].

For this work, vertical profiles of wind and temperature including turbulent fluctuations were constructed for several cases of atmospheric stability and jointed to time series. The sound propagation for each time series were averaged arithmetically to estimate the effects of turbulence on the sound attenuation.

2 Meteorological effects on the sound propagation

The adiabatic sound speed is a function of the air temperature T. The propagation velocity of the sound also depends on the wind vector. Therefore, there the effective sound speed [4] is introduced as

$$c_{eff}(z) = c(z) + u(z),\qquad(1)$$

with the adiabatic sound speed c and the wind velocity component u along the propagation direction of the sound. A vertical increase of temperature or wind velocity leads to a vertical increase of the effective sound speed and a downward refraction of the sound ray. A vertical decrease of c_{eff} causes an upward refraction.

The sound propagation model SMART uses these properties for calculating the sound attenuation level. It is introduced in the following section.

3 The sound propagation model SMART

In the model SMART a sound source emits a number of sound rays into the atmosphere, which is regarded as horizontal homogeneous. The computation of the sound path is based on the special refraction law for a moving medium [6]. Meteorological effects on the refraction are considered by vertical profiles of wind velocity, wind direction and temperature. After the ray tracing, between two sound rays with only a small difference in the emission angle a sound tube is constructed. The cross-section of such a tube is inversely proportional to the sound intensity I. The ratio of these cross-sections at a sampling point i and at a reference distance from the source (here: 1 m) leads to the change in the sound intensity level, called sound attenuation level [3], [7]:

$$\Delta L_I = -10 \cdot \lg \frac{I_i}{I_{ref}}.\qquad(2)$$

These calculations are made for 36 horizontal directions with an azimuth angle resolution of 10 deg. Therefore the output of SMART involves a horizontal sound attenuation field. The immission level was set to a height of 2 m above ground.

The model input data include vertical profiles of temperature, wind speed and wind direction. These profiles can be taken from measurements or – as in this study – can be constructed synthetically.

3 Synthetical construction of vertical turbulent wind and temperature profiles

In a first step, undisturbed profiles were simulated. The wind profiles are based on the logarithmic wind law

$$\overline{u}(z) = \frac{u_*}{\kappa} \ln \frac{z}{z_0},$$ (3)

with the mean wind speed $\overline{u}$, height over the ground z, the *von Kármán*-constant κ ($\kappa = 0.4$) and the friction velocity u_* [8]. The roughness length z_0 was taken for $z_0 = 0.01$ m, which is an adequate value for grassland [9], was used. To take into account atmospheric stability, u_* is calculated for several stability classes, borrowed from the *Pasquill*-stability classes [10]: *Very unstable*, *unstable*, *neutral to light unstable*, *neutral to light stable*, *stable* and *very stable*. This classification is based on the *Obukhov*-length L, an stability parameter which refers to the ratio of the flux of momentum and the sensible heat flux. Profiles were constructed for the following values of L (unit: m): -10; -30; -50; -100; -200; -300; 500; 250; 150; 60; 7.

The creation of vertical temperature profiles rests upon the gradient-*Richardson*-number

$$R_i = \frac{g}{\overline{T}} \cdot \frac{\dfrac{\partial \overline{\Theta}}{\partial z}}{\left(\dfrac{\partial \overline{u}}{\partial z}\right)^2},$$ (4)

with the acceleration due to gravity g and the parameterizations $R_i = \dfrac{z}{L \cdot \varphi_M}$ for a

stably and $R_i = \dfrac{z}{L}$ for an unstably stratified atmosphere [11]. Θ is the potential

temperature and $\overline{T}$ the layer-average temperature. φ_M represents a stability depending function.

In the real atmosphere, such simple profiles are disturbed by turbulent eddies. A turbulent flow contains a number of eddies on different scales. The largest of them gain turbulent kinetic energy from the main airstream. These large eddies transfer their energy – without any loss of energy – to smaller ones, which convey energy by the same way. The smallest eddies with dimensions depending on the viscosity of the medium are dissipating the mechanic energy into heat. The range of energy transfer (inertial subrange) in this energy spectrum was described by *Kolmogorov* (1941) by the relation

$$E(f) \propto f^{-5/3},$$ (5)

where f is the frequency [12]. Within simulated profiles, atmospheric turbulence was included by considering the mixing length theory of *Prandtl* [11]. By a vertical impulse, an air parcel with its specific properties $\overline{u}(z)$ and $\overline{\Theta}(z)$ is mixed into a higher (or lower) altitude $(z+l)$, retaining its properties. The observation of this particle in the level $(z+l)$ is $u = u(z) = \overline{u}(z+l) + u'$. $\overline{u}$ can be seen as average wind speed and

u' as turbulent fluctuation. These relations can also be considered for Θ. The mixing length is calculated by

$$l = \kappa z / \varphi_{M,H} . \qquad (6)$$

There are several parameterizations for $\varphi_{M,H}$, according to u (φ_M) and Θ (φ_H) [11]. They are all based on the *Obukhov*-length L.

In a fixed height over ground (in this special case 0.25 m) the mixing length is calculated and added to this height. The result is saved as a first interim stage. To the values of $\bar{u}$, $\bar{\Theta}$ or $\bar{\vartheta}$ at this height, a turbulent fluctuation u' respectively Θ' or ϑ' is added (ϑ: wind direction). For the altitude of the first interim stage, the mixing way length is calculated and added to this height. This leads to a new interim stage. This procedure is repeated until the maximum height of the model is reached.

Such profiles are constructed over a time range of 10 minutes [13]. A time series $u(z,t) = \bar{u}(z) + u'(z,t)$, $\Theta(z,t) = \bar{\Theta}(z) + \Theta'(z,t)$ and $\vartheta(z,t) = \bar{\vartheta}(z) + \vartheta'(z,t)$ is created for each interim stage.

The time- and height-dependent turbulent fluctuations u', Θ' and ϑ' are simulated in the following way:

A series of random data points is produced and assigned to a discrete time t_i, while $\Delta t = t_i - t_{i-1} = 0.5$ s. The energy spectrum [14] of this time series has the form $E(f) \propto f^0$. After a modification, the energy spectrum becomes a *Kolmogorov* spectrum with $E(f) \propto f^{-5/3}$.

The result of a re-transformation is a time series with the typical characteristics of the inertial subrange. The adaptation of the amplitude by a scaling factor does not influence the energy spectrum.

The amplitudes of the fluctuations depend on the altitude and the atmospheric stability and are calculated according to the turbulence characteristics given by *Foken* [10] and *Thomas et. al* [15]. Examples of such profiles are shown in figure 1.
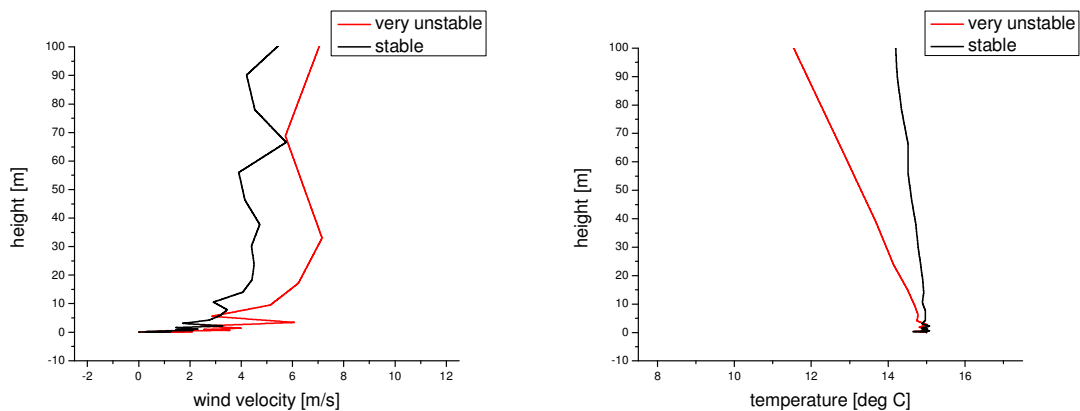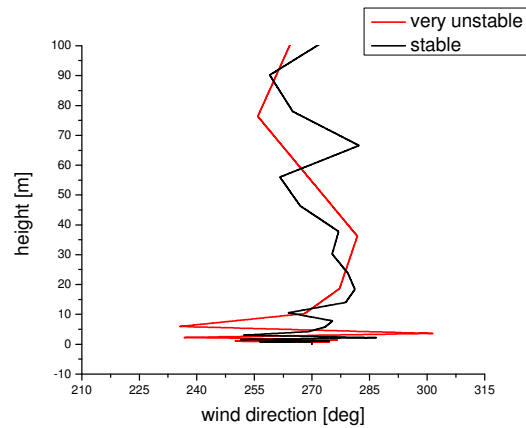
Figure 1: Examples of synthetically constructed vertical profiles of
the quantities wind velocity, temperature and wind direction (from left
to right). Red curves: *very unstable* case. Black curves: *stable* case.

In a next step, based on the constructed profile-time series the sound attenuation level
was calculated by SMART. After first sensitivity studies about the influence of the
single properties wind velocity, wind direction and temperature, profiles of all
properties were combined. The sound attenuation was calculated for each selected
value of the *Obukhov*-length *L* and arithmetically averaged over the simulated 10
minute time range.

4 Results of the SMART simulations

Figure 2 shows the sound attenuation calculated by SMART based on an undisturbed
wind profile (left) and the attenuation field, averaged over the simulated ten-minute-
range (right).
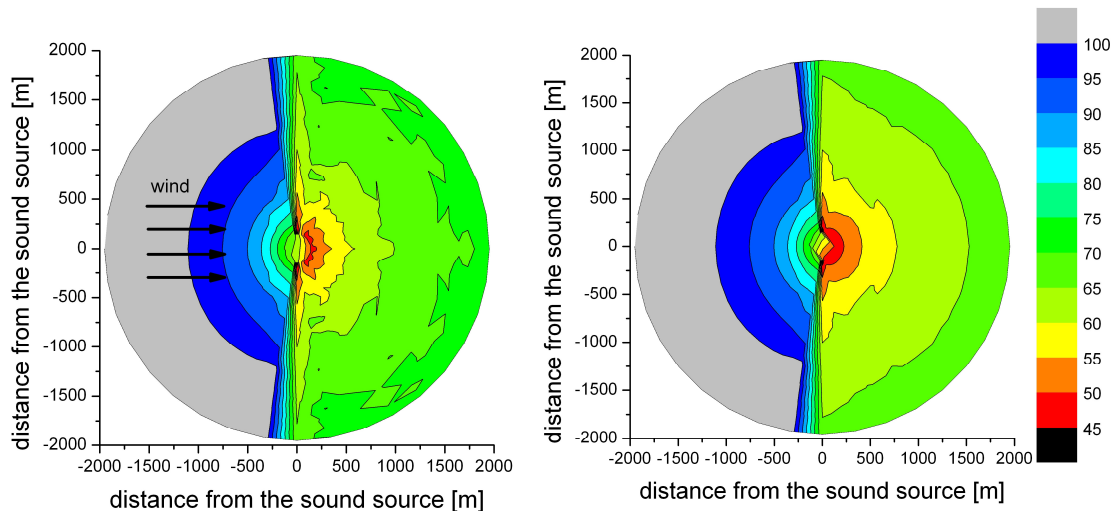
Figure 2: Sound attenuation level [dB] calculated by SMART for an undisturbed wind velocity profile (left) and averaged over a ten-minute time series of turbulent wind velocity profiles for a *very unstably* stratified atmosphere ($L = -10$ m) (right).

The sound source is located in the center of the circle area, right over the ground whereas the immission level lies at 2 m height above ground. Both attenuation fields are based on a *very unstable* atmosphere (stability class A, *Obukhov*-length $L = -10$ m) and a vertical wind gradient is taken into account. In the upwind area, the upward refraction of the sound rays makes no sound rays penetrating this region. This area is called *sound shadow*. In natural surroundings, diffracted and scattered sound reaches this region, hence there is no absolute silence. Referring to *Salomons* [14] SMART takes the energy conservation on the surface of a sound wave into account. With growing distance from the sound source, the wave surface is getting taller. The resulting decrease of energy density per unit of area leads to an attenuation of 6 dB per doubled distance from the source (spherical wave divergence). Additionally to this values SMART adds a constant attenuation of 40 dB [4].

It comes out that the sound shadow region is not influenced by turbulence. In the downwind area, there seems to be a decrease of the sound attenuation by the influence of turbulence. A comparison between the averaged turbulent attenuation field and the attenuation without any turbulence approves this first finding (see figure 3). To find out how strong the influence of the turbulence is for every point of the analyzed area, the attenuation field without the influence of turbulence was subtracted from the attenuation field containing turbulence. The result is the additional attenuation due to turbulence.
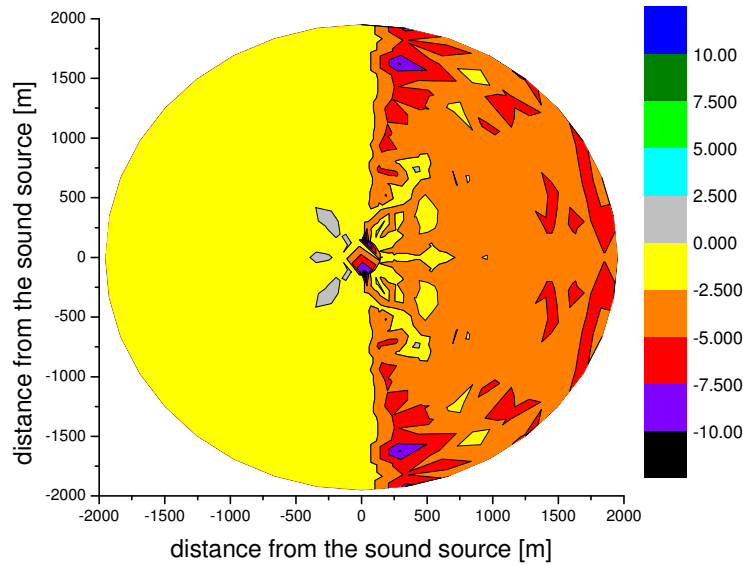
Figure 3: Additional sound attenuation [dB] caused by turbulence averaged over a ten minute time series of turbulent wind velocity profiles in a *very unstable* atmosphere ($L = -10$ m).

Similar considerations were made for vertical profiles of the temperature without wind vector influence. In this case, the effects of turbulence strongly depend on the algebraic sign of the temperature gradient, as figure 4 shows.
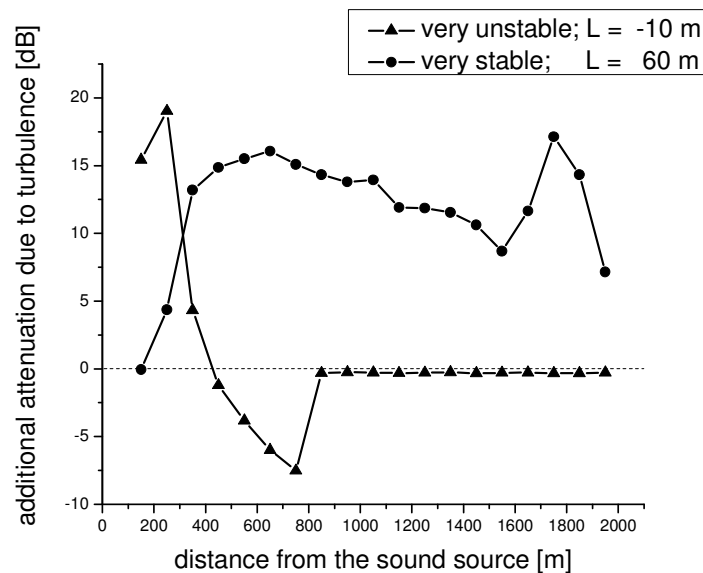
Figure 4: Additional sound attenuation [dB] caused by turbulence averaged over a ten-minute-time series of turbulent temperature profiles in a *very unstable* ($L = -10$ m) and a *very stable* atmosphere ($L = 60$ m).

The curves show the additional sound attenuation level caused by turbulence in the case of a vertical temperature decrease (*very unstable* case) and a vertical temperature increase (*very stable* case), respectively. As can be seen, there is an additional attenuation for almost all distances in the *very stable* case. In the *very unstable* case, there is an additional attenuation due to turbulence only for small distances from the sound source. For larger distances, because of the developing sound shadow no turbulence influence can be observed.

In the atmosphere wind gradients are common as well as temperature gradients. So the next step combines these profiles and uses them as new input data for SMART.
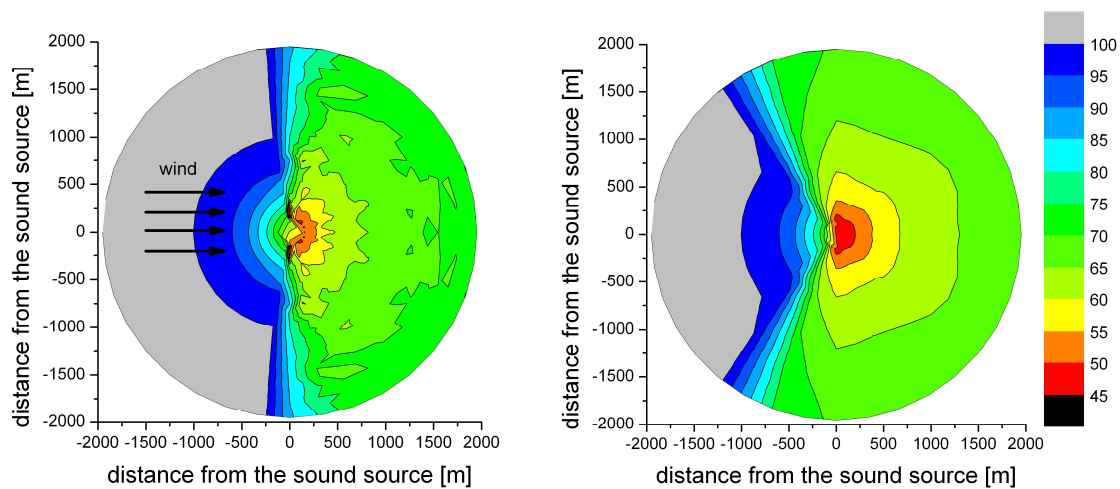
Figure 5: Sound attenuation level [dB] calculated by SMART for undisturbed combined wind and temperature profiles (left) and averaged over a ten-minute-time series of turbulent wind and temperature profiles (right) for a *very unstable* atmosphere ($L = -10$ m).

Figure 5 displays the results of these calculations. The picture on the left side was simulated with undisturbed wind and temperature profiles. On the right side, the averaged attenuation over 10 minutes with turbulent fluctuations of wind velocity, wind direction and temperature can be seen. Beside a smoothed map because of the averaging procedure, the picture of the turbulent case shows a reduced sound attenuation in the downwind area. Furthermore, the region of the sound shadow is smaller, attributed to turbulent fluctuations of the wind direction.

Among the studied stability classes, the curves of attenuation caused by turbulence have similar structures. Therefore all calculations for the same stability class (but based on different values of the *Obukhov*-length, see above) are summarized by averaging them. Figures 6 and 7 give information about the stability classes *very unstable* and *very stable*. Both of the illustrations show exemplarily two of 36 sound directions: downwind and 30 deg crosswind to downwind.
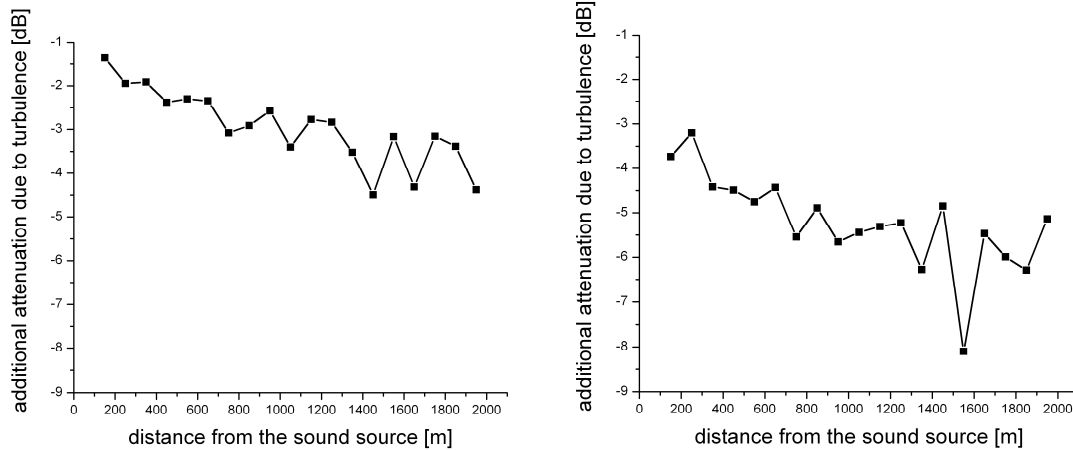
Figure 6: Additional sound attenuation [dB] caused by turbulence averaged over a ten minute time series of combined turbulent profiles of wind vector and temperature in a *very unstable* atmosphere. Left: downwind, right: 30 deg crosswind to downwind.
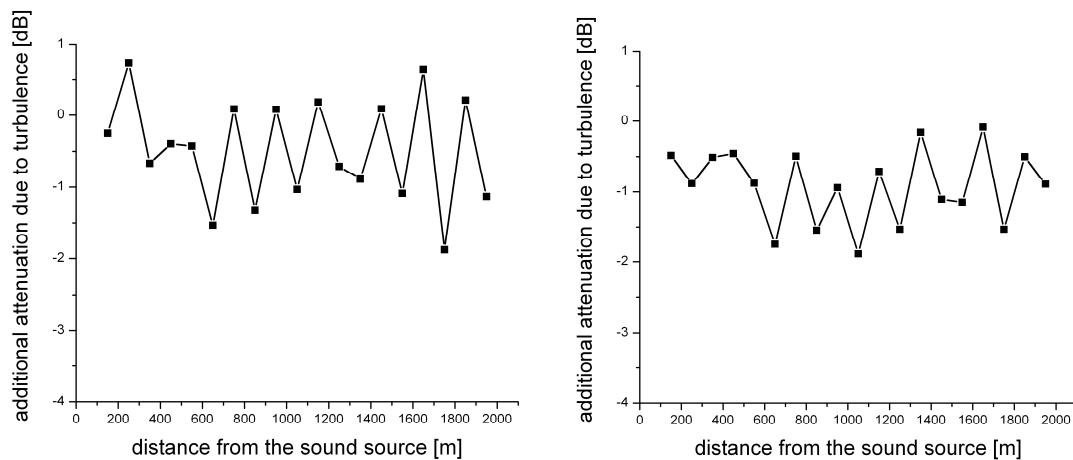
Figure 7: Additional sound attenuation [dB] caused by turbulence averaged over a ten minute time series of combined turbulent profiles of wind vector and temperature in a *very stable* atmosphere. Left: downwind, right: 30 deg crosswind to downwind.

It comes up that turbulence leads to a decrease of sound attenuation in the *very unstable* case. This behavior amplifies with growing distance from the sound source because of the longer sound path through the turbulent atmosphere. Due to turbulent fluctuations of the wind direction, the influence in the crosswind area is larger than in the downwind direction (see figure 6).

The case of a *very stable* atmosphere shows a significant lower influence of turbulence and nearly no variation with growing distance (see figure 7).

5 "Worst case" scenarios

Beside the average additional attenuation, especially regarding noise protection, the maximal additional sound input caused by turbulence is of interest. This "worst case" selects the lowest sound attenuation values for each point of the attenuation field over the complete time range. The additional attenuation due to turbulence for this case in an *unstable* atmosphere is shown in figure 8.
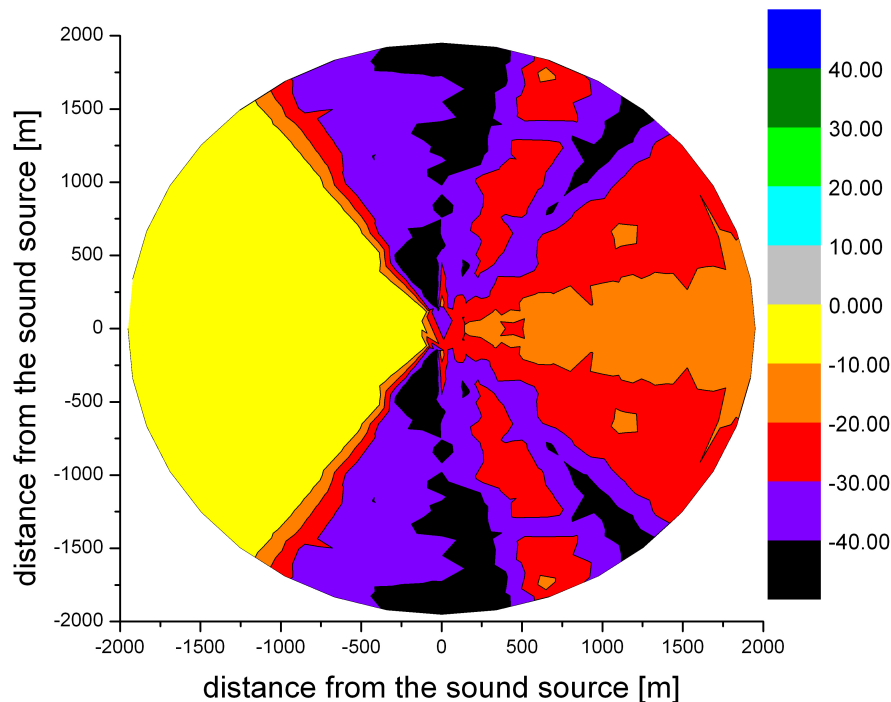
Figure 8: Minimal additional sound attenuation [dB] due to turbulence averaged over a ten-minute-time series of combined turbulent profiles of wind vector and temperature in an *unstable* atmosphere.

It can be seen that the maximal reduction of the sound attenuation caused by turbulence lies between 10 and 20 dB in the downwind direction and between 30 and 40 dB in the crosswind sections. Identical studies about a *very stable* stratified atmosphere showed a weaker influence of turbulence. There is an attenuation reduction of less than 10 dB in the downwind direction and less than 30 dB in the crosswind sections.

6 Development of a turbulence-module for the sound propagation model SMART

Based on the presented work, a supplementary module for the sound propagation model SMART was developed. The additional sound attenuation due to turbulence dependent on the distance to the sound source was parameterized by regressions of their determined values in the prefixed case studies.
The module just deals with the region from 0 to 50 deg around the downwind direction and calculates the sound attenuation due to turbulence depending on the atmospheric

stability. The applicable input parameter is one of the introduced stability classes. An example for the simulated attenuation without and with this module shows figure 9 for a *very unstable* stratified atmosphere.
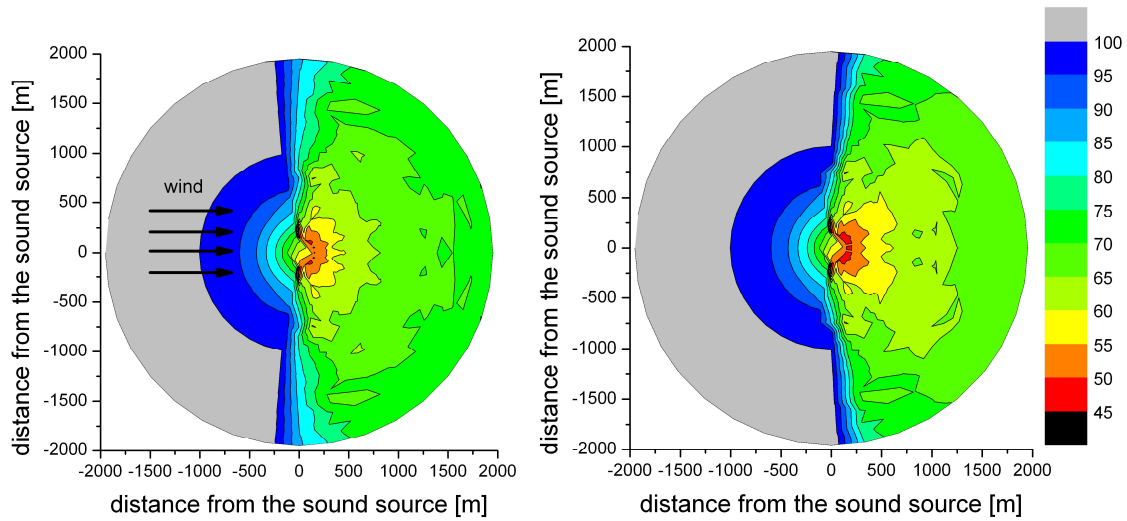
Figure 9: Sound attenuation level [dB] calculated by SMART for an undisturbed combined wind and temperature profile. Left: without any turbulence, right: including parameterized turbulence effects for a *very unstable* atmosphere.

The developed module also provides the facility to estimate the "worst case". The region is shown in grey. An example shows figure 10.
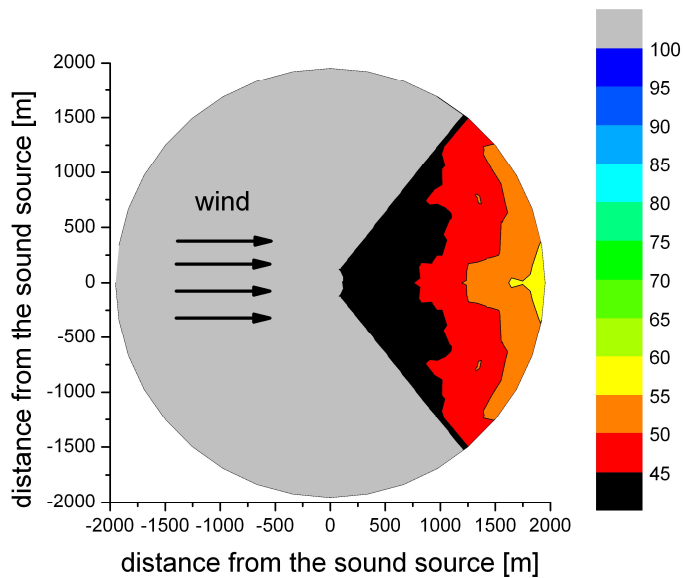
Figure 10: Minimal sound attenuation [dB] in a turbulent atmosphere calculated with the new developed turbulence module of SMART for combined profiles of wind vector and temperature in a *very unstable* atmosphere.

7 Conclusions and further prospects

The conducted studies show, that turbulent fluctuations of wind vector and temperature affect the sound propagation in the atmosphere. These fluctuations result in small-scale, local supplementary gradients in the wind and temperature profiles, which lead to a changed refraction of the sound rays.

As a result of the simulations for the stability range from *very unstable* to *stable*, turbulence causes a reduction of the sound attenuation of 2 to 8 dB in the focused area of 0 to 50 deg crosswind to the downwind direction, compared with a turbulence free atmosphere. That means in average turbulence results in a higher noise immission for a *very unstable* to *stable* atmosphere. The main influences on the initial sound shadow can be ascribed on turbulent fluctuations of the wind direction. The region 0 to 50 deg around to the upwind direction is only weakly influenced.

Furthermore it comes up, that the influence of turbulence increases with growing distance to the source. This conforms to expectations, because the sound ray passes more and more turbulence elements (eddies) during its propagation through the atmosphere, so the influence of turbulence increases.

A particular position takes up the stability class *very stable*. In this case, the average additional attenuation due to turbulence in sound directions between 0 and 30 deg is neglectable. In 30 to 50 deg, turbulence leads to a reduction of the attenuation of not more than 2 or 3 dB. Furthermore, the effect of turbulence depends only weakly on the distance of the source (see figure 7). Further calculations with various profiles can also help to specify the obtained parameterizations, like simulations for other values of the *Obukhov*-length L.

As can be seen from figure 1, the strongest fluctuations of wind and temperature (and consequently the largest values of their vertical gradients) can be found close to the ground. In all simulated cases the sound source was set on the ground, so the effects near the earth surface prevail. Studies with a sound source centimeters or meters above ground verified this assumption [16] and should be continued.

A limitation of the introduced results is the fact that SMART is only able to simulate a horizontal homogeneous atmosphere. In general, this assumption is inapplicable for regarding turbulence.

The parameterization of the "worst case" scenario does not take a range of time into account, for that the sound attenuation reduction takes place. This can be modified by using another selection algorithm, which takes an immission time into account.

This study is designed to give a first idea how to consider turbulence in SMART. The new version of SMART considering turbulence is a further advance in the sound immission forecast. The option to calculate a "worst-case" scenario helps to estimate the maximal noise exposure due to meteorological effects.

References:

[1]   Flasbarth, J., 2009: Lärm ist das am stärksten unterschätzte Umweltthema. Epoch Times Deutschland

[2]   Babisch, W., 2006: Transportation Noise and Cardiovascular Risk. WaBoLu-Hefte 01, Umweltbundesamt

[3]   Ziemann, A., 2003: Auswirkungen unterschiedlicher Schallausbreitungs-modelle auf die Lärmprognose. Wiss. Mitteil. Inst. f. Meteorol. Univ. Leipzig 30

[4]   Salomons, E. M., 2001: Computational Atmospheric Acoustics. Kluwer Academic Publishers

[5]   Albrecht, H.-J., Peters, E., 2007: Der Einfluss turbulenter Temperatur- und Windfluktuationen auf die Standardabweichung des akustischen Beurteilungspegels. Fachbeiträge des Landesumweltamtes Brandenburg 106

[6]   Ostashev, V. E., Hohenwarter, D., Attenborough, K., Blanc-Benon, Ph., Juvé, D., Goedecke, G.H., 2001: On the refraction law for a sound ray in a moving medium. Acustica 87, p. 303 – 306

[7]   Ziemann, A., Balogh, K., 2006: Gekoppelter Atmosphäre-Boden-Einfluss auf die Schallausbreitung einer höher gelegenen Schallquelle. Wiss. Mitteil. Inst. f. Meteorol. Univ. Leipzig 37

[8]   Kraus, H., 2008: Grundlagen der Grenzschichtmeteorologie. Springer Berlin

[9]   Zmarsly, E., Kuttler, W., Pethe, H., 2002: Meteorologisch-klima-tologisches Grundwissen. Verlag Eugen Ulmer Stuttgart

[10]   Foken, T., 2003: Angewandte Meteorologie. Springer Berlin

[11]   Kraus, H., 2008: Grundlagen der Grenzschichtmeteorologie. Springer Berlin

[12]   McComb, W.D., 1991: The Physics of Fluid Turbulence. Oxford University Press

[13]   Seifert, H., 1999: VDMA Forschungsprojekt: Ermittlung von Ermü-dungsdaten an großen Windenergieanlagen. DEWI Magazin 15, p. 58 – 64

[14]   Press, W.H., Teukolsky, S.A., Vetterling, W.T., Flannery, B.P., 1992: Numerical Recipes in Fortran 77. Camebridge University Press

[15]   Thomas. C., Foken, T., 2002: Re-evaluation of integral turbulence characteristics and their parameterizations. 15th Conference on Boundary Layer and Turbulence

[16]   Rost, F., 2010: Untersuchung und Simulation des Einflusses von Turbulenz auf die Schallausbreitung in der Atmosphäre, Universität Leipzig, Institut für Meteorologie, Diplomarbeit

Acoustic anemometry and thermometry

B. M. Brecht, A. Raabe and A. Ziemann

Abstract

Acoustic travel-time measurement is a method for remote sensing of the atmosphere. The temperature-dependent sound speed as well as the flow field can be detected by measuring the travel time of a defined acoustic signal between a sound source and a receiver when the distance between them is known. In this study the properties of the flow field are reconstructed using reciprocal sound rays to separate the direction-independent sound speed from the effective sound velocity including the flow velocity component in direction of the sound path. The measurements are taken on a horizontal scale of about 2 m x 2 m. By measurements in interiors, where no flow of air exists, the temperature can be determined with an accuracy of 0.6°C and the flow component in direction of the sound path with an accuracy of 0.3 m/s. If flow of air exists the measurements gets complicated because the phase shifts, which have been detected by the receivers, cannot be corrected like it was possible without the influence of flow.

1   Introduction

The motivation to do travel-time tomography in the atmosphere is to get consistent, measured data to validate numerical atmosphere-models like Large-Eddy simulations (LES), which has become a common tool to investigate several questions of the micro scale structure of the atmosphere (Arnold et al., 2003). Therefore area or volume-averaged values are needed, which the travel-time tomography provides. Conventionally such spatially data have been provided by point measurements and additional interpolation or up-scaling algorithms. Travel-time tomography provides this data directly with a high spatial and temporal resolution (Arnold et al., 2003).

Acoustic tomography exists a long time. At first Spiesberger and Fristrup (1990) verified an experimental application of a tomographic horizontally–sliced scheme to the atmospheric surface layer. They described a method for passively locating the calls of animals. Wilson and Thomson (1994) also verified this method with the concentration on the characteristics of the atmosphere (Tetzlaff et al., 2002). Then the work with acoustic tomography has started at the Institute of Meteorology of the Leipzig University (LIM). Arnold et al. (1999), Raabe et al. (2001) and Ziemann et al. (1999 a, b) demonstrated the applicability of acoustic travel-time tomography to detect absolute values of the temperature and the wind vector with no additional information apart from air humidity (Tetzlaff et al., 2002).

There were several projects relating to acoustic travel-time tomography at the LIM, inter alia the STINHO-project, a field-campaign at the boundary layer field site of the

Meteorological Observatory Lindenberg of the German Meteorological Service in the summer of 2002. The intention was to compare conventional meteorological point and vertically integrated measurements with area-covering air flow observations and numerical simulations. To observe horizontally variable flow and temperature fields above a heterogeneous land surface they used, inter alia, travel-time tomography (Raabe et al., 2005). In this project the researched area had a range of 300 m x 440 m. Besides the application on meteorological boundary layer field sites to get consistent data to validate numerical atmosphere-models like LES the method of acoustic travel-time tomography can be used on other questions as well. It can also be applied on shorter distances between the sound source and receiver, like only a few meters. This work began on the LIM using an apparatus that worked with audible sound signals and was suitable for wind and temperature measurements on a scale of 1 m (Barth et al., 2007). The travel times between a sound source and a sound receiver were detected with a correlation technique, where the travel time was that time, in which the correlation between the transmitted and received signal was the biggest. On these shorter distances it is possible to measure flow patterns in wind channels or the flow in atmosphere-chambers or halls. Another field of application in which travel-time measurements could be useful is in Greenhouses, because the air speed distribution is a key factor influencing heat and mass transfer there. Wang et al. investigated the air speed profiles in the centre of a naturally ventilated greenhouse with a tomato crop by means of a customized multi-point two dimensional sonic anemometer system and the experimental results showed that air speed was linearly dependent both on external wind speed and greenhouse ventilation flux (Wang et al., 1999). For this acoustic travel-time tomography could be used as well.

Aim of this work is to develop a progress of the acoustic travel-time measurement on a horizontal scale of about 2 m x 2 m, like Barth did, with a start-stop measuring technique. The presented method uses ultrasound and can carry up to ten measurements per second. A fact, that is especially for measurements in turbulent flows of advantage.

2   Basics of acoustic travel-time measurements

Sound waves, or acoustic waves, are longitudinal waves. Sound is propagated by the alternating adiabatic compression and expansion of the medium (Holton, 2004).
The speed of sound in a medium is determined by its characteristics, that means in the atmosphere the temperature, the moisture and the flow vector of the air.

2.1   Speed of sound in gases

For an ideal gas, which is a valid idealization for air (Pierce, 1994), and the assumption of adiabatic change of condition by the propagation of sound, the adiabatic speed of sound c_L results from the pressure p and the density ρ to

$$c_{\mathrm{L}} = \sqrt{\gamma_{\mathrm{dry}} R_{\mathrm{dry}} T} \,, \tag{2.1}$$

where γ_{dry} is the ratio of the specific heat capacities for constant pressure to constant volume, R_{dry} is the specific gas constant for dry air and T the air temperature in Kelvin. The sound velocity c_{L} is also called Laplace's speed of sound. The specific gas constant R_{dry} amounts 287.05 J kg^{-1} K^{-1} and γ_{dry} can be assumed to be constant for air in the temperature range of interest and is equal to 1.4 (Pierce, 1994).

The presence of water vapor changes both the gas constant and the specific heat capacity. The resulting equation for Laplace's speed of sound, depending on the specific humidity q, becomes

$$c_{\mathrm{L}} = \sqrt{\left[(1 + 0.51q)\gamma_{\mathrm{dry}} \cdot R_{\mathrm{dry}} \cdot T\right]} \,. \tag{2.2}$$

The temperature has a bigger influence on the speed of sound as the humidity. For the using here the moisture is not negligible, but it is sufficient to make the assumption of a constant value.

In a real atmosphere the velocity of sound depends also on the flow of air. This dependence is vectorial and not scalar, like that from the temperature and the moisture. To describe the influence of the wind vector $\mathbf{v}$ on the sound speed, the effective speed of sound is often used:

$$c_{\mathrm{eff}} = c_{\mathrm{L}}\big(T_{\mathrm{av}}(\mathbf{r}, t)\big) + \mathbf{v}(\mathbf{r}, t) \cdot \mathbf{s} = c_{\mathrm{L}}\big(T_{\mathrm{av}}(\mathbf{r}, t)\big) + v_{\mathrm{ray}}. \tag{2.3}$$

Here $\mathbf{s}$ represents an unit vector, which is tangential to the sound path from the sound source to the receiver (Ostashev, 1997), $\mathbf{r}$ represents the space vector, t the time and v_{ray} describes the projection of the flow vector to the direct line between the sound source and the receiver and therefore the flow component in the direction of the sound ray. Consequently c_{eff} has both a temperature-depending part (c_{L}) and a flow-depending part (v_{ray}). Therefore the vectorial influence of the wind is attributed to the scalar addition of Laplace's sound velocity c_{L} and the wind component in the direction of the sound ray v_{ray}. Equation 2.3 is an approximation, because the unit vector $\mathbf{s}$ is bending with the influence of wind. The approximation is valid if the properties of the ambient medium ($\mathbf{v}$) changes much slower than the characteristically time of the energy transport (c_{eff}).

2.2   Separation of the temperature and flow dependence

To separate the scalar influence of the temperature and the directional influence of the flow vector on the speed of sound there are used bidirectional, nearly reciprocal, sound paths. The application of this principle is used, e.g., by ultrasonic anemometers. Therefore reciprocal sound propagation can be assumed. Laplace's sound speed can be

derived by adding the forward and backward travel times (Equation 2.4). The flow's velocity component along the sound ray path can be derived by subtracting the forward and backward travel times (Barth, 2007). The resulting equations look like the following:

$$c_{\text{L}} = \frac{d}{2}\left(\frac{1}{\tau_{0,\text{forward}}} + \frac{1}{\tau_{0,\text{backward}}}\right),$$ (2.4)

$$v_{\text{ray}} = \frac{d}{2}\left(\frac{1}{\tau_{0,\text{forward}}} - \frac{1}{\tau_{0,\text{backward}}}\right).$$ (2.5)

Here d is the distance between a sound source and receiver and τ_0 is the travel time of a sound signal.

3 The measuring system

To get the effective speed of sound it is necessary to have exact information both about the travel time of a sound wave between the sound source and receiver and the distance between them. The more exact the information about the travel time and the path length between the sound source and receiver the more precisely is the determination of the meteorological parameters. From the travel time of a sound signal Laplace's sound speed c_{L} and therefore both the temperature T and the flow vector **v** can be determined by using reciprocal straight-lined sound paths and knowledge about the length of these paths.
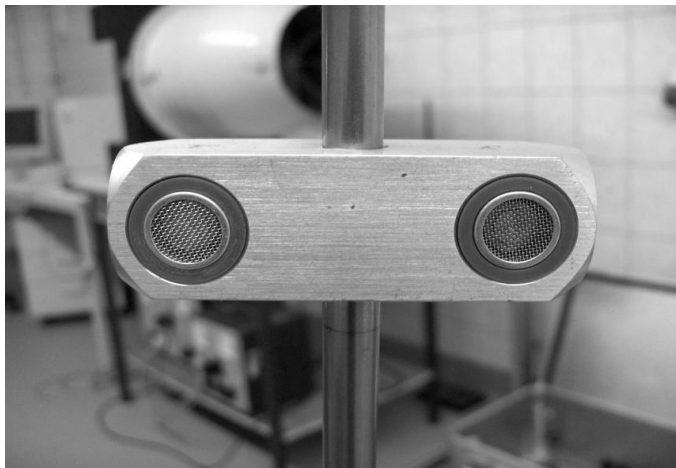
Fig. 3.1: Transmitter-receiver couple

3.1 Properties of the measuring instrument

The measuring equipment consists of a data logger with eight channels, a notebook and eight transmitter-receiver couples (Figure 3.1). The data logger is connected with the notebook, which contains a program to control the measurement and makes it possible to change a few measuring parameters. The measuring parameters which can be changed are the transmitting power and the trigger threshold of the signal. It is also possible to take the mean of the received travel times up to ten times automatically. The transmitter-receiver couples detect travel-times on bidirectional (reciprocal sound propagation can be assumed) ways at two different planes and between these two planes. They have a club-directional characteristic. An arrangement for the transmitter-
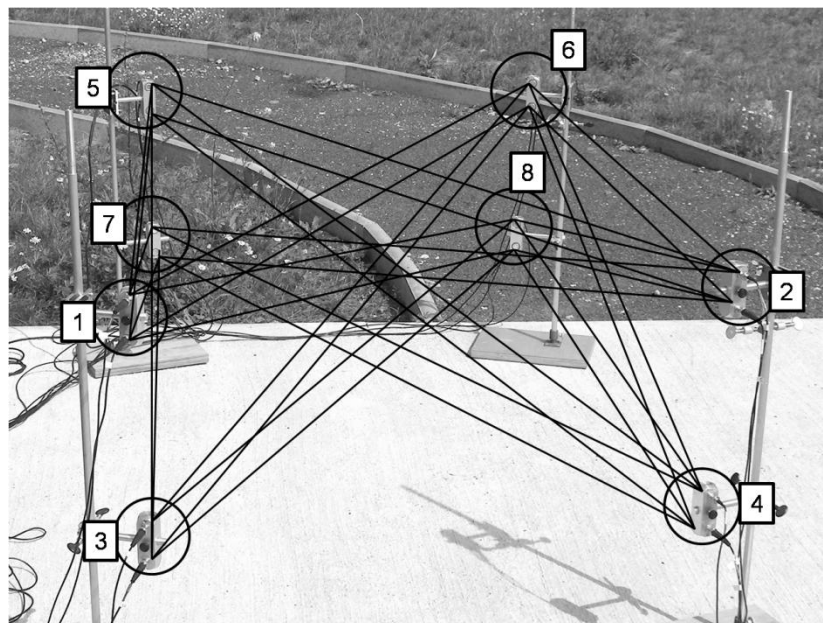
Fig. 3.2: Arrangement of the 8 transmitter and receiver couples

receiver couples is shown in figure 3.2. The transmitter-receiver couples number 1, 2, 3 and 4 always transmits respectively receives sound rays to/from the transmitter-receiver couples 5, 6, 7 and 8. The transmitting frequency is in the ultrasonic range and is 40 kHz ± 1 kHz. Therefore it is possible to detect the travel-times with a high temporal resolution. The current configuration of the measuring instrument detects one value of travel time every three seconds. It is also possible to get an average of ten values per three seconds.

3.2   Detection of the travel-time

The detection method of the travel-times is a so called "Start-Stop-Measurement". The electronic transmitting impulse is a sinus burst with five oscillations. One period has
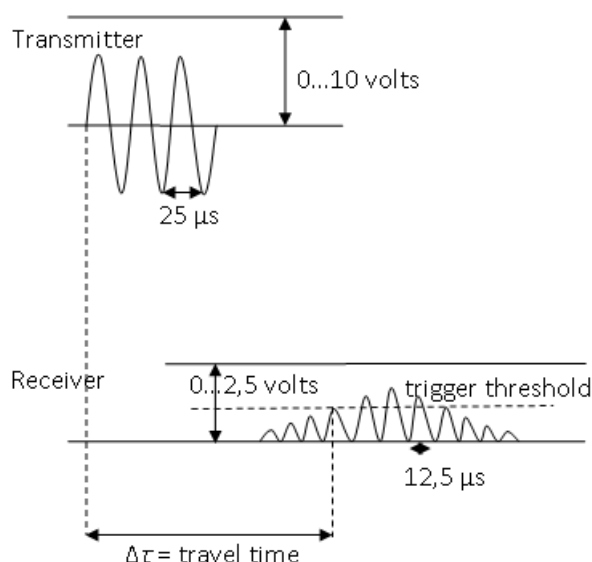
Fig. 3.3: Principle of the travel-time detection

25 µs. The wave peaks arriving at the receiver have, after filtering and rectification, an interval of 12.5 µs. The transmitting power can be set between 0 and 10 volts. There is a trigger-threshold at the receiver, which can be set between 0 and 2.5 volts. If a sinus burst is sending out, the travel-time begins to start. The measurement stops, when the first wave peak, which is higher than the trigger-threshold, is detected by the receiver. This period of time is the travel time (Figure 3.3). The order of the measurement is as follows: At first transmitter 1 sends a signal, which is received by receiver 5, 6, 7 and 8. Then transmitter 2 sends a signal to receiver 5, 6, 7 and 8, then 3 and 4 to 5, 6, 7 and 8. Afterwards transmitter 5 sends to receiver 1, 2, 3 and 4, then 6, 7 and 8 to 1, 2, 3 and 4. That gives 8·4 = 32 travel times. The travel time will be shorter for both if the trigger

threshold would be reduced, because the waves would be detected earlier and if the transmitting power would be raised, because the amplitudes of the waves would be higher and consequently the trigger threshold would be arrived earlier.

3.3   Measuring accuracy

The measuring accuracy depends in principle on the exactness in the determination of the distance and the travel time between a transmitter and receiver. The path length was determined with a ruler and the accuracy was assumed to $u(d) = 5$ mm. By the following equation

$$u_{\max}(Y) = \left|\frac{\partial Y}{\partial X_1}\right| u(X_1) + \cdots + \left|\frac{\partial Y}{\partial X_m}\right| u(X_m),\qquad (3.1)$$

by equation 2.2, with the precondition that there is no flow of air ($\mathbf{v} = 0$) and the assumption that the travel time has no error ($u(\tau_0) = 0$) the maximal error for the temperature results to

$$u_{\max}(T) = \left|2 \cdot \frac{d}{\tau_0{}^2 \cdot \gamma_{\mathrm{dry}} \cdot R_{\mathrm{dry}} \cdot (1 + 0.51 \cdot q)}\right| \cdot u(d).\qquad (3.2)$$

Here d means the path length between a transmitter and receiver, τ_0 is the travel time of the sound wave, γ_{dry} the ratio of the specific heat capacities for dry air, R_{dry} the specific gas constant for dry air and q the specific humidity. The resulting temperature inaccuracy is $u_{\max}(T) = \pm 1{,}5°C$ using a path length of 2 m and the following ambient conditions: $T = 20°C$, $p = 1000$ hPa and $r.h.$ (relative humidity) $= 70\,\%$.

The travel-time accuracy is closely connected to the error of the dead time of the system. There are two modes of dead time error.

The first one is the electronic dead time, which is an error that is based on processes inside the electronic system. This error is of the dimension of maximal 10 µs, but not exactly determinable, which corresponds to a temperature error of almost 1°C by a path length of 2 m and the same ambient conditions as mentioned above.

The second dead-time error takes place because the first wave peak, which arrives at the trigger threshold, is generally not by the first wave, which was transmitted by the transmitter and would represent the real travel time (Figure 3.3). This error ensues probable from a delayed oscillating phase and from the noise. But it has to be investigated further. Therefore a travel-time error of n phase shifts appears, which is in the range of $n \cdot 12.5$ µs and leads to a temperature error of $n \cdot 1.25°C$ by a path length of 2 m and the same ambient conditions as mentioned above. The problem is that it is not possible to find out which wave peak was detected; therefore it is impossible to determine the travel time with a satisfying accuracy. The resulting dead time error therefore is 10 ± $n \cdot 12.5$ µs. That matches a temperature error of $u_{\max}(T) = 1°C \pm n \cdot 1.25°C$.

The dead time error is a systematically error, which theoretically could be corrected with a measurement varying the path lengths between the transmitter and receiver and build a linear fit to get the dead time. The problem by changing the path lengths by a fixed setting for the transmitting power and the trigger threshold is that other wave peaks will always be detected. This would distort the measurement. For example, by changing the distance between transmitter and receiver from a higher to a lower length the receiver will detect the travel time one or more phase shifts before, because the amplitude which arrives the receiver is higher for shorter path lengths. Therefore this error cannot be corrected.
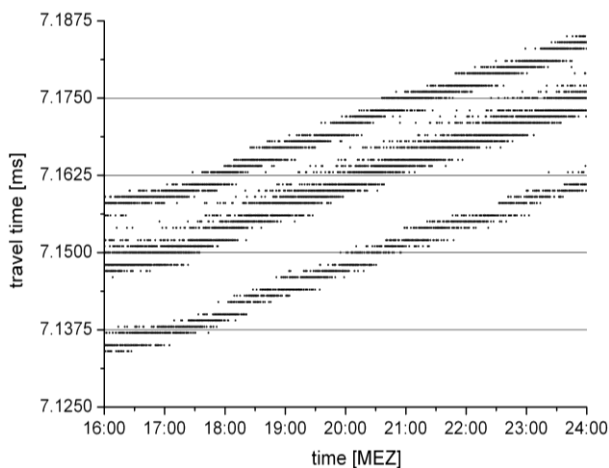
Fig. 3.4: Example for a travel-time measurement from transmitter 1 to receiver 6 (path 1_6). There are three phase shifts visible.
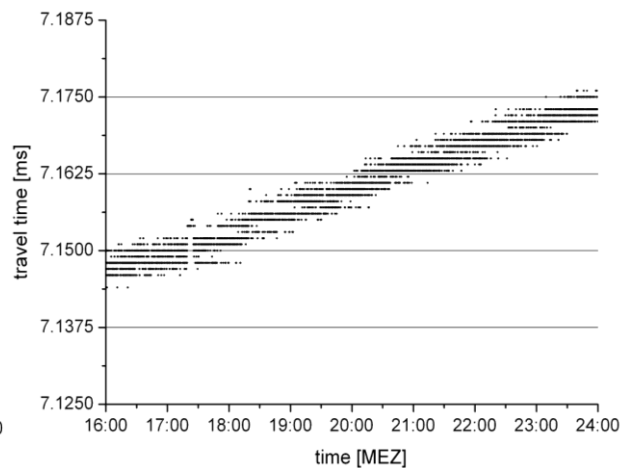
Fig. 3.5: The same travel-time measurement as shown in figure 3.4. The three phase shift beams are summarized to one.

The consequence of these unsatisfactory errors is to make relative measurements which require information about the temperature, the relative humidity, the air pressure (a constant value of 1000 hPa can be assumed) and the flow of air at a starting time. In a period of time, in which these measurements are constant and uniform, the effective speed of sound can be calculated by equation 2.2. With the assumption that $c_L = c_{eff}$ (**v** = 0) and the equation

$$c_{eff} = \frac{d}{\tau_0} <=> d = c_{eff} \cdot \tau_0 \qquad \textbf{(3.3)}$$

there can be new path lengths calculated, which deletes occurring path-length and travel-time errors. The variable d is the new path length and τ_0 is the measured travel time including the path-length and travel-time errors. The accuracy of the relative measurements is, of course, only so exact like the measurements from the parallel measurements of the temperature, the relative humidity and the air flow are.

Another problem that leads to an inaccuracy in the measurement is that there are several phase shifts for one measurement setting (transmitting-power and trigger-threshold). This problem is shown in figure 3.4. If there is no air flow it is possible to

summarize the phase shifts by adding and subtracting the several phase shift beams to one phase shift beam (Figure 3.5). If there is an air flow this procedure is impossible.

4   Results

The measurements represented here exemplarily were made in a room with no flow of air. Figure 4.1 shows the temperature of the acoustic measurement of path 1_6 (transmitter 1 to receiver 6) and the temperature of the humitter from VAISALA, which supplies parallel information about the temperature and the relative humidity, versus time. The dispersion of these both measurements is nearly the same and it seems to be possible to determine the temperature with an accuracy of 0.6°C.
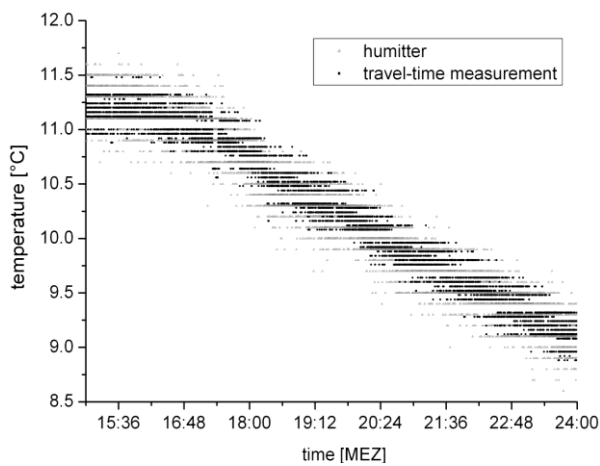
Fig. 4.1: Temperature of path 1_6 (black points) and temperature of the humitter (grey triangles) versus time.
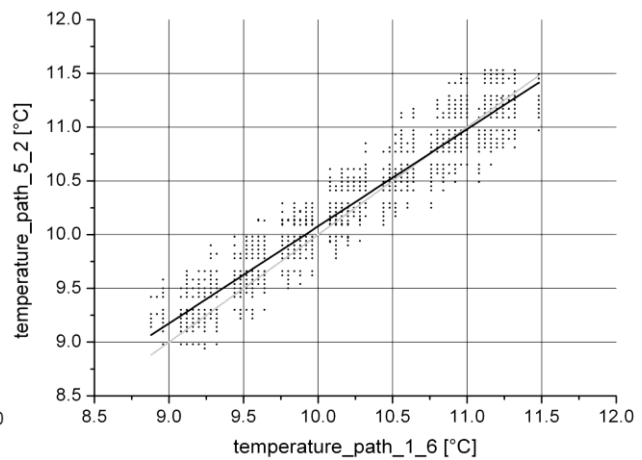
Fig. 4.2: Temperature of path 1_6 versus temperature of path 5_2 with a linear regression line (black line). The regression coefficient is $R^2 = 0.92$.

Therefore temperature oscillations greater 0.6°C should be detectable. Figure 4.2 shows the correlation between the acoustic measurement of path 1_6 and path 5_2. It shows a good correlation with a regression coefficient of $R^2 = 0.92$. In a room without air flow the value of v_{ray} should be zero, because the travel-times forward and backward should be the same for the same path length (Equation 2.5). Figure 4.3 shows such a case. The flow component in the direction of the sound ray v_{ray} of path 1_6_1 (forward path 1_6 and backward path 6_1) fluctuates here about maximal ± 10 cm/s around zero, which is adequately a good result. The sensitivity of this

Fig. 4.3: The flow component in the direction of the sound ray v_{ray} of path 1_6_1 versus time.

measurement method could be estimated about the dispersion to ~ 0.2 m/s.

The displayed results provided up to now were all in absence of the flow of air. If a wind velocity greater zero exists, the phase shift beams, seen in figure 3.4, are not distinguishable. Consequently it is not possible to use the same procedure for the temperature analysis (see figures 3.4 and 3.5). Thus the results for the wind component along ray path and therefore for the resulting wind vector are unsatisfactory, as seen in figure 4.4. The figure shows a measurement in a wind channel. A directional-independent thermo-anemometer was used to evaluate the acoustic measurement by comparing the results. In the first minutes there were no flow of air and four phase shift beams can be seen (see figure 4.4). After the wind channel was switched on (from 11:38 – 13:00 with a constant voltage and from

Fig. 4.4: Wind channel measurement: black dots show the acoustic measurement of path 2_6_2 and grey triangles show the measurement of an anemometer to have a comparison. The voltage values of the wind channel were constant from both 11:38 – 13:00 and 13:00 – 14:25.

13:00 – 14:25 with a higher constant voltage) no more phase shift beams can be seen, so it is impossible attributing the high dispersive values to values with lower dispersion. But the right tendency of the wind vector in comparison with the anemometer measuring can be seen. This shows that this method could work with a satisfying accuracy if there would be no phase shifts in the travel-time detection.

5   Conclusions

As shown in chapter 4 it is possible to determine the temperature and flow component in the direction of the sound ray v_{ray} with a good accuracy if there is no flow of air. The temperature T has an accuracy of 0.6°C (figure 4.1), which is in the range of the accuracy of the humitter, and v_{ray} has an accuracy of ~ 0.2 m/s (figure 4.3). The problems are the several phase shift beams which occur at the measurements. If the wind velocity is greater zero the phase shift beams cannot be corrected. Therefore it must be the aim to change the measuring instrument in such a way that the phase shifts won't occur any more. Where the changes in the electronic system have to follow exactly is not sure yet, it has to be tested and investigated further. Another expansion of the measuring equipment could be a higher temporal resolution like the display of 10 values of the travel-time per three seconds without averaging. A possible application of this method is a flow balance measurement of incoming and outcoming flow of gases, e.g. by windows or over areas of lysimeters. By a high temporal

resolution of the temperature and wind field it could be also possible to solve micro-scale turbulence in the atmosphere.

Acknowledgements

References

Arnold, K., Ziemann, A., Raabe, A. and Spindler, G., 2003: Acoustic tomography and conventional meteorological measurements over heterogeneous surfaces. Meteorol. Atmos. Phys. 85, 175-186

Barth, M.:2009: Akustische Tomographie zur zeitgleichen Erfassung von Temperatur- und Strömungsfeldern. Wissenschaftliche Mitteilungen, Institute of Meteorology from the Universiy of Leipzig, Volume 44

Barth, M., Raabe A., Arnold, K., Resagk, C. and du Puits, R., 2007: Flow field detection using acoustic travel time tomography. Meteorologische Zeitschrift, Vol. 16, No. 4, 443-450

Holstein, P., Raabe, A., Müller, R., Barth, M., Mackenzie, D. and Starke, E., 2004: Acoustic tomography on the basis of travel-time measurement. Meas. Sci. Technol. 15, 1420–1428

Holton, J. R., 2004: An Introduction to Dynamic Meteorology. Fourth Edition. Elsevier Academic Press, 535 S.

Ostashev, V. E., 1997: Acoustics in Moving Inhomogeneous Media. E & FN Spon, London, Weinheim, New York, Melbourne, Madras, 259 S.

Pierce, A. D., 1994: Acoustics – An Introduction to Its Physical Principles and Applications. Published by the Acoustical Society of America through the American Institute of Physics, 678 S.

Raabe, A., Arnold, K., Ziemann, A., Beyrich, F., Leps, J.-P., Bange, J., Zittel, P., Spiess, T., Foken, T., Göckede, M., Schröter, M., and Raasch, S., 2005: STINHO – Structure of turbulent transport under homogeneous surface consitions – part 1: The micro-α scale field experiment. Meteorologische Zeitschrift, Vol. 14, No. 3, 315-327

Tetzlaff, G., Arnold, K., Raabe, A. and Ziemann, A., 2002: Observations of area averaged near-surface wind- and temperature-fields in real terrain using acoustic travel time tomography. Meteorologische Zeitschrift, Vol. 11, No. 4, 273-283

Wang, S., Boulard, T., Haxaire, R., 1999: Air speed profiles in a naturally ventilated greenhouse with a tomato crop. Agricultural and Forest Meteorology 96, S. 181-188

Comparison of wind measurements between a Mini-SODAR PA0, a METEK-SODAR and a 99 m tower

K. Louca, A. Stadler, A. Raabe, A. Ziemann

ABSTRACT

Doppler-SODAR measurements are commonly used to derive the vertical wind profile. One main advantage of the Mini-SODAR (from the company Remtech) is its small size and weight and therefore it is easy to handle and set up in short time. Two long-term measurements were operated in September and October 2009. A statistical comparison was made between the Mini-SODAR, the tower and the DWD-SODAR (from the company METEK) for the two measurement periods. It is presented here that the Mini-SODAR overestimates the tower measurements and also the measurements of the DWD-SODAR. It is also shown, that the Mini-SODAR is able to determine the mean flow conditions in the lower boundary layer (up to 200 m).

1. INTRODUCTION

For the understanding and the research of the planetary boundary layer it is necessary to provide a validated knowledge about the flow and stratification characteristics of the lower atmosphere (up to 1000 m). Therefore the SODAR (**SO**nic **D**etecting **A**nd **R**anging) as an acoustic remote sensing method is a reasonable entrancement of the conventional measurements of the wind vector with a tower. In the SODAR method, pulses of audible sound are emitted into the atmosphere by an antenna. They get scattered on turbulent structures in the atmosphere and the backscattered signals are received by the same antenna (monostatic SODAR) or by a second antenna (bistatic SODAR). Just a fraction of the emitted sound energy is detected. The SODAR instrument allows measurements of the wind components and their standard deviation as a function of height.

First applications of SODAR systems started in the early 1970s (Kallistratova and Coulter, 2004) but the theoretical background about the turbulent scattering of sound were done in the 1940s by Obukhov (1941) and Kolmogorov (1941) and in the late 1950s and the early 1960s by Kallistratova (1959 and 1961), Tatarskii (1961) and Monin (1969). While the first SODAR gadgets just received the backscattered sound intensity to determine the thermal stratification, the development of SODAR systems leads to Doppler-SODAR and multi-frequency SODAR systems.

Details of the principles and the signal analysis are given by VDI (1994) and Bradley (2008).

SODAR systems are used for the investigation of the meso-scale and micro-scale flows and wind systems as well as turbulent and wave-like structures under stable and unstable conditions.

There are some intercomparisons between SODAR and tower measurements (e.g. Reitebuch, 1999, Vogt and Thomas, 1994) or even between two SODAR systems (e.g. Vogt and Thomas (1994)) which can be found in the literature. Some authors, e.g. Bradley et al. (2005), were engaged with the calibration of SODAR systems and their sources of error.

Recently, Pietschmann (2007) operates some first short test-measurements at the boundary layer field site Falkenberg that belongs to the Meteorological Observatory Lindenberg of the German Weather Service and concentrates on the features given by the Remtech Mini-SODAR. The question of the performance of a long-term measurement with the SODAR and therefore the comparison with measurements of the tower and the DWD-SODAR is still unknown and shall be investigated here.

2.   SETUP AND MEASUREMENT PRINCIPLE OF THE MINI-SODAR PA0

The Mini-SODAR PA0 of the French company Remtech is a monostatic system with an antenna size of 0.4 x 0.4 m^2. Because of the antenna weight of only 12 kg (including supporting equipment) it offers a high agility and it is built up in a short time. After the installation it is important to determine the azimuth angle α (angle against north clockwise).

The PA0 consists of a phased-array antenna with 52 loudspeakers. It features a 5-beam system with one beam aimed vertically the other four beams are inclined with an angle $\theta = 30°$ and their azimuth angles are 90° apart.

The signal of the PA0 consists of several frequencies. During one pulse duration it emits up to nine different frequencies between 600 Hz and 18 kHz. Thereby the most frequent frequency is 3.5 kHz. Because of the use of several frequencies the detection of the backscattering signal out of the background noise is much easier according to the manufacturer Remtech.

In addition to the main system (antenna) there exists a sound protection which is lined with an absorbing material. This sound protection, with a height of 1.60 m, reduces fixed echoes (reflection of sound on fixed obstacles, e.g. houses or trees) and also serves as a noise protection for the environment. The acoustic power of the PA0 is 1 W and the manufacturer offers an average vertical range under typical conditions of 600 m. It operates over the power network (20 V) or with the help of batteries (12 V).

After emitting a sound pulse, the monostatic SODAR switches into the receive mode to detect the backscattering signal from the atmosphere. Thereby the Doppler spectrum (it shows the spectral power against the frequency) is recorded. From this the Doppler parameters are calculated: (i) the backscattering amplitude A, (ii) the shift in frequency Δf_d and (iii) the width of the Doppler spectrum σ_f. The shift in frequency is the result of the so called Doppler effect (which is just mentioned here; for more information see Bradley, 2008 and Pierce, 1989). The radial wind velocity (v_{rad}) along one sound beam can be determined with the help of the Doppler effect:

$$v_{rad} = \frac{c}{2} \frac{\Delta f_d}{f_0} .$$
(1)

In Equation (1) c is the speed of sound, f_0 is the emitted frequency and Δf_d is the shift in the Doppler frequency. A positive (negative) radial wind velocity means that the scattering volume moves toward (away from) the antenna. With the help of the width of the Doppler spectrum, it is possible to achieve the standard deviation of the radial wind. In nature the speed of sound depends on the temperature. But in practice the SODAR uses a constant surface value. This leads to a systematic error in determining the radial wind velocity and the height of the backscattering volume.

3.   DESCRIPTION OF MEASURING FIELD AND INSTRUMENTS

The measurements took place at the boundary layer field site (in German: Grenzschichtmessfeld, GM) Falkenberg which is controlled by the Richard-Aßmann Observatory - Meteorological Observatory Lindenberg (RAO-MOL) of the German Meteorological Service (in German: Deutscher Wetterdienst, DWD). The GM (Figure 1) is located 5 km to the south of the MOL near the village Falkenberg in the north-east of Germany (52° 10' N and 14° 07' E, 73m above sea level). It was established as a central base point for field studies of land surface and boundary layer processes (Neisser et al., 2002). The terrain around the GM is flat and slightly slanted from NNE towards SSW with hight differences of less than 5 m over a distance of about 1 km. The surrounding area of the GM is dominated by forests and agricultural fields (more than 40% each) and the rest of the area is covered by lakes, traffic roads and villages (Beyrich and Mengelkamp, 2006). For more information see also Neisser et al. (2002) and Beyrich and Foken (2005).

The DWD operates a 99 m tower and a SODAR-system of the type METEK DSDPA.90-64 on the GM. The tower is equipped with three crossarms mounted at each level pointing towards S, W and N. The wind sensors are mounted on each of the three crossarms at the heights of 10, 20, 40, 60, 80 and 98 m in order to ensure that there is always at least one sensor not influenced from the structure of the tower (Neisser et al., 2002). The SODAR-system is a monostatic phased-array antenna (like

the Mini-SODAR PA0) with an array aperture of 1 x 1 m^2. It works with a 5-beam system and transmits a single frequency of 1598 Hz. For more details see Engelbart et al. (1999).

The Mini-SODAR was build up in the middle of the connecting line between the
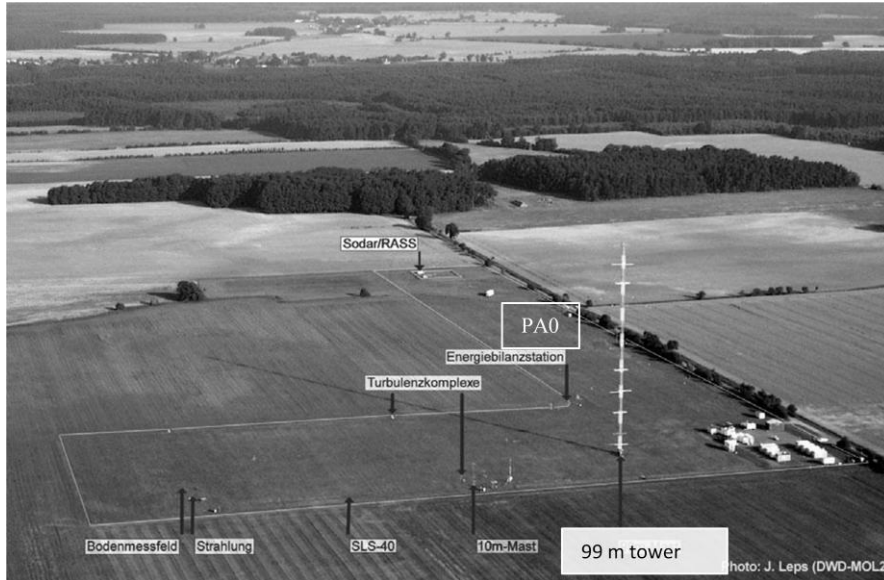
Figure 1: *Boundary layer field site Falkenberg, modified from [Beyrich and Foken, 2005].*

DWD-SODAR and the tower (see Figure 1) during two measurement periods. The Mini-SODAR was directed to the north ($\alpha = 0°$), so that one beam was vertically directed and two beams were directed to the north and to the west with a zenith angle of $\theta = 30°$. There were some small trees and bushes along a country road in the northern direction. But the distance between these obstacles and the Mini-SODAR was big enough (~ 50 m) to avoid strong fixed echoes. During both measuring periods the sound protection of the manufacturing company REMTECH was used.

The settings of the Mini-SODAR were tried to match with the settings of the DWD-SODAR and the tower (see Table 1).

Parameter	Mini-SODAR	DWD-SODAR	Tower
Averaging period	10 min	15 min	10 min
Minimum height	20 m	40 m	10 m
Thickness of each gate	20 m	20 m	20 m
Maximum height	880 m	700 m	98 m

Table 1: *Comparison of the settings between DWD-SODAR, Mini-SODAR and the tower.*

4. INTERCOMPARISON OF DATA

The Mini-SODAR was operated at the GM Falkenberg during two measurement periods. The first period took place from the 7th September to 16th September 2009. For a direct comparison, the SODAR and the tower data are plotted versus the time. An example of the wind speed and direction at 100 m agl on the 14th September 2009 are given in Figures 2.
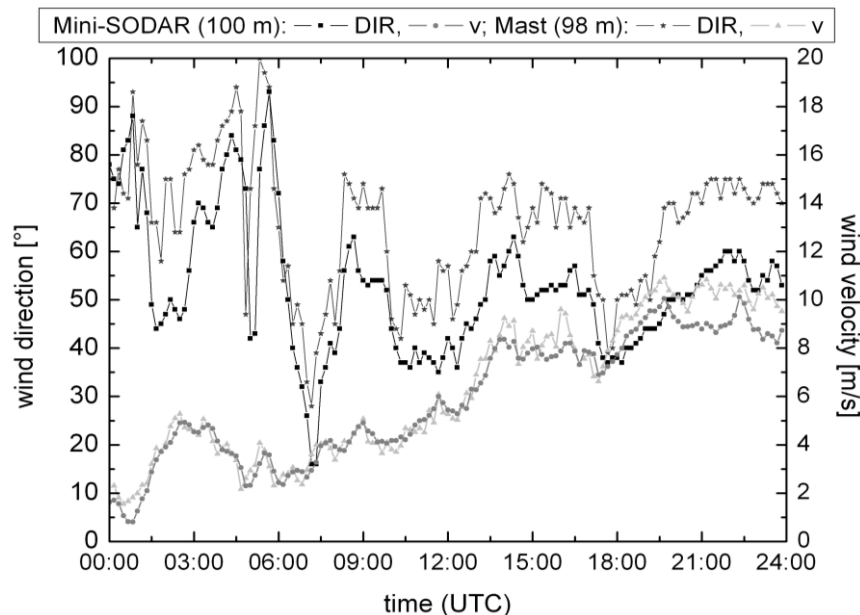
Figure 2: *Comparison of wind direction (DIR) and the horizontal wind velocity (v) between the Mini-SODAR (black square, grey dot) and the tower (dark star, triangle) for the 14.09.2009 at a height of 100 m altitude; the averaging time was 10 min.*

The following conclusions can be drawn from the time series:

(1) The wind speed measured by both instruments is well comparable. The temporal behavior of the wind speed is shown by both instruments in a similar manner. In the second half of the day the discrepancies between the tower and the Mini-SODAR become greater.

(2) The wind directions measured with both instruments are not well comparable. Both instruments represent a similar time behavior but the tower measures wind directions with a difference of about 10-15° compared to the Mini-SODAR. A probably reason for this discrepancy could be due to uncertainties in the orientation of the Mini-SODAR and the accuracy of the SODAR itself.

The scatter diagrams of the horizontal wind velocity of the tower and the SODAR data are represented in Figures 3 for two different heights (20 m, left panel and 100 m, right panel) over the whole first measurement period. The dashed lines of these diagrams represent the perfect fit lines and the black lines represent the linear regression lines. Figure 3 (left panel) clearly shows that the Mini-SODAR overestimates the wind speed of the tower at the 20 m level. In contrast the Mini-SODAR results in Figure 3 (right panel) underestimates the wind velocity for wind speeds less than 3 m/s and for wind speeds more than 8 m/s. For wind speeds more than 3 m/s and less than 8 m/s the Mini-SODAR overestimates the wind speed a little.

Figure 3: *Correlation between Mini-SODAR (20 m) and tower (20 m) (left panel) and between the Mini-SODAR (100 m) and the tower (98 m) (right panel) for the period 7.09. – 16.9.2009 regarding the horizontal wind velocity.*

For the second measurement period at the GM Falkenberg the data of the DWD-SODAR were additionally available. For a direct comparison, the Mini-SODAR, the DWD-SODAR and the tower data are plotted versus the time. Examples of the wind speed and direction at 100 m agl on the 22nd October 2009 are given in Figure 4. Following conclusions can be drawn:
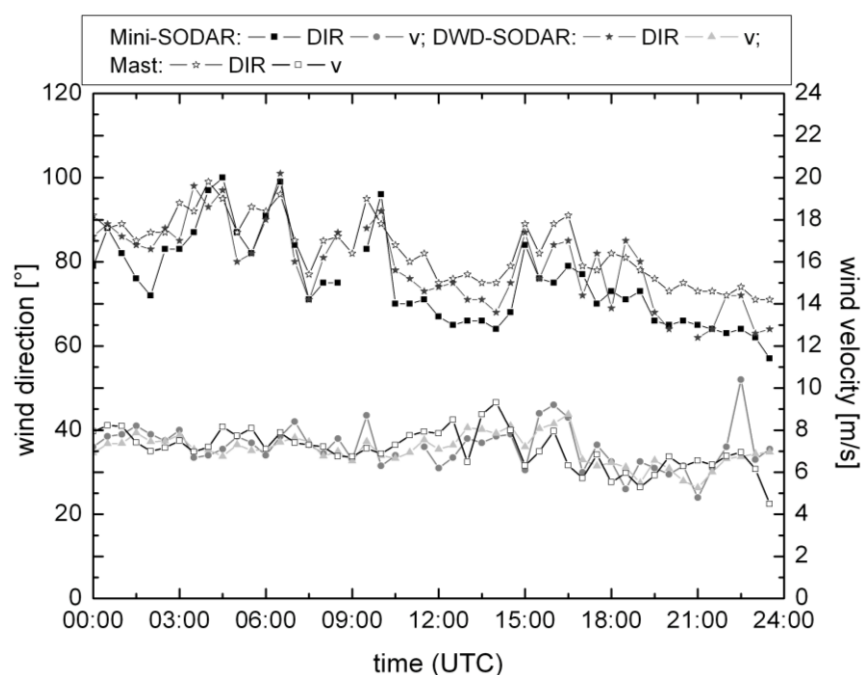
Figure 4: *Comparison of wind direction (DIR) and the horizontal wind velocity (v) between Mini-SODAR (black square, diamond), DWD-SODAR (black star, triangle) and tower (white star, white square) for the 22.10.2009 in a height of 100 m altitude. Values of each hour and half hour are plotted.*

(1) The wind speed measured by all three instruments is well comparable. The temporal behavior of the wind speed is shown by all three instruments in a similar manner.

(2) The wind directions measured with all three instruments are also well comparable. But in the second half of the day the DWD-SODAR data fluctuates a bit more then the Mini-SODAR data.
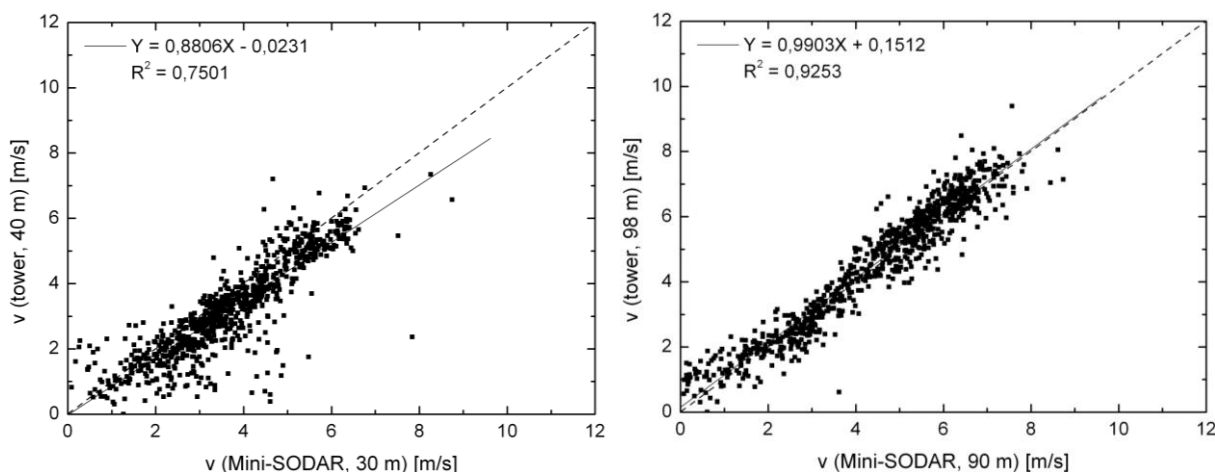
Figure 5: *Correlation between Mini-SODAR (30 m) and tower (40 m) (left panel) and between the Mini-SODAR (90 m) and the tower (98 m) (right panel) for the period 23.09. – 29.10.2009 regarding the horizontal wind velocity.*

The scatter diagrams of the horizontal wind velocity of the tower and the SODAR data are represented in Figures 5 for two different heights (40 m and 100 m) over the whole second measurement period. The dashed lines of these diagrams represent again the perfect fit lines and the black lines represent the linear regression lines. It must be stated that in Figure 5 the tower level of 40 m (98 m) agl is plotted versus the 30 m (90 m) level of the Mini-SODAR data. This is because the settings (minimum height: 30 m) of the Mini-SODAR were changed. Figure 5 (left panel) show that the data of the lower levels of the Mini-SODAR overestimates the tower data. While the data of the higher level (Figure 5 right panel) show an adequate agreement between the two systems.

For the second measurement period the data sets of the horizontal wind velocity of the three instruments were averaged for the time of 23.10. to 29.10.2009 up to an altitude of 110 m. These three vertical profiles are plotted in Figure 6. The vertical gradients of the wind velocity measured by the DWD-SODAR and the Mini-SODAR are not well comparable. There are greater discrepancies for lower altitudes and these discrepancies get less up to 100 m. But over the whole vertical profile the Mini-SODAR measures a higher wind velocity then the DWD-SODAR. Also the tower measures a higher wind

Figure 6: *Vertical profile of the horizontal wind velocity of the Mini-SODAR, the DWD-SODAR and the tower for the period 23. – 29.10.2009.*

velocity over the whole vertical profile then the DWD-SODAR. The wind velocity

measured by the tower and the Mini-SODAR is in good accordance for higher altitudes. But for lower altitudes the Mini-SODAR measures higher wind speeds then the tower. For a statistical comparison between the three instruments see the section about the *BIAS* and Tables 2 and 3.

To see how comparable the measurements of the two SODAR systems are, Figure 7 shows a plot of the vertical profiles of the wind velocity up to an altitude of 510 m.
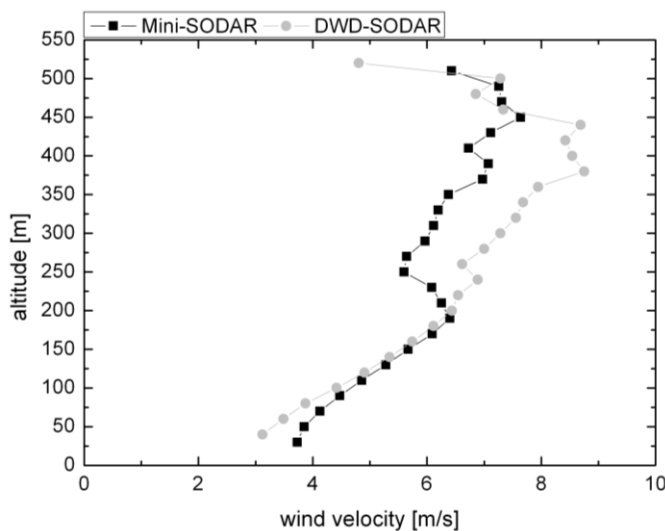
Figure 7: *Vertical profile of the horizontal wind velocity of the Mini-SODAR and the DWD-SODAR for the period 23. – 29.10.2009.*

These profiles were averaged over the time from 23.10. to 29.10.2009. Up to an altitude of 60 m agl there are little discrepancies between these two systems. But above 60 m up to 200 m there is an adequate accordance between the two SODAR systems. In the next range gate between 200 m and 450 m there is a big difference between both systems. The reason for this is not clear up to now. Furthermore there is a good accordance between both measurements for the altitudes from 450 m up to 510 m.

The systematic deviation *BIAS* is calculated to compare the three different data sets. The *BIAS* is the difference between the mean values of the Mini-SODAR and the tower data and can be expressed by the Equation (2) and also the standard deviation (Equation (4)) of *BIAS* the is calculated.

$$BIAS = \frac{1}{n}\sum_{i=1}^{n}(Y_i - X_i) = \hat{Y} - \hat{X} \tag{2}$$

$$\sigma_{BIAS}^2 = \frac{1}{n-1}\sum_{i=1}^{n}\left[(Y_i - X_i) - \frac{1}{n}\sum_{i=1}^{n}(Y_i - X_i)\right]^2 \tag{3}$$

$$STD = \sqrt{\sigma_{BIAS}^2} \tag{4}$$

In this Equation (2 and 3) the Mini-SODAR data are indicated by Y_i, whereas X_i presents the data of the tower. The fact that this comparison is done between two different measurement methods and each of them got his own uncertainties, the true *BIAS* will not be equal zero.

Horizontal wind [m/s] /Height	20 m	40 m	60 m	80 m	98 m/100 m
BIAS	0.99	0.37	0.01	-0.09	-0.08
STD	1,00	0,63	0,59	0,67	0,68

Table 2: *Summary of the statistical parameter BIAS and the standard deviation for the comparison of the horizontal windspeed [m/s] between the tower and the Mini-SODAR for the first measurement period (08.09.-14.09.2009).*

The *BIAS* between measurements of the tower and measurements of the Mini-SODAR in the first period regarding the horizontal wind velocity is listed in Table 2. It is noticeable that for heights up to 60 m the *BIAS* is positive which means that the Mini-SODAR detect higher wind speeds then the tower. This is differs from the theory and therefore some other factors must be relevant. Bradley et al. (2005) listed some possible factors for the uncertainties in the measurements with a SODAR: (1) an inexact horizontal orientation of the Mini-SODAR, (2) uncorrected effects of the temperature (influence of the temperature field on the sound path through the atmosphere) and (3) turbulent widening of the beam because of multiple scattering. For the two higher altitudes the *BIAS* is negative which is consistent with the theory.

The Table 3 shows the *BIAS* for the comparison between the three measurement systems for the second measurement period. There is a positive systematic deviation for all altitudes up to 100 m. Possible reasons were already discussed. It should be mentioned that there is a difference ($\Delta h = 10\,m$) between the heights which are compared because of a little rearrangement in the settings of the Mini-SODAR. But it can be seen that the systematic deviation decreases with height. This could be because of the fact that the mechanical turbulence decreases with height and therefore the measurement over a volume with a SODAR might be more precise.

The comparison between the tower and the DWD-SODAR leads to a negative *BIAS* which is consistent with the above mentioned reasons and be caused by the effect of "overspeeding",

Horizontal wind [m/s] / Height	20 m	40 m	60 m	80 m	98 m/100 m
BIAS Mini-S. (*Y*) vs. tower (*X*)	0.89	0.57	0.29	0.24	0.23
STD	-	0,83	0,62	0,45	0,46
BIAS DWD-S. (*Y*) vs. tower (*X*)	-	-0.36	-0.42	-0.35	-0.24
STD	-	1,71	1,34	0,59	0,87
BIAS Mini-S. (*Y*) vs. DWD-S. (*X*)	-	0.93	0.72	0.59	0.47
STD	-	1,93	1,49	0,70	0,93

Table 3: *Summary of the statistical parameter BIAS for the comparison between the tower, the Mini-SODAR and the DWD-SODAR for the second measurement period (23.10.-29.10.2009).*

through to none filtering of fixed echoes or because of differences in the averaging method.

The third comparison is provided between the Mini-SODAR and the DWD-SODAR. The first two comparisons have shown that the Mini-SODAR overestimates the measurements of the tower and the DWD-SODAR underestimates the tower measurements regarding to the horizontal wind velocity. Thus a larger deviation results between the two SODAR systems.

For the first measurement period these overestimation of the tower measurement was only found in altitudes of 80 m and 100 m. In the altitudes of 20 m to 60 m the SODAR measurement overestimates the wind velocity. In the second measurement period the Mini-SODAR overestimates the tower measurement over all altitudes. The comparison between the DWD-SODAR and the tower leads to a negative *BIAS*. This implies an overestimation of the wind velocity by the tower. It is noticeable that the *BIAS* between the systems decreases with height.

The systematic deviation is also calculated with regard to the wind direction. The *BIAS* between the Mini-SODAR and the tower for the first period showed that the values of the Mini-SODAR deviate from the values of the tower with an absolute value of about 7° (in an altitude of 40 m agl) and 9.8° (in an altitude of 100 m/98 agl). The deviation between these two instruments is for the second period half as much as for the first period. The absolute value of about 3.5° is in an acceptable range. A reason for the differences of both periods could be due an inexact orientation to the north ($\alpha \neq 0°$). It was tried that the installation in both periods was the same but it was not possible to orientate it exactly the same.

The comparison between the tower and the DWD-SODAR leads to much better systematic deviations then the comparison between the tower and the Mini-SODAR. The deviation of an absolute value of less than 1° is negligible.

The third comparison for the second period was provided between the two SODAR systems. In an altitude of 100 m the absolute value of the deviation is comparable with the deviation between the tower and the Mini-SODAR. Just in an altitude of 40 m the deviation is a bit greater for the comparison between the two SODAR systems than between the tower and the Mini-SODAR.

5. CONCLUSION AND OUTLOOK

The comparisons during the first measurement period resulted in an overestimation in the wind velocity of the Mini-SODAR in the lower altitudes up to 60 m and to an overestimation by the tower measurements in the higher altitudes of 80 m and 100 m. The comparison between the tower and the Mini-SODAR leads to an overestimation

of the horizontal wind velocity by the Mini-SODAR during the second measurement period. Possible reasons are not clear yet. The difference between the Mini-SODAR and the DWD-SODAR is greater because the DWD-SODAR underestimated the horizontal wind velocity compared to the tower. But the measurements of the Mini-SODAR are quite comparable with the tower measurements for the heights from 60 m up to 100 m ($BIAS$ of 0.2 – 0.3 ms^{-1}). The measurement with the Mini-SODAR is in adequate agreement with the measurement of the DWD-SODAR for a range gate from 60 m up to 200 m. The comparisons between the Mini-SODAR and the DWD-SODAR above an altitude of 500 m are possible but the reliability of the results is limited due to the weak data availability. The data availability amounts nearly 70 % at a height of 330 m. Furthermore, the data availability of the Mini-SODAR decreases distinctively for height levels above 400 m. Therefore it is not very useful to compare these two systems above 500 m.

It is not possible to get inside of the software of the Mini-SODAR to customize the SODAR to different environmental conditions. Nevertheless it is possible to get an overview about the mean flow conditions for the lowest 60 m to 200 m of the planetary boundary layer.

In further work the dependence of the data availability of the Mini-SODAR on the stratification will be investigated. There will be also investigations about the development of low-level jet events, the development of the stable boundary layer and a possible connection between these two atmospheric phenomenons.

ACKNOWLEDGEMENTS

REFERENCES

Beyrich, F. and Foken, T., 2005: *Untersuchung von Landoberflächen- und Grenzschicht-Prozessen am Meteorologischen Observatorium Lindenberg*, Promet **31**, Nr.2-4, 148-158.

Beyrich, F. and Mengelkamp, H.-T., 2006: *Evaporation over a heterogeneous land surface: EVA_GRIPS and the LITFASS-2003 experiment – an overview*, Boundary-Layer Meteorol. **121**, 5-32.

Bradley, S., 2008: *Atmospheric acoustic remote sensing*, CRC Press, Boca Raton, 271 S.

Bradley, S., Antoniou, I., von Hünerbein, S., Kindler, D., de Noord, M. and Jørgensen, H., 2005: *SODAR calibration for wind energy applications*, final reporting on WP3, EU WISE project NNE5-2001-297, Salford, 70 S.

Engelbart, D., Steinhagen, H., Görsdorf, U., Neisser, J., Kirtzel, H. J. and Peters, G., 1999: *First Results of Measurements with a Newly-Designed Phased-Array Sodar with RASS*, Meteorol. Atmos. Phys. **71**, 61-68.

Kallistratova, M. A., 1959: *An experimental investigation in the scattering of sound in turbulent atmosphere* (in Russisch), Doklady Akademii Nauk SSSR **125**, 69-72.

Kallistratova, M. A., 1961: *Experimental investigation of sound wave scattering in the atmosphere* (in Russisch), Tr. Inst. Fiz. Atmos., Atmos. Turbulentnost **4**, 203-256.

Kallistratova, M. A. and Coulter, R. L., 2004: *Application of SODARs in the study and monitoring of the environment*, Meteorol. Atmos. Phys. **85**, Nr. 1-3, 21-37.

Kolmogorov, A. N., 1941: *The local structure of turbulence in incompressible viscous fluid for very large Reynolds numbers*, Doklady Akademii Nauk SSSR **30**, 301-305.
Monin, A. S., 1962: *On the Scattering of Sound in a Turbulent Medium*, Sov. Phys. Acoustics **7**, 370-373.

Obukhov, A. M., 1941: *Scattering of sound in turbulent flow* (in Russisch), Doklady Akademii Nauk SSSR **30**, 611-614.

Neisser, J., Adam, W., Beyrich, F., Leiterer, U. and Steinhagen, H., 2002: *Atmospheric boundary layer monitoring at the Meteorological Observatory Lindenberg as part of the "Lindenberg Column": Facilities and selected results*, Meteorol. Zeitschrift, Vol. **11**, Nr. 4, 241-253.

Pierce, A. D., 1989: *Acoustics – An Introduction to its Physical Principles and Applications*, Acoustical Society of America (2. Auflage), Melville, NY, 678 S.

Pietschmann, K., 2007: *Anwendung eines Multi-Frequenz Mini-SODARs zur hochaufgelösten Untersuchung der atmosphärischen Grenzschicht*, Diplomarbeit Inst. für Meteorol. Univ. Leipzig, 91 pp.

Reitebuch, O., 1999: *SODAR-Signalverarbeitung von Einzelimpulsen zur Bestimmung hochaufgelöster Windprofile*, Schriftenreihe des Institut für Atmosphärische Umweltforschung, Garmisch-Partenkirchen, Vol. **62**, 175 pp. (Available from: Shaker Verlag GmbH, Postfach 1290, D-52013 Aachen, ISBN: 3-8265-6208-9).

Tatarskii, V. I., 1961: *Wave Propagation in a Turbulent Medium*, McGraw-Hill Book Company, New York, 163 pp.

Verein Deutscher Ingenieure (VDI), 1994: *Determination of the Vertical Wind Profile by Doppler SODAR Systems*, VDI Richtlinie **3786**, Part 11.

Vogt, S. and Thomas, P., 1994: *Test of a Phased Array Sodar by Intercomparison with Tower Data*, J. Atmos. Oceanic Technol. **11**, 94-102.

Comparison of a Backscatter LIDAR during LICL 2009

Jörg Walter, Marlene Brückner

1   Summary

In May 2009 the European Aerosol Research Lidar Network (EARLINET) started an intercomparison campaign took place in Leipzig, Germany. The main objective was to compare the mobile Earlinet-LIDARs to have characteristically reference systems and to ensure permanent qualitative Measurements. To test the LIDAR of the Leipziger Institute for Meteorology (LIM) measurements during the comparison time periods were performed and compared to two EARLINET – LIDARs. The main objective was to compare the range-corrected total signal as well as backscatter and extinction coefficients to get information of the accuracy of the system for further independent measurements in the future. It will be shown that the ALS300 is able to achieve results which are in agreement to other lidar systems. However the deviation to the other Lidars depends strongly on the background radiation so that there is a smaller deviation of the mean signal during nighttime measurements then daytime measurements.

2   Introduction

As a relatively young remote sensing technique LIDAR (LIght Detection And Ranging) showed its potential investigating different atmospheric components e.g. cloud particles, aerosol or molecules as well as wind profiles (Doppler LIDAR) and temperature profiles (Raman LIDAR). Among these applications optical properties like extinction and backscatter coefficient can be identified for cloud particles and aerosol. The thermodynamic phase (liquid water/ice) can also be described by polarization lidars. With high temporal and spatial resolution as well as the possibility of high range coverage from the ground up to 100 km LIDAR became an attractive tool for atmospheric research. Several meteorological phenomena such as frontal passages were studied via lidar but also the climate effect of aerosol as well as emission rates were monitored. Therefore a verification of the results achieved by the lidar is essential for further independent measurements.

3   Measurements

The LIDAR used during the campaign were the Leosphere ALS300 with an additional polarization channel. In the following there will be a short introduction to basic LIDAR theory as well as a description of the ALS300.

3.1   LIDAR principal and equation

LIDAR is an active remote sensing technique which uses the scattering of electro-magnetic waves in the atmosphere. The LIDAR principle is similar to RADAR with use of a different segment of the electro-magnetic spectrum. In general most LIDAR systems use wavelengths from UV to NIR, commonly with 355nm, 532nm and 1064nm due to limitations by laser manufacturer.

A lidar system consist of a receiving and transmitting unit. The transmitting unit consists of a laser emitting monochromatic and coherent light. The receiving unit consists of a telescope which collects the incoming (backscattered) light and a detector that counts the incoming photons. Through the runtime of the laser pulse and the speed of light the distance between the LIDAR and the scattering volume can be calculated by

$$z = \frac{tc}{2}.$$

The received power from a range z for elastic backscattering at the emission wavelength λ can be described by the LIDAR equation

$$P(z, \lambda) = P_0 \frac{O(z)}{z^2} C_S(\lambda) \beta(z, \lambda) exp\left[2 \int_0^z \alpha(z, \lambda) dr\right].$$

With the emitted power P_0, the overlap function O(z), a height-independent constant $C_S(\lambda)$, the backscatter coefficient $\beta(z, \lambda)$ and the extinction coefficient $\alpha(z, \lambda)$. The overlap function describes the overlap between the laser beam and the receivers field of view. Close to the LIDAR there is no overlap and the function become zero. The height were a complete overlap is achieved and O(z) become 1 differs between a few tens of meters to several thousands of meters depending on the lidar system. The height-independent constant $C_S(\lambda)$ includes information about the lidar system itself as detector efficiency and telescope size. The backscatter coefficient $\beta(z, \lambda)$ has the dimension $m^{-1}sr^{-1}$. The exponential term describes the extinction of light by scattering and absorption and has the dimension m^{-1}. The coefficients for backscatter and extinction can be split into a molecular and a particle part:

$$\alpha = \alpha_{mol} + \alpha_{par}$$

and

$$\beta = \beta_{mol} + \beta_{par}.$$

3.2   Leosphere ALS300

Figure 1: The ALS300 on the roof of the IfT

The Leosphere ALS300 is an elastic backscatter LIDAR with an additional channel for detection of perpendicular light. The emitted wavelength of 355nm is achieved by a frequency-tripled Nd:YAG laser. The emitted light pulses have an energy of 16 mJ and a repetition rate of 20 Hz with a divergence of the laser beam of 0.25 mrad. The telescope collecting the backscattered light has a diameter of 150 mm. Therefore a complete overlap is achieved between 150 m and 200 m. For the acquisition of the incoming signal both analogue-to-digital-converter and photomultiplier can be used separately or together.

A scanning device is also part of the setup for azimuthal and zenithal alignment of the ALS300. The scanning device can not only be used just to angle the lidar but also for vertical, horizontal and volume scanning. During the campaign a zenithal angle of 3° was chosen because of the near range to the roof of the IfT.

4   Results and discussion

In May 2009 an intercomparison took place within the scope of the EARLINET program on the Institute for Tropospheric Research (Ift) in Leipzig. Beside various participants the LIM with the EZ Lidar ALS300 also took part in the campaign. The aim of this comparison was to check the measuring results from the LIM lidar relating to total signal, particle backscatter and particle extinction coefficients, so that reasonable and independent results are possible with this device in future.

All participants have measured parallel 24-hours under different atmospheric conditions. Afterwards the achieved results were directly compared and evaluated, so that possible corrections could be carried out in the system setting immediately. The main interest of the LIM lidar working group was the comparison of the uncorrected total signal at $\lambda = 355$ nm wavelength. The minute values for the appropriate period were averaged and depicted with a height resolution of 60 m. Whereas the LIM lidar detects in two channels, parallel and perpendicular polarized to the plane of polarization of the power transmitted, the total signal must be formed first. Because the sensitivity of both channels is different, however, the addition of both components to gain the total signal delivers no sensible results. Hence, a detection ratio c that puts both channels in relation must be determined first. This can be obtained from the depolarization ratio δ :

$$\delta(R) = c \frac{P_\perp(R)}{P_\parallel(R)} .$$

This results from the ratio of perpendicularly polarized to parallel polarized transmitted power at a distance R. The detection ratio can be determined on the supposition that the depolarization rate amounts to 1.5% in clear air by molecular depolarization in the suitable height area. This relation could be specified in the course of the work to $0.02 \ldots 0.04$. The detection ratio makes only a small contribution to the determination of the total signal, as well as the calculation of the particle backscatter and extinction coefficients. The influence of this correction factor on the depolarization profiles is of high relevance and must be examined more exactly in future.

Figure 2 shows the range corrected total signal in the near field for a clear sky day profile from the 13th of May 2009.
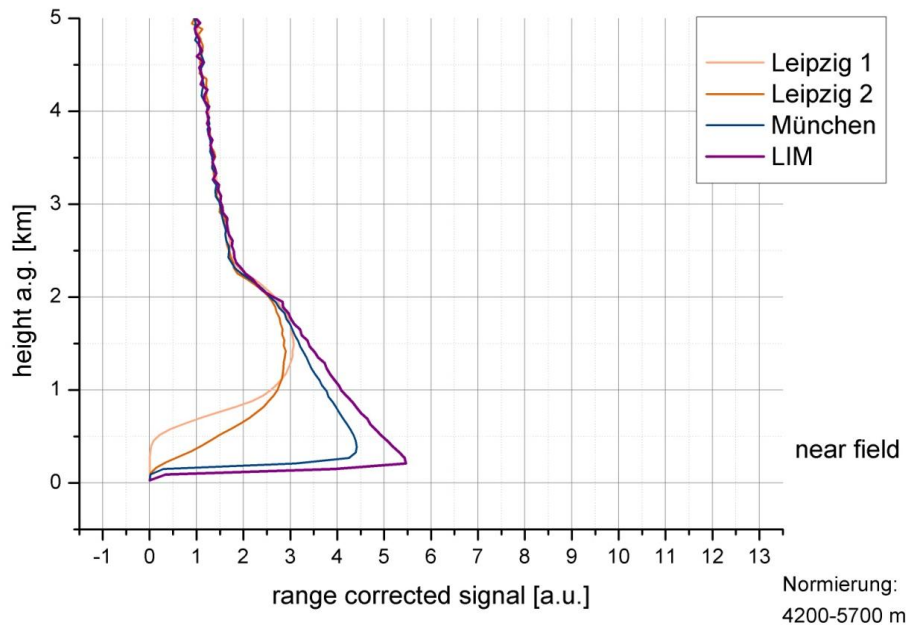
Figure 2: *normalized range corrected total signal at 355 nm for near field on 13.05.2009 13:45-14:15 MESZ*

The signals were multiplied with their respective height square ($X(R) = P(R)R^2$) and normalized in an area of clear air. These are only uncorrected signals, in other words the here necessary overlap correction is absent, which enabled a more exact representation of the atmospheric boundary layer in the lower range.

The Raman lidar (Leipzig 1,2) receives the backscattered signals with large far range telescopes and afterwards the transmitting photons are detected by photo counting. This countable manner is suited particularly for measurements over large distances, because also weak signals (single photons) can be detected. Both the Raman lidar Munich (POLIS) and the LIM lidar use in each case a small near range telescope as well as both countable manners in photo count and analog mode. The latter is suited mostly for short distance measurements if intensive signals (a lot of background light) must be detected. On account of these facts the obvious differences arise in the lower range. In Figure 3 the matching far field up to 20 km height of this measurement is shown.
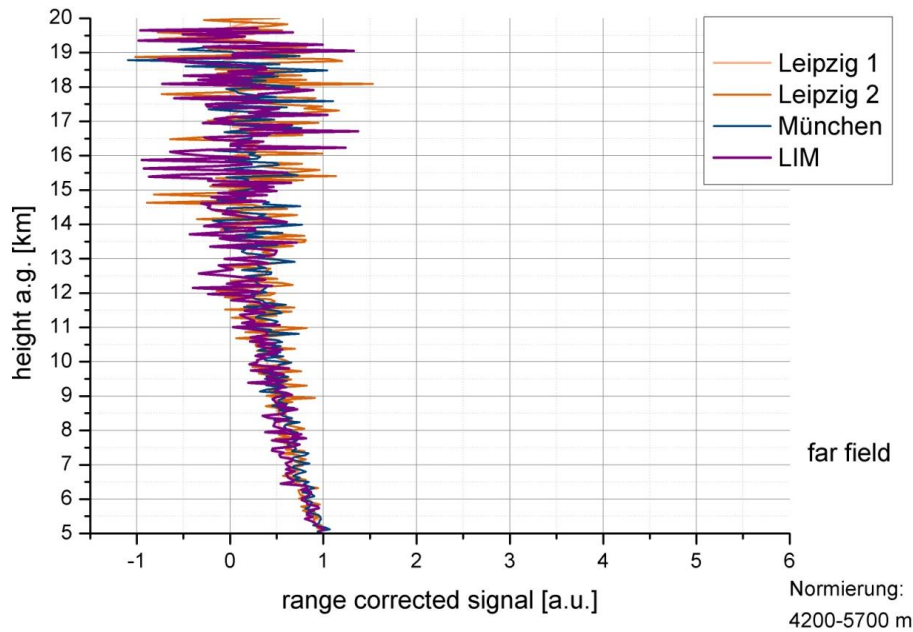
Figure 3: *normalized range corrected total signal at 355 nm for far field on 13.05.2009 13:45-14:15 MESZ*

Because there is particularly in the daytime a lot of background radiation it is difficult to detect still single photons from the upper range. Hence, in this range there is a lot of signal noise so that the signals connect with large error values. This is also shows the relative deviation from mean total signal at $\lambda = 355$ *nm* (figure 4a, b). For better illustration the signals were averaged in different bin-ranges to avoid data noise (see table 1).

Additionally binned		
from	to	bin
[m]	[m]	[m]
0	4000	60
4000	13000	600
13000	20000	1200

Table1: *bin-averaging 13.05.2009 13:45-14:15MESZ*

In the upper part of the atmosphere the relative deviation amounts >30% (see figure 4b) based on the weak signals which leads to large fluctuations of the calculated particle backscatter coefficients around zero. The obvious deviations of the mean total signal arise below 2 km (see figure 4a) because the suitable overlap correction is absent and different system configurations were used. Good agreement can be found in the range between 2 and 10 km with values <15%. Reasonable results can be expected from particle backscatter and particle extinction profiles in this range.
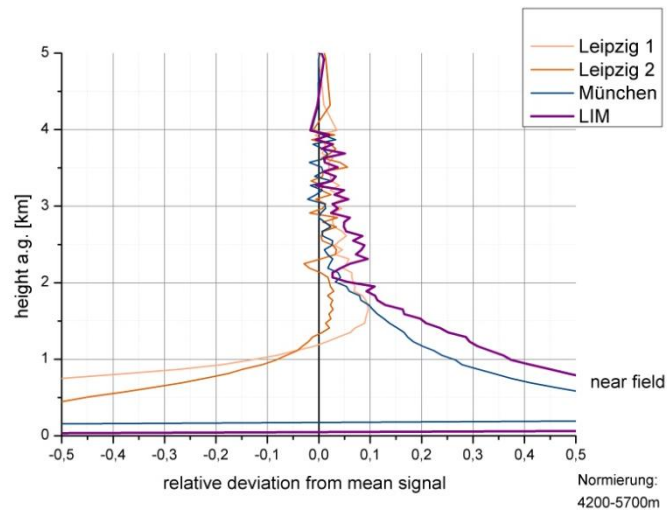
(a)
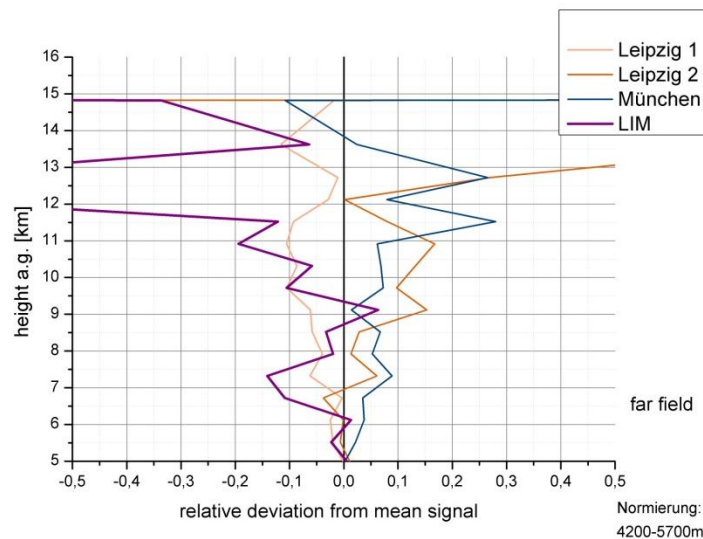
(b)

Figure 4: *relative deviation from the mean total signal at 355 nm from 13.05.2009 13:45-14:15 MESZ, (a) near field, (b) far field*

Better results can be reached by nighttime if only sparsely background light exists. The Raman channels of the other lidars can be operated only at night and achieve best results in photo counting mode. Figure 5 shows the range corrected total signal of a night measurement from the 25th of May 2009 where the normalization was chosen in the range from 4 to 6 km.
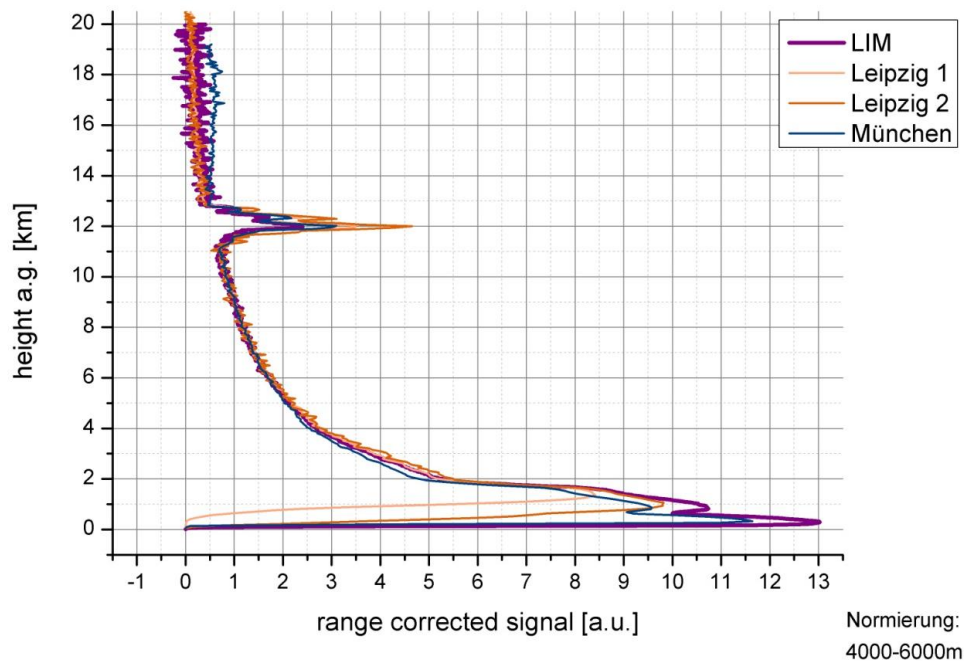
Figure 4: *normalized range corrected total signal at 355 nm on 25.05.2009 21:15-22:30 MESZ*

At night or in the evening hours the atmospheric boundary layer is trained more stable. That results the clearly increased backscatter values in the low range. Furthermore the differences in the total signal arise below 1,5 km on account of the already mentioned different receiver telescopes as well as the missing overlap correction. Because of the weak background radiation the signal noise in the upper height range is clearly less whereas the Raman lidars achieve better results as the LIM elastic backscatter lidar. In the range between 11 and 13 km all appliances shows increased backscatter values. The LIM lidar shows lower values in comparison to the other lidars. The cloud base or top height of cirrus clouds can still be clearly recognized what matters in view of later parameter setting in the evaluating algorithm. The good agreement of the signals was also reflected in the consideration of relative deviations from the mean total signal which is shown in figure 6. Except the lower uncorrected range (below 1,5 km) the deviation is less than ~10%. In the range of clear air (excluding molecular backscattering (Rayleigh scattering)) from 3 to 11 km it is ~3%, so that here the particle backscatter coefficients can be determined later without large errors. Sensible results are expected for the cirrus because the deviations are within the given limits of >20% (Bösenberg et al. 2003). In contrast to the measurement during daytime (see figure 4b), one still receives results in the upper part of the atmosphere through less signal noise. Admittedly another bin-averaging was chosen (see table 2), the values still stay in an acceptably limit.

Additionally binned		
from	to	bin
[m]	[m]	[m]
0	2500	60
2500	13000	240
13000	20000	1800

Table 2: *bin-averaging 25.05.2009 21:15-22:30 MESZ*

Starting point for a determination of the optical parameters is a reliable total signal, because large fluctuations also affect the particle backscatter and extinction coefficients accordingly. The intercomparison with some EARLINET members has shown that the LIM lidar can achieve reasonable results. In spite of the different delicacy of both channels the deviations from mean total signal remain in a suitable limit. It will be possible to make independent measurements with the lidar in the future. The best results were achieved during nighttime when the influence of the background radiation is weaker and insists a good agreement of the total signal. But also the measurements during daytime indicate that the lidar is suitable for the observation of the lower layers of the atmosphere as well.

5. Outlook

The comparison of the LIMs ALS300 with other lidar-systems showed good conformity especially for lower layers as well as for nighttime measurements. The intercomparison showed also problems with the polarization channels were strong background radiation results in non-conformities of the depolarization ratio. This is known by Leosphere and will be solved in the first half of 2010. Afterwards there will be a new compare of depolarization ratios with the Polly XT of the IfT. On a second step a combination of the ALS300 with radiance detector head is planned. Beneath the optical properties by lidar, e.g. extinction and backscatter coefficient, microphysical properties will be retrieved for convective clouds by screening their vertical profile.

6. References

Bösenberg, J., Matthias V., 2003:EARLINET: A European Aerosol Research Lidar Network to Establish an Aerosol Climatology. MPI-Report No. 348, S. 16-22.

Tesche, M., 2006: Optische und mikrophysikalische Charakterisierung anthropogener Partikel in Südchina (Pearl River Delta) und Nordchina (Peking) anhand von Ramanlidar- und Sonnenphotometermessungen. Diplomarbeit Universität Leipzig, 91 S.

Pätzold, Th., 2008: Wolkenmessung mit dem mobilen Lidar. Diplomarbeit Universität Leipzig, 63 S.

Sassen, K., 2005: Polarization in Lidar, In: Weitkamp, C. (Hrsg.): LIDAR: Range–Resolved Optical Remote Sensing of the Atmosphere. Springer series in optical sciences (2005), S. 19-42

Wandinger, U., 2005: Introduction to Lidar, In: Weitkamp, C. (Hrsg.): LIDAR: Range–Resolved Optical Remote Sensing of the Atmosphere. Springer series in optical sciences (2005), S. 1-18.

Werner, Ch., Streicher, J., Leike, I., Müncke, Ch., 2005: Visibility and Cloud Lidar, In: Weitkamp, C. (Hrsg.): LIDAR: Range–Resolved Optical Remote Sensing of the Atmosphere. Springer series in optical sciences (2005), S. 165-185.

EJECTION AND IMPACT ANGLES OF SALTATING PARTICLES MEASURED WITH A HIGH-SPEED CAMERA

M. Raddatz, H.-J. Schönfeldt

ABSTRACT

3D and 2D trajectory data of sand grains saltating over a bed are presented from high-speed camera measurements. They were obtained at Zingst peninsula and in laboratory using a wind tunnel. Trajectories, calculated with a Runge-Kutta procedure, using values of the mean wind profile and the air flow were fitted to the measured ones. The trajectory with the lowest RMSE against the measured one was used to estimate the grain diameter of the saltating grain. Also ejection and impact angle, ejection and impact speed of the grain were determined. The results confirm earlier findings that ejection angles decreases with increasing grain diameter. Ejection angles between 57° and 27° for fine (63-200 µm) and middle (200-630 µm) ejecta and between 38° and 20° for coarse grains (630-2000 µm) were found. The impact angle β increases with increasing grain diameter. Impact angles between 8° and 15° for fine impactors and between 12° and 36° for middle and coarse grains were found. Additionally the ratio between the mean ejection angle α and mean impact angle β, which decrease with increasing grain diameter (Rice et al., 1995), could be confirmed. The ration between the ejection speed u_e and impact speed u_i was found nearly the same for all determined grain sizes, but the grains ejected from the bed had an average speed of one order of magnitude less than the impact speed.

1. INTRODUCTION

Desertification is a major problem connected with the global climate. Grassland worldwide desolates into dry land or even deserts because of overgrazing, wrong fertilization and irrigation. Also commercial logging is a problem because the lost shading of the trees will increase evaporation of the soil. The structure of the soil gets porous. At this stage it is easy for wind and rain to blow off and wash out surface particles. Understanding the appearance of desertification it is crucial to conceive the basic mechanisms of sand transport. Dust emission generated by wind erosion is by far the largest source of aerosols which directly or indirectly influence the atmospheric radiation balance and hence global climatic variations (Shao, 2000). The Taklimakan desert in central Asia is extending faster than any other desert in the world. Hyper arid climate conditions and strong winds in the eastern part of the desert accelerate the rambling of the dunes (Laity, 2008). According to the UNCCD (*United Nations Convention to Combat Desertification*) office there are 110 countries and over one billion people threatened by desertification worldwide.

2. EXPERIMENTAL SETUP AND METHOD

Measurements of moving particles over a surface were done by several researchers like Willetts and Rice (1995), Anderson and Haff (1988, 1991), McEwan and Willetts (1993) and Rioual et al. (2000). They also used high-speed cameras but they only recorded trajectories from the grains in two dimensions. For our measurements a stand with a special mirror, a swiveling holder with 20 white LED´s and a clamp for the high-speed camera were constructed. This setup allows to measure trajectories in three dimensions. Figure 1 shows the setup which was used in the measurements at the

beach on Zingst peninsula. During the measurements the plate and the battery were moved a little bit side wards so that they do not disturb the air flow. The purpose of the experiments was to measure trajectories from moving grains, preferential saltating, creeping and reptating grains under natural conditions. Therefore the test area was not "cleaned". On the windward side of the measurement array there were smaller and bigger shells, some seaweed, and

Figure 1: *Setup used at the beach in Zingst, including a plate to shield the horizon, the stand with the mirror, the swiveling holder with the LED´s and the high-speed camera. A plastic body for smoothing the air flow is fitted in front of the stand.*

footsteps from tourists and sometimes sand ripples which can trigger saltation. Before starting recording high-speed movies the camera (SANYO Xacti 1010) had to be set up. The time of the video sequence was set to 10 seconds with 300 frames per second. In this mode the resolution of the video lasts 448×336 pixel. The focal point was set to 10 cm because of the dimensions of the stand. Aperture and ISO value were adjusted automatically. The zoom was changed to +1.5 to get an adequate acuity of the saltating grains. With all these adjustments a square with 1×1 mm equals a square with 7×7 pixel. Knowing this the computer program was able to convert every pixel value into a metric value. A chart including our measurement configuration was made with a CAD (*Computer Aided Design*) program. The imaginary rays from the camera and the rays from a virtual camera behind the mirror to the selected grain are shown in Figure 2. The marked bead (red dot) and the imaginary rays (black lines) are labeled with the expressions used in the program for calculating the position of the grain. Availing the virtual camera it was easier to form the three equations (Eq. 1-3) for calculating the position of the grain.

$$z = \frac{x_b \cdot y_s \cdot z_{cam}}{(x_s \cdot z_{cam} + x_b \cdot y_s)} \qquad x = \frac{x_s \cdot z}{y_s} \qquad y = \frac{y_b \cdot x}{x_b}$$

Eq. 1-3
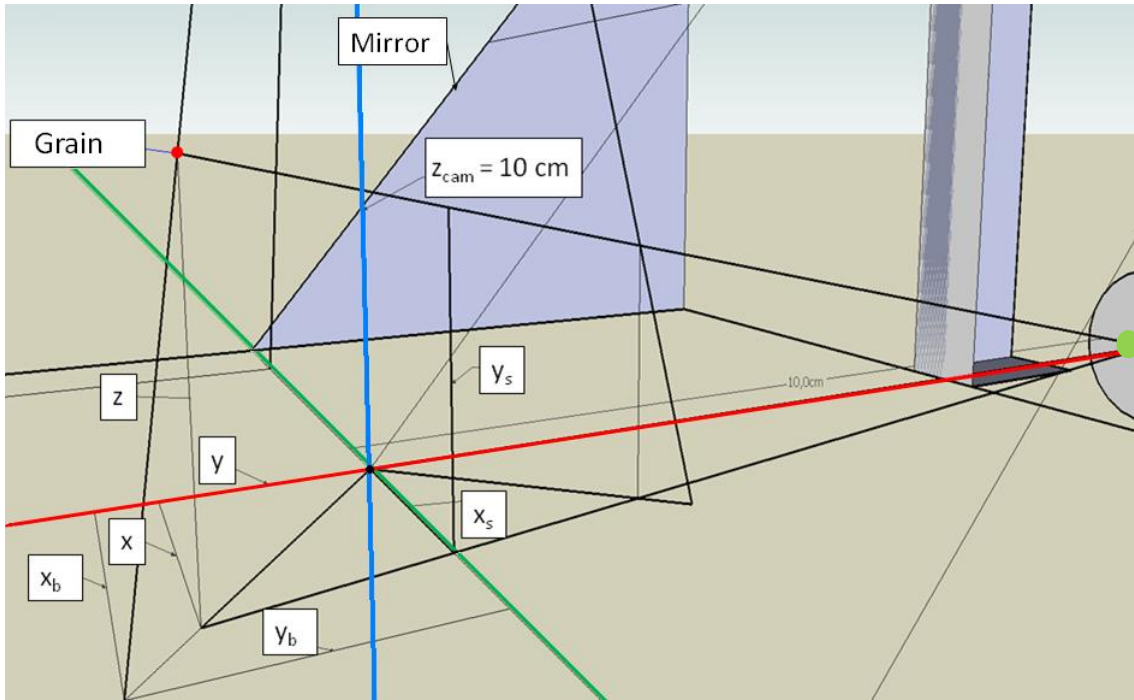
Figure 2: *CAD chart with the marked grain (red dot) and the imaginary rays (black lines) from the camera to the grain and from a virtual camera (green dot) behind the mirror to the grain. The green line symbolizes the x-axis, the red line the y-axis and the blue line the z-axis. The labeled expressions were used in the program for calculating the position of the grain.*

The whole geometry of the measurement array is very complex. Figure 3 illustrates a blueprint of the light path for better demonstration of the coherence between the grain (red dot), the camera, the mirror (blue triangle) and the virtual camera (green dot). In the upper part of the picture there is an upright projection of the configuration and in the lower part there is shown the plan view. As seen in Figure 1 a plate had to be build, to shield the horizon and to create a good contrast between the bright saltating grains and the background.
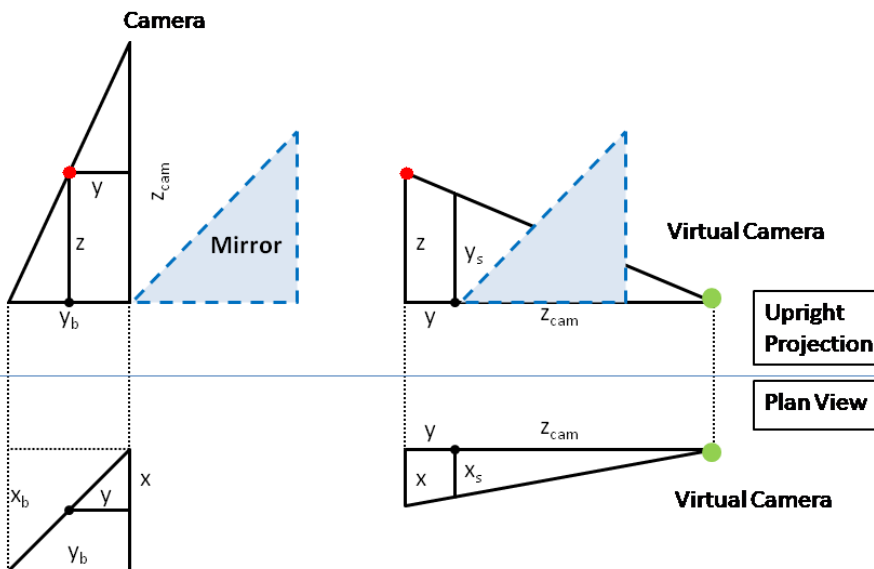
Figure 3: *Blueprint of the light path for better demonstration of the coherence between the grain (red dot), the camera and the mirror (blue triangle. It also shows the importance of the virtual camera (green dot) for forming the equations 1-3.*

Figure 4 shows a typical collision and resulting trajectory of a saltating grain. This chart also explains what is meant by a trajectory. The grain ejected by collision leaves the surface with a speed, u_e and an ejection angle α and approaches the bed with a speed, u_i and an impact angle β. Because of the non smooth trajectories of the recorded grains a Runge-Kutta procedure was included in the evaluation program. Adjusting measured values of the trajectory which are defective

Figure 4: *Typical trajectory of saltating grains. The grain ejected by collision leaves the bed with a speed, u_e, and an angle α and approaches the bed with a speed, u_i, and an angel β.*

and scattered around the correct value the Runge-Kutta procedure calculates theoretical trajectories for 41 before given grain diameters and selects the one with the lowest RMSE (*Root Mean Square Error*) comparing to the measured trajectory. The trajectory with the lowest RMSE was then printed against the measured trajectory and symbolizes now the smooth path of the real saltating grain, see Figure 5. This procedure was done to all measured trajectories from the campaign as well as to the trajectories measured in the laboratory. Additionally, the output of the RMSE for each calculated trajectory with changed grain diameter allows an inference on the grain size of the saltating grain.
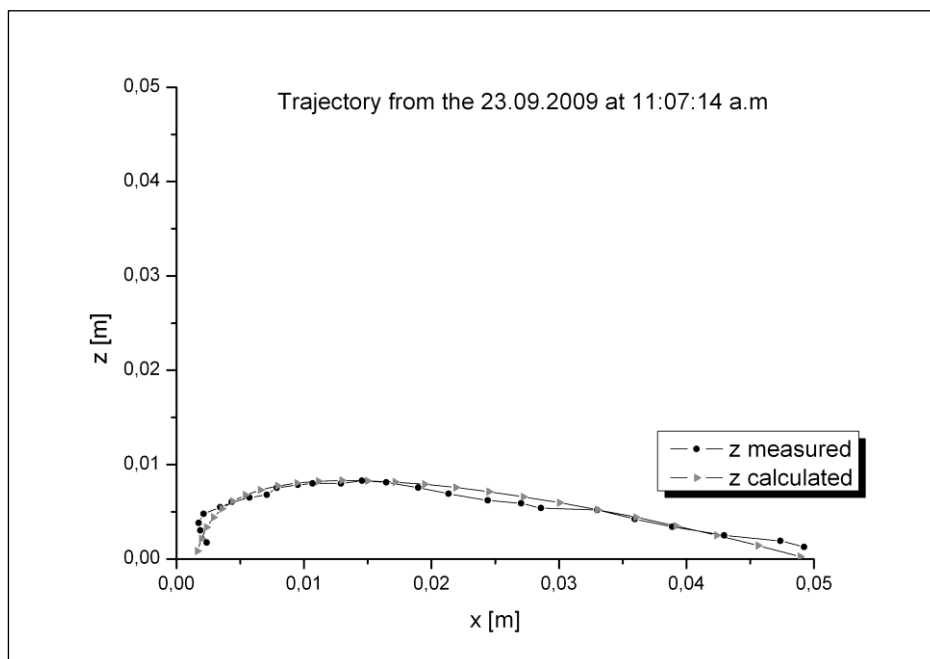
Figure 5: *Measured trajectory (dots) and the numerically approximated trajectory (triangle) with the lowest RMSE compared to the measured one.*

3. MEASUREMENTS AND DATA INTERPRETATION

First test measurements were done in the laboratory to evaluate the capabilities of the 3D trajectory analysis. Therefore a wind tunnel with a diameter of 0.5 m was used. A thin layer of sand, from the beach of Zingst peninsula, was put on a table after we installed the stand with the camera.

In September 2009 there was a campaign in Zingst at the Baltic Sea. The aim of the campaign was to record as much data as possible at the beach under natural conditions. More than 300 videos were recorded in these two weeks. Additional to the video measurements of the saltating grains a wind mast with three cup anemometers, in heights of 0.2, 1.0 and 2.0 m, was build to reconstruct the wind profile. Also an ultrasonic anemometer (*USA*) was arranged at the surface to recognize the wind direction, wind speed and also for comparing the values with the cup anemometers. Problematic were the fast changing cloudiness from clear sky to total clouded. These different illumination conditions are seen in Figure 6, and had effects on the visibility of the grains in the mirror and also over the surface.

Therefore a classification was made: 1. shady surface / mirror irradiated by the sun; 2. cloudy surface and mirror and 3. sunny surface / mirror irradiated by the sun.
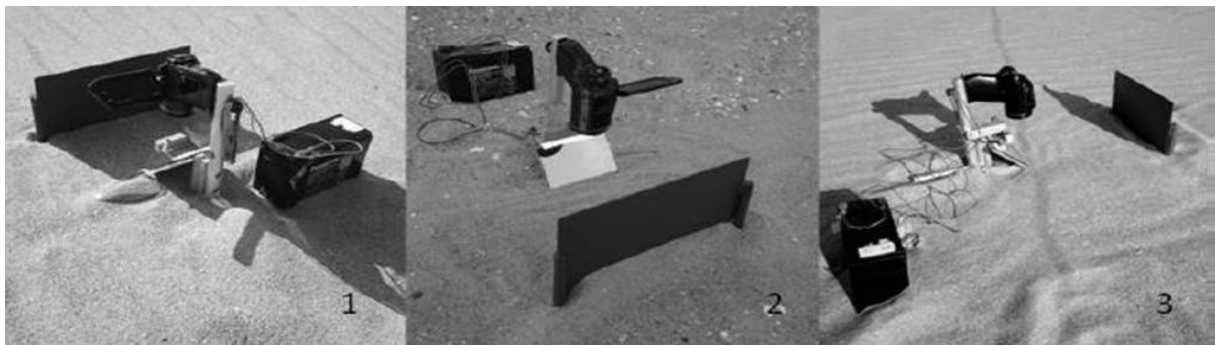
Figure 6: *Different illumination conditions at the beach of Zingst. (1) shady surface / mirror irradiated by the sun; (2) cloudy surface and mirror; (3) sunny surface / mirror irradiated by the sun.*

The best and rich in contrast movies were recorded when the sun was at the zenith and the whole surface was well illuminated (3) and therefore all edges got very sharp even the grains. Also good movies were logged when the sky was totally clouded and the surface got shady (2).

4. RESULTS

For evaluation 100 representative trajectories were selected. Ejection angles typically decrease with increasing grain diameter. The results show ejection angles between 57° and 27° for fine (63-200 µm) and middle (200-630 µm) ejecta and between 38° and 20° for coarse grains (630-2000 µm). The impact angle β increases with increasing grain diameter. Impact angles between 8° and 15° for fine impactors and between 12° and 36° for middle and coarse grains were found. Mean values of the ejection and impact angle, for all 100 trajectories, are shown in Figure 7. The values for grain sizes over 500 µm had to be handled with care, because there was only one trajectory recorded for each grain size. Therefore, significant information could only be made for smaller grain diameter. Figure 8 shows the mean ejection and impact angle for grain sizes between 140 and 280 µm.
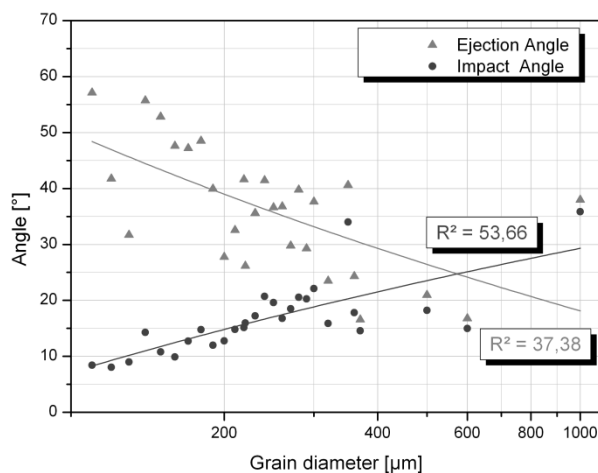
Figure 7: *Mean values of the ejection and impact angle, for all 100 trajectories. To both series, a logarithmic regression was fitted. A decreasing trend for the mean ejection angle (triangle) with increasing grain diameter is apparent in the plotted data. The mean impact angle (dots) increase with increasing grain diameter.*
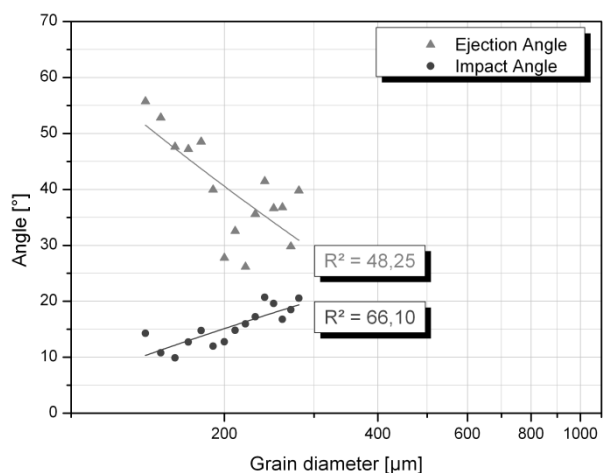
Figure 8: *Mean values of the ejection and impact angle for grain sizes from 140-280 µm. To both series, a logarithmic regression was fitted. The decreasing trend for the mean ejection angle (triangle) with increasing grain diameter is more significant than in Figure 7. Also for the mean impact angle, the increasing trend with increasing grain diameter is even better than in Figure 7.*

The mean ejection angle over all 100 evaluated trajectories was 41.7° and the mean impact angle was 15.15°. Additionally the ratio between the mean ejection angle α and mean impact angle β, which decrease with increasing grain diameter (Rice et al., 1995), could be confirmed. Figure 9 shows the ratio between the mean ejection angles and the mean impact angles of the 100 selected trajectories. The decreasing trend of the ratio is perceptible.
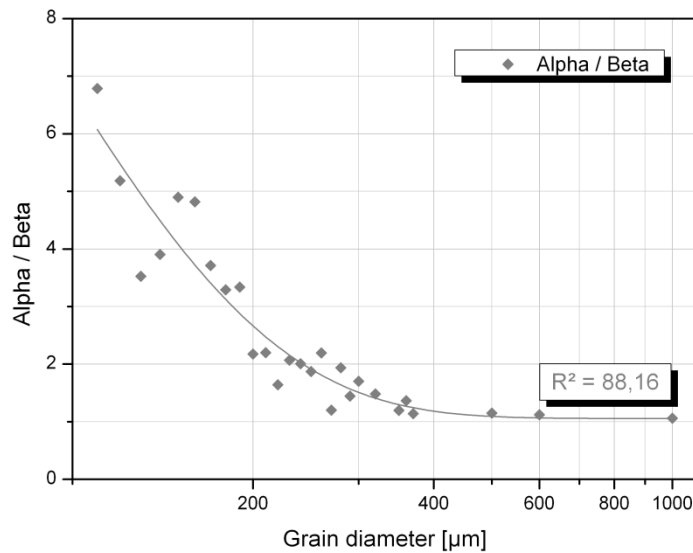
Figure 9: *The ratio between the mean ejection angle and the mean impact angle decreases with increasing grain diameter. An exponential regression was fitted to the serie.*
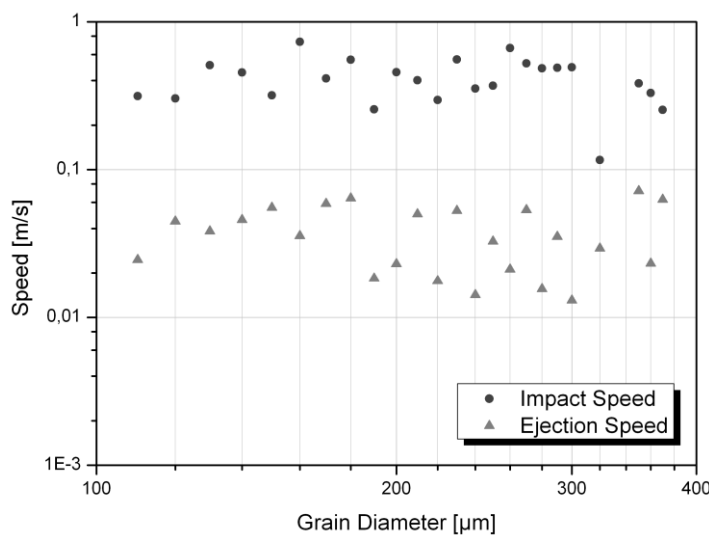
Figure 10: *Mean ejection and mean impact speed for grain sizes from 110-400 μm. The grains ejected from the bed had an average speed of one order of magnitude less than the impact speed.*

The results for ejection and impact speed of the saltating grains could be summarized as follows. Nalpanis et al. (1993) found values between 1.6 – 2.0 for the ratio u_i / u_e . Rice et al. (1995) confirmed also these results but they changed the ratio to u_e / u_i and got values of 0.5 – 0.6. These results could not be confirmed. The ration between the mean ejection speed u_e and the mean impact speed u_i was found nearly the same for all determined grain sizes. The grains ejected from the bed had an average speed of one order of magnitude less than the impact speed. Also Beladjine et al. (2007) found this coherence, whereby the mean ejection speed is one order of magnitude less than the mean impact speed. Figure 10 shows the mean ejection and mean impact speed for grain sizes from 110-400 μm. The shortage of data for bigger grain sizes leads to no significant results. Also values for saltation length and saltation height were only available for smaller grain sizes. Values of the mean saltation length and mean saltation height for bigger grain sizes (>400 μm) in Figure 11 were only shown for the sake of completeness. For grain sizes between 110 and 400 μm the mean saltation height is one order of magnitude less than the mean saltation length. Looking at the saltation height as a function of the saltation length, a linear coherence was found. This means that, if the grain has jumped far the higher it has been flown, see Figure 12 (left). The mean saltation length of the 100 evaluated grains was 1.99 cm. On the contrary the mean saltation height was 2.4 mm. In Figure 12 (right), a 3D trajectory from the evaluation could be seen.
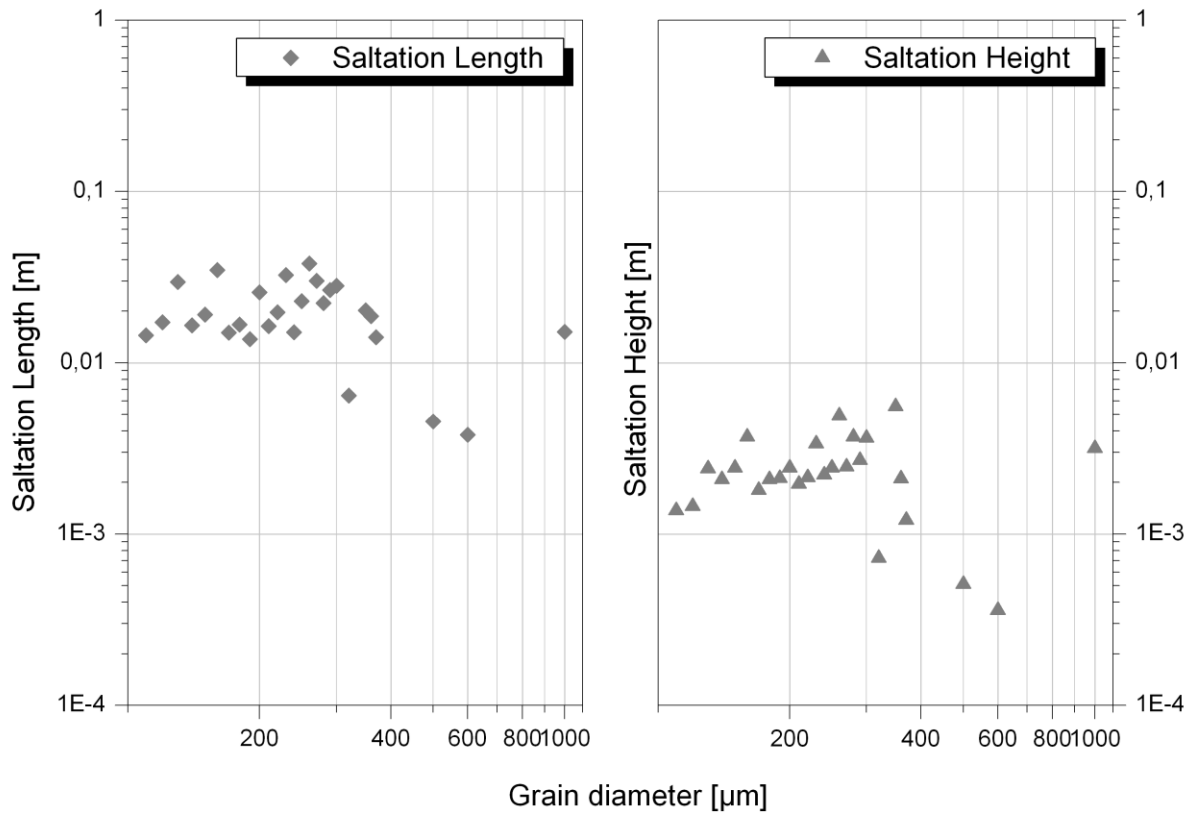
Figure 11: *Mean saltation length and mean saltation height for all 100 evaluated grains. For grain sizes between 110 and 400 µm the mean saltation height is one order of magnitude less than the mean saltation length.*
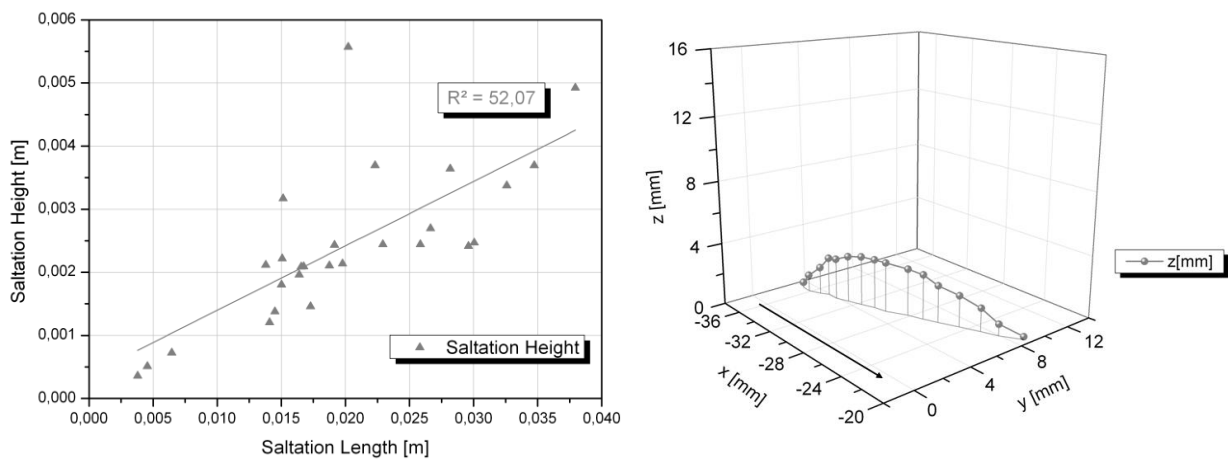
Figure 12: Left:*The saltation height as a function of the saltation length. A linear regression was fitted to the serie. The farer the grain has been jumped the higher it has been flown.* Right: *A 3D trajectory, of a saltating grain, measured at Zingst peninsula. The black arrowhead symbolizes the mean wind direction. The flange of the mirror is parallel to the x-Axis.*

5. CONCLUSION

With a new measurement setup, including a high-speed camera and a mirror plate, trajectories of saltating grains were characterized in 2D and 3D under natural and laboratory conditions. The trajectories were used to determine the ejection and impact angle, the ejection and impact speed as well as the saltation length and height of saltating grains. Also their size could have been calculated. The revealed results show, that high-speed film measurements in 3D are comparable to 2D measurements with high-speed photography presented in literature. The main striking results, obtained with the new system, can be summarized as follows.

- Ejection angles decrease with increasing grain diameter. They vary between 57° and 27° for fine and middle grains and between 38° and 20° for coarse grains. The mean ejection angle for all 100 evaluated trajectories was found with 41.7°.
- The impact angle increases with increasing grain diameter. Impact angles vary between 8° and 15° for fine grains and from 12 to 36° for middle and coarse grains. The mean impact angle for all 100 evaluated trajectories was found with 15.15°.
- Additionally the ratio between the mean ejection angle α and mean impact angle β, which decrease with increasing grain diameter (Rice et al., 1995), could be confirmed.
- The ration between the ejection speed u_e and impact speed u_i was found nearly the same for all determined grain sizes, but the grains ejected from the bed had an average speed of one order of magnitude less than the impact speed, which confirm the findings of Beladjine et al. (2007).
- The Runge-Kutta procedure is a good way to simulate the trajectory of the grain by using real measured values of the mean wind speed and fitting them to the measured trajectory of the saltating grain.
- With the calculated RMSE for each simulated grain diameter of a trajectory, picking the grain diameter with the lowest RMSE compared to the measured grain, it is possible to determine the diameter of the measured saltating grain.

The first measurements with the new camera system presented here, indicate the potential of 3D trajectory analysis. However, further effort has to put into the system to improve the estimation of the grain diameter and the calculation of the RMSE with reference to the trajectory.

REFERENCES

Anderson, R.S. and Haff, P.K. *Simulation of Eolian Saltation*. Science VOL. 241, Pages 820 - 823, 1988

Anderson, R.S. and Haff, P.K., Acta Mechanica Suppl. 1, 21, 1991

Bagnold, R.A. *The Physics of Blown Sand and Desert Dunes*, 253 pp. reprinted by Chapman and Hall Methuen, London, 1954

Beladjine, D., Ammi, M., Oger, L. and Valance, A. *Collision process between an incident bead and a three-dimensional granular packing*. The American Physical Society, Physical Review E 75, 061305, 2007

Greeley, R. and Iversen, J.D. *Wind as a geological process on Earth, Mars, Venus, and Titan*. Cambridge University Press, The Pitt Building, Trumpington Street, Cambridge CB2 1RP, 1985

Julien, P.Y. *Erosion and Sedimentation*. Cambrigde University Press, 1995

Laity, J. *Deserts and Desert Environments*. Wiley-Blackwell, November 2008

McEwan, I.K. and Willetts, B.B. Acta Mechanica Suppl. 1, 53, 1991

Mitha, S., Tran, M.Q., Werner, B.T. and Haff, P.K. *The grain-bed impact process in aeolian saltation*. Acta Mechanica, 63, 14, Pages 267 - 278, 1986

Pye, K. *Aeolian dust and dust deposits*. Academic Press Inc. London LTD., 24-28 Oval Road, London NW1 7DX, 1987

Rice, M.A., Willetts, B.B. and McEvan, I.K. *An experimental study of multiple grain-size ejecta produced by collisions of saltating grains with a flat bed*. International Association of Sedimentologists, Sedimentology 42, Pages 695 - 706, 1995

Schönfeldt, H.-J. *Quantitative Bestimmung des äolischen Sedimenttransports*. F.- M. Chmielewski, T. Foken, Beiträge zur Klima- und Meeresforschung, Seiten 249 - 258, Berlin und Bayreuth, 2003

Shao, Y. *Physics and Modelling of Wind Erosion*. Atmospheric and Oceanographic Sciences Library, Kluwer Academic Publishers, 2000

Willetts, B.B. and Rice, M.A. *Collision in aeolian saltation*. Acta Mechanica, 14, Pages 255 - 265, 1986

Reinforcement of edge waves by beach cusps

Hans-Jürgen Schönfeldt

Universität Leipzig, Institut für Meteorologie, Stephanstr. 3, D04103 Leipzig
Fax: (+341) 9732899 e-mail: schoenfeldt@ uni-leipzig.de

Summary. Beach cusps, formed during a storm are observed. The storm acted for three hours together with high water conditions. These beach cusps exhibited a quasi-uniform wavelength of 8 m. The measured topography after the storm, the calculated drift velocity of the incident wave and the synchronous edge wave are similar in scale and shape. The over one wavelength measured grain size is also correlated to the topography.

A nonlinear hydro-numerical model is used to investigate the reaction of edge waves on alongshore change in bottom topography. Edge waves are greatly amplified over beach cusps. The relative amplification of edge waves on beach cusps is more than 17 times that without a change in longshore topography. Amplification is slightly greater for edge waves travelling in the same direction as the longshore current during the storm.

An almost random positioning of sediment starts a feedback loop, which allows edge waves to grow and build short periodic cusps.

Keywords: beach cusps, edge waves Baltic Sea, German Coast, Zingst peninsula

Introduction

The coastal profile can vary considerably over a year or even during a single storm event. Longshore bars can be formed and existing bars can be shifted or destroyed. The problem of sediment transport modelling is not yet completely solved - particularly the resulting direction of sediment transport outside the surf zone and the detailed morphology of the bars, which must be investigated more thoroughly. The wave theory with an onshore/offshore sediment-transport model suggests that the undertow gives an offshore-directed transport in the surf zone and that the transport outside the surf zone is weak, with a tendency to be in the onshore direction. This means that a longshore bar will tend to form on a constant-slope profile as a result of the cross-shore transport (Fredsøe and Deigaard, 1992). However these bars are forming offshore continuously and are not stable. Schönfeldt (1989, 1991) constructed an onshore/offshore sediment-transport model on the basis of edge waves. In this model, the bars move toward the beach. It seems that in nature both wave processes take part.

In principle, numerical models include edge waves, but excitation is only possible in non-linear models. On the other hand, the boundary conditions are simple only for standing edge waves. For effective excitation of edge waves, the alongshore extension of the model must be big enough that excitation and dissipation can reach equilibrium. On the cross-shore boundaries, these waves leave the model. An inject of these waves on the opposite boundary is possible only where there are identical depth profiles of at least 1.5 wave length on the cross-shore boundaries as well as other restrictions.

At beaches with bars, edge waves may be trapped at the location of the bar, their cross-shore shapes strongly amplified relative to their shoreline values (Kirby et al. 1981, Schönfeldt, 1991, Bryan and Bowen, 1996, 1998), with the strongest amplification occurring at incident-wave frequencies. The trapping of edge waves on near shore wave-guides, such as bars and longshore currents, has been presented as a mechanism for the growth, movement, or even formation of longshore bars (Schönfeldt, 1989, 1991, 1995; Howd et al.,1992; Bryan and Bowen, 1996, 1998).

Of particular interest have been shoreline features that show a regular longshore periodicity down the beach, variously described as beach cusps, sand waves, rhythmic topography, or grain cusps (Hom-ma and Sonu, 1963; Dolan et al., 1974; Guza and Inman, 1975; Komar, 1981). Beach cusps are crescentic shoreline features, concave seaward, that are characterised by a quasi-uniform longshore wavelength ranging from less than 3 m to at least 30 m (Dolan et al., 1974). Cusp formation is usually rapid, requiring only a few hours (Miller et al., 1989).

Holman and Bowen (1982) show how a variety of regular longshore patterns may be generated by two edge waves of the same frequency but different mode. Superimposition of incident waves on edge waves also generates longshore periodicity in drift velocity (Sallenger, 1979, Schwarzer, 1989).

There is a second explanation of beach cusps formation, the self-organisation theory using more advanced computer simulations (Werner and Fink, 1993, Coco et al., 1999). There is a positive feedback in areas with lower relief and a negative feedback will decrease the amount of net erosion and deposition within a well formed cusp. The feedback between the morphology of the beach and the flow of the water creates relief patterns. Almar et al. (2008) were unable to conclusively refute any of the mechanisms causing beach cusp formation since both existing theories, standing edge wave and self-organization, can predict the trend in the observed beach cusp spacing. We will show that in the presented case the beach cusp grow and spacing is a result of superposition of incident wave and synchronous edge wave and that the so formed topography will starts a feedback loop, which allows edge waves to grow and build short periodic cusps.

Location of study

Measurements of wave characteristics, water level, and the topography after a storm were carried out in the western part of the Baltic Sea on the Zingst peninsula. On the measuring point there is a negligible tide of 0.1 m. The coast of the Zingst peninsula is a straight sandy coast, 18 km long and east-west orientated. The measuring point of the University of Leipzig is situated in the centre of this. The coast is protected by arrayed groins, approximately 100-150 m apart.

Storm characteristics

On January 25th to 26th 1993 the mean wind velocity was for a relatively short time of 6 hours 17 m/s from NW. The storm caused for a short time a water-level rise of 1.17 m above mean water level (see Figure 1). During this time, the waves increased up to a significant wave height of H_S =1.5 m measured 100 m from the coastline at a depth of
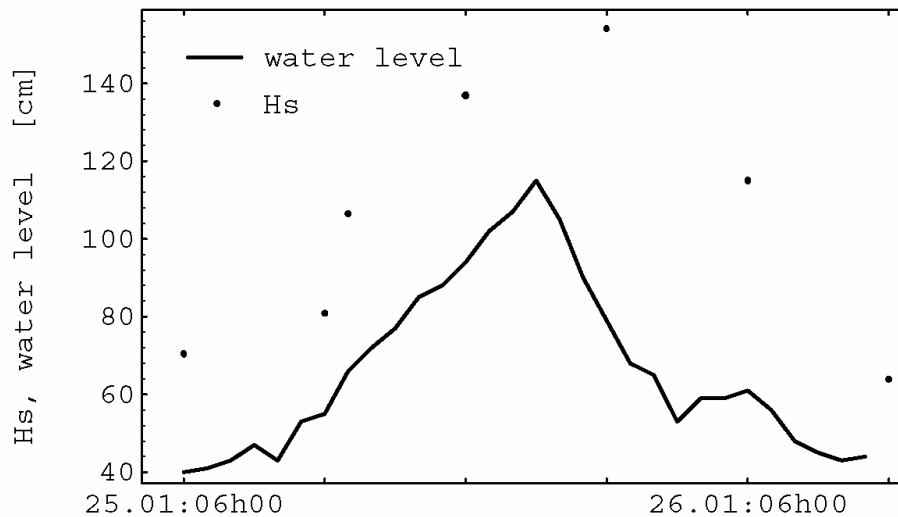
Fig. 1 Time series of water level and significant wave height H_s
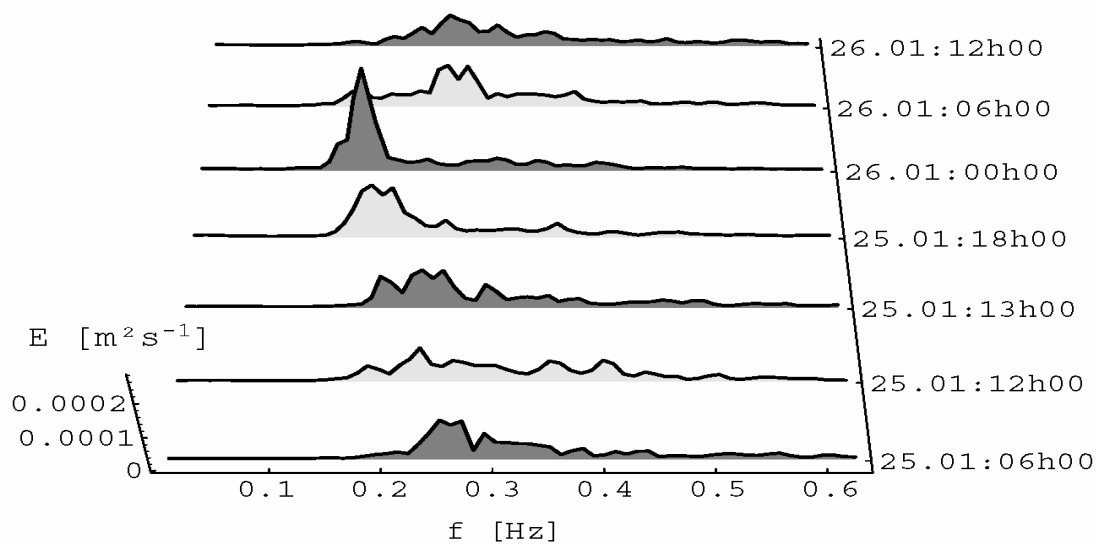
Fig. 2 Dimensionless frequency spectra; waves measured to a depth of 3.5 m, 100 m from the coastline.

3.5 m (mean water level). The wave frequency of the significant waves moves from a typical value for the Baltic of 0.25 Hz to 0.16 Hz and quickly increases to the same value of 0.25 Hz (see Figure 2). Due to these unusual conditions the waves act only for 3 hours on the foreshore and this region was not wash over for many days after the storm and the topography was defended for erosion.

Methodology

After the storm, asymmetric beach cusps were formed with a quasi-uniform longshore wavelength of 8 m, which was measured over 10 cusps from cusps top to cusps top. We studied the topography in detail in a 10 m x 9 m section normal to the coast. The

topography in the dry fallen foreshore cups region was measured on a raster of 1 m alongshore and 0.5 m cross-shore over one beach-cusp wavelength. This measured and for numerical study extrapolated topography is shown in Figure 3.

The basic data set for this study are measurements of 1) waves at a depth of 3.5 m for 7 minutes every 6 hours; 2) water level every hour; and 3) continuous wind measurements. The sampling interval for waves is 0.2 sec with a vertical resolution of 3 cm. Power spectra were calculated from the wave data and are shown in Figure 3. The wave spectra during high water were put in the non-linear wave model BOWAM2 of the University of Hanover (Schröter, 1991). The measured topography was interpolated on a grid of 0.5 m x 0.5 m and then put into the model. The model has 96 cross-shore and 92 longshore grid points. The boundary conditions are open on the sea side of the model and vary from closed (sea side) to open (shoreline) on the cross-shore boundaries. These boundary conditions give the possibility for edge-wave excitation of up to 40 meters in wavelength in the two longshore directions. We have the results from two runs 1) with the measured topography and 2) similar to 1) but with an average of the topography over all grid points alongshore. To obtain the edge-wave energy, a Fourier longshore wavelength spectrum was employed, where the infinite wavelength ($\lambda \rightarrow \infty$) represents the incoming wave.
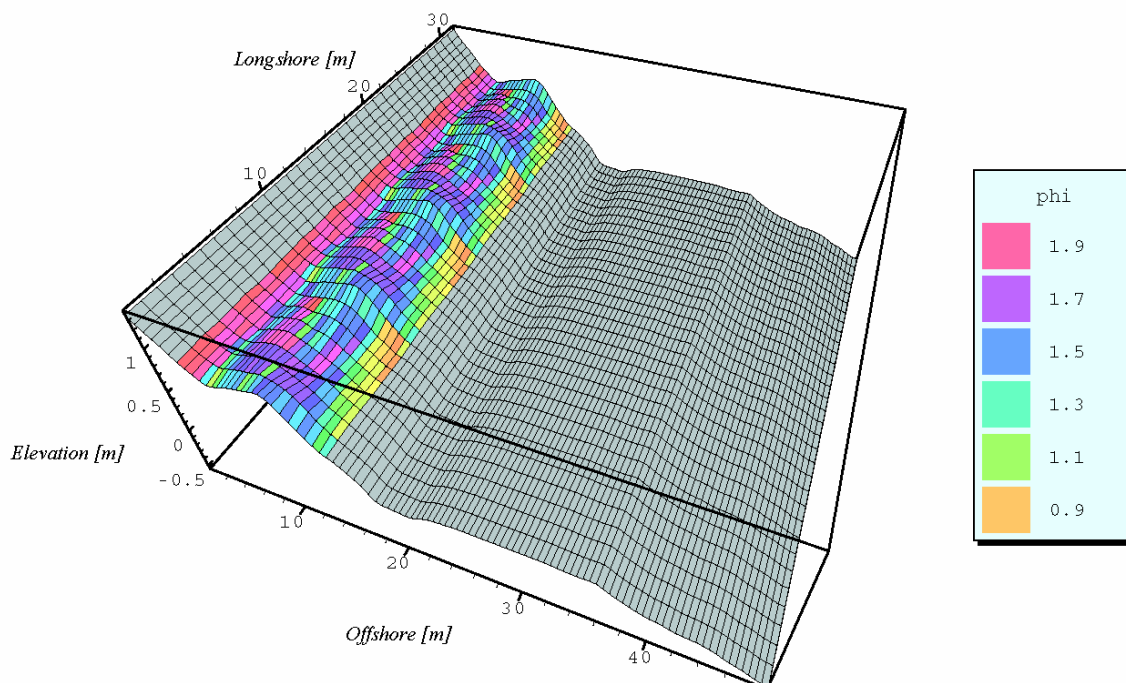
Fig. 3 The topography examined by the numerical model BOWAM2. Shown also in the picture is the grain size of an area of 8x12 m in phi=$\log_2$(mm). This area is duplicated. The grain-size results are not discussed in the text.

Let x and y be distance from the shore and distance alongshore, respectively. The time is denoted by t. We examined numerically the edge-wave dispersion relation and the edge-wave amplitude on the topography, which is the same as in numerical run 2), that

is variable in the cross-shore direction x but constant in the longshore direction y, by assuming that the cross-shore velocity u, the longshore velocity v, and the sea-surface elevation η are wave-like in the longshore direction

$$\eta(\mathrm{x}, \mathrm{y}, \mathrm{t}) = \eta^*(x)e^{i(ky-\sigma t)}, \tag{1}$$

where k and σ are the longshore radian wave number and wave frequency, respectively and $\eta^*(x)$ the edge wave amplitude on a barred topography $h(x)$. For a flat beach $\eta^*(x) \sim L_n(x)$ where $L_n(x)$ denote the Laguerre Polynomals. Substituting (1) and analogous equations for u and v into the irrotational, inviscid shallow water equations of momentum and continuity gives

$$\left[\frac{gh\eta_x^*}{\sigma^2}\right]_x + \eta^*\left(1 - \frac{k^2 gh}{\sigma^2}\right) = 0, \tag{2}$$

the classic edge-wave differential equation, where h is the water depth, g is the gravitational acceleration, and subscripts indicate differentiation. The differential equation (2) can be solved numerically by a Runge-Kutta algorithm starting with the boundary conditions $hu=0$ at $x=0$ and the requirement $\eta \to 0$ for $x \to \infty$ (Holman and Bowen, 1979). For a given frequency σ, there is a set of edge waves of different modal numbers n (where $n=0, 1, 2, ...$) with the longshore radian wave number k_n.

Results

The topography of the beach after a storm is shown in Figure 3 and 4b. Periodic erosions (and/or accretional processes) are seen in the swash zone after the storm. The topography has a quasi-uniform longshore wavelength of 8 m. The beach was uniform in slope from the dune to the swash zone before the storm of January 25th – 26th 1993. With the measured topography we examined the dispersion relation on the edge wave wavelength of 8 m. First we used Eq. (2) and the measured topography averaged in longshore direction as described above. The mode-zero edge wave frequency belonging to the wavelength $\lambda_0 = 8$ m is 0.16 Hz. That is the same frequency as the measured significant incident wave frequency on high water. These incident waves acted only for 3 hours on the foreshore.

Equation (2) gives a solution for constant beach profile alongshore. Schönfeldt (1995) showed that edge waves can be trapped on bars and longshore currents. On bars and currents trapped edge waves have here the maximum of amplitude contrary to edge waves on planar beaches with uniform slope. Therefore we tested the influence of the alongshore not uniform cusps profile on the edge waves in a non-linear two-dimensional wave model BOWAM2. On the sea side we used the wave spectra during high water as boundary conditions and the two-dimensional sea-bed topography in the two cases: 1) the topography measured after storm plus high water level and 2) similar to 1) but with averaging in longshore direction. After Fourier transformation of the calculated time series in space we get the longshore wavelength spectrum. We calculated the edge-wave amplitude for the wavelength at $\lambda = 8$ m in the two cases.
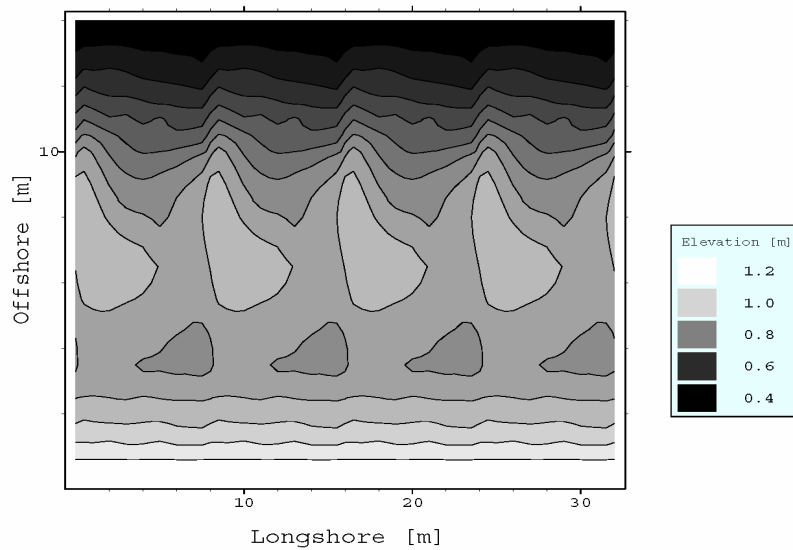
Fig. 4a Measured topography. Since high resolution topography data fail for understanding we have it duplicated alongshore.
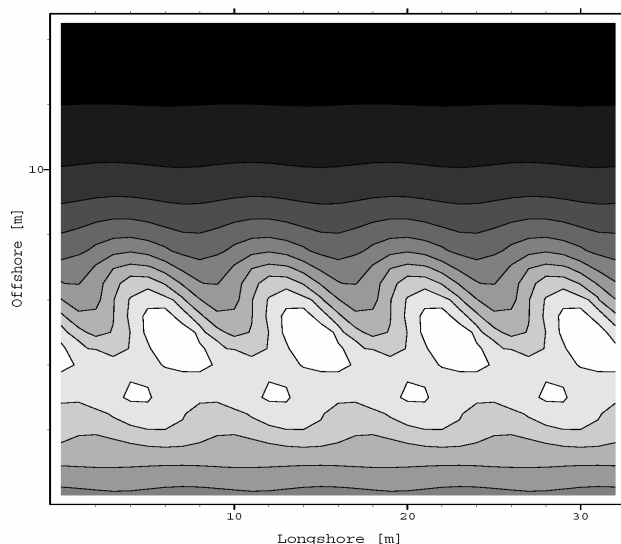
Fig. 4b The norm of the superimposition velocity of the incoming wave with an amplitude of 1.0 and the synchronous mode-zero edge wave running from west to east (to the right when one look to the sea) with an amplitude of 0.2 with constant phase-coupling between this waves.

The ratio of amplitude a_1/a_2 and the edge wave frequency are present in Figure 5. This ratio of amplitude is an average in cross-shore direction of all spectral elements with a wavelength of $\lambda = 8$ m, but the highest amplitudes were found 5 m away from the coast at the top of the cusps during high water. In agreement with Eq. (2) this is the region of mode-zero edge waves. In the model run with the measured two-dimensional sea-bed topography, the amplitudes were up to 18 times greater than in the case 2). We have a slight asymmetry in the amplitude ratio. The waves running from the left to the right are something preferentially forced. This is an influence of the topography only. Note, the incident waves running normal towards the coast in the model. The higher edge-wave modes are also amplified but not so much. Another influence of the sea-bed

topography is an asymmetry in edge wave frequency, edge waves running from the right to left are less intense forced and have a lower frequency. Equation (2) and the model runs do not give the same edge-wave dispersion relation (see Fig. 5), Equation (2) gives the free wave solution and the model gives the equilibrium solution forced by wave braking and damped down by friction.
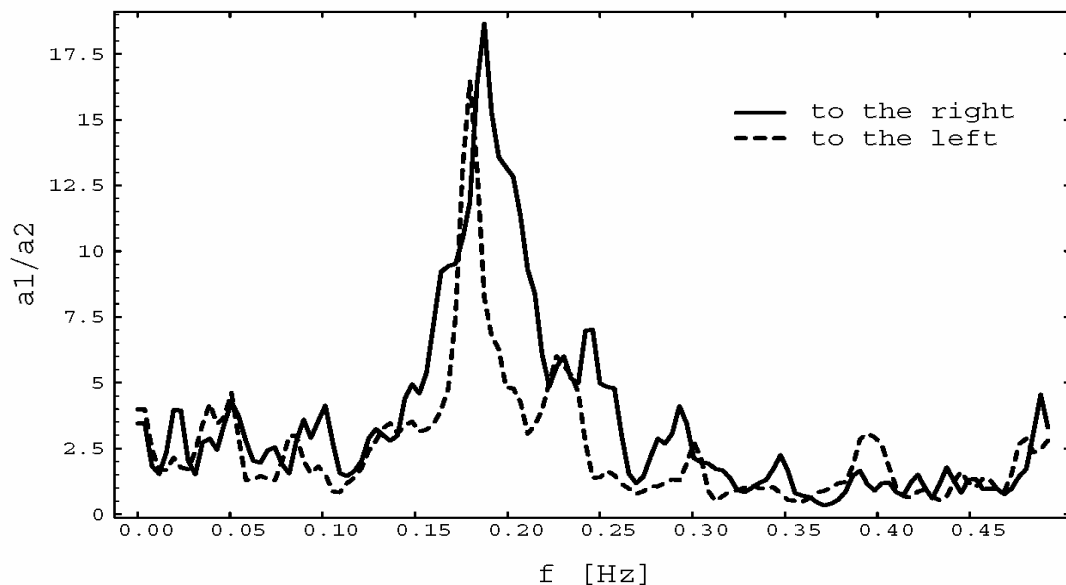
Fig. 5 The ratio of the edge-wave elevation a_1 with an 8 m wavelength on a rhythmic alongshore sea-bottom topography (Fig. 4a) to the edge-wave elevation a_2 on the same seabed profile but with a mean over all longshore grid points.

The directions denote the propagation of the edge waves when you look to the sea. The elevations were determined by the numerical model BOWAM2.

The incident wave amplitude can be calculate analogous to the edge wave by Eq. (2) with $k = 0$ (wave number in lonshore direction). This calculation gives the amplitudes for a standing wave on variable topography in cross-shore direction. As a result, the amplitudes for an incoming wave can be reconstructed as envelope of the standing wave amplitude (Bessel function on uniform slope).

The cross-shore velocity u and the longshore velocity v of the synchronous mode-zero edge wave and the incoming wave are calculated by the shallow water equations of momentum and continuity with the edge wave amplitude η^* calculated by Eq. (2). The two components u and v of superimposition of an incoming wave and the synchronous mode-zero edge wave running from west to east (from the left to the right when looking seaward) was calculated with constant-phase coupling between these waves and without wave breaking. In principle these restrictions do not disturb the result and conclusions. The norm of resulting velocity u and v of a superimposition of incoming wave with the arbitrary amplitude of 1.0 and the synchronous mode-zero edge wave with amplitude of 0.2 of the incident wave is shown in Figure 4b. This picture can only exist if phase-coupling between the waves occurs. At the occurrence of every incident wave crest, synchronous edge waves will cause a longshore spacing of wave-height maximums equal to one synchronous edge-wave wavelength (Bowen and Inman, 1969, Sallenger, 1979, Schwarzer, 1989). Evidence for phase-coupling between edge-wave modes is given by Huntley (1988). Figure 4a and 4b look similar.

Discussion

„If a beach were exposed to waves having an exactly symmetrical, orbital velocity, all the sediment would slide down the slope and out to sea. The existence of the beach depends on small departures from symmetry in the velocity field balancing this tendency for gravity to move material offshore" (Bowen, 1980). Alongshore departure from symmetry in the velocity field will be produced by the superimposition of incident wave and mode zero edge wave (Fig.4b). This superimposition has the structure of a standing wave where the nodes of standing wave are replaced by minima of the drift velocity. Suspended load tends to accumulate at these minima. We have a positive feedback from the morphology to initial edge waves. The periodic crests and troughs in a line at a distance of 5m from the coast force waves are formed during the wave run-up. The mode-zero edge wave has the greatest excitation probability.

The initial topography has no structure. At the beginning the mode-zero edge wave are excited without resonance, the amplitudes will be small. If we have in one place a random structure that agrees with the edge-wave wavelength, then phase-coupling and the positive feedback begin. The periodicity in a wave-induced current (incident wave and edge wave) causes a periodicity in sediment transport. The resulting topography has a positive feedback on edge waves, and so on. This initial event will spread over the entire coastline. The initial process can begin on several locations at the same time. To the extent that the sea-bed topography changes from alongshore constant to rhythmic, the energy of edge waves causes the crests and troughs to rise.

Standing sub harmonic edge waves can also cause a rhythmic topography. The sub harmonic edge wave with the peak frequency of the wave spectrum has a wave length of 16 m, and the superimposition of two waves running in opposite directions extinguish and reinforce themselves with a spacing of 8 m. But the resulting drift velocity of superimposition is strongly symmetrical and not asymmetrical like the measured topography (cf. Fig. 4a).

Huntley and Bowen (1975) observed shoreline beach cusps and noted an apparent correspondence between the spacing of cusps found in the field and that due to n = 0 synchronous edge waves. Figure 4a (measured topography) and 4b (superimposed drift velocity) are similar but not mirror-image exact. Lines of equal phase of the superimposed wave are not perpendicular to the shore.

It has been shown both theoretically (Bowen and Guza, 1978) and in field data (Oltman-Shay and Guza, 1987; Oltman-Shay et al.,1989; Bryan and Bowen, 1998) that, under obliquely incident wave conditions, edge waves may be preferentially forced in the same direction as the forcing of longshore current. The incoming waves (wave direction NW in deep water) will preferentially force edge waves in the direction from west to east. Note that the numerical model also preferentially forces edge waves running to the right (Fig. 5) though we have deliberately chosen a wave direction perpendicular to the coast. We have two reasons for excitation of synchronous edge waves running from west to east (left to right): the wave direction NW (coast line west east the sea in north direction) and the preferentially forcing of edge waves by the cusps profile even if the wave run up is perpendicular to the coast.

Conclusions

There are two theories with any real credibility as to why beach cusps are formed, the standing edge wave theory and the self-organisation theory. The latter discuss that positive feedback between the morphology of the beach and the flow of the water creates relief patterns. The problem of this theory is that this method of cusp formation would take time and if one observes their formation, then one would see a number of random cusps form along the beach, which then slowly spread along the shore as they even out in size, with small cusps joining together and larger cusps being separated in two. But in the field, cusps form a regular pattern almost instantly and they all appear at the same time.

Our results suppose that for unsymmetrical beach cusps (periodic but not mirror-image exact) both of the two theories must be taken into account. One or more of the number of random cusps will be suitable for resonant excitation of edge wave and phase-coupling between edge-wave and incident wave. In this manner the here starting edge wave affect the neighbouring random cusps and bring these in "phase". The missing link in the self-organisation theory are the edge waves. We can not say that this causal chain act in any case of beach cusps generation. We only have this hints for asymmetric periodic but not mirror-image exact beach cusps.

References

Almar, R., Coco, G., Bryan, K.R., Huntley, D.A., Short, A.D. and Senechal, N., 2008: Video observations of beach cusp morphodynamics. Marine Geology, 254, 216-223

Bryan, K. R. and Bowen, A. J., 1996: Edge waves trapping and amplification on barred beaches. J. Geophys. Res. 101 (C3), 6543-6552.

Bryan, K. R. and Bowen, A. J., 1998: Bar-trapped edge waves and longshore currents. J. Geophys. Res. 103 (C12), 27867-27884.

Bowen, A. J. and Inman, D. L., 1969: Rip currents, 2. Laboratory and field observations. J. Geophys. Res. 74, 5479-5490.

Bowen, A. J. and Guza, R. T., 1978: Edge waves and surf beat. J. Geophys. Res. 83, 1913-1920.

Bowen, A.J., 1980. Simple models of nearshore sedimentation; beach profiles and longshore bars. In: McCann S.B. (Ed.), The Coastline of Canada, Geological Survey of Canada, Paper 80-10: 1-11.

Coco, G., T.J. O'Hare and Huntley, D.A., 1999: Beach cusps: a comparison of data and theories for their formation, J. Coast. Res. 15 (3), pp. 741-749.

Dolan, R., L. Vincent, and Hayden, B., 1974: Crescentic coastal landforms. Z. Geomorph. 18, 1-12.

Fredsøe, J. and Deigaard, R., 1992: Mechanics of coastal sediment transport. Advanced Series on Ocean Engineering, Volume 3.

Guza, R. T., and Inman, D. L., 1975: Edge waves and beach cusps. J. of Geopy. Res. 80, 2997-3012.

Holman, R. A. and Bowen, A. J., 1979: Edge waves on complex beach profiles. J. Geophys. Res. 84, 6339-6346.

Holman, R. A. and Bowen, A. J., 1982: Bars, bumps, holes: Models for the generation of complex beach topography. J. Geophys. Res. 87, 457-468.

Hom-ma, M., and Sonu, C.,1963: Rhythmic patterns of longshore bars related to sediment characteristics, In: Proceedings 8th Conference on Coastal Engineering, American Society of Civil Engineering, New York, pp. 248-278.

Howd, P.A., Bowen, R. A., Holman, R. A., 1992: Edge waves in strong longshore currents. J. Geophys. Res. 97, 11357-11371.

Huntley, D. A. and Bowen, A. J., 1975: Field observations of edge waves and their effect on beach material. J. Geol. Soc. Lond. 131, 69-81.

Huntley, D. A., 1988. Evidence for phase coupling between edge wave modes. J. Geophys. Res. 93, 12392-12408.

Kirby, J. T., R. A. Dalrymple, and P. L. F. Lui, 1981: Modification of edge waves by barred-beach topography, Coastal Eng. 5, 35-49.

Komar, P. D., 1981: Rhythmic shoreline features and their origins, In: Gardener, R., et al. (Ed.), Large-scale Geomorphology, Oxford University Press, New York.

Miller, J.R., Orbock Miller, S.M., Torzynski, C.A. and Kochel, R.C., 1989: Beach-cusp destruction, formation, and evolution during and subsequent to an extratropical storm. Duck, North Carolina. J. of Geology 97, 749-760.

Oltman-Shay, J. and Guza, R.T., 1987: Infragravity edge wave observations on two California beaches. J. Phys. Oceanography 17, 644-663.

Oltman-Shay, J., Elgar, S., Howd, P., 1989: Observations of infragravity-frequency long waves, II. Comparisons with a 2-D wave group generation model (abstract). Eos Trans. AGU 70, 1333.

Sallenger Jr., A.H., 1979: Beach-cusp formation. Mar. Geol. 29, 23-37.

Schönfeldt, H.-J., 1989: Are edge waves responsible for the location of sand reefs ? Beitr. zur Meereskunde 60, 35-40.

Schönfeldt, H.-J., 1991: Randwellen und Sedimentation. Geophysikalische Veröff. der Universität Leipzig 4, 75-87.

Schönfeldt, H.-J., 1991. Dispersionsbeziehungen von Randwellen auf natürlichen Bodenprofilen mit uferparallelen Sandbänken. Beitr. Meereskd. 62, 53-68.

Schönfeldt, H.-J., 1994: Randwellen in der Ostsee und anormale Dispersion in der Brandungszone. D. Hydrogr. Z. 46, 81-98.

Schönfeldt, H.-J., 1995: On the modification of edge waves by longshore currents. Continental Shelf Research 15, 1213-1220.

Schröter, A., 1991. Das numerische Seegangsmodell BOWAM2 1990 - Grundlagen und Verifikationen. Univ. Hannover, Inst. f. Strömungsmechanik, Bericht 31, Teil 2.

Schwarzer, K., 1989: Sedimentdynamik in Sandriffsystemen einer tidenfreien Küste unter Berücksichtigung von Rippströmen. Berichte-Reports, Geol.- Paläont. Inst. Univ. Kiel, 33.

Werner, B.T. and Fink, T.M., 1993: Beach cusps as self-organised patterns, Science 260, pp. 968-971.

Jahresbericht des Instituts für Meteorologie der Universität Leipzig 2009

Direktor　　　　　　Prof. Dr. W. Metz
　　　　　　　　　　Prof. Dr. M. Wendisch　　　(ab 01.09.09)

1. Bearbeitete Forschungsprojekte

AG Atmosphärische Strahlung

Hubschraubergetragene Strahlungsmessungen zur Bestimmung des Einflusses von Wolkeninhomogenitäten tropischer Grenzschichtbewölkung auf die Strahlungsbilanz
Helicopter-borne radiation measurements to investigate the influence of cloud heterogeneities of tropical boundary layer clouds on radiative budget

F. Henrich　　(f.henrich@uni-leipzig.de), M. Wendisch (m.wendisch@uni-leipzig.de)
H. Siebert　　(siebert@tropos.de)

　　　　Die Vernachlässigung von horizontalen Wolkeninhomogenitäten in Modellen zur Berechnung der solaren Strahlungsbilanz von Wolken kann zu erheblichen Diskrepanzen zwischen Modellergebnissen und Messungen führen. In Zusammenarbeit mit dem Leibniz-Institut für Troposphärenforschung wird der Einfluss von Inhomogenitätseffekten von tiefer Cumulusbewölkung in den Tropen auf den Strahlungshaushalt untersucht. Hierfür wird ein neues, kompaktes Messsystem für spektrale Strahlungsmessungen gebaut, welches zusammen mit einer Messplattform für Aerosol-, Turbulenz- und Mikrophysikalischen Wolkenparametern (ACTOS) erstmals die gleichzeitige Beobachtung von Wolkenmikrophysikischen und Strahlungsgrößen ermöglichen wird. Hierfür wird ein Hubschrauber als Instrumententräger genutzt. Ergänzend sollen dreidimensionale Rechnungen mit einem Strahlungstransfermodell zur Interpretation der Messungen durchgeführt werden.
　　　　Das Messgebiet (Barbedos) bietet aufgrund seiner Lage zusätzlich die Möglichkeit der Untersuchung von anthropogenen Einflüssen auf den atmosphärischen Strahlungstransfer und die Beeinflussung des solaren Strahlungshaushaltes durch Feuchtigkeits-Halos.

　　　　Weiterführung: ja

　　　　Finanzierung:　　Uni Leipzig

AG Atmosphärische Strahlung

Räumliche Verteilung von Eis- und Flüssigwasser in Arktischen Mischphasenwolken und deren Einfluss auf Energiehaushalt und Fernerkundung
Spatial distribution of ice and liquid water in Arctic mixed-phase clouds and its impact on energy budget and remote sensing
A. Ehrlich　　(a.ehrlich@uni-leipzig.de), E. Bierwirth　(e-bierwirth@uni-leipzig.de)
M. Wendisch (m.wendisch@uni-leipzig.de)

Mischphasenwolken mit nebeneinander existierendem flüssigem Wasser- und Eisanteil, treten häufig in arktischen Regionen auf. Sie können theoretisch in einem Temperaturbereich zwischen -40 °C und 0 °C über längere Zeit hinweg stabil existieren. Wie bekannt ist unterscheiden sich die optischen Eigenschaften von reinen Wasser- und Eiswolken und damit auch ihr Einfluss auf die solare Strahlung. Zur Untersuchung der horizontalen Verteilung von Eis- und Flüssigwasser und deren Einfluss auf den Strahlungstransport wird dieses Projekt in Zusammenarbeit mit dem Alfred Wegener Institut für Polar- und Meeresforschung (AWI), Bremerhaven durchgeführt.

Kern des Projektes ist die internationale Messkampagne „Solar Radiation and Phase Disrcimination of Arctic Clouds" (SORPIC), bei der spektrale solare Strahlungsmessungen an Bord des POLAR 5 Forschungsflugzeuges des AWI durchgeführt werden.

Zur Vorbereitung der Messkampagne wurde die Lagestabilisierung des SMART-Albedometer überarbeitet. Ein neues Inertialsystem zur verbesserten Messung der Flugzeuglagewinkel wurde in die Lagestabilisierung integriert. Erste Bodentests wurden bereits durchgeführt. Weiterhin wurde die flugtechnische Kampagnenzulassung der POLAR 5 vorbereitet. Dazu fand im Oktober 2009 ein erster Testeinbau aller für die Kampagne benötigter Messgeräte am Flugzeug statt. Weiterhin wurde das während der Messkampagne eingesetzte Kamerasystem AisaEAGLE des AWI in Zusammenarbeit mit dem LIM in unserem Strahlungslabor kalibriert.

Weiterführung: ja

AG Atmosphärische Strahlung

Einfluss von SAHARA-Staubschichten und Biomasseverbrennungsprodukte auf den atmosphärischen Strahlungsantrieb
Influence of Saharan dust layers and biomass burning on atmospheric radiative forcing

S. Bauer   (mail@bauerstefan.com), M. Wendisch (m.wendisch@uni-leipzig.de)
B. Heinold   (heinold@mail.tropos.de), I. Tegen (itegen@tropos.de)
A. Torge   (atorge@ifm-geomar.de), A. Macke (macke@tropos.de)

Das Projekt untersucht den Einfluss von Saharastaub und Biomasseverbrennungsprodukte auf den atmosphärischen Strahlungshaushalt. Dafür stehen flugzeuggetragene und bodengebundene Messungen von solaren Radianzen und Irradianzen während der Kampagne SAMUM 2 (Saharan Mineral Dust Experiment) auf den Kap Verden im Januar/Februar 2008 zur Verfügung. Somit wurden Strahlungsmessungen unter und über Staub- und Biomasseschichten durchgeführt. Die gesammelten Daten werden unter Zuhilfenahme von eindimensionalen Strahlungstransfersimulationen auf Abkühlungs- und Erwärmungseffekte solarer Strahlung in Staub- und Biomasseschichten untersucht. Die gemessenen aufwärtsgerichteten Radianzen über Staubschichten werden zudem mit Messungen des Meteosat-Second-Generation-Satelliten (MSG) verglichen. Unter Annahme von isotroper atmosphärischer Strahlung können

Irradianzen aus MSG-Radianzen abgeleitet und mit den gemessenen Irradianzen auf dem Flugzeug verglichen werden.
Weiterhin werden Ergebnisse aus Staubtransportmodelle, die im Zuge von SAMUM 1 im Jahr 2006 entwickelt wurde, mit den gemessenen Irradianzen verifiziert.

Weiterführung: ja

AG Atmosphärische Strahlung

Bestimmung optischer und mikrophysikalischer Wolkeneigenschaften im Vertikalprofil mittels bodengebundener Fernerkundung
Measurements of vertical profiles of optical and microphysical cloud properties by means of surface-based remote sensing

J. Walter   (jwalter@uni-leipzig.de), M. Brückner   (mbrueck@rz.uni-leipzig.de)
A. Raabe   (raabe@uni-leipzig.de), M. Wendisch (m.wendisch@uni-leipzig.de)

Mittels Kombination eines einfachen Rückstreulidars mit Radianzmessköpfen sollen Vertikalprofile von sowohl mikrophysikalischen als auch optischen Eigenschaften n konvektiver Bewölkung untersucht werden. Hierzu wurde das LIDAR in einem ersten Schritt während einer EARLINET-Messkampagne im Mai 2009 mit anderen LIDAR-Systemen verglichen. In einem zweiten Schritt wird ein Radianzmesskopf zusätzlich im LIDAR implementiert. Neben der Bestimmung optischer Wolkeneigenschaften soll mit Hilfe des LIDAR die thermodynamische Phase der Wolkentropfen bestimmt und mit den Ergebnissen der Bestimmung der thermodynamischen Phase mittels Radianzmessungen verglichen werden. Die Radianzmessungen werden weiterhin zur Bestimmung des effektiven Wolkentropfenradius verwendet. Die gewonnenen Ergebnisse sollen anschließend mit dreidimensionalen Strahlungstransportmodellrechnungen verglichen werden.

AG Allgemeine Meteorologie

Megacities - Hochaufgelöste spektrale Albedo-Karten von Megastädten und ihre Anwendung in Aerosol-Satelliten Datengewinnung
Megacities - High-resolution spectral albedo maps of megacities and its application in aerosol retrievals from satellite data

B. Mey   (b.mey@uni-leipzig.de) , M. Wendisch (m.wendisch@uni-leipzig.de)
H. Jahn   (heiko.jahn@uni-bielefeld.de) ,A. Krämer (alexander.kraemer@uni-bielefeld.de) , Chen Xingfeng (chenxf@irsa.ac.cn) , Yu Tao (yutao@irsa.ac.cn)
Gu Xingfa   (guxingfa@irsa.ac.cn)

Megastädte sind eines der größten Quellgebiete anthropogenen Aerosols. Sie fungieren daher als Punktquellen für Aerosole im globalen Kontext und beeinflussen lokal die Gesundheit der Menschen. Daher ist es wichtig den Aerosolgehalt der Atmosphäre in Megastadt-Regionen möglichst genau zu bestimmen. In Regionen ohne dichtes Messnetz für Spurenstoffe, ist die Satelliten-Fernerkundung ein

geeignetes Mittel, um Spurenstoffe regelmäßig zu messen. Zur Ableitung der Aerosoloptischen Dicke aus Satellitendaten muss das empfangene Signal der reflektierten Strahlung in einen atmosphärischen Anteil und den Bodenanteil getrennt werden. Der Bodenanteil ist durch die Boden-Albedo oder –Reflektivität gegeben, welcher schwierig aus Satellitenmessungen bestimmt werden kann.

Spektral und räumlich hochaufgelöste Messungen der Bodenalbedo wurden mit der Kombination aus den flugzeuggetragenen Messsystemen SMART-Albedometer (400-2100 nm) und einer Kamera (Geospatial Systems, MS 4100) mit 3 spektralen Kanälen gemessen. Der erste Datensatz wurde in Leipzig im Jahr 2007 aufgenommen, der zweite Datensatz konnte im Dezember 2009 in Zhongshan, China, gemeinsam mit unseren chinesischen Kooperationspartnern des Institute of Remote Sensing Applications erfasst werden.

Das Satelliten-Tool IMAPP der Universität Wisconsin wurde auf Computern des Instituts für Meteorologie installiert und steht nun für wissenschaftliche Zwecke in diesem, sowie anderen Projekten bereit.

Es wird erwartet, dass durch Verwendung der hochaufgelösten Messdaten der Bodenalbedo im Aerosol-Retrieval der Satellitendaten das Resultat der Aerosol Optischen Dicke verbessert werden kann.

Weiterführung: ja

Finanzierung: DFG, SPP 1233 (WE 1900/16-2)

****

Entwicklung eines tomographischen Wasserdampfsondierungssystems auf der Basis von GNSS Daten.
Development of a tomographic water vapour sounding system based on GNSS data

Prof. Dr. G. Tetzlaff (tetzlaff@uni-leipzig.de), Dr. A. Raabe (raabe@uni-leipzig.de), Dr, M. Bender
Prof. Dr. M. Rothacher, Dr. J. Wickert, Dr. G. Dick, Dr. G. Gendt, (GFZ Potsdam)

Die hochgenaue Positionsbestimmung mit Hilfe des GPS oder auch demnächst verfügbarem GALILIEO-Systems ist erst möglich, wenn die Atmosphäreneinflüsse auf die Signallaufzeiten korrigiert werden. Diese Korrekturen repräsentieren auch den Einfluss des atmosphärischen Wasserdampfes auf die Laufzeiten der GPS-Signale an der entsprechenden Bodenstation. Die GNSS-Bodennetze (*Global Navigation Satellite System*) in Europa erreichen eine solche räumliche Dichte, so dass es mit Ihnen möglich wird eine dreidimensionale Verteilung des Wasserdampfes in der Atmosphäre unter Zuhilfenahme von tomografischen Rekonstruktionstechniken abzuleiten.

Dazu sind Abschätzungen der Genauigkeiten notwendig und Algorithmen zu erarbeiten, die ein Zusammenfassen der an einzelnen Stationen vorliegenden Daten ermöglicht.

Ziel ist es, den numerischen Wettermodellen quasi Echtzeit-Informationen über die dreidimensionale Wasserdampfverteilung in der Atmosphäre z.B. über Europa zur Verfügung zu stellen.

Weiterführung: Ja

Abschätzung des Wasserdargebotes durch gleichzeitiges Auftreten von Schneeschmelze und Starkregen in Sachsen
Estimation of the flow of water when fall together snowmelt and heavy rain in Saxony

Prof. Dr. G. Tetzlaff (tetzlaff@uni-leipzig.de), Dr. A.Raabe (raabe@uni-leipzig.de), Dipl. Phys. C. Walther, Dipl. Met. D. Sabath

Die Maximalen Abflussmengen aus spezifischen Wassereinzugsgebieten in der Mittelgebirgsregion von Sachsen werden abgeschätzt, wobei die Abflussmengen für den Fall des Zusammentreffens einer maximalen Niederschlagmenge und einer maximalen Schneeschmelzrate berechnet werden.

Weiterführung: nein

****

Auswirkung möglicher Klimaänderung auf das Wasserdargebot in verschiedenen Wassereinzugsgebieten Sachsens
Potential climate change impacts on the water supply in different drainage basins of Saxony

Prof. Dr. G. Tetzlaff (tetzlaff@uni-leipzig.de), Dr. A. Raabe (raabe@uni-leipzig.de), Dr. M. Barth (mbarth@uni-leipzig.de)

Klimaveränderungen wirken sich auf das Wasserdargebot im Einzugsgebiet von Talsperren aus. Aus den Langfristvorhersagen unterschiedlicher Klimamodelle, deren Grundlage verschiedene Emissions-Szenarien sind, sollen Wasserdargebotsaussagen für die Region der sächsischen Talsperren abgeschätzt werden.

Weiterführung: Ja

****

Arbeitsgruppe Hochatmosphäre
Upper Atmosphere

Strukturelle Änderungen von langfristigen Trends in dynamischen Parametern der mittleren Atmosphäre
Structural changes in long-term trends of the dynamics of the upper atmosphere

Prof. Dr. Christoph Jacobi (jacobi @ rz.uni-leipzig.de), Dr. J. Lastovicka, P. Krisan (IAP der Akademie der Wissenschaften, Prag), Prof. Yu.I. Portnyagin, Dr. E.G. Merzlyakov (Institut für Experimentelle Meteorologie, Obninsk)

Die Analyse experimenteller Daten hat gezeigt, dass, im Gegensatz zum Verhalten der Temperatur der mittleren Atmosphäre, die Dynamik der Mesosphäre und unteren Thermosphäre (MLT) keinen eindeutigen Trend aufweist, was wahrscheinlich auf das Zusammenwirken verschiedener Einflussfaktoren aus der unteren und mittleren Atmosphäre zurück zu führen ist. Um die Rolle dieser verschiedenen Faktoren zu klären, sollen Windzeitreihen der MLT im Hinblick auf Trends und speziell Trendänderungen untersucht werden, wobei aufgrund der relativen Kürze der verfügbaren Datensätze neue statistische Verfahren zum Einsatz kommen werden. Die Analysen werden durch Vergleiche mit stratosphärischen, troposphärischen und ionosphärischen Parametern vervollständigt, sowie die Rolle externer Einflüsse geklärt (solarer Fluss, Geomagnetismus). Numerische Simulation der Antwort der mittleren Atmosphäre auf Änderungen der troposphärischen und stratosphärischen Zirkulation wird ebenfalls zur Klärung der Frage, welche Einflüsse die Windänderung der MLT steuern, beitragen.

Weiterführung: ja

Finanzierung: Drittmittel (DFG JA836/22-1, GA-CR)

****

Arbeitsgruppe Hochatmosphäre
Upper Atmosphere

Selbstkalibrierende EUV/UV-Spektrophotometer SolACES
Auto-Calibrating EUV/UV Spectrophotometers SolACES

Prof. Dr. Christoph Jacobi (jacobi @ rz.uni-leipzig.de), Dr. B. Nikutowski

Das vom Fraunhofer IPM entwickelte Instrument SolACES (Solar Auto Calibrating EUV / UV Spectrometers), soll die solare Strahlung im Wellenlängenbereich von 17 bis 220 nm spektral aufgelöst mit hoher radiometrischer Absolutgenauigkeit messen. Im Projekt erfolgt neben Unterstützung der Missionsvorbereitung und -begleitung die Aufbereitung der Rohdaten, Datenauswertung, Erstellung empirischer Modelle der EUV-Strahlung, und Analyse der ionosphärischen Reaktion auf EUV-Variabilität.

Weiterführung: ja

Finanzierung: Auftrag (Fraunhofer-Institut für Physikalische Messtechnik)

****

Arbeitsgruppe Hochatmosphäre
Upper Atmosphere

Aufbau einer Streudatenbank SCATDB
Constructing a scatter characteristics data bank

Prof. Dr. Christoph Jacobi (jacobi @ rz.uni-leipzig.de), Dr. J. Wauer

Es hat sich gezeigt, dass Chebyshev-Teilchen ein gutes Modell zur Beschreibung der Lichtstreuung an rauen Teilchen darstellen. Ziel ist es, mittels Störungstheorie den Konvergenzbereich für diese Teilchengeometrie zu erweitern. In der Datenbank SCATDB am DLR sind bislang die Streueigenschaften von Rotationsellipsoiden enthalten. Diese Streudatenbank wird auf weitere Geometrien ausgedehnt und die dazugehörige Nutzeroberfläche weiter auszubauen.

Weiterführung: ja

Finanzierung: Auftrag (DLR)

****

Arbeitsgruppe Hochatmosphäre
Upper Atmosphere

Wellen in der mittleren Atmosphäre
Waves in the middle atmosphere

Prof. Dr. Christoph Jacobi (jacobi @ rz.uni-leipzig.de), Prof. A.I. Pogoreltsev, E.N. Savenkova, A.S. Zarubin, Russian State Hydrometeorological University

Das Projekt umfasst experimentelle und numerische Studien atmosphärischer Wellenaktivität insbesondere in den Schichten oberhalb der Tropopause. Die Arbeiten beinhalten sowohl langperiodische planetare Wellen als auch kurzperiodische Schwerewellen. Spezielle Arbeitsziele sind einerseits die detaillierte Darstellung und Analyse des Übergangs von der stratosphärischen Winter- zur Sommerzirkulation, und die Untersuchung der Ausbreitung von Schwerwellen bis in die Thermosphäre. Zur Anwendung kommen dabei sowohl Reanalysedaten als auch ein numerisches Zirkulationsmodell.

Weiterführung: nein

Finanzierung: DAAD, Leonard-Euler-Stipendienprogramm

****

Arbeitsgruppe Hochatmosphäre
Upper Atmosphere

Analyse atmosphärischer Zirkulationsmuster
Analysis of atmospheric circulation

Prof. Dr. Christoph Jacobi (jacobi @ rz.uni-leipzig.de), Prof. A.I. Pogoreltsev, V. Nikolaeva, M. Vasilenko, Russian State Hydrometeorological University

Innerhalb des Projekts wird die Variabilität der Atmosphäre der Nordhemisphäre anhand der Quasi-zweijährigen Schwingung im Detail untersucht werden, und Fernwirkungen dieses Zirkulationsmusters analysiert. In einem zweiten Teil wird die Variabilität der polaren Hochatmosphäre aufgrund extraterrestrischer Einflüssen experimentell und numerisch untersucht.

Weiterführung: ja

****

Arbeitsgruppe Hochatmosphäre
Upper Atmosphere

Aktivierung von Wolkenkondensationskernen
Activation of cloud condensation nuclei

Prof. Dr. Christoph Jacobi (jacobi @ rz.uni-leipzig.de), Prof. G. Shved, V.V. Merkulov, St. Petersburg State University

Innerhalb des Projekts sollen die hygroskopischen Eigenschaften und die Aktivität als Wolkenkondensationskern verschiedener organischer und anorganischer Partikel mit Hilfe von HDFA untersucht werden. Die Arbeiten umfassen Messungen und theoretische Analyse.

Weiterführung: nein

****

Arbeitsgruppe Hochatmosphäre
Upper Atmosphere

Signature of Planetary Waves in the Thermosphere/Ionosphere System
Signatur planetarer Wellen im System Thermosphäre-Ionosphäre

Prof. Dr. Christoph Jacobi, jacobi @ rz.uni-leipzig.de,
Dipl.-Met. P. Hoffmann

Die Untersuchung der Reaktion des Systems Thermosphäre/Ionosphäre (thermo-sphere/ionosphere system, TIS) auf planetare Wellen (PW) in der neutralen Atmosphäre ist Inhalt des Projekts. Da PW sich nicht direkt in die Thermosphäre ausbreiten können, PW-typische Oscillationen (PWTO) aber in diesen Höhenregionen (Ionosphäre) beobachtet werden, müssen indirekte Prozesse für die Ausbreitung verantwortlich sein. Die Arbeit besteht aus drei Teilen: Der erste Teil fokussiert auf die Analyse von PW Signaturen im Gesamtelektronengehalt sowie ionosphärischen Störungen (beide basierend auf GPS-Messungen). Im zweiten Teil werden stratosphärische und mesosphärische Daten (Reanalysen, SABER-Temperaturen und Radardaten) für PW und Schwerewellenanalysen herangezogen, um eine mögliche Interaktion von Schwerewellen und PW nachweisen zu können. Im dritten Teil werden die Ergebnisse beider Analysen verglichen, um die Effekte von Schwerewellen in der Ionosphäre zu bestimmen, und den möglichen Transport der PW Energie durch Sekundärwellen nachzuweisen. Die Arbeit erfolgt in Zusammenarbeit mit dem DLR-IKN, Neustrelitz.

Weiterführung: nein

****

AG Akustik
Acoustics

Akustische Fernerkundungsstudie zum Einfluss interner Gravitationswellen auf die untere Atmosphäre
Acoustic remote sensing study of the influence of internal gravity waves on the lower atmosphere

Dr. Anke Kniffka, Dr. Armin Raabe,
Jun.-Prof. Dr. Astrid Ziemann (ziemann@uni-leipzig.de)

Dr. Igor Chunchuzov, Dr. Sergey N. Kulichkov, Dr. Vitaly G. Perepelkin (Russian Academy of Science, Obukhov Institute of Atmospheric Physics)

Interne Gravitationswellen (IGW), die durch verschiedene Ursachen erzeugt werden, tragen in bedeutendem Umfang zum Power-Spektrum von Windgeschwindigkeits- und Temperaturfluktuationen innerhalb der Atmosphärischen Grenzschicht (AGS) bei. Das Hauptziel des Projektes ist die Untersuchung der räumlichen Struktur und statistischen Eigenschaften der meso- und mikroskaligen Windgeschwindigkeits- und Temperaturfluktuationen in der AGS innerhalb von Raum-Zeit-Skalen, die für die IGWs bedeutsam sind. Dabei werden verschiedene akustische Fernerkundungsverfahren eingesetzt, welche vertikale und horizontale Schnittbilder durch Temperatur- und Windfelder liefern. Die erzielten Ergebnisse sollen zur Entwicklung von Parametrisierungen der stabilen AGS in numerischen Modellen der Atmosphäre beitragen.

Weiterführung: nein

****

AG Akustik
Acoustics

Darstellung von Strömungen mittels akustischer Tomografie im Windkanal
Observation of air streams with acoustic tomography in a wind channel

Dr. Armin Raabe (raabe@uni-leipzig.de),
Dipl. Met. M. Barth (mbarth@uni-leipzig.de)

Das am Institut für Meteorologie entwickelte System zur Erfassung von Strömungseigenschaften und Temperaturverteilungen innerhalb einer Messfläche mittels akustischer Laufzeitmessungen soll hinsichtlich der räumlichen Auflösung

des Strömungsfeldes, sowie der Möglichkeit, Felder 3-dimensional zu erfassen, erweitert werden. Wobei die Auflösung in Zeit- und Raumbereiche hinein verfeinert wird, die für die Skala eines Windkanals Verwendung finden können.
Hierfür sollen Algorithmen zur Vektortomographie entwickelt, in das Messsystem integriert und bei experimentellen Untersuchungen analysiert werden.

Weiterführung: nein

****

AG Akustik
Acoustics

Räumlich explizite Modellierung der Ausbreitung von Pflanzen-Diasporen
Explicit spatial modelling of long-distance dispersal of plant diaspores

Dr. Armin Raabe (raabe@uni-leipzig.de) Dipl. Phys. S. Horn,
Dr. O. Tackenberg, Dipl.-Ing. Heidrun Will , Univ. Frankfurt M.

Die Fernausbreitung (>100m) von Pflanzendiasporen hat signifikante Auswirkungen auf eine Reihe von ökologischen und evolutions-biologischen Prozessen. Aufgrund von methodischen Problemen sind diese Prozesse durch Messungen allein nicht erfassbar. Um diese Probleme zu lösen werden mechanistische bzw. stochastische Ausbreitungsmodelle verwendet. Auf der Grundlage des existierenden mechanistischen Windausbreitungsmodells PAPPUS und dem dreidimensionalen Stömungsmodell ASAM soll ein mikroskaliges Windfeldmodell entwickelt werden, welches unter Berücksichtigung der Struktur der Landschaft neben der Diagnose auch eine Prognose der räumlichen Ausbreitung von Pflanzendiasporen ermöglicht. Dazu sollen in dem Modell vor allem die räumliche Verteilung der Turbulenz, speziell thermisch induzierte Auf- und Abwinde (burst events) in der bodennahen atmosphärischen Grenzschicht berücksichtigt werden. Um die numerischen Simulationen zu validieren werden Experimente in flachem homogenen Terrain und in gegliedertem Gelände mit unterschiedlichen Pflanzenarten durchgeführt. Diese Experimente liefern genaue Beobachtungen der Windbedingungen und dienen zur Bestimmung der turbulenten Strukturen in Abhängigkeit von den thermischen und orographischen Bedingungen.

Weiterführung: nein

****

AG Akustik
Acoustics

Erprobung eines neuen Emissionsmessverfahrens mittels FTIR-Spektrometrie und längenmittelnder Messung des turbulenten Austauschkoeffizienten

Test of a new emissions measuring procedure with FTI-Spectrometry and line averaged measurement of the turbulent eddy coefficient.

Prof. Dr. Klaus Schäfer FZ Karlsruhe, Institut für Meteorologie Garmisch-Partenkirchen
Dr. A. Raabe, Dipl.Ing. F. Kaiser, Dipl. Met. M. Barth, Dipl. Met. M. Wilsdorf

Unter Verwendung eines über der gesamten Beobachtungsfläche angeordneten akustischen Messverfahrens wird die höhenveränderliche, bodennahe Windgeschwindigkeit bestimmt. Das so bestimmte Windprofil repräsentiert die längengemittelten vertikalen Windverhältnisse auf der Linie der FTIR-Spektrometermessungen. Auf dieser Art werden zum ersten Mal räumliche Mittel von akustischen Geschwindigkeitsmessungen und Emissionsraten eines klimarelevantes Gases (N_2O) kombiniert.

Weiterführung: nein

****

AG Akustik
Acoustics

Schallausbreitung in urbanen Gebieten unter Berücksichtigung des Atmosphärenzustandes
Sound propagation in urban areas considering the state of the atmosphere

Dipl. Met. Gabi Fischer,
Jun.-Prof. Dr. Astrid Ziemann (ziemann@uni-leipzig.de)

Aufgrund der dynamischen Entwicklung von Stadtregionen sind diese verdichteten Räume besonders anfällig gegenüber kurz- und langfristig wirkenden Risikofaktoren, wie z.B. Lärm, für die Gesundheit und Lebensqualität der Stadtbewohner. Vor allem der Straßenverkehrslärm stellt im urbanen Raum ein ungelöstes Umweltproblem mit Langzeitauswirkungen dar.
Unter Verwendung eines Schallstrahlenmodells wird der Einfluss der Atmosphärenstruktur auf die Ausbreitung des Schalls von einer Punkt- bzw. Linienquelle im urbanen Raum simuliert, um die Raum-Zeitskalen zu ermitteln, auf welchen der Atmosphäreneinfluss im städtischen Lärmmanagement zu berücksichtigen ist. Untersucht wird dabei die Schallausbreitung ab einigen 10 m Entfernung, da dort die Einflüsse meteorologischer Parameter, wie z.B. Lufttemperatur, Windvektor und Luftfeuchte, signifikant nachweisbar sind. Zur Validierung der Modellergebnisse sowie zur Abschätzung der Fehler und Grenzen des Modells soll eine Messkampagne im urbanen Raum von Leipzig stattfinden. Die Durchführung von Sensitivitätsstudien mit dem validierten Modell ermöglicht es, charakteristische Längenskalen für die Lärmbelastung abzuschätzen und Lärmindikatoren in Abhängigkeit von verschiedenen atmosphärischen Grenzschichtbedingungen zu bewerten.

Weiterführung: ja

****

AG Akustik
Acoustics

Adaption eines mikrometeorologischen Messsystems zur Bestimmung von Temperatur- und Windfeldern im Bereich einer Lysimeterfläche
Adaption of a micrometeorological measurement system to determine temperature and wind fields within a lysimeter surface

Dr. Armin Raabe (raabe@uni-leipzig.de), Dipl. Met. M. Barth, Dipl. Met. G. Fischer
Dr. M. Seyfarth, Umwelt-Geräte-Technik GmbH Müncheberg
Dr. S. Reth, Helmholtz Zentrum München

Das mikrometeorologische Messsystem der akustischen Laufzeittomographie ermöglicht es, flächengemittelte Verteilungen der Temperatur und des Windvektors in einem Medium zu bestimmen. Zur Visualisierung von Strömungsvorgängen und Temperaturverhältnissen über einem einzelnen Lysimeter mit einer Grundfläche von 1m² wird die akustische Messtechnik eines am Leipziger Institut für Meteorologie entwickelten Labormesssystems über selbigem aufgebaut, um die gesuchten meteorologischen Felder rekonstruieren zu können. Hierzu ist eine Anpassung der bereits vorhandenen Software an das speziell für das Lysimeter entwickelte Messkonzept notwendig. Verschiedene Testmessungen dienen zur Bewertung der Anwendbarkeit des entwickelten Systems auf der beschriebenen Skala. Insbesondere werden dabei die Genauigkeiten der rekonstruierten Felder, auch in Bezug auf die Messkonstruktion, analysiert.

Weiterführung: nein

****

AG Akustik
Acoustics

Wetterabhängige Schallausbreitung, Lärmschutz an Schießplätzen der Bundeswehr
Weather permitting sound propagation, noise protection at artillery range of the Bundeswehr

Dr. Armin Raabe (raabe@uni-leipzig.de),
Jun.-Prof. Dr. Astrid Ziemann (ziemann@uni-leipzig.de
Dipl. Met. Michael Wilsdorf (mwils@uni-leipzig.de)

Dieses Projekt setzt die langjährige und erfolgreiche Zusammenarbeit des Institutes für Meteorologie der Universität Leipzig mit der Bundeswehr, hier im speziellen mit dem AGeoBw, fort. Anlass waren Artillerieschießen, bei denen die akustische

Belastung in der Nachbarschaft von TrÜb-Plätzen derart erhöht war, dass es zu Beschwerden / Klagen von Bürgern und der Kommunen kam. Ein verstärkender Faktor war in den betreffenden Fällen u.a. die Wettersituation, bei der eine ausgeprägte Temperaturinversion zu einer anomalen Schallausbreitung führte.

Ziel dieser Studie ist deshalb die weitere Verbesserung der bestehenden Schallimmissionsprognose, sowohl in konzeptioneller Hinsicht, als auch in ihrer Praktikabilität sowie in der statistischen Absicherung der zu Grunde liegenden Auswertungen.

Datengrundlagen der schallklimatologischen Untersuchungen sind Radiosondenaufstiege des Deutschen Wetterdienstes und der Bundeswehr, die im Zeitraum 2001 bis mindestens 2007 an 14 Stationen im Bundesgebiet jeweils zu den Terminen 00 UTC und 12 UTC durchgeführt wurden. Damit erweitern diese Daten den untersuchten Datenumfang einschließlich der Vorgängerstudie (von 1990 bis 2000) auf 18 Jahre.

Weiterführung: ja

****

2. Wiss. Veröffentlichungen Institut für Meteorologie 2009

Haupt autor	Autoren / Herausgeber	Titel, in: Zeitschrift, Ort; Verlag, Jahr, Seite von – bis ….
	Arras, C. ; Jacobi, Ch. ; Wickert, J.	Semidiurnal tidal signature in sporadic E occurrence rates derived from GPS radio occultation measurements at midlatitudes. Ann. Geophys. 27, 2009, 2555–2563
	Barth, M.	Akustische Tomographie zur zeitgleichen Erfassung von Temperatur- und Strömungsfeldern. Wiss. Mitt. Inst. f. Meteorol. Uni. Leipzig, Bd. 44, 2009, 178 S.
	Bender, M.; Dick, G.; Wickert, J.; Ramatschi, M.; Ge, M.; Gendt, G.; Rothacher, M.; Raabe, A. & Tetzlaff, G.	Estimates of the information provided by GPS slant data observed in Germany regarding tomographic applications Journal of Geophysical Research, 2009, 114, D06303
	Beyer, M.; Raabe, A.	Standardisierte Turbulenzspektren für die numerische Berechnung der windgetriebenen Ausbreitung von Pflanzensamen Wiss. Mitt. Inst. für Meteorol. Univ. Leipzig, 45, 2009, 23-36
	Beyer, M.; Schönfeldt, H.-J.	Vermessung von äolischen Sandrippeln,, Wiss. Mitt. Inst. für Meteorol. Univ. Leipzig, 45, 2009, 1-12
	Bierwirth, E., Wendisch, M.; Ehrlich, A.; Heese, B.; Tesche, M.; Althausen, D.; Schladitz, A.; Müller, D.; Otto, S.; Trautmann, T.; Dinter, T.;. von Hoyningen-Huene, W; Kahn, R.	Spectral surface albedo over Morocco and its impact on radiative forcing of Saharan dust. *Tellus,* 61B, 2009, 252-269, DOI: 10.1111/j.1600-0889.2008.00395.x
	Chunchuzov I.; Kulichkov, S.; Perepelkin, V.; Ziemann, A.; Arnold, K.; Kniffka, A.	Mesoscale variations of the parameters of acoustic signals induced by atmospheric gravity waves. J. Acoust. Soc. Am. 125, 2009, , 651-663
	Dinter, T.; von Hoyningen-Huene, W.;. Burrows, J. P.;. Kokhanovsky, A.; Bierwirth, E.; Wendisch, M.; Müller, D.; Kahn, R.; Diouri, M.	Retrieval of aerosol optical thickness for desert conditions using MERIS observations during the SAMUM campaign. *Tellus,* 61B*,* 2009, 229-238, DOI: 10.1111/j.1600-0889.2008.00391.x
	Ehrlich, A.; Wendisch, M.; Bierwirth, E.;. Gayet, J.-F; Mioche, G; Lampert, A.; Mayer, B.	Evidence of ice crystals at cloud top of Arctic boundary-layer mixed-phase clouds derived from airborne remote sensing. Atmos. Chem. Phys., 9, 9401–9416, 2009. www.atmos-chem-phys.net/9/9401/2009/
	Eichler, H.; Ehrlich, A.; Wendisch, M.; Mioche, G.; Gayet, J.-F.; Wirth, M.; Emde, C.; Minikin, A.	Influence of ice crystal shape on retrieval of cirrus optical thickness and effective radius: A case study. *J. Geophys. Res.*, 114, 2009, D19203, doi:10.1029/2009JD012215
	Eichler, K.; Raabe, A.; Bender, M.	Untersuchung des Einflusses atmosphärischer Strukturen auf GPS-Laufzeitverzögerungen, Wiss. Mitt. Inst. für Meteorol. Univ. Leipzig, 45, 2009, 99-114
	Fischer, G.; Ziemann, A.	Untersuchung des Einflusses der variierenden urbanen Grenzschicht auf die Schallausbreitung. Wiss. Mitt. Inst. für Meteorol. Univ. Leipzig, 45, 2009, 57-68
	Frey, W.;. Eichler, H; de Reus, M.; Maser, R.; Wendisch, M.; Borrmann, S.	A new airborne tandem platform for collocated measurements of microphysical cloud and radiation properties. *Atmos. Meas. Tech.*, 2, 2009, 147-158. www.atmos-meas-tech.net/2/147/2009/
	Gayet, J.-F.; Mioche, G.; Dörnbrack, A.; Ehrlich, A.; Lampert, A.; Wendisch. M.	Microphysical and optical properties of Arctic mixed-phase clouds. The 9 April 2007 case study. Accepted by *Atmos. Chem. Phys. Discuss.,* 9, 2009, 11333–11366, www.atmos-chem-phys-discuss.net/9/11333/2009/
	Hoffmann, P.; Jacobi, Ch.; Gimeno-Garcia, S.	Using Python language for analysing measurements from SABER instrument on TIMED satellite. Wiss. Mitt. Inst. f. Meteorol. Univ. Leipzig 45, 2009, 139-151
	Hoyningen-Huene v., W.; Dinter, T.; Kokhanovsky, A. A.; Burrows, J. P.;	Measurements of desert dust optical characteristics at Porte au Sahara during SAMUM, *Tellus*, 61B, 2009, 206-

Wendisch, M., Bierwirth, E.; Müller, D.; Diouri, M.	215, DOI: 10.1111/j.1600-0889.2008.00405.x
Jacobi, Ch.	Fünf Jahrzehnte Hochatmosphärenforschung am Observatorium Collm. Mitteilungen der DMG 02/2009, 8-9
Jacobi, Ch.	Possible signal of tropospheric circulation patterns in middle atmosphere dynamics, Collm (51.3°N, 13°E) mesosphere lower thermosphere winds 1979-2008. Wiss. Mitt. Inst. f. Meteorol. Univ. Leipzig 45, 2009, 153-162
Jacobi, Ch.; Arras, C.; Kürschner, D.; Singer, W.; Hoffmann, P.; Keuer, D.	Comparison of mesopause region meteor radar winds, medium frequency radar winds and low frequency drifts over Germany. Adv. Space. Res. 43, 2009; 247-252
Jacobi, Ch.; Fröhlich, K.; Portnyagin, Y.,; Merzlyakov, E.; Solovjova, T.; Makarov, N.;. Rees, D.; Fahrutdinova, A.;. Guryanov, V; Fedorov, D.; Korotyshkin, D.; Forbes, J.;. Pogoreltsev, A. ; Kürschner, D.	Semi-empirical model of middle atmosphere wind from the ground to the lower thermosphere. Adv. Space Res. 43, 2009, 239-246
Jacobi, Ch.; Hoffmann, P.; Liu, R.Q.; Križan, P.; Laštovička, J.; Merzlyakov, E.G.; Solovjova, T.V.; Portnyagin, Yu.I.	Midlatitude mesopause region winds and waves and comparison with stratospheric variability. J. Atmos. Solar-Terr. Phys. 71, 2009, 1540-1546
Kahn, R.; Petzold, A.; Wendisch, M.; Bierwirth, E.; Dinter, T.; Esselborn, M.; Fiebig, M.; Heese, P.; Knippertz, B.; Müller, D.; Schladitz, A.; von Hoyningen-Huene, W.	Desert dust aerosol air mass mapping in the western Sahara, using particle properties derived from space-based multi-angle imaging. *Tellus ,* 61B*,* 2009, 239-251, DOI: 10.1111/j.1600-0889.2008.00398.x.
Kniffka, A.; <u>Ziemann</u>, A.; Chunchuzov, I.; Kulichkov, S.; Perepelkin, V.	Anisotropy in internal gravity waves in conditions of a stable nocturnal boundary layer. Meteorol. Z., 18, 2009, 331-337
Knippertz, P.; Ansmann, A.; Althausen, D.; Müller, D.; Tesche, M.; Bierwirth, E.; Dinter, T.; Müller, T.; von Hoyningen-Huene, W.; Schepanski, K.; Wendisch, M.; Heinold, B.; Kandler, K.; Petzold, A.; Schütz; L.; Tegen, I.	Dust mobilization and transport in the northern Sahara during SAMUM 2006 – A meteorological overview. *Tellus,* 61B*,* 2009, 12-31. DOI: 10.1111/j.1600-0889.2008.00380.x
König, M.; Schönfeldt, H.-J.; Raabe, A.	Zur Korrektur von Infrarot-Thermografie-Bildern in der Meteorologie, Wiss. Mitt. Inst. für Meteorol. Univ. Leipzig, 45, 2009, 115-130
Lampert, A.; Ritter, C.; Hoffmann, A.,; Gayet, J.–F.; . Mioche, G.; Ehrlich, A.; Dörnbrack, A.; Wendisch, M.; Shiobaro, M.	Observations of boundary layer, mixed-phase and multi-layer Arctic clouds with different lidar systems during ASTAR 2007. *Atmos. Chem. Phys. Discuss.*, 9, 2009, 15125-15179, www.atmos-chem-phys-discuss.net/9/15125/2009/
Lampert, A.; Ehrlich, A.; Dörnbrack, A.;. Jourdan, O; Gayet, J.-F.; Mioche, G.; Shcherbakov, V.; Ritter, C.; Wendisch, M.	Microphysical and radiative characterization of a subvisible midlevel Arctic ice cloud by airborne observations – a case study. *Atmos. Chem. Phys.*, 9, 2009, 2647-2661. www.atmos-chem-phys.net/9/2647/2009/
Manson, A.H.; Meek, C.E.; Chshyolkova, T.; Aso, T.; Drummond, J.R.;. Hall, C.M; Hocking, W.K.; Jacobi, Ch.; Tsutsumi, M.; Ward, W.E.	Arctic tidal characteristics at EUREKA (80°N, 86°W) and SVALBARD (78°N, 16°E) for 2006/07: seasonal and longitudinal variations, migrating and non-migrating tides. Ann. Geophys. 27, 2009, 1153-1173
Merzlyakov, E.G.; Jacobi, Ch.; Portnyagin, Yu.I.; Solovjova, T.V.	Structural changes in trend parameters of the MLT winds based on wind measurements at Obninsk (55°N, 37°E) and Collm (52°N, 15°E). J. Atmos. Solar-Terr. Phys. 71, 2009,1547-1557
Otto, S.; Bierwirth, E.; Weinzierl, B.; Kandler, K.; Esselborn, M.; Tesche, M.; Wendisch, M.; Trautmann, T.	Solar radiative effects of a Saharan dust plume observed during SAMUM assuming spheroidal model particles. *Tellus,* 61B*,* 2009, 270-296, DOI: 10.1111/j.1600-0889.2008.00389.x

	Ostashev, V. E.; Vecherin, S. N.; Wilson, D. K.; Ziemann, A.; Goedecke, G.H.	Recent progress in acoustic travel-time tomography of the atmospheric surface layer. Meteorol. Z., 18, 2009,125-133
	Plagemann, S.; Schönfeldt , H.-J.	Mittlere Saltationslänge und deren Bestimmung, Wiss. Mitt. Inst. für Meteorol. Univ. Leipzig, 45, 2009, 13-22
	Sathishkumar, S.; Sridharan, S.; Jacobi, Ch.	Dynamical response of low-latitude middle atmosphere to major sudden stratospheric warming events. J. Atmos. Solar-Terr. Phys. 71, 2009, 857-865
	Schmidt, Ch.; Ziemann, A.; Schlink, U.	Lässt sich die Aerosolbelastung von Stadtgebieten aus Satellitenbildern ableiten? Wiss. Mitt. Inst. für Meteorol. Univ. Leipzig, 45, 2009, 83-98
	Schmidt, K. S.; Feingold, G.; Pilewskie, P.; Jiang, H.; Coddington, O.;. Wendisch, M.	Irradiance in polluted cumulus fields: Measured and modeled cloud-aerosol effects. *Geophys. Res. Lett.*, 36, 2009, L07804, doi:10.1029/2008GL036848.
	Stober, G.; Ch. Jacobi	Cosmic Noise Observation with a Standard Meteor Radar. Wiss. Mitt. Inst. f. Meteorol. Univ. Leipzig 45, 2009, 163-177
	Walther, C.	Einfluss der Orografie auf konvektiven Niederschlag, Wiss. Mitt. Inst. für Meteorol. Univ. Leipzig, 45, 2009, 37-44
	Wilsdorf, M.; Fischer, G.; Ziemann, A.	Einfluss der vertikalen Auflösung der Eingangsprofile bei einem Schallstrahlenmodell. Wiss. Mitt. Inst. f. Meteorol. Uni. Leipzig, 45, 2009, 45-56
	Xu, X.; Manson, A.H.; Meek, C.E.; Chshyolkova, T.; Drummond, J.R.; Hall, C.M.; Jacobi, Ch.; Riggin, D.; Hibbins, R.E.; Tsutsumi, M.; Hocking, W.K.; Ward, W.E.	Relationship between variability of the semidiurnal tide in the Northern Hemisphere mesosphere and quasi-stationary planetary waves throughout the global middle atmosphere. Ann. Geophys. 27, 2009, 4239–4256
	Ziemann, A.; Schimmel, R.	Abschätzung des Atmosphäreneinflusses auf Messung und Prognose von Schallpegeln an Autobahnen. Wiss. Mitt. Inst. für Meteorol. Univ. Leipzig, 45, 2009, 69-82

Wiss. Mitarbeiter am Institut für Meteorologie, 2009

Name	Titel	Vorname
Barth	Dr.	Manuela
Bauer		Stefan
Bierwirth	Dr.	Eike
Braun		Nico
Ehrlich	Dr.	André
Feck-Yao		Wolfgang
Fischer		Gabi
Henrich		Frank
Hirsch		Kerstin
Hoffmann		Peter
Jacobi	Prof. Dr.	Christoph
Kaiser		Falk
Liu	Dr.	Renqiang
Metz	Prof. Dr.	Werner
Mey		Britta
Nikutowski	Dr.	Bernd
Raabe	Dr.	Armin
Rehnert		Jutta
Schönfeldt	Dr.	Hans-Jürgen
Staake		Karin
Tetzlaff	em. Prof. Dr.	Gerd
Walter		Jörg
Wauer	Dr.	Jochen
Weiße		Frank
Wendisch	Prof. Dr.	Manfred
Wilsdorf		Michael
Ziemann	Jun.-Prof. Dr.	Astrid

| Immatrikulationen Meteorologiestudenten | | | | | | BSC | | | | | | | |
Datum	Semester	1.FS	2. FS	3.FS	4.FS	5.FS	6. FS	7.FS	8.FS	9. FS	10.FS	>10.FS	Summe
15.10.2009	WS 09/10	67	0	21	0	20	0	11	0	14			
15.04.2009	SS 09	0	71	0	28	0	12	0	14	0	23		
15.10.2008	WS 08/09	71	0	28	0	12	0	14	0	23	1	25	174
15.04.2008	SS 08	0	54	0	14	0	19	0	25	1	18	13	144
15.10.2007	WS 07/08	98	0	15	0	22	0	26	1	18	2	19	201
15.04.2007	SS 07	0	23	0	32	0	35	1	19	2	13	12	137
13.12.2006	WS 06/07	31	0	40	0	36	0	24	2	14	1	17	175
	SS 06	0	82	0	46	0	29	3	14	1	17	7	200
15.10.2005	WS 05/06	109	0	49	0	30	2	16	1	17	1	13	237
07.06.2005	SS 2005	0	83	0	33	1	19	0	17	1	12	8	177
08.12.2004	WS 04/05	97	0	35	1	20	0	19	0	12	1	15	200
07.06.2004	SS 04	0	57	0	24	0	18	1	13	0	11	10	134
03.12.2003	WS 03/04	68	1	25	0	20	1	13	1	12	1	13	155
26.05.2003	SS 03	0	42	0	19	0	15	0	14	1	12	6	109
14.10.2002	WS 02/03	45	0	19	0	16	0	15	1	12	1	9	118
29.05.2002	SS 02	0	38	0	20	0	17	1	13	2	7	4	102
06.12.2001	WS 01/02	43	0	21	0	16	0	13	0	7	0	5	105
31.05.2001	SS 01	0	31	1	22	0	19	0	8	0	5	3	89
07.12.2000	WS 00/01	41	1	27	0	22	0	8	0	6	1	6	112
05.05.2000	SS 00	0	34	0	24	0	8	0	8	1	6	3	84
01.12.1999	WS 99/00	40	0	24	0	9	0	9	0	6	1	6	95
31.05.1999	WS 99	0	29	0	11	0	13	0	8	1	5	3	70
16.12.1998	WS 98/99	36	0	11	0	17	1	9	1	5	0	8	88
22.04.1998	SS 98	1	21	0	17	0	8	1	6	0	7	2	63
10.11.1997	WS 97/98	29	0	17	0	10	1	8	0	7	0	4	76

(MSC marked in yellow in the BSC column; 11 in the 7.FS column of row WS 09/10 highlighted in yellow)

Abschlussarbeiten Institut für Meteorologie 2009

Promotionen

Manuela Barth
(Betreuer: Prof. Tetzlaff; Verleihungsbeschluss: 19.01.2009)
„Akustische Tomographie zur zeitgleichen Erfassung von Temperatur- und Strömungsfeldern"

Andreas Tilgner
(Betreuer: Prof. Herrmann; Verleihungsbeschluss: 20.04.2009)
„Modelling of the physico-chemical multiphase processing of tropospheric aerosols"

Verena Grützun
(Betreuer: Prof. Renner; Verleihungsbeschluss: 20.07.2009)
„Influence of Aerosol Particles on Deep Convective Clouds: Investigations with the New Model LM-SPECS"

Diplom-Abschlüsse 2009

Beyer, Marcus	Aeolian Sand Ripples: Theory and Experiments
Bräuer, Peter	Mechanismusentwicklung zur troposphärischen Halogenchemie
Braun, Nico	Optimierung des Downscaling in der Mikroskala auf der Basis eines 3D-Mesoskalen-Modells
Ditas, Florian	Aerosolnumber-size distributions inside and outside clouds: Characterisation of a new measurement system and first results
Eichler, Karolin	Untersuchung von atmosphärischen Einflüssen auf simulierte GPS-Laufzeitverzögerungen
Freitag, Steffen	Callenging HYSPLIT Trajectories over the equatorial Pacific with measured aerosol physiochemistry and trace gases
Fruntke, Julia	Charakterisierung der Grenzschicht anhand von Vertikalwindmessungen mit einem Doppler-Lidar
Hartmann, Susan	First Experimental and theoretical Studies concerning Heterogeneous Ice Nucleation at the Leipzig Aerosol Cloud Interaction Simulator
Herold, Christian	Wasserdampf- und Temperaturmessung mittels Lidar während COPS und SAMUM
Jendrzi, Doreen	Zusammenhang zwischen der persönlichen Belastung durch Partikel und Lärm
Katzwinkel, Jeannine	Investigation of the thermodynamics of deliquescence/efflorescence induced hysteresis in hygroscopic growth of soluble particles
König, Marcel	Infrarotmesstechnik und ihre Anwendung in der Meteorologie
Kunze, Thomas	Einfluss der Rand- und Anfangsbedingungen sowie der Eisnukleation auf die Starkregenvorhersage des COSMO-DE am Beispiel des Elbehochwassers 2002
Pfeifer, Sascha	Bestimmung der Schwellengeschwindigkeit und Parameter der Transportgleichung des äolischen Sedimenttransports unter Berücksichtigung der Statistik des Windfeldes und der Saltation
Plagemann, Sabrina	Bestimmung der Sedimenttransportschwellen, der Saltationslängen und -höhen mittels Messungen am Zingster Strand

Schmidt, Christian	Anwendung und Validierung der Differentiellen Texturanalyse von Satellitenbildern zur Bestimmung der Aerosolbelastung in Leipzig
Schrödner, Roland	Modellierung von wolkenchemischen Prozessen mit dem Chemie-Transport-Modell MUSCAT
Stanislawsky, Juliane	Parameterizing temperature and ozone changes in 2-D atmospheric chemistry models

Bachelor-Abschlüsse 2009

Augustin, Stefanie	Untersuchung des Innenraumklimas und dessen Zusammenhänge zu den Wetterbedingungen
Bach, Stefan	Ertragsvorhersagen für landwirtschaftliche Kulturen auf Basis von phänologischen und meteorologischen Daten am Beispiel von Wintergetreide
Bethke, Julia	Algorithmus zur Erkennung von Frontendurchgängen anhand von Zeitreihen der Beobachtungsdaten einer Station
Bley, Sebastian	Globale Darstellung von Klimaänderung in der unteren Troposphäre
Fischer, Stephan	Atlas zu Trends und Entwicklungen in der Stratosphäre
Heyner, Frank	Untersuchung des Hagelwachstums anhand der Unwetterlage vom 16.6.2006 im Raum Leipzig
Höpner, Friederike	Einfluss von Wolken auf die Aerosolpartikelkonzentration in der oberen Troposphäre
Wagner, Janet	Sonnenbrandgefährdung an gartenbaulichen Kulturen: Mögliche agrarmeteorologische Ursachen
Wenzel, Julia	Barokline Wellen in einem rotierenden asymetrischen Tank

Wissenschaftliche Mitteilungen aus dem Institut für Meteorologie der Universität Leipzig

Band 24   *O. Fanenbruck*, 2001: Ein thermophysiologisches Bewertungsmodell mit Anwendung auf das Leipziger Stadtgebiet

Band 25   *M. Lange*, 2001: Modellstudien zum CO_2-Anstieg und O_3-Abbau in der mittleren Atmosphäre und Einfluß des Polarwirbels auf die zonale Symmetrie des Windfeldes in der Mesopausenregion

Band 26   *A. Raabe* und *K. Arnold* (Edn.), 2002: Meteorologische Arbeiten aus Leipzig VII

Band 27   *M. Simmel*, 2002: Ein Modul zur spektralen Beschreibung von Wolken und Niederschlag in einem Mesoskalenmodell zur Verwendung auf Parallelrechnern

Band 28   *H. Siebert*, 2002: Tethered-Balloon Borne Turbulence Measurements in the Cloudy Boundary Layer

Sonderband   *G. Tetzlaff* (Hrsg.), 2002:- Atmosphäre - Aktuelle Beiträge zu Luft, Ozon, Sturm, Starkregen und Klima

Band 29   *U. Harlander*, 2003: On Rossby wave propagation in atmosphere and ocean

Band 30   *A. Raabe* und *K. Arnold* (Edn.), 2003: Meteorologische Arbeiten aus Leipzig VIII

Band 31   *M. Wendisch*, 2003: Absorption of Solar Radiation in the Cloudless and Cloudy Atmosphere

Band 32   *U. Schlink*, 2003: Longitudinal Models in Biometeorology: Effect Assessment and Forecasting of Ground-level Ozone

Band 33   *H. Heinrich*, 2004: Finite barotrope Instabilität unter synoptischem Antrieb

Band 34   *A. Raabe* und *K. Arnold* (Edn.), 2004: Meteorologische Arbeiten aus Leipzig IX

Band 35   *C. Stolle*, 2004: Three-dimensional imaging of ionospheric electron density fields using GPS observations at the ground and onboard the CHAMP satellite

Band 36   *A. Raabe* und *K. Arnold* (Edn.), 2005: Meteorologische Arbeiten (X) und Jahresbericht 2004 des Institutes für Meteorologie der Universität Leipzig

Band 37   *A. Raabe* und *K. Arnold* (Edn.), 2006: Meteorologische Arbeiten (XI) und Jahresbericht 2005 des Institutes für Meteorologie der Universität Leipzig

Band 38   *K. Fröhlich,* 2006: The Quasi Two-Day Wave – its impact on zonal mean circulation and wave-wave interactions in the middle atmosphere

Band 39   *K. Radtke*, 2006: Zur Sensitivität von Starkwindfeldern gegenüber verschiedenen meteorologischen Parametern im Mesoskalenmodell LM

Band 40   *K. Hungershöfer*, 2007: Optical Properties of Aerosol Particles and Radiative Transfer in Connection   with Biomass Burning

Band 41   *A. Raabe* (Hrsg.), 2007: Meteorologische Arbeiten (XII) und Jahresbericht 2006 des Institutes für Meteorologie der Universität Leipzig

Band 42   *A. Raabe* (Hrsg.), 2008: Meteorologische Arbeiten (XIII) und Jahresbericht 2007 des Institutes für Meteorologie der Universität Leipzig

Band 43   *A. Kniffka ,* 2008: Einfluss der Inhomogenitäten von Aerosol, Bodenalbedo und Wolken auf das aktinische Strahlungsfeld der Atmosphäre

Band 44   *M. Barth, 2009*: Akustische Tomographie zur zeitgleichen Erfassung von Temperatur- und Strömungsfeldern

Band 45   *A. Raabe* (Hrsg.), 2009: Meteorologische Arbeiten (XIV) und Jahresbericht 2008 des Institutes für Meteorologie der Universität Leipzig

Band 46   *G. Stober, 2009*: Astrophysical Studies on Meteors using a SKiYMET All-Sky Meteor Radar

Band 47   *A. Raabe* (Hrsg.), 2010: Meteorologische Arbeiten (XV) und Jahresbericht 2009 des Institutes für Meteorologie der Universität Leipzig